COBALT-BASED CATALYSTS TO BOOST WATER SPLITTING REACTION FOR WEARABLE APPLICATION

MING YANG

PhD

The Hong Kong Polytechnic University

2024

The Hong Kong Polytechnic University

School of Fashion and Textiles

Cobalt-Based Catalysts to Boost Water Splitting Reaction for Wearable Application

MING Yang

A thesis submitted in partial fulfilment of the requirements for the degree of Doctor of Philosophy

September 2023

CERTIFICATE OF ORIGINALITY

I hereby declare that this thesis is my own work and that, to the best of my knowledge and belief, it reproduces no material previously published or written, nor material that has been accepted for the award of any other degree or diploma, except where due acknowledgement has been made in the text.

_____ (Signed)

Yang MING (Name of student)

ABSTRACT

The energy shortage caused by the consumption of fossil fuels has imposed threats to the modern society. Hydrogen as a clean energy can be generated from various sources by consuming thermal energy, solar energy, electricity. Among these energy sources, the intensive exploration of photo/electrocatalysts during the past three decades attested water splitting reaction as a promising solution. In current situations, there is urgent demand in lowering down the cost of hydrogen/oxygen production by electricity/solar energy. One solution is to substitute the noble metal catalysts by earth abundant element. Therefore, the enhancement of catalytic performance via modulating the catalysts' intrinsic properties (e.g. electronic environment), morphologies and topologies has been continuously studied. Meanwhile, hydrogen therapy as its terminal application also attracts increasing interests. Herein, the synthesis and evaluation of cobalt-based electro/photocatalysts have been investigated. Moreover, a customized electrolyzer has been designed and constructed, based on the as-synthesized catalysts and textile substrates.

Firstly, cobalt oxides at carbons derived from metal-organic frameworks (ZIF-8/ZIF-67) were prepared and modulated by post-phosphine treatment (P-CoO_x/NCs). With the assistance of polyvinyl pyrrolidone, the resultant carbons obtained a high surface area (S_{BET}= 645.7 m^2 g^{-1}) as well as mesoporous topologies after pyrolysis. Moreover, the electronic environment of cobalt-cobalt oxides protected by carbon layers was further tuned by doping phosphorus atoms. These strategies not only enhanced the catalytic performance but also facilitated the electron transfer from carbons to cobalt atoms. As

a result, the constructed water splitting cell fabricated with 900P-CoO_x/NCs required a low overpotential (89 mV and 343 mV vs. reservable hydrogen electrode respectively) to drive hydrogen evolution reaction (HER) and oxygen evolution rection (OER) at 10 mA cm^{-2}, a low cell voltage (1.69 V) and a high stability with only 4.7% decay after 15 hours operation in1M KOH.

Secondly, based on the disulphide bonds in wool keratin structure, cobalt sulfide content (4.76wt%) supported by nitrogen/phosphorus co-doped carbons (Co_9S_8/N,P-ACs) were prepared by reduction, carbonization and activation treatments. Owing to the well-constructed pore system (S_{BET} = 439.3 m^2/g), heteroatom doping and distinctive metal electronic environment, the as-prepared catalysts required a low overpotential of 90.7 mV and 295.2 mV to drive HER and OER at 10 mA cm^{-2}. The as-fabricated two electrode cell system possessed a low cell voltage (1.62 V at 10 mA cm^{-2}) and a high stability with 2.7% decay after 15 hours operation in 1M KOH. Meanwhile, an all-flexible and wearable device has been designed and fabricated by 3D printing technique by utilizing hydrogel separator, moisture sensitive salts. This work not only demonstrated a biomass conversion strategy, but also provided a solution for personalized water splitting device.

Thirdly, a close contact core-shell Cadmium Zinc Sulfide @ NiCo layered double hydroxides cocatalyst (CZS@NiCo-LDHs) was facilely synthesized by surface modification of CZS using thioglycolic acid, followed by a hydrothermal growth of electrocatalyst. The obtained CZS@NiCo-LDHs cocatalyst exhibiting an average diameter of 105±5 nm with a firm LDHs shell thickness of 24 nm was obtained. Such

close contact core-shell structure illustrated a hierarchical topology (S_{BET}= 87.69 m^2/g), resulting in easy diffusion of electrolyte, rapid electron-hole separation and efficient transfer of photogenerated electrons. In addition, NiCo-LDHs, as typical water splitting electrocatalysts (η_{10} for HER= 185 mV in 0.1M Na_2SO_4), received the excited electrons. Meanwhile, the metal ions in LDHs functioned as active sites. The high coverage of LDHs on CZS, as a result, contributed to a high PHE rate of ~18.75 mmol g^{-1} h^{-1}, and a favorable photostability in 5 cycles under visible light irradiation (300W, λ> 420nm). Further density function theory calculations indicate an apparent redistribution of electron after introducing LDHs. Moreover, nickel sites on CZS@NiCo-LDHs are responsible for adsorption of hydrogen atoms, which provide cocatalyst with enhanced PHE activity.

In conclusion, this thesis not only explored cobalt-based photo/electrocatalyst by the strategies of protective shell design, hetero atom doping, morphology control and heterojunction construction, but also prepared one flexible customized electrochemical cell. These designing principles have shown significant improvement in catalytic performance and stability, which explore potential industrial applications. Hence, this work based on the synthesis of cobalt-based catalysts and its optimizing strategy paved new ways to design highly efficient electro/photocatalysts.

LIST OF PUBLICATIONS

Related Journals

(1) **Ming, Y.**; Wang, Y.D.; Hua, J.C.; Liu, C.; Li, J.S.; Fei, B. N/P codoped Micro-Mesoporous Carbons Derived from PVP-Zn0.2@ZIF-67 with Tunable Metal Valence States towards Efficient Water Splitting, *ChemElectroChem*, **2023**, DOI: 10.1002/celc.202300283.

(2) **Ming Y.**, Liu C., Hu X., Yu R.J., Shi S., Li J.S., Fei B. Sustainable Engineering of Wool Keratin Towards Cobalt Atoms Fixation for Enhanced Electrocatalytic Water Splitting, *Materials Today Sustainability*, **2023**, 25, 100635.

(3) **Ming Y.**, Cheng Z.X., Shi S. Su J., Wu H.B., Chen D.M., Cai W., Yang M.Y., Hu X., Yu R.J., Li J.S, Fei B. Interfacial Engineering towards Full Coverage of CdZnS Nanospheres by Layered Double Hydroxides for Boosted Visible-Light Driven H_2 Evolution, *Small*, **2024**, https://doi.org/10.1002/smll.202309750.

Other Journals

(1) Shi, S.; **Ming, Y.**; Wu, H.; Zhi, C.; Yang, L.; Meng, S. A Bionic Skin for Health Management: Excellent Breathability, in-Situ Sensing, and Big Data Analysis. *Adv. Mater.* **2023**, 1–33. https://doi.org/10.1002/adma.202306435.

(2) Shi, S.; Si, Y.; Li, Z.; Meng, S.; Zhang, S.; Wu, H.; Zhi, C.; Io, W. F.; **Ming, Y.**; Wang, D.; Fei, B.; Huang, H.; Hao, J.; Hu, J. An Intelligent Wearable Filtration System for Health Management. *ACS Nano* **2023**, 17 (7), 7035–7046.

(3) Shi, S.; Wu, H.; Zhi, C.; Yang, J.; Si, Y.; **Ming, Y.**; Fei, B.; Hu, J. A Skin-like Nanostructured Membrane for Advanced Wound Dressing. *Compos. Part B Eng.*

2023, *250* (August 2022), 110438.

(4) Shi, S.; Zhi, C.; Zhang, S.; Yang, J.; Si, Y.; Jiang, Y.; **Ming, Y.**; Lau, K. T.; Fei, B.; Hu, J. Lotus Leaf-Inspired Breathable Membrane with Structured Microbeads and Nanofibers. *ACS Appl. Mater. Interfaces* **2022**, 144, 39610-39621.

Book Chapter

(1) Fei, B.; **Ming, Y.** Assembly of nanomaterials for textile applications. *Encyclopedia of Nanomaterials*, **2021**, 3, 324-338, ISBN: 9780128224236.

(2) Fei, B.; Li, Y.C.; **Ming, Y.** Layered Boron Nitride Derived Flame Retardants for Fire-Safe Polymeric Materials. Two-Dimensional Nanomaterials for Fire-Safe Polymers, **2023**, 16, ISBN: 9781003327158.

Conferences

(1) **Ming, Y.** Fei, B. Fixation of Cobalt Atoms in Keratin-Based Activated Biochar for Efficient Electrocatalytic Water Splitting. **PAIR Conference 2023: Research Excellence for Societal Impacts**, 8th -11th May 2023, HongKong, China (Poster).

(2) **Ming, Y.** Fei, B. Strongly coupled heterojunctions between NiCo layered double hydroxides (NiCo-LDHs) nanosheets and Cd0.75Zn0.25S particles for enhanced photocatalytic H2 evolution**. 74th Annual Meeting of the International Society of Electrochemistry,** 3rd-8th September 2023, Lyon, France (Oral).

ACKNOWLEDGEMENTS

First of all, I would like to express my sincere appreciation to my supervisor Prof. Fei Bin, Professor at the School of Fashion and Textiles, the Hong Kong Polytechnic University for offering the opportunity to conduct my PhD research. The detail guidance and discussion let me learn how to design and conduct my further research with critical thinks and sensitivity to the frontier.

I am grateful for the discussion and guidance from my groupmates in all four years. I also appreciate for those technicians from school and research centre for guiding my research and support my studies at PolyU.

Last but not least, I'd like to express my sincere thanks to my parents and beloved one for their kindly supporting and comforts when I encounter difficulties and loses. Without abovementioned discussion and supporting, I cannot devote my all efforts to my PhD career.

TABLE OF CONTENTS

LIST OF ABBREVIATIONS

1D	One-dimensional
2D	Two-dimensional
3D	Three-dimensional
ACF	Amorphous Carbon Framework
CB	Conduction Band
CV	Cyclic Voltammetry
CVD	Chemical Vapor Deposition
C_{dl}	Double Layer Capacitance
CNTs	Carbon Nano Tubes
ECSA	Electrochemical Surface Area
EXFAS	Extended X-ray Absorption Fine Structure
HER	Hydrogen Evolution Reaction
LSV	Linear Sweep Voltammetry
LDHs	Layered Double Hydroxides
MOFs	Metal Organic Frameworks
NCs	Nitrogen doped carbons
OER	Oxygen Evolution Reaction
PHE	Photocatalytic Hydrogen Evolution
RHE	Reversible Hydrogen Electrode
RDS	Rate Determining Step
SACs	Single Atom Catalysts

VB	Valence Band
XANES	X-ray Absorption Near-edge Structure
ZIFs	Zeolitic Imidazolate Frameworks

LIST OF FIGURES

Fig. 2.10. Schematic illustration of the effect of O-vacancy on tensile strain of CoO nanorods; (b) corresponding HER performance of strain-engineered CoO nanorods; (c) HRTEM and SEM images of prepared CoO nanorods on stainless steel foam [37].

Fig. 2.11. (a) Top and side views of relaxed MoS_2 (top) and $Co(OH)_2$ (bottom) edges with *OH and *H adsorption. (b) Top and side views of relaxed MoS_2 (top) and $Co(OH)_2$ (bottom) edges with *H adsorption. Dark green, yellow, blue, red and white spheres represent Mo, S, Co, O and H atoms, respectively. (c) Free energy diagrams of HER on the edges of MoS_2, $Co(OH)_2$, and Co-Ex-MoS_2 sample. (d) Diagram showing HER catalytic reaction in Co-Ex-MoS_2[1].

Fig. 2.12. (a) Schematic representation of the synthesis of Co_9S_8@C; (b) TEM images ; corresponding elemental mapping images of Co_9S_8@C, and comparison of the chemical stabilities in 0.5 M H_2SO_4 for 24 h of Co_9S_8@C versus Co_9S_8; (c) SEM image and TEM image of Co_9S_8/WS_2 nano rhombus arrays; (d) HRTEM image of one side edge of the Co_9S_8/1L MoS_2, HAADF-STEM, STEM-EDX mapping images of Co_9S_8/1L MoS_2 supported on CNFs; (e) Reaction pathways of hydrogen atom adsorption and hydrogen molecule desorption on Co_9S_8/1L MoS_2, Co_9S_8/2L MoS_2, and Co_9S_8/3L MoS_2 for HER.

Fig. 2.13. (a) Calculated free energy diagram of the HER for (i) *H_2O and (ii) *1/2H_2 on Co, Co_2P, Co/Co_2P@ACF/CNT HNCs-800, 900 and 1000. (b) The contact angles of a drop of 1.0 M KOH on (i): ZIF67 precursor, (ii): Co/Co_2P@ACF/CNT HNCs-800, (iii): Co/Co_2P@ACF/CNT HNCs-900 and (iv): Co/Co_2P@ACF/CNT HNCs-1000. (c) NBO charge distribution on Co, Co_2P, Co/Co_2P@ACF/CNT HNCs-800, 900 and 1000. (d) Calculated DOS of Co/Co_2P@ACF/CNT HNCs-800, 900 and 1000 and their corresponding d-band center potentials[2]. Ji *et al*[3] reported the synthesis of nano

porous CoP_3 nanowire located on the Ti mesh by acid etching of MnO_2 forming agent. The obtain np-CoP_3/TM possess high performance with overpotential of 76 mV at 10 mA cm^{-2} and good stability for at least 60 h in alkaline environment.

Fig. 2.14. (a) The orbital splitting Co octahedra and tetrahedra sites in cobalt oxides; (b) Representative illustration of Co 3d - O 2p interactions and corresponding DOS plots; (c) SEM and TEM images of Cu_2O nanowires and derived CoO_x hollow nanowires; (d) Corresponding water oxidation performance of CoO_x hollow nanowires[61].

Fig. 2.15 (a) The synthetic process of N-CoS_2 and CoS_2; (b) Linear sweep voltammetry (LSV) plots of Co(OH)F, N-CoS_2, CoS_2, and IrO_2 ; (c) The corresponding Tafel slope plots; (d) Top view of the optimized structure of CoS_2 (001) surface; (e)**.** The Mülliken charge analysis of Co1 site in CoS_2 (001) and N-CoS_2 (001) (left panel), and the adsorption free energies of water on Co1 top sites of CoS_2 (001) and N-CoS_2 (001) surfaces (right panel; (f) The schematic diagram of polarity water molecule and the water adsorption equation[4].

Fig. 2.16. (a) Schematic illustration of the synthetic process of hierarchical NiCo-LDH/P-CdS. HRTEM of (b) P-CdS and (c) NiCo-LDH/P-CdS composites. (d) Synthetic process of Co_9S_8/Cd/CdS Z-heterojunction; (e) TEM image of Co9S8/Cd/CdS nanorods; and (f) PHE course plot of various CdS based photocatalysts [80].

Fig. 2.17. (a) Illustration of wearable devices based on conductive textile substrates; (b) Electronic units in this wearable device; (c) Design of data processing procedures and wireless communication [91].

Fig. 2.18 Potential electron pathways for an electrochemical wearable device (a)

Chapter 4

nanoparticles (Scale bar: 500 nm); and (e) Corresponding EDS spectrum and table summary of composition.

Fig. 4.11. (a-e) SEM and corresponding digital images of PVP-Zn_x@ZIF-67 (x= 0, 0.2, 0.4, 0.6, 0.8).

Fig. 4.12. XRD patterns of (a) PVP-Zn_x@ZIF-67, and (b) Carbonized PVP-Zn_x@ZIF-67; (c) Raman spectra and (d) HER polarization curves of carbonized PVP-Zn_x@ZIF-67.

Fig. 4.13. (a) HER polarization curves, (b) Corresponding Tafel slopes and (c) Nyquist plots of CoO_x/NCs treated with 0, 600, 900, 1200 mg of P precursors and 20 wt% Pt/C benchmark at a sweep rate of 5mV/s; (d) OER polarization curves, (e) Corresponding Tafel slopes and (f) Nyquist plots of CoO_x/NCs treated with 0, 600, 900, 1200 mg of P precursors and IrO_2 benchmark at a sweep rate of 5 mV/s in 1_M NaOH; (g) Double layer capacitance; (h) LSV curves of 900 P-CoO_x/NCs after cycling; (i) SEM image of 900 P-CoO_x/NCs after cycling.

Fig. 4.14. CV scans at different scan rates for (a) 20 wt% Pt/C; (b) 600P-CoO_x/NCs; (c) 900P-CoO_x/NCs and (d) 1200P- CoO_x/NCs.

Fig. 4.15. (a) Cell voltage of overall water splitting reaction (900 P-CoO_x/NCs || 900 P-CoO_x/NCs); (b) Chronopotentiometry curve for 900P-CoO_x/NCs at 1.69 V vs. RHE; (c) XRD pattern and (d) Raman spectrum of 900 P-CoOx/NCs after cycling test; (e) Digital image of water splitting device; (f) Collected gas volume and calculated Faraday efficiency of 900 P-CoOx/NCs.

Chapter 5

Fig. 6.2 Thermogravimetric analysis of obtained PVP capped CZS nanoparticles and PVP polymer.

Fig. 6.3 (a) TEM and (b) High-resolution TEM of cadmium zinc sulfide (CZS) nanospheres, (c) Optimized geometry of one TGA molecule on the CZS (101) plane (upper: on top site of Cd atom, lower on top site of Zn atom, purple: Cd atom, grey: Zn atom, yellow: S atom, brown: carbon atom, red: oxygen atom, light pink: hydrogen atom), (d-e) ζ-potential plot of CZS, Thioglycolic acid modified CZS (TGA-CZS) and NiCo-layered double hydroxides dispersed in ethanol.

Fig. 6.4 TEM images of (a) NiCo-LDHs, CZS@NiCo-LDHs core-shell structure at (b) low and (c) high magnification, (d) HRTEM image of selected area (enlarged figure: inverse FFT image of corresponding CZS and NiCo-LDHs lattice spacing), (e) HADDF-STEM image and (f-j) corresponding EDS elemental mapping of Cd, S, Ni, Co and overlayed elements.

Fig. 6.5 SEM image of (a) pure NiCo-LDHs nanoflower; TEM image of (b) CZS@NiCo-LDHs sample; (c) CZS@Ni-LDHs and corresponding (d) HRTEM image (insert: inverse FFT image of CZS@Ni-LDHs); (d) TEM image and (f) HRTEM image of CZS/NiCo-LDHs composites (insert: inverse FFT image of composite).

Fig.6.6 Raman spectra; (b) N_2 adsorption and desorption isotherms of CZS; CZS@Ni-LDHs; CZS@NiCo-LDHs; CZS/NiCo-LDHs and pure NiCo-LDHs.

Fig. 6.7 (a) X-ray diffraction patterns, (b) Pore size distributions of CZS, CZS@NiCo-LDHs, NiCo-LDHs, CZS/NiCo-LDHs, and NiCo-LDHs; (c) Water contact angles of FTO glass substrate, CZS, CZS@NiCo-LDHs, NiCo-LDHs, CZS/NiCo-LDHs, and NiCo-LDHs; X-ray photoelectron spectroscopy of (d) Cd 3d, (e) Ni 2p, (f) Co 2p of corresponding samples.

Fig. 6.8 (a)Zn 2p and (b) S 2p spectra of CZS; CZS@Ni-LDHs; CZS@NiCo-LDHs; CZS/NiCo-LDHs and pure NiCo-LDHs.

Fig. 6.9. (a) Time courses of photocatalytic H_2 evolution (PHE) and (b) PHE rate of CZS, CZS@Ni-LDHs, CZS@NiCo-LDHs, CZS/NiCo-LDHs, and NiCo-LDHs in 10 v% TEOA aqueous solution (note: Eosin Y sensitization is employed for pure NiCo-LDHs, which functions as semiconductor); (c) PHE stability test of CZS, CZS@NiCo-LDHs, and CZS/NiCo-LDHs over 12 hrs; (d) linear sweep voltammetry (5 mV/s), (e) Tafel slopes of commercial 20wt% Pt/C, CZS, CZS@Ni-LDHs, CZS@NiCo-LDHs, CZS/NiCo-LDHs, and NiCo-LDHs in 1_M KOH; (f) LSV curve of CZS@NiCo-LDHs on ITO substrate before and after light irradiation; (g) TEM; (h) Ni 2p; and (i) Co 2p spectra before and after PHE stability test.

Fig. 6.10 (a) XPS survey, (b) Cd 3d spectra, (c) Zn 2p spectra, (d) S 2p spectra of CZS@NiCo-LDHs after PHE stability test.

Fig. 6.11 Post TEM image of CZS/NiCo-LDHs composites after stability test.

Fig. 6.12 (a) Photoluminescence (PL) spectra (insert: excitation spectrum of CZS, λ_{exc} = 340 nm), (b) Time-resolved PL decay spectra (insert table: summary of electron lifetime) of CZS, CZS@NiCo-LDHs and CZS/NiCo-LDHs; (c) Chopped i-t curves, (d) Electrochemical impedance spectra (EIS) under illumination of CZS, CZS@Ni-LDHs, CZS@NiCo-LDHs, CZS/NiCo-LDHs in 0.1 M Na_2SO_4, load 0.4 mg/cm^2.

Fig. 6.13 UPS spectra of CZS, NiCo-LDHs, and CZS@NiCo-LDHs.

Fig. 6.14 (a) UV-visible absorption spectra, (b) Tauc plots of CZS, CZS@Ni-LDHs, CZS@NiCo-LDHs, CZS/NiCo-LDHs and NiCo-LDHs; (c) VB-XPS spectra of CZS, NiCo-LDHs and CZS@NiCo-LDHs; (d) Band alignment between CZS and NiCo-LDHs under different conditions; (e) Band alignment of CZS@NiCo-LDHs, related to

water splitting potentials; (f) Charge density plot and (g) Density of states of CZS, CZS@NiCo-LDHs and NiCo-LDHs.

Fig. 6.15. AFM height profiles and corresponding kelvin-probe force microscopy of (a) CZS, (b) CZS/NiCo-LDHs, and (c) CZS@NiCo-LDHs.

Fig. 6.16. Comparison between Zeta potentials and Kelvin probe measured surface potentials of CZS, CZS/NiCo-LDHs, and CZS@NiCo-LDHs.

LIST OF TABLES

Chapter 1. Introduction

1.1 Background

Water splitting to generate hydrogen and oxygen via electro/photocatalytic approach has attracted intensive attentions as an effective solution to the global warming[5,6]. Among various candidates, cobalt-based materials (e.g. cobalt oxides, sulfides, selenides) have been regarded as one of promising catalysts to boost the water splitting reaction. Nevertheless, scientists have devoted tremendous efforts towards the modulation of synthetic and tuning strategies such as heteroatom doping, defects engineering, atom intercalation and topographical control. By adopting these approaches, they achieved significantly increase in the number of active sies; modulation of the corresponding electronic environment to enhance the catalytic performance[7–10]. Moreover, understand of the binding energies of intermediates onto the catalysts surfaces gives rational design of catalysts and possibility to explore the reaction pathways. Typically, metal atoms can be coordinated with adjacent non-metal atoms such as M-N-Cs which have distinctive electronic environment of M-M bond as well as adsorption energy for intermediates. Under this situation, those sites exhibit lowest adsorption free energy are active sites which facilitates the reaction kinetics[11–13]. Although by modifying and design suitable catalysts can improve the activity of reactions in a huge magnitude[14,15], there is still physical limit to the amount of catalyst loaded onto the electrode. As a result, the in-situ growth of catalyst on the electrode can a promising solution to the stability of the cell and is free of polymer binders which partially hinders the catalytic performance. In addition to this, the overall energy consumption of electrocatalytic water splitting reaction is still high in which the high electricity input usually results into low production rate of H_2 and O_2. Nevertheless, the

utilization of electrochemical reactions in wearable applications has been recognized as a promising approach for the continuous monitoring of human body health. Consequently, this thesis also addresses the investigation of appropriate electrocatalysts tailored for wearable applications.

Apart from the electricity as driving force, the photocatalytic water splitting reaction which utilizes light as the driving force shows an alternative and more environmental-friendly reaction can be achieved. It should be noticed that the band gap of photocatalyst should be exactly at 1.23 eV since thermodynamical determined potential of water splitting reaction is 1.23 eV. Moreover, the conduction band and valence band of the catalysts should be located at the redox potentials of H_2 and O_2 evolution reaction which restricts the choices of photocatalysts[16–18]. In practice, the utilization of higher incident light energy such as ultraviolet light is employed to trigger the redox reaction. Moreover, the heterojunctions, cocatalysts (e.g. Pt) photosensitizes and electron donors are usually employed to improve the hydrogen evolution rate[19].

1.2 Research objectives

With all the problems and promising materials commented as above, we aim to develop robust and efficient cobalt oxides/sulfides/hydroxides catalysts towards electro/photocatalytic water splitting reaction. In this case, the following aspects of electro/photo catalysts will be mainly focused: i) the physical and chemical properties (e.g., morphology, topology, surface electronic environment) of electro/photocatalysts; ii) explore the effects of experimental treatments including doping, pore system construction on catalytic performance; iii) identify the active sites in the cobalt oxides/sulfides/hydroxides samples by post treatments, and proposed corresponding

reaction pathways for understanding; iv) the design and construction of electrochemical device for wearable application. Finally, the detail research objectives are listed as follows:

(1) To fabricate Co oxides nanoparticles using MOFs precursors and dope heteroatoms into carbonized MOFs for water splitting reaction.

(2) To synthesize Co sulfide nanoparticles by chemically fixing cobalt atoms in wool fibers directly, explore the advantages of chemical fixation strategy over traditional biomass conversion method.

(3) To design and create an electrochemical water splitting device for wearable application and assess its performance in moisture conversion to H_2/O_2.

(4) To combine photocatalysts with Co based electrocatalysts for the photo/electrochemical hydrogen evolution reaction, explore their related built-in electric field effect.

1.3 Research significance

This thesis focusses on the synthesis, physical and photo/electrochemical characterization of as-obtained catalysts for water splitting applications. The research significance and value can be summarized as follows:

(1) Explore the role of PVP polymer in ZIFs frameworks. Identification of PVP's structural evolution during carbonization process and protective role in post phosphorization. Instead of the formation of CoP nanoparticles, the P hetero atom doping into carbons also influence the electronic environment of cobalt active sites. Moreover, a series of post treatments are conducted to confirm the active sites in HER and OER, respectively.

(2) Biomass conversion to electrocatalysts show potentials in carbon neutralization and

waste conversion. An innovative approach is developed to selectively fix cobalt element, utilizing the natural disulfide bonds in wool keratin structure. Compared with traditional absorption strategy, this reductive fixation method shows outstanding in the catalysts' loading, and superior catalytic performance.

(3) Based on above biomass derived electrocatalysts, a flexible and attachable moisture digester is designed, constructed, and assembled for practical applications. Such digester can obtain a continuous current for 8 hrs at 3V input and electrochemically convert absorbed moisture to hydrogen.

(4) Rational design of heterojunction between semiconductor and cocatalysts have been successfully achieved by interfacial engineering method. By carefully modifying the semiconductor's surface electronic environment, the cocatalyst can be loaded onto light absorber's surface with complete coverage. Moreover, this approach is repeatable and of easy fabrication at room temperature.

1.4 Thesis outline

The thesis is organized as following sections:

Chapter 1 is to introduce the research background and remaining challenges in the field of electro/photo catalytic water splitting reaction. Research objectives are also included in this chapter.

Chapter 2 is to conduct the literature review of electrocatalytic/photocatalytic water splitting reaction, the fundamental principles of water splitting reaction, utilizing electricity and solar energy are covered. The optimization strategies for electro/photocatalysts are detailly introduced and analyzed. Finally, the introduction of electrochemical devices for wearable applications based on textile substrates is covered.

Chapter 3 is to introduce major synthetic methods, fundamental setups of electro/photo chemical cell, and characterization methods in this thesis.

Chapter 4 is to synthesize multivalence state of cobalt oxides by carbonization of PVP assisted ZIF-8/ZIF-67, followed by a series of post treatments (phosphine treatment, oxidation treatment, acid leaching). The catalytic performance of CoO_x is studied by electrocatalytic water splitting reactions.

Chapter 5 is to synthesize cobalt sulfides by innovatively utilizing the disulfide bonds in natural wool keratin structure. Further design of personalized water splitting device is given and tested in real environment.

Chapter 6 is to synthesize core-shell structure of NiCo-layered double hydroxides onto the cadmium zinc sulfides by surface engineering. The heterostructure is studied by optical measurements and DFT simulations. While the catalytic performance is studied by photocatalytic hydrogen evolution and DFT simulations.

Chapter 7 is the conclusion of whole thesis, perspectives and outlook for photo/electrocatalytic water splitting reaction are discussed.

Chapter 2. Literature review

The industrial application of water photo/electrolysis for hydrogen production is still challenging. A significant issue is the lack of low-cost, highly efficient photo/electrocatalyst, which results in low utilization of solar energy/ high consumption of electricity. Current studies have demonstrated that Mo-based catalysts[20,21] exhibit attracting potentials in water splitting reactions. However, their scarcity in earth leads to a high price (Mo: USD 53/kg, Co: USD 33/kg, Ni: USD 20/kg, Cu: USD 8/kg, Zn: USD 2/kg). Hence the large-scale production is still far beyond satisfaction. Consequently, the development of efficient and cost-effective non-noble metal photo/electrocatalyst holds reaction implications for enhancement in water splitting.

In recent years, researchers have extensively designed and developed a plethora of low-cost catalyst for water splitting, including transition metal oxides, sulfides, selenides, carbides and nitrides, single-atom catalysts. However, the intrinsic activity of these materials falls significant drawbacks compared to platinum-carbon catalysts. Therefore, modifying these materials exhibits crucial research significance. By incorporating morphology design, surface doping, vacancies engineering, heterostructure construction (**Fig.2.1**), it is possible to regulate the intrinsic electronic structure of the materials. This optimization of catalyst surface micro-environment can enhance the adsorption and activation of reactant species, thereby improving their catalytic performance. Owing to the development of characterization techniques, techniques such as X-ray absorption fine structure, X-ray photoelectron spectroscopy, Spherical aberration-corrected TEM allow researchers to investigate the localized coordinative environment, and valence state of metal active sites. Moreover, the in-situ techniques

equip the research with real-time information of metal catalysts, which facilitate the rational design of photo/electrocatalysts.

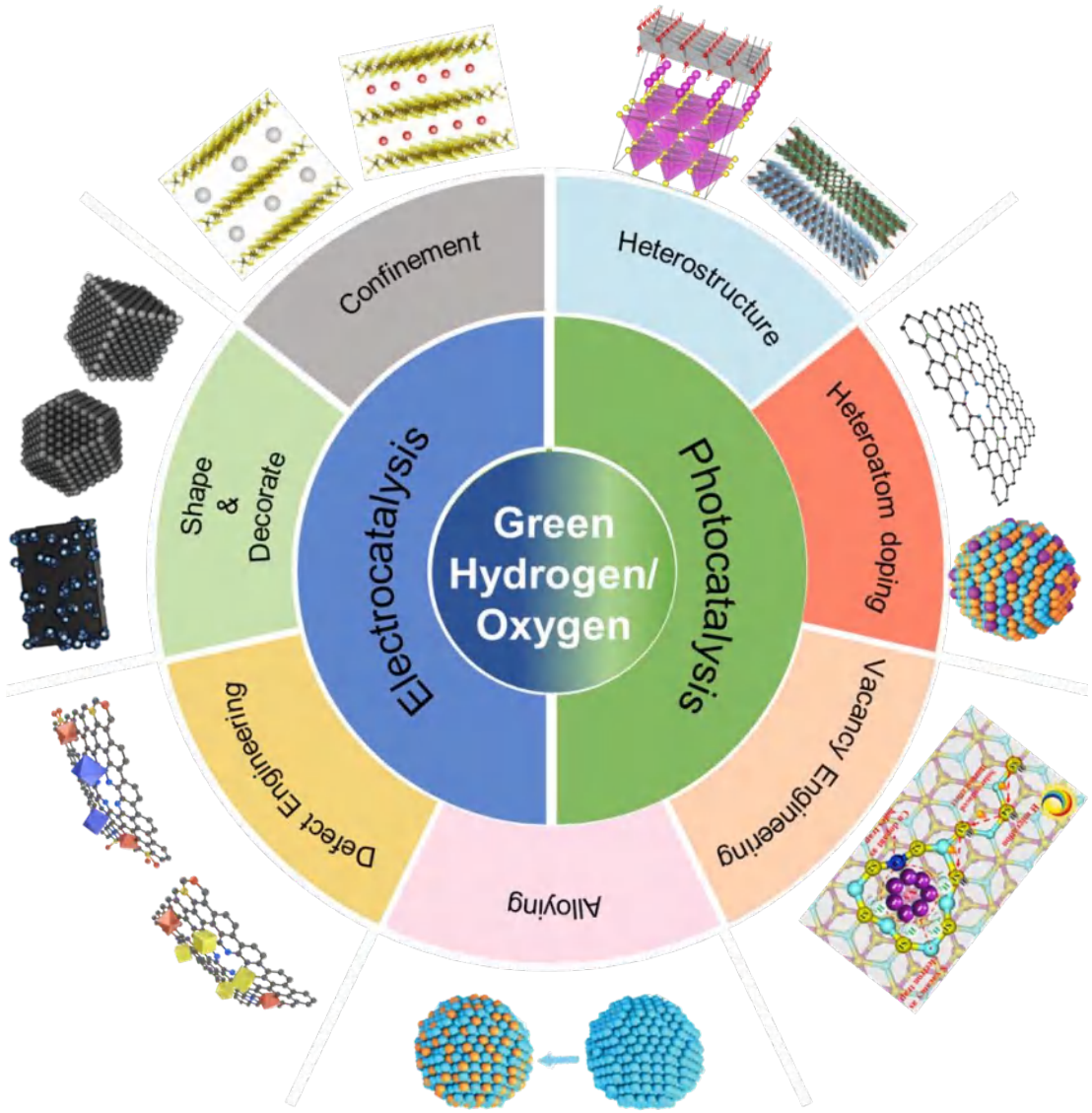

Fig. 2.1. Schematic illustration of potential strategies to enhance the performance of catalysts[7,9,22–24].

In this chapter, the first part of the recent progress and potential studying trend about cobalt-based catalysts for hydrogen evolution reaction (HER), oxygen evolution reaction (OER), and photocatalytic hydrogen evolution (PHE) reaction have been demonstrated and analysed. What's more, based on the above design principle for

catalysts, detail analysis will be paid to understand the catalytic role of these transition-metal based derivatives. With respect to the understanding of mechanism of both reactions, density functional theory (DFT) gives researchers opportunities to obtain a series of reactions intermediate adsorption energies and study the kinetics for a certain catalytic process. Therefore, by combining the modification approach and theoretical investigation, people can design more reasonable experiments. After the discussion of electro/photo catalysts, the introduction of electrochemical devices for wearable application is designed and developed.

2.1 Fundamental principles and electrocatalytic pathways for HER and OER

2.1.1 Principles and electrocatalytic pathways for HER

Hydrogen evolution reaction (HER) is the half reaction of water splitting reaction which is considered as the most efficient way to generate hydrogen. Its mechanism is divided into several steps dependent on the acidic medium (usually 0.5 M H_2SO_4) or alkaline medium (usually 1 M KOH) respectively[25]:

For Volmer step, the electrons first transfer onto the surface of the electrode, then contact with the H_3O^+ sites causing the formation of H_{ads} (Hydrogen atoms adsorbed onto the catalyst surface) while in alkaline medium, water molecules will firstly undergo the dissociation process to provide proton sources. Therefore, for Pt free catalysts, most of them are still of low activity in the alkaline medium due to the sluggish water dissociation kinetics in the Volmer step (**Fig.2.2**).

The HER pathway in acidic medium can be described as follows:

$$H_3O^+ + e^- \rightarrow H_{ads} + H_2O \text{ (}\textit{Volmer step}\text{)} \quad (2.1)$$

$H_{ads} + H_3O^+ + e^- \rightarrow H_2 + H_2O$ (*Heyrovsky step*) (2.2)

$H_{ads} + H_{ads} \rightarrow H_2$ (*Tafel step*) (2.3)

The HER pathway in alkaline medium can be described as follows:

$H_{ads} + H_2O + e^- \rightarrow H_2 + OH^-$ (*Volmer step*) (2.4)

$H_2O + e^- \rightarrow H_{ads} + OH^-$ (*Heyrovsky step*) (2.5)

$H_{ads} + H_{ads} \rightarrow H_2$ (*Tafel step*) (2.3)

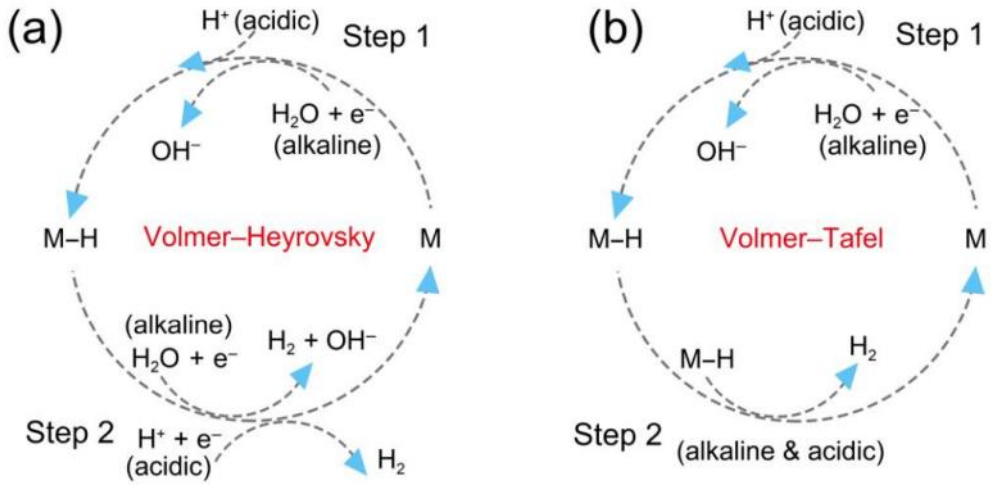

Fig. 2.2. Proposed electron transfer pathway in HER under both acidic and alkaline medium: (a) Volmer-Heyrovsky mechanism, (b) Volmer-Tafel mechanism[26].

For Heyrovsky reaction, an electron coupled with proton transfers to the adsorbed hydrogen atoms, and then generates hydrogen. Another possible Tafel process which can generate hydrogen: two adsorbed hydrogen atoms can produce hydrogen after the combination on the surface. It is important to work out the rate-determining step in HER as it requires the highest energy barrier which is also defined as the elementary step. In acidic medium, if the Volmer reaction is the determining step (Tafe slope of 120 mV dec^{-1}), electrodes should provide more active sites and vacancies for adsorbed

hydrogen atoms to lower the barrier. For Heyrovsky (Tafe slope of 40 mV dec^{-1}) and Tafel reaction (Tafel slope of 30 mV dec^{-1}), the rate of electrolysis can be improved by increasing the reaction area therefore providing more H_{ads}, and this can be achieved by increasing the surface roughness[27]. In most cases, the Volmer reaction is the rate-determining step and the Sabatier principle that one catalyst should possess not too strong or too weak interactions between reactants is a suitable guidance for designing appropriate catalysts[28,29].

Moreover, from the aspects of different catalytic materials, scientists indicated a 'volcano plot' which considers the hydrogen adsorption free energy(ΔG_{H*}) when the intermediate H* undergoes either Volmer-Heyrovsky or Volmer-Tafel pathway (Fig. 2.3)[30] to illustrate catalytic performance. Among these candidates, Pt[31] and Rh [32] based materials are regarded as the outstanding material since it requires lowest Gibbs free energy as well as possesses highest exchange current while their prices limit the large-scale application. Moreover, metals with different facets have been intensively investigated to reveal the mechanism of electrochemical reactions [33–36], and so-called 'single-atom catalysts' (SACs) has been proposed to include this kind of single metal-based catalysts. Recent study[37] showed that Pt atoms which further form clusters with aid of pydirine N possessed better performance and better charge transfer compared with single Pt-based SACs.

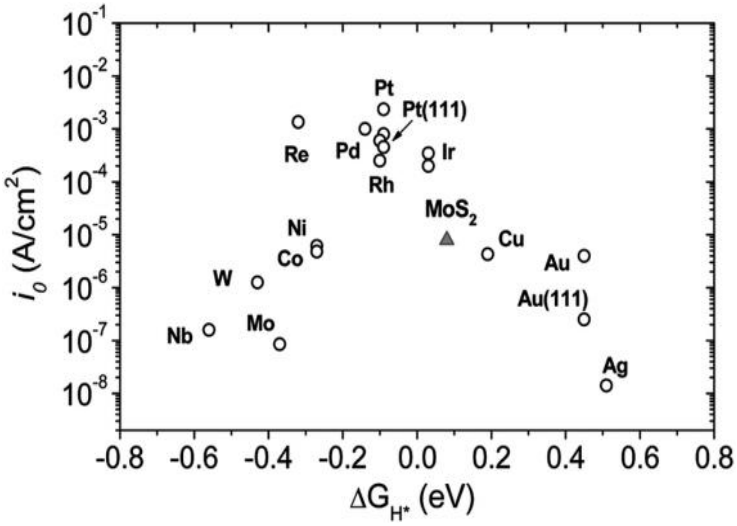

Fig. 2.3. The volcano plot of exchange current density as a function of DFT calculated Gibbs free energy of adsorb hydrogen atoms[38].

2.1.2 Principles and electrocatalytic pathways for OER

Oxygen Evolution Reaction (OER) is the other half reaction of overall water splitting. Currently, two major pathways for the explanation of OER mechanism have been well studied (**Fig.2.4**): 1. Adsorbate evolution mechanism (AEM), and 2. Lattice oxygen oxidation mechanism (LOM). The first one is consisting of a four-electron transfer reaction with the formation of different intermediates including HO_{ads}, O_{ads} and HOO_{ads} where ads represents for the metal active sites. The AEM for OER pathway in acidic medium can be described as follows: [7]

$$H_2O \rightarrow HO\text{ads} + H^+ + e^- \quad (2.6)$$

$$HO_{ads} \rightarrow O_{ads} + H^+ + e^- \quad (2.7)$$

$$O_{ads} + H_2O \rightarrow HOO_{ads} + H^+ + e^- \quad (2.8)$$

$$HOO_{ads} \rightarrow O_2 + H^+ \quad (2.9)$$

The AEM for OER in alkaline medium can be described as follows:

$$OH^- + \text{ads} \rightarrow HO_{ads} + e^- \quad (2.10)$$

$$HO_{ads} + OH^- \rightarrow O_{ads} + H_2O + e^- \quad (2.11)$$

$$O_{ads} + OH^- \rightarrow HOO_{ads} + e^- \quad (2.12)$$

$$HOO_{ads} + OH^- \rightarrow O_2 + H_2O + e^- \quad (2.13)$$

The AEM mechanism is the most adopted mechanism in OER. It is highly related to the catalytic behavior of surface atoms in catalysts. During this process, the water molecular will be oxidized at the catalyst site, forming ox hydroxyl groups or hydroxyl groups in alkaline medium will be directly utilize as the source. Meanwhile, the metal active sites are also oxidized to metal oxyhydroxide species (HOO_{ads}), which is the key intermediate during OER. Currently, efforts have been devoted to detecting this intermediate. Moreover, the adsorption and desorption kinetics on the active sites are also influenced by factors such as pH and temperature of electrolyte.

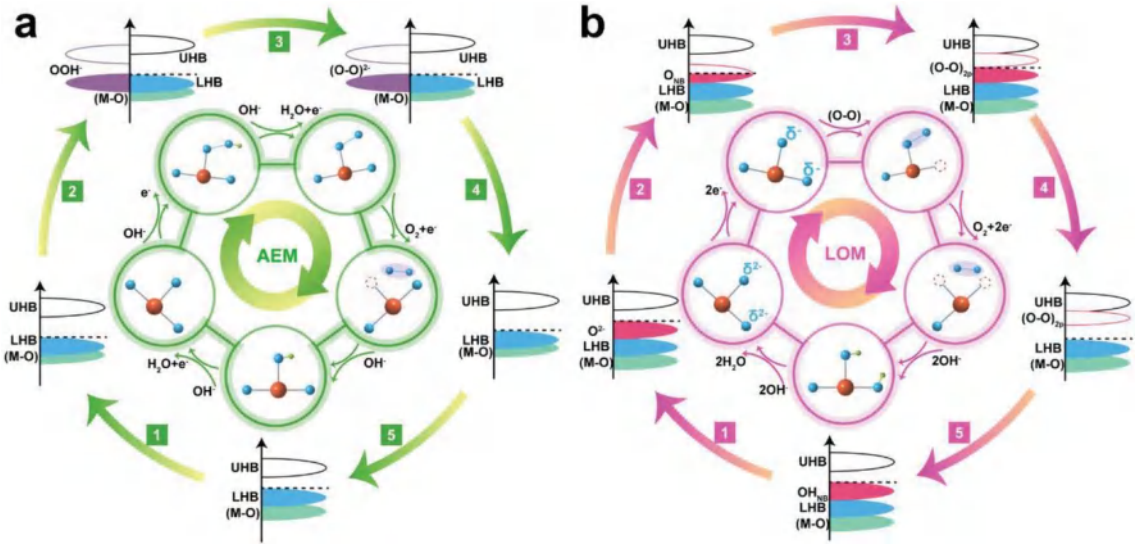

Fig. 2.4. Proposed electron transfer pathway in (a) adsorbate evolution mechanism, where metal atoms function as active sites; and (b) lattice oxygen oxidation process, where oxygen atoms in the lattice act as active sites[39].

The LOM is another major mechanism to explain the intermediate and electron pathway.

Under this circumstance, the catalysts usually are metal oxides with distinguished lattice structure, where metal-oxide bonds/oxygen vacancies may be responsible for catalytic performance. Once the oxygen atoms in the lattice are oxidized and detached to form oxygen molecule, the hydroxyl groups in the electrolyte will be attached to metal atom, for the formation of metal-oxygen bond again. However, the extraction of lattice oxygen, compared with direct utilization of hydroxyl groups, requires higher overpotential to trigger the reaction, and exhibits slower kinetics. Moreover, the debonding of surface metal-oxygen bonds may cause the irreversible reaction, which further reduce the lifetime of electrocatalysts. Such mechanism is highly dependent on the composition of catalysts, e.g., metal phosphides, sulfides will suffer different lattice oxidation mechanisms.

In general, it has been found that the binding energies between OER reaction intermediates OH, O, HOO and surface-active sites are linearly correlated. (shown in **Fig. 2.5**) [7] This implies that the active site, exhibiting a stronger affinity for bonding with hydroxide (OH), also exist enhanced bonding capabilities with oxygen (O) and peroxide (HOO) compared to other active sites. The optimal catalytic surface sites should establish interactions with intermediates, avoiding excessively weak and overly strong binding. Insufficient binding may impede the activation of the reaction, while excessive binding may hinder the effective release of reaction products. In this context, transition metal oxides, including but not limited to Ni, Fe, Co, Cu, and Mn, demonstrate heightened catalytic efficacy in the Oxygen Evolution Reaction (OER). The pivotal step involves the formation of metal hydroxide (HOO-M) through the cleavage of water on an adsorbed oxygen species (O*) located on the crystal facet, thereby playing a critical role in the overall water-splitting process [40].

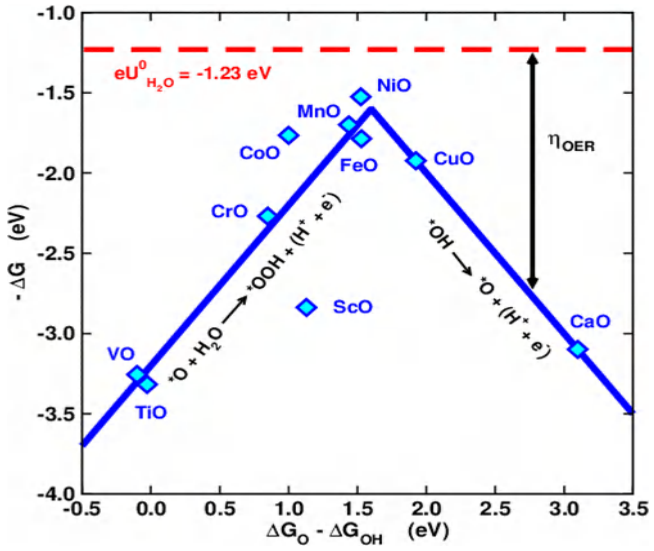

Fig. 2.5. The Sabatier-type volcano plot for the pristine (001) surfaces of the monoxides in the range between CaO and CuO. The descriptor in the x axis is the difference between the adsorption energies of oxygen and hydroxyl. The vertical differences between the red line and the blue lines and points provide an estimation of the oxygen evolution overpotential on the oxides[7].

2.1.3 Electrolyzer design for electrocatalytic splitting reaction

2.1.3.1 Electrolyzer in laboratory and industry

For a typical electrochemical cell, cathode and anode compartments are filled with aqueous electrolyte, and a membrane is inserted into the cell. (Known as H-cell and shown in the **Fig. 2.6**). In this reactor, for HER, the generation of hydrogen takes place at cathode and electrolyte is usually 1_M KOH and OER occurs at anode. In this case, anode and cathode are usually glassy carbon, carbon paper or metal-based electrode on which electrocatalysts can be deposited. An ion exchange membrane which can be proton-conducting or anion-exchange polymer membrane helps the exchanges of ions. [7,41] Therefore current can be generated in between. H-cell configuration can be easily set up and the stability of it is dependent on the properties of catalysts, however, three

electrode working system is limited to the choice of electrolytes (neutral or acidic) which may poison the reaction and possess low current densities (≈ 100 mA cm^{-2}) [42].

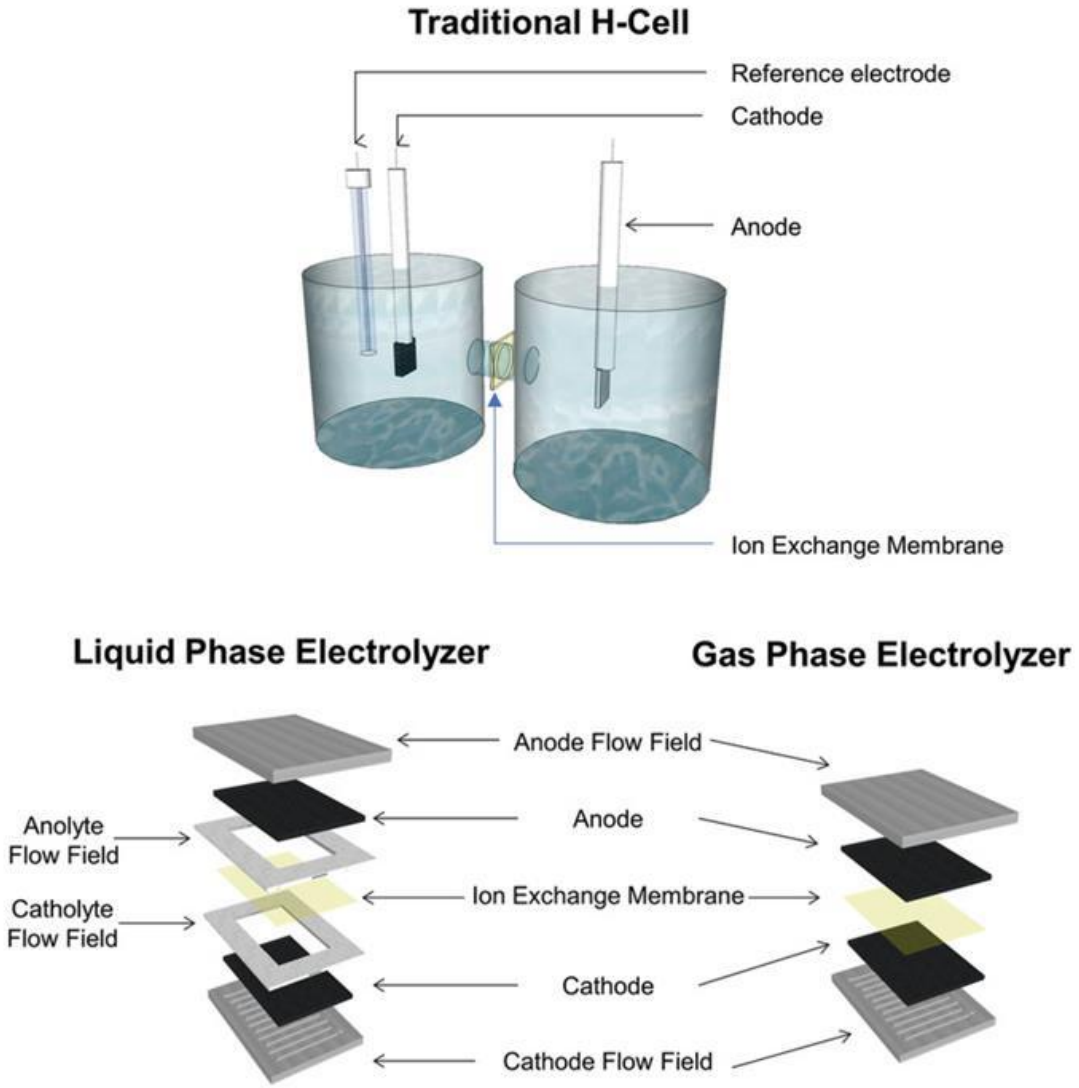

Fig. 2.6. Schematic illustration of traditional H cell, liquid-phase and gas-phase electrolyzer [25].

Currently, alkaline electrolysis technology has advanced to the commercial production scale of megawatts (MW). Alkaline electrolysis employs a liquid potassium hydroxide (KOH) solution as the electrolyte. The membrane separator is a crucial component of the alkaline electrolysis cell. In recent years, polymer membranes with hydroxide ion

conductivity have been developed (e.g., nafion membrane). Traditional alkaline systems have certain limitations in practical applications, particularly in achieving maximum current densities, which are generally lower than 400 mA cm^{-2}. This is because at higher current densities, bubbles generated during electrolysis tend to flow upward along the electrode surfaces, leading to the formation of continuous non-conductive gas films across the entire electrode surface. This sieving effect increases energy consumption and hinders gas transport across the membrane. In current alkaline cells design, the electrodes are consisting of porous grids pressed against the membrane to minimize distance and reduce ohmic resistance. This zero-gap configuration significantly improves electrolysis efficiency, allowing for current densities of up to 2 A cm^{-2}. However, most recent research efforts are still focused on developing highly efficient and stable catalysts. Although significant progress has been made in this regard, there is still a considerable gap to meet the requirements of sustained hydrogen production at high current densities.

The resolving diagram of a PEM electrolysis water system's basic unit is shown in **Fig.2.6**. Typically, the connections between each component are tightly integrated, with a thickness of 5-7 mm. Titanium is commonly used for the metal plates on both ends. The assembly of the membrane is placed in the central part of the electrolysis cell, where water decomposition reactions occur. The membrane is generally a 90-200 μm thick perfluoro sulfonic acid-based proton-conducting polymer membrane (PFSA). The membrane's two sides are porous catalytic layers, which can be coated on both sides of the membrane or on two porous conducting layers. They can also be self-supported catalytic electrode material layers. Liquid water is pumped through the cathode and anode chambers to provide reactants for the reactions on the anode side and remove

excess heat generated during cell operation. There is a quantitative relationship between water flow, working current density, and the temperature difference (temperature difference between the cell inlet and outlet). The produced H_2 and O_2 are collected behind the porous transport layer, and the gas-liquid mixture is pumped to a separator for mass separation. Compared to alkaline electrolysis technology, PEM electrolysis technology offers higher load flexibility and grid-balancing capabilities. PEM electrolysis cells can achieve high current densities (up to 10 Acm^2) and produce high purity hydrogen (up to 99.9999%). PEM electrolysis operates under acidic conditions and has already been commercialized at a multi-megawatt scale. However, further improvements are needed to reduce the cost of electrolytic hydrogen production for mobile applications in European countries. One of the challenges to achieve this cost target is to replace platinum group metals (PGMs) with transition metal-based materials as catalysts. There are two main approaches to reduce the cost of PGMs: using alternative support materials or dispersing PGMs in carbon materials to decrease their usage, and developing non-precious metal catalysts that combine cost advantages with performance benefits as substitutes for PGMs. For the anode reaction, which operates at a voltage range of 1.8-2.0 V, there are fewer alternatives to replace Ir or Ru oxides for the oxygen evolution reaction (OER) under acidic conditions. The loading of IrO_2 can be reduced to 0.5 mg cm^{-2}, but its activity decreases over prolonged electrolysis. Current research focuses on coupling IrO_2 nanoparticles with electronically conductive metal oxides, such as SnO_2, as the substrate.

2.2 Fundamental principles for photocatalytic HER

2.2.1 General principles for photocatalytic hydrogen evolution reaction

Another way to generate the oxygen and hydrogen is to utilize solar energy. Under this

circumstance, semiconductors are explored as the potential light absorption agent. On one hand, the band gap of semiconductors should be smaller than that of equivalent light wavelength (**Fig.2.7. a**), and larger than that of energy for water splitting reaction (ΔG= 1.23 eV, in practical at least 1.6 eV) to achieve efficient solar energy conversion. One the other hand, from the solar energy distribution diagram (**Fig.2.7 b**), only 5% of solar energy lies in the UV region, 43% of the energy accounts in the visible light, which indicates band gap around 2.2 eV is ideal to utilize the half of solar energy.

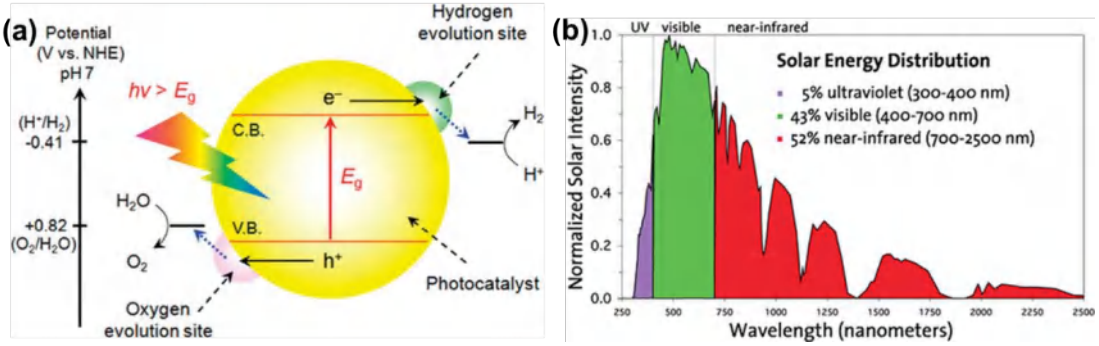

Fig. 2.7. (a) Illustration of photocatalytic water splitting mechanism, (b) Solar energy distribution across the spectrum.

Three steps have been identified during the light absorption at different time scales: 1. the excitation of photoinduced charges happens within a few femtoseconds, 2. charge recombination takes place on the nanosecond scale, 3. the charge separation and surface reaction within the material require a much longer time, in the order of microseconds. It is evident that the time taken for charge separation and surface reaction is relatively longer, making it a crucial intermediate process that links the preceding and subsequent steps.

Therefore, achieving efficient charge separation is of utmost importance for the smooth progress of photocatalytic reactions. However, in the absence of external or intrinsic

driving forces, photoinduced charges tend to distribute randomly and migrate slowly to the surface in the bulk phase. This slow kinetics increases the chances of collisional recombination between photoelectrons and holes in the bulk phase, as well as their capture by defects at the bulk or interface. Consequently, the mentioned questions reduce the actual concentration of photoinduced charges reaching the material surface. Unfortunately, there is currently a lack of effective experimental techniques for directly observing the processes of charge separation, migration, and recombination. The diagram (**Fig.2.8**) below shows the potential substances for photocatalytic splitting, in which metal oxides, sulfides and nitrides show great potentials in overall water splitting reaction.

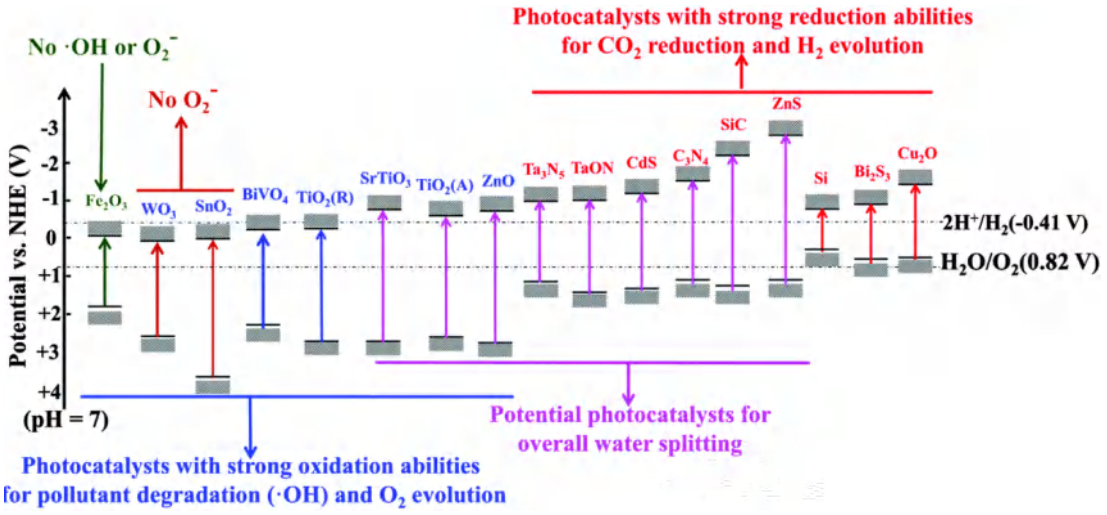

Fig. 2.8. Typical band gaps of semiconductors for the applications of photocatalytic water splitting reaction[43].

The surface electronic structure of semiconductor materials typically poses challenges to the occurrence of electrocatalytic reactions, thereby limiting the favorable reaction kinetics of photoinduced charges at the material surface during photocatalytic processes. Additionally, water splitting reactions involve two interconnected half-reactions (oxidation and reduction) with a positive change in Gibbs free energy for the overall

reaction. This propensity facilitates the recombination of generated hydrogen and oxygen species at the material surface, thereby hindering efficient surface reactions. Specifically, the intrinsic activity, density, and abundance of active sites on semiconductor material surfaces can modulate the dissociation and desorption of surface H_2O molecules and reaction intermediates, thereby influencing the surface catalytic activity. To ameliorate these characteristics, three strategies have been proposed to address photocatalytic activity, the electron transfer efficiency, light absorption: (1) to deposit of highly active electrocatalysts (e.g., metal Pt) onto semiconductor material surfaces to enhance the quantity and activity of catalytic sites. Consequently, an effective photocatalytic material system typically entails the strategic integration of semiconductors with highly active electrocatalysts. (2) Another important procedure is to add sacrificial agents (e.g., methanol, lactic acid, TEOA). The sacrificial agent can help consume the generated holes to boost PHE when electrons are excited to reduce the water molecules. (3) More recently, dye molecules are also found to improve the efficiency of PHE. Different from the sacrificial agent, dye molecules can help to enhance the light absorption of semiconductor, which complement the energy levels of semiconductors. When the dye molecule absorbs light, it can efficiently transfer the energy to the semiconductor, exciting electrons across the dye-semiconductor interface.

2.2.2 Typical band alignments between semiconductor and cocatalysts

The formation of heterojunctions between semiconductor and catalysts, compared to single semiconductors, has emerged as a highly promising approach for the development of advanced photocatalysts, due to the effectiveness in spatially separating electron-hole pairs of heterojunctions.

Conventionally, there are three types of heterojunctions (**Fig.2.9**): straddling bandgap (type-I), staggered bandgap (type-II), and broken bandgap (type-III). In type-I heterojunctions, both electrons and holes accumulate in the conduction band (CB) and valence band (VB) of the semiconductor, respectively. Consequently, efficient separation of electron-hole pairs is hindered, due to the fact that electrons cannot be transferred to higher conduction band. Similarly, type-III heterojunctions do not facilitate effective separation due to the lack of overlapping bandgaps between the two semiconductors or semiconductor/catalysts interface.

Type-II heterojunctions, on the other hand, result in the accumulation of electrons and holes in the CB of the semiconductor with lower reduction potential and the VB of the semiconductor with lower oxidation potential. Although separation of charge carriers is achieved, this arrangement compromises their strong oxidation and reduction capabilities.

To address this issue, the direct Z-scheme heterojunction was introduced. The direct Z-scheme system shares similar band structures with type-II heterojunctions but exhibits a distinct charge-carrier migration mechanism. The direct Z-scheme configuration enables the migration of charge carriers along a pathway resembling the letter "Z". Specifically, electrons accumulate in the CB of semiconductor A. The holes accumulate in the VB of semiconductor B, preserving their strong redox abilities and spatially segregated sites for reduction and oxidation.

In all abovementioned systems, the cocatalysts are regarded as semiconductors. While

for the metallic cocatalyst, the fermi level of cocatalysts should lie in the band gap region of semiconductor, forming Schottky barrier. Consequently, the accumulated electrons will transfer to the Fermi-level of cocatalyst, achieving electron/hole separation after irradiation.

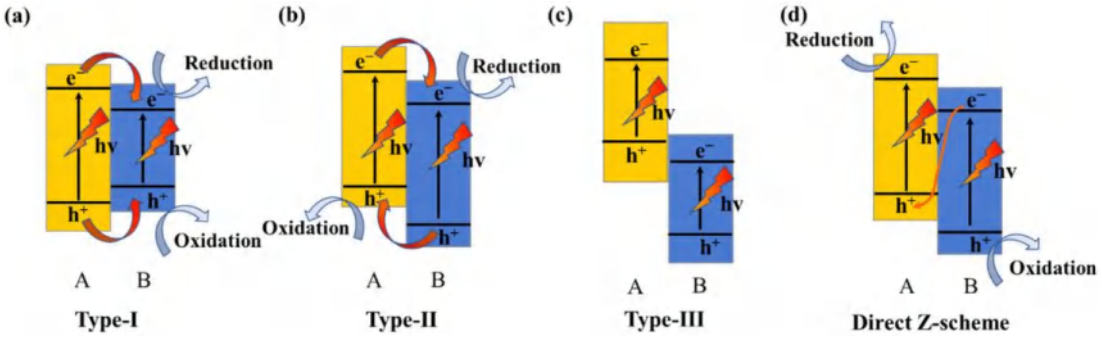

Fig. 2.9 Typical band alignment between semiconductor and cocatalysts [43].

2.3 Cobalt-based electrocatalysts for water splitting reaction

Catalysts are essential components for reducing the overpotential in water electrolysis. Currently, the most efficient catalyst for HER is still platinum-based catalysts (Pt-based) and for OER, is still Ir-based catalysts, but their limited crustal abundance and high cost pose significant challenges for large-scale commercial applications. To solve these issues, two main solutions have been proposed: (1). Control and manipulate the dose of Pt/Ir element in the catalysts to achieve better catalytic performance, (2). Design and develop non-Pt-based catalysts. Examples include transition metals such as Fe, Co, Ni, Cu, Mo, W, and their corresponding compounds, as well as non-metallic elements like B, C, N, P, S, Se. Various efficient non-precious metal catalysts have been synthesized using these elements. It should be noted that when designing non-precious metal catalysts, the abundance, potential cost, and activity differences should be considered comprehensively. Given the advantages of transition metals (Fe, Co, Ni) in terms of abundance and price, the design and development of efficient Co or Ni-based

HER/OER electrocatalysts are crucial for achieving lower industrial hydrogen production costs.

Under this circumstance, various transition-metal based catalysts have been developed, including transition metal sulfide, transition metal phosphides (TMPs), transition metal nitrides (TMNs), transition metal carbides (TMCs), transition metal oxides (TMOs). Moreover, studies according to the above-mentioned design principles, e.g. vacancies, defects engineering, doping, alloying, etc. have successfully proven the dramatic potentials in the industrial applications. Another promising strategy to introduce the hetero atoms into the cobalt oxides based- catalyst is the utilization of Metal Organic Framework (MOF) instead of commercial nickel foam. Moreover, MOF also has several other merits for HER[12,44,45]: (1) ultrahigh porosity with accessible active sites; (2) tuneable catalytical metal active sites; (3) functionalize organic linkers. In this section, we mainly categorize and understand the electrocatalysts according to the composition in line with the catalysts design principles.

2.3.1 Cobalt-based electrocatalysts for HER

2.3.1.1.1 Cobalt oxides-based electrocatalysts for HER

Among 3d transition metal-based catalysts that facilitate HER, cobalt based electrocatalysts possess moderate intermediate adsorption energy, and hence their derivates show potential application in HER. However, it is widely believed that bulk cobalt oxides are inactive for the hydrogen evolution reaction (HER) due to their poor conductivity, inadequate hydrogen adsorption capacity, and limited catalytic active sites. To address these issues, researchers have been devoting to developing advanced metal oxide-based materials that can serve as highly efficient HER electrocatalysts in recent years. The generation of oxygen vacancies (OVs)[46] is considered one of the most

commonly used and effective methods to enhance the intrinsic catalytic activity by modulating electronic structure, conductivity, and hydrogen adsorption energy.

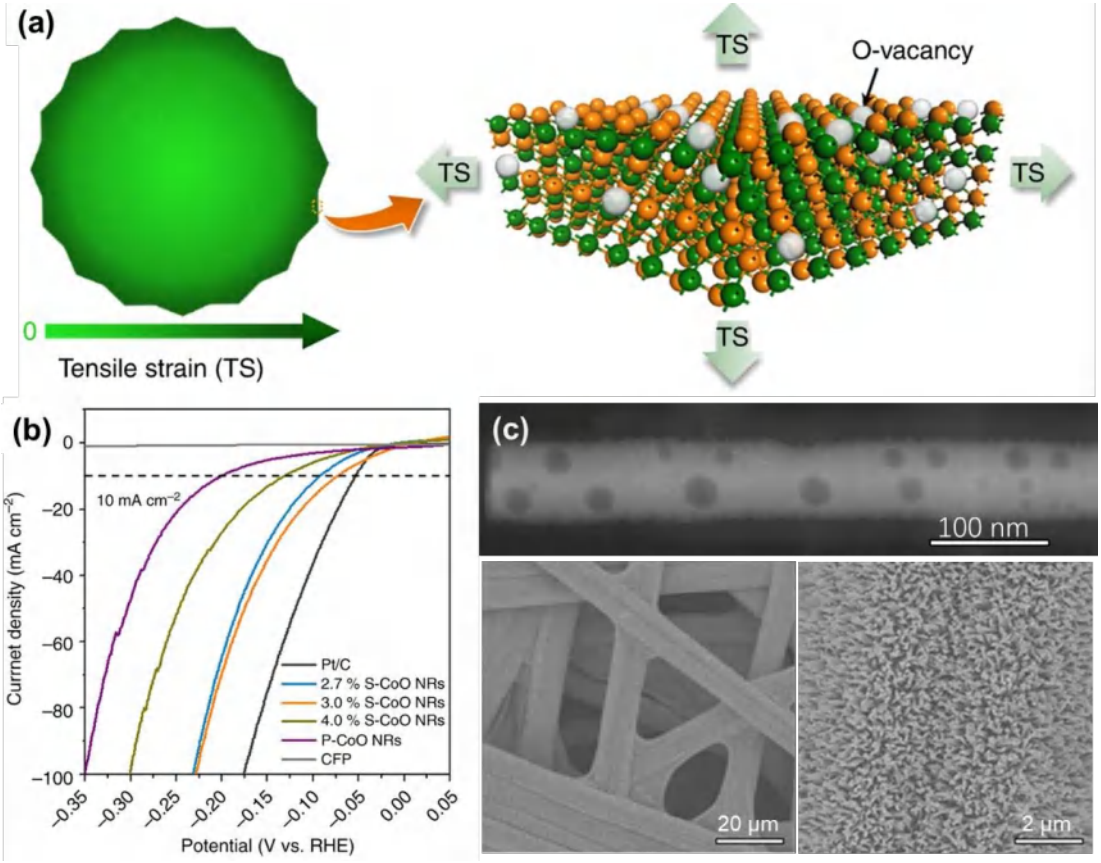

Fig. 2.10. Schematic illustration of the effect of O-vacancy on tensile strain of CoO nanorods; (b) corresponding HER performance of strain-engineered CoO nanorods; (c) HRTEM and SEM images of prepared CoO nanorods on stainless steel foam [37].

Qiao and coworkers[46] employed surface strain engineering through a combination of theoretical analyses and experimental investigations (**Fig.2.11**). It is demonstrated that the optimization of atomic and electronic structural properties could be achieved by inducing substantial tensile strain. The presence of tensile stress at surface layer of Co-O was found to cause an upward shift of the O p-orbitals, thereby reinforcing the covalent nature of the Co-O bonds and consequently attenuating the adsorption affinity towards H. Moreover, the existence of oxygen vacancies (OVs) on the surface acted as

adsorption sites for water molecules, facilitating their adsorption and subsequent dissociation. As a result, CoO NRs with surface-induced strain and abundant oxygen vacancies exhibited exceptional HER activity in alkaline solutions, approaching the performance levels of benchmark Pt/C catalysts. The same group further demonstrated a dual doping method into Co_3O_4 can enhance the electrocatalytic HER. The experimental and theoretical results demonstrate that the high activity is attributed to the dual-doping-induced modulation of the surface and bulk electronic structures of Ni and Zn. Specifically, Ni doping provides an ideal surface electronic environment for hydrogen intermediate binding, while Zn doping regulates the overall conductivity. What's more, Wang and co-workers employed a plasma-assisted method to introduce P atoms into Co_3O_4, generating in-situ oxygen vacancies to enhance the HER activity. Theoretical calculations substantiate that P filling into OVs can improve the material's electrical conductivity and the adsorption energy of adsorbate species. These findings collectively underscore the broad applicability of oxygen vacancy modulation and heteroatoms doping as effective strategies for enhancing the performance of metal oxide based HER systems. Besides doping and vacancy engineering, the morphological and topological control is another key parameter in catalytic enhancement. The conversion of MOFs to carbon supported electrocatalysts, without turbulence of pore system has been widely reported. Zheng *et al.*[47] reported the encapsulation of glucosamine into ZIF frameworks, not only retains the topology of ZIFs, but also provides the N sources for the fixation of Co-N_x active sites. As a result, the CoO_x with Co-N_x doped electrocatalysts, requires an overpotential of 290 mV to achieve 10 mA cm^{-2}. Similarly, Yang *et al*[48] achieved the encapsulation of FeCo nanoparticles into the N-doped graphene layers via MOF. The precursor consists of iron and cobalt nodes and therefore can function as catalytic active sites, moreover, final products were also rich

in nitrogen content (8.2 at %) due to the cyanides (CN^-) as organic linkers. The final catalyst possessed an overpotential of 262 mV at 10 mA cm^2 and a Tafel plot of 74 mV Dec^{-1}. Gao *et al*[49] reported the preparation of hollow NiCo alloy ($NiCo_2O_4$), instead of pure cobalt monoxides can significantly reduce the required overpotential (η_{10} =-110 mV for HER). The high catalytic performance not only originates from the introduction of Ni atoms, but also from the 3D hierarchical structure, which facilitates the electrolyte diffusion and exposes more active sites. Apart from the generation of oxygen vacancies and heteroatom doping, Kang *et al*[50] also reported the growth of cobalt oxides into ceria nanosheets also achieved highly efficient HER. Due to the high temperature pyrolysis and introduction of Co atoms, more oxygen vacancies were formed in such nanosheets, hence increased the hydrogen binding energy and number of active sites.

Apart from CoO and Co_3O_4, cobalt layered double hydroxides (Co-LDHs), commonly prepared by either coprecipitation of cobalt containing salts in an alkaline medium or direct conversion of MOFs, are regarded to be a promising candidate towards water splitting reaction. However, the intrinsic property of $Co(OH)_2$ towards HER is poor, due to the low dissociation kinetics of water molecules on top of Co atoms in hydroxides. Hence, the binary metal hydroxides (NiCo, CoFe, Ni-Cr-LDHs) are adopted to lower down the HER overpotentials. In this case, Baranton and co-workers [51] suggests that the introduction of Ni atoms in Co binary LDHs (varied ratios between Ni: Co from 9:1 to 1:9) can boost HER. The results indicate that the existence of Ni^{2+}/Ni^{3+} redox center in the samples can shift the overpotentials more cathodically with a Ni: Co ratio of 1:0.4. Similarly, Feng *et al*[52] reported a composite of Co-Ni LDHs on Ni foam requires an overpotential of 130 mV at 10 mA cm^{-2}. Yang *et al.*[53] reported the conversion of ZIF-67s to LDHs by hydrolysing ZIFs to release the Co atom,

which further coordinates with Al^{3+} atoms. Rajeshkhama *et al*[54] also reported a CoFe-LDHs system can significantly improve the electrocatalytic performance, by pointing out the electron transfer from cobalt atoms to water molecules. Under such condition, a lower Tafel slope can be obtained, indicating the fast water dissociation and proton adsorption process. Moreover, the construction of heterostructures between metal oxides and other conductive compounds have been proposed as a solution to HER. Luo *et al*[1] reported a two-step synthetic pathway of MoS_2 confined $Co(OH)_2$ (shown in the **Fig.2.11**): (1) the exfoliation of MoS_2 nanosheets with the lithium intercalation which can introduce the Lithium into the Van Der Waals gaps between the nanosheets; (2) the cobalt and lithium ion exchange in alkaline media. The products exhibit low overpotential (89 mV at 10 mA cm^{-2}), remarkable exchange density which is around 72.9 μA cm^{-2}, and good stability after 1000 CV cycles. It revealed in the experiment that the $Co(OH)_2$ nanoclusters can absorb oxygen molecules onto the surface, hence decrease the energy barrier to break O-H bonds, which is beneficial for water dissociation in alkaline medium.

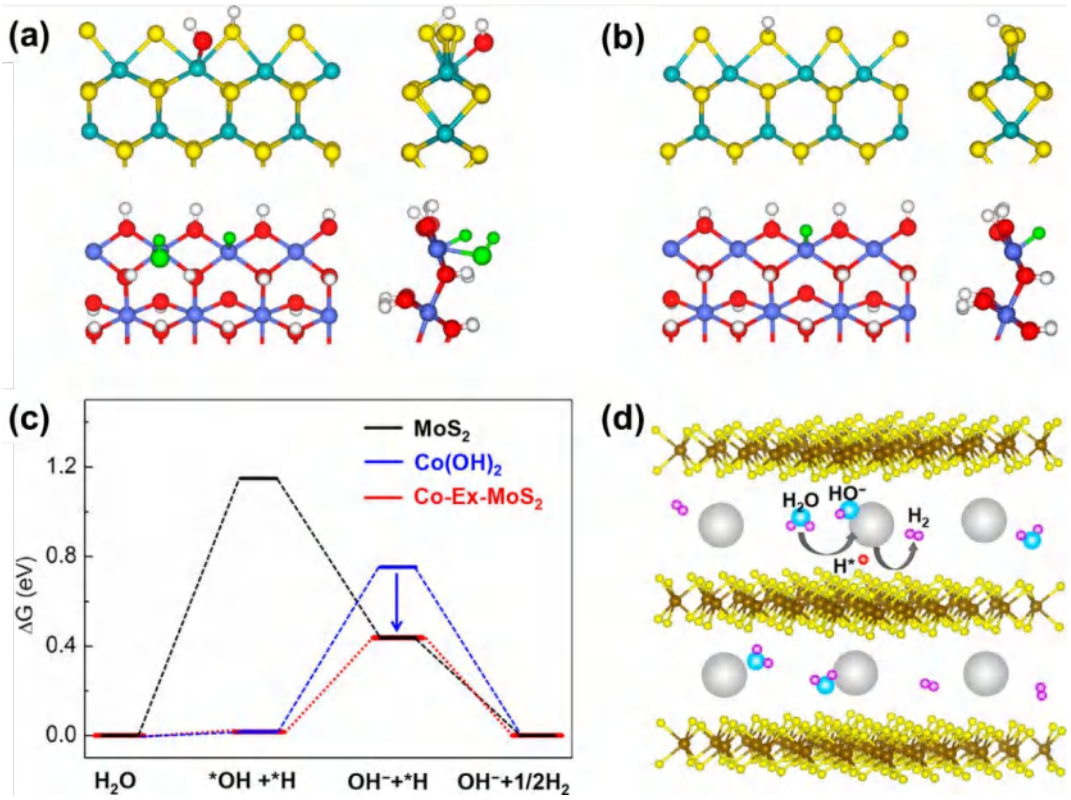

Fig. 2.11. (a) Top and side views of relaxed MoS_2 (top) and $Co(OH)_2$ (bottom) edges with *OH and *H adsorption. (b) Top and side views of relaxed MoS_2 (top) and $Co(OH)_2$ (bottom) edges with *H adsorption. Dark green, yellow, blue, red and white spheres represent Mo, S, Co, O and H atoms, respectively. (c) Free energy diagrams of HER on the edges of MoS_2, $Co(OH)_2$, and Co-Ex-MoS_2 sample. (d) Diagram showing HER catalytic reaction in Co-Ex-MoS_2[1].

The heterojunction between carbon-based materials and Co-LDHs has been constructed to boost HER. Feng *et al.*[55] directly electrodeposited Co hydroxides on Ni foam, followed by a polymerization of a conductive layer PANI, the core-shell $Co(OH)_2$@PANI possess a porous structure and an electron transfer from N atoms and Co atoms. The electron redistribution at interface suggests an enhanced proton adsorption kinetics, which further improves the HER. Similarly, Jia *et al.*[56] reported the exfoliation and self-assembly process between LDHs and defective graphene for

the construction of nano sheets@ defective graphene structure. The obtained catalyst achieved a high catalytic performance (η= 115 mV @ 20 mA cm^{-2}) and stability at 10 mA cm^{-2} more than 10 hrs. Simulations results suggest that the accumulated electrons at defects in the graphene structure facilities the water molecules dissociation process.

2.3.1.1.2 Co_xA_y (A= S,Se) based electrocatalysts for HER

In comparison with cobalt oxides electrocatalyst, the valence states in cobalt sulfides (e.g. CoS_2, Co_3S_4, Co_9S_8), selenides (CoSe, $CoSe_2$) are significantly smaller than that in cobalt oxides. Moreover, the high electronegativity difference in O, S and Se promotes predominantly ionic structures. The less electronegative chalcogenides S and Se in metal chalcogenides exhibit unique interactions with the metals[57]. Hence, efforts have been dedicated to enhancing the electrocatalytic performance of Co_xA_y (A= S, Se) based electrocatalysts. Zou *et al*.[58] investigated the HER performance of pristine Co_9S_8. The electrode exhibited an overpotential of 340 mV at 10 mA cm^{-2} under neutral pH conditions. However, the stability of pristine Co_9S_8 is limited to in acidic and alkaline medium. Hence, an extra layer of carbon is loaded to enhance its stability. This "carbon-armored" Co_9S_8@C catalyst, reported to demonstrate stability under acidic (pH= 0) and basic (pH= 14) conditions, along with significantly improved overpotentials for the HER (280 mV at 10 mA cm^{-2}). Peng *et al*.[59] have fabricated an integrated 3D nano-architecture comprising self-supporting Co_9S_8/WS_2 arrays (nanobelts, nanoneedles, **Fig.2.12 c**) on conductive Ti plates. The Co_9S_8/WS_2 electrocatalyst, exhibiting superior HER activity in alkaline solution, is attributed to synergistic effects arising from its expansive physical surface area and substantial electrochemical surface area. These characteristics facilitate mass diffusion and expose a greater number of accessible active centers during the electrochemical process. More recently, Zhu *et al.*[17] achieved

the precisely growth of multilayers of MoS_2 onto Co_9S_8 nanoparticles, by controlling the amount of sulfur precursors and pyrolysis temperatures. The introduction of heterojunction, as a result, decreases the dissociation energy of water molecules. Density functional theory calculations were conducted to elucidate the characteristics of the Co_9S_8/1L MoS_2 core/shell nanostructure, exhibiting the most favorable hydrogen adsorption energy (ΔE_H) of -1.03 eV and a minimal transition state energy barrier (ΔE_{2H^*}) of 0.29 eV. In comparison, MoS_2 alone demonstrated a hydrogen adsorption energy (ΔE_H) of -0.86 eV and a transition state energy barrier (ΔE_{2H^*}) of 0.49 eV. These findings are pivotal for enhancing the hydrogen evolution reaction (HER) activity, as the Co_9S_8/1L MoS_2 structure effectively stabilizes the HER intermediate, captures H ions, and facilitates the release of H_2 gas. Daoud *et al.*[60] also reported the cobalt monosulfide (CoS@CoNi-LDHs) by aqueous sulfidation of oxidized Co-MOF nanorods. Due to the pre-oxidation of MOFs to stable cobalt oxides nanorods, the morphology can be well retained. The as prepared nanorods possess a low η_{10} value (189 mV in 1M KOH), with a stability over 50 hrs operation at -0.1 V.

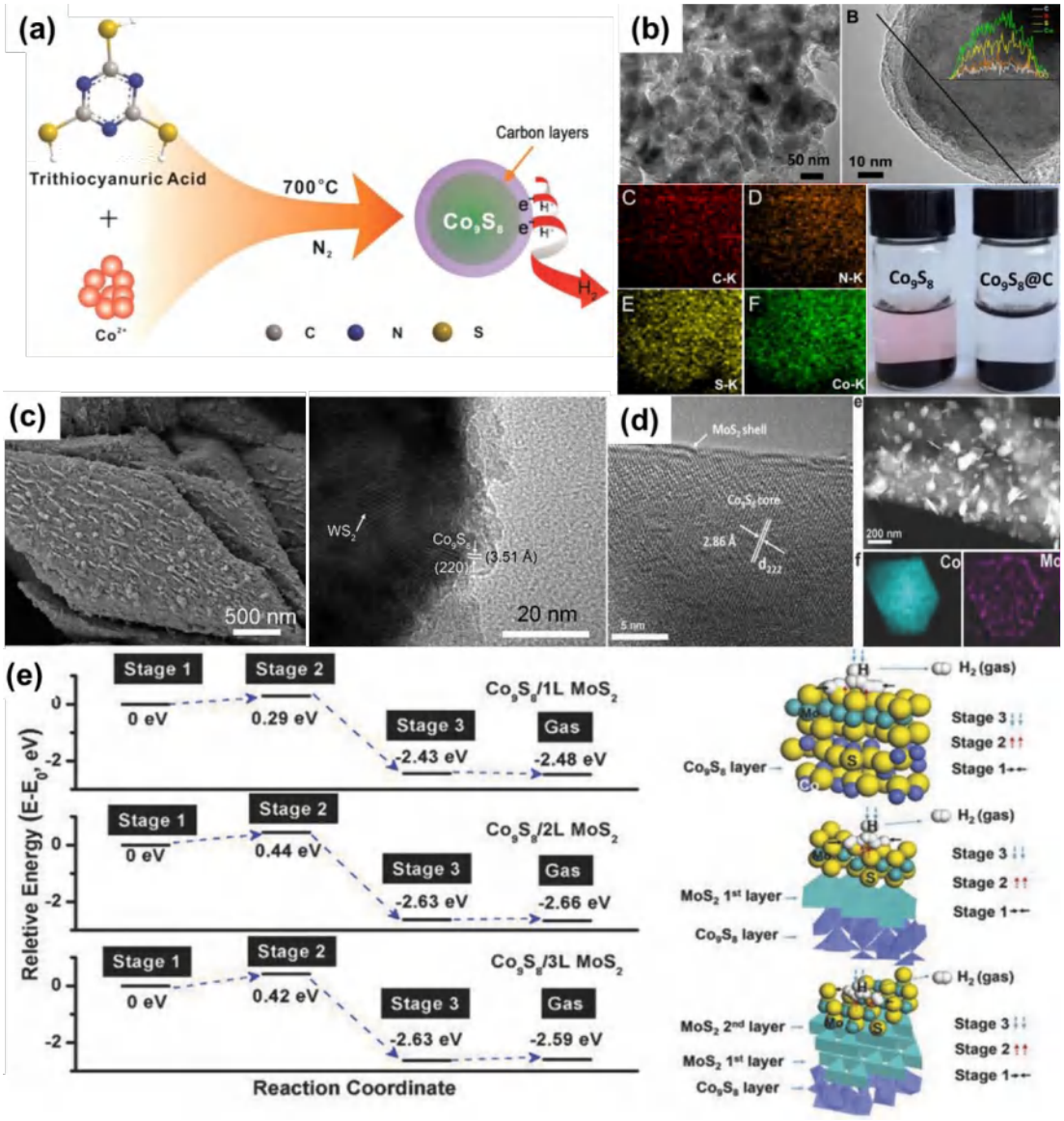

Fig. 2.12. (a) Schematic representation of the synthesis of Co_9S_8@C; (b) TEM images ; corresponding elemental mapping images of Co_9S_8@C, and comparison of the chemical stabilities in 0.5 M H_2SO_4 for 24 h of Co_9S_8@C versus Co_9S_8; (c) SEM image and TEM image of Co_9S_8/WS_2 nano rhombus arrays; (d) HRTEM image of one side edge of the Co_9S_8/1L MoS_2, HAADF-STEM, STEM-EDX mapping images of Co_9S_8/1L MoS_2 supported on CNFs; (e) Reaction pathways of hydrogen atom adsorption and hydrogen molecule desorption on Co_9S_8/1L MoS_2, Co_9S_8/2L MoS_2, and Co_9S_8/3L MoS_2 for HER[13].

In order to address the dissociation of H_2O which produces chemisorbed H_{ads} towards H_2, the modification of surface content and morphologies can significantly enhance the catalytic performance compared with Pt/C based catalysts. Yang and coworkers[61] reported a strategy to synthesize selenide-based heterostructures which is decorated with layer-double-hydroxides (LDHs). From EDS mapping, it confirms the uniform dispersion of Co, Se and O in nanorods on the nickel frameworks. The obtained rod-like catalyst possessed extreme high activity for overall water splitting (η= 106 mV at 10 mA cm^{-2}). Furthermore, the DFT calculations indicate the reduction in the electronic density of $CoNiSe_2$, which then facilitates the electron transferring through the bimetallic interface between Se and Ni. Kang *et al*.[62] reported the synthesis of Co/$(NiCo)Se_2$ by direct selenization of LDHs, which is originally derived from the etching of ZIF-67s. The as-obtained cobalt selenide composites retain the cubic morphology from MOFs, which ultimately contributes to a low overpotential (η_{10} =198 mV).

2.3.1.1.3 Cobalt phosphides based electrocatalysts for HER

Apart from the metal-oxides/sulphides/selenides, metal-phosphide materials also show potential application in electrocatalytic water splitting. Schaak *et al*[63] recently reported the synthesis of MnP type CoP via the decomposition of Co precursors [$Co_2(CO)_8$] and reacted with tri-n-octyl phosphine (TOP), the prepared quasi-spherical particles with average diameter of 13±2 nm shows a promising electrocatalytic performance in HER in acidic medium, the as-synthesized catalysts require 85 mV in overpotential to achieve a current density of 20 mA/cm^2. It is noticed that the adsorbed hydrogen atoms give a sufficient coverage on the intermediates while the desorption of hydrogen atoms sluggish the reaction. Based on this, people further investigate the decoration of CoP

particles onto different non-metal substrates including carbon nanotube[2,64], graphene oxides sheets[65] which also improved catalytic performance due to the enhanced conductivity and stability. Moreover, the synthesis of CoP from MOF precursors has been widely reported. Such synthetic procedure can be achieved by either direct or post phosphorization[66,67] of MOFs. Hu *et al.*[68] reported the direct functionalization of ZIF-67s to hollow CoP nano cubes by the Prussian blue analogue layer coating, with subsequent phosphorization process. Due to the relatively low thermal treatment (400℃), rare collapse of the hollow cube was observed. While Li *et al.* [63] reported the phosphorization of ZIF derived cobalt nanoparticles embedded in N-doped carbons for enhanced HER performance (η_{10}= 115 mV). This process requires a slow heating rate (2°/min) to avoid the loss of pore system. The electrocatalytic performance of polycrystalline Co_2P (Co_2Si type) which contains edge-sharing tetrahedra structure[69] is also examined. The synthesis of Co_2P nanoparticles followed the controlled temperature reaction, further extended X-ray absorption fine structure (EXAFS) confirmed an increased average distance between Co-Co atoms while a shorter distance in Co-P structure existed in the structure. However, the overpotential required to achieve 10mA cm^{-2} is 95mV at Ti electrode which is comparable higher than that of CoP catalyst in HER. This indicates although two crystalline structure shares similar metal-phosphorus bonding length, the Co-P character on a low-index surface show superior catalytic performance and optimized the phosphorus content as well electronic environment of active metal site is critical in the catalyst design. More recently, Wang *et al*[2] reported the strategy to tune the electronic environment via the hybridization of N-doped carbons, carbon nanotubes phosphorus (Co/Co_2P@ACF/CNT), the resultant products possess a decreased overpotential of 78 mV at 10 mA cm^{-2}. From the free energy calculation (**Fig.2.13a**), Co/Co_2P@ACF/CNT-900 has a relative lower

adsorption energy for H* intermediate which promotes the Volmer reaction in alkali environment. Moreover, the d band center of it is close to its Fermi level as well as the introduction of N and P content optimizes (**Fig.2.13 b**) the electronic state of Co atoms which is in consistent with electrochemical results. Apart from this, the amorphous Co based catalysts which is based on the concept of SACs also showed promising catalytic performance, Cao *et al*[70] reported the Co_4N nanoparticles dispersed on the CNT to achieve synergistic effect that facilitating the HER with an overpotential of 78 mV at 10 mA cm^{-2} and a Tafel slope of 82.2 mV dec^{-1}. Ji *et al*[3] reported the synthesis of nano porous CoP_3 nanowire located on the Ti mesh by acid etching of MnO_2 forming agent. The obtain np-CoP_3/TM possess high performance with overpotential of 76 mV at 10 mA cm^{-2} and good stability for at least 60 h in alkaline environment [55].

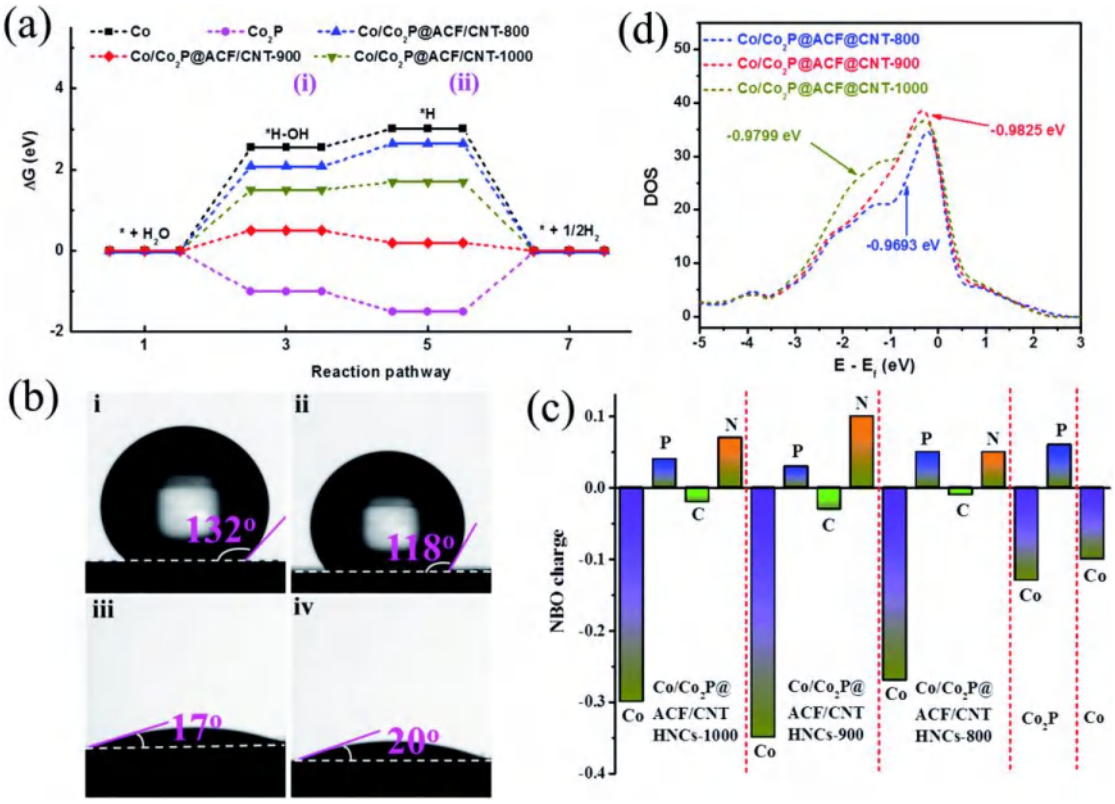

Fig. 2.13. (a) Calculated free energy diagram of the HER for (i) *H_2O and (ii) *1/2H_2 on Co, Co_2P, Co/Co_2P@ACF/CNT HNCs-800, 900 and 1000. (b) The contact angles of a drop of 1.0 M KOH on (i): ZIF67 precursor, (ii): Co/Co_2P@ACF/CNT HNCs-800,

(iii): Co/Co_2P@ACF/CNT HNCs-900 and (iv): Co/Co_2P@ACF/CNT HNCs-1000. (c) NBO charge distribution on Co, Co_2P, Co/Co_2P@ACF/CNT HNCs-800, 900 and 1000. (d) Calculated DOS of Co/Co_2P@ACF/CNT HNCs-800, 900 and 1000 and their corresponding d-band center potentials[2].

2.3.2 Cobalt-based electrocatalysts for OER

2.3.2.1 Cobalt oxides and hydroxides-based catalysts for OER

Unlike the potential candidate such as MoS_2, metal oxides' preference towards adsorption of H* restricts the application in OER, due to the fact that the key intermediates in OER is the formation of HOO* on adsorbed O*. While the cobalt-based materials possessing moderate bonding strength as well as Fe, Ni shows promising potentials to OER. In general, cobalt oxides-based materials refer to CoO and Co_3O_4, in which Co_3O_4 has a higher cobalt valence state. Sun *et al.*[71] systematically study the activities cobalt tetrahedral and octahedral sites in cobalt oxides by EXFAS. It implies that octahedral sites have higher OER activity compared to tetrahedral sites (**Fig.2.14 a**). To understand this phenomenon, the subsequent orbital analysis of interactions between metals and oxygen indicate that metal and oxygen sites exhibit a strong σ-σ interaction, while tetrahedral metal and oxygen sites show a relatively weak π-π interaction. The strong and weak interactions are important manifestations of electron cloud overlap and charge distribution (**Fig.2.14 b**).

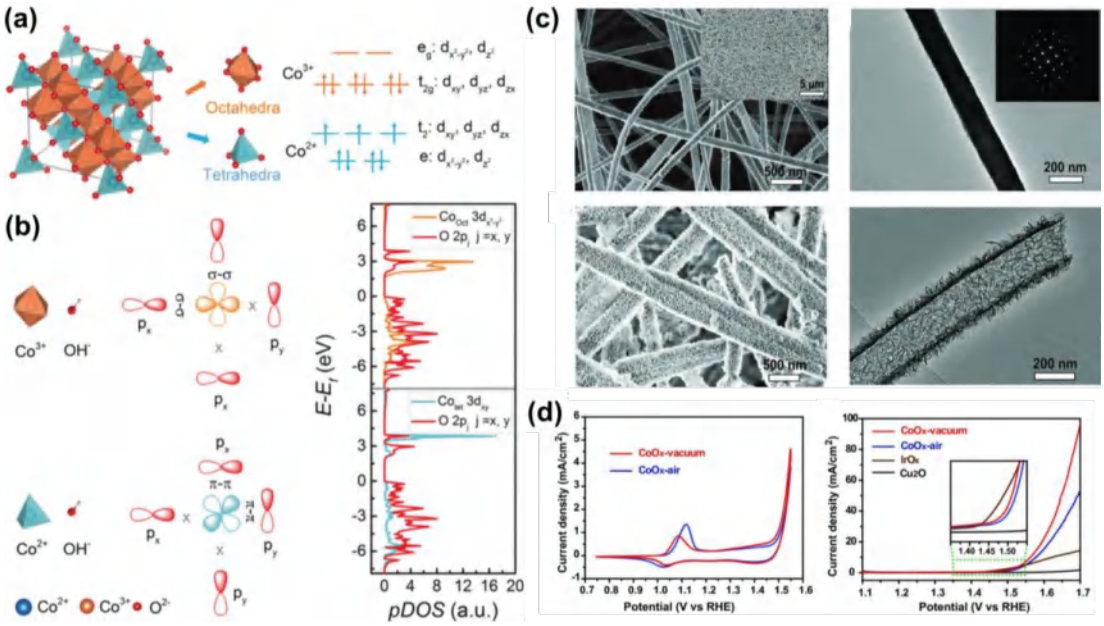

Fig. 2.14. (a) The orbital splitting Co octahedra and tetrahedra sites in cobalt oxides; (b) Representative illustration of Co 3d - O 2p interactions and corresponding DOS plots; (c) SEM and TEM images of Cu_2O nanowires and derived CoO_x hollow nanowires; (d) Corresponding water oxidation performance of CoO_x hollow nanowires [61].

The oxygen vacancies in cobalt oxides are also investigated. Wang *et al*[72] employed Ar plasma treatment on Co_3O_4. The resultant BET surface area increased from 95.3 to 160.3 $m^2 g^{-1}$ after the treatment. It is supposed oxygen vacancies has been increased as well as the number of active sites. In addition to this, the post treatment also enhances the conductivity of Co_3O_4 has been achieved. Apart from Ar plasma, Wang further employed ammonia gases which are further ionized to plasma to convert Co_3O_4 to N-doped cobalt oxides. The abundant vacancies as well as N-doping facilitate the electron transfer and intermediate adsorption resulting a low overpotential of 280 mV to achieve a current density of 10 mA cm^{-2}. What's more, scientists also found similar trend in Ni oxides. In this case, the introduction of N atoms and creation of oxygen vacancies show

the similar trend in the cobalt case, a narrowed band gap can be achieved improving the conductivity and number of exposed active sites.

In addition to the oxygen vacancies, Zou *et al*[73] explores the role of Co vacancies in Co_3O_4, the calcination of cobalt acetate at different temperatures introduced disordered structures inside the sample. Further XANES confirmed a lower coordination number of Co indicating the Co vacancies insides the catalysts. The catalysts presence in metallic vacancies shows an enhanced catalytical performance with an overpotential of 268 mV at 10 mA cm^{-2}. The DFT calculations further indicated the adsorption of water molecules on the Co vacancies lower the energy barrier for the formation of intermediates which as a result boosts the OER. Apart from pristine cobalt oxides, Wang *et al*[74] utilized the interface between Cu_2O nanowires and $Co(OH)_2$ tubes to facilities the formation CoO_x, and the post chemical etching of Cu to expose the Co active sites (**Fig.2.14 c**). This CoO_x nanosheets/nanotube reveals the domination of Co^{2+} octahedral structure at the interface which further facilitate the intermediate formation. The resultant products require an overpotential of 340 mV to achieve current density of 10 mA cm^{-2}. Zhang *et al*[75] explored similar effects in the Fe-based catalyst, in this work, the creation of Fe vacancies via solution based wet-chemistry method, the ultrathin δ-FeOOH nanosheets based on Nickel foam exhibits superior catalytic performance towards OER compared with that of Co based examples. (overpotential of 265 mV at a current density of 10 mA cm^{-2}). Further XANES analysis confirms that a reduction of coordination number of iron to 1.6 which is significantly smaller than Fe-Fe coordination number suggesting the sample is rich of Fe vacancies. Moreover, DFT calculations indicate a decreased overpotential on Fe_2 sites (0.46 V) after introduction of Co atoms, which facilitates the OER while the rate determining step is the formation

of HOO* on the absorbed O groups. More recently, Zhuang *et al*[76] investigate the activities of universal transition metal-based 2D MOFs for electrocatalytic water splitting. In this case, Fe, Cu, Co and Ni are linked by the 2,5-dihydroxyterephthalic acid (H4dobc) to construct 2D nanosheets with an average thickness ~ 1.9 nm. Among all synthesized catalyst, FeCo amorphous metal oxide nanosheets exhibits the best catalytic performance with an overpotential of 298 mV at 10 mA cm^{-2}. This superior catalytic performance originates from the unsaturated coordinatively metal sites and low required frees energy on Co sites as well as the electron affinity changes between iron and cobalt sites. The e^--e^- repulsion of Co-O is enhanced due to the electrons transferred to the Fe^{3+} sites and hence lowers the formation of intermediate HOO* to achieve a better catalytic performance.

2.3.2.2 Co_xA_y (A= S,Se) based electrocatalysts catalysts for OER

Cobalt sulphides and selenides have also been explored as the candidates for OER. In general, the cobalt sulphides and selenides will experience surface reconstruction towards oxyhydroxides, which are regarded as the true active center. While most of conversion takes place at surface of cobalt sulphides, especially at the high oxidation potentials. Hence, the surface modification and vacancy engineering are introduced by the researchers. Li *et al.*[77] reported a surface vacancy rich Co_3S_4 hollow particles, by one pot carbonization of hollow ZIF-67s. The direct carbonizations introduced a hollow structure, with oxygen vacancies. The subsequent sulfidation process allowed the transformation of oxides to sulphides, which exhibited a high OER catalytic (η_{10} =270 mV) performance and stability (20 hrs at 10 mA cm^{-2}). Manjunatha et al.[78] indicated a hybrid composite of $Co_3S_4/Co_{0.85}Se$ by one pot hydrothermal reaction. The OER performance, as indicated, originates from the oxidation states in Co_3S_4 as well as in

selenides. Similarly, the exploration of cobalt sulphide (CoS_x) nanovesicles decorated with iron sulphide (FeS_x) heterostructure for OER was conducted by Cui *et al.*[79]. the operando-Raman and X-ray absorption spectroscopy measurements revealed that the catalytic efficiency of OER was primarily governed by the in-situ formation of cobalt oxyhydroxide active species on the surface of cobalt sulphide. The transition of active species from CoS_x nanovesicles was observed to be prompted by FeS_x, a phenomenon attributed to the increased average valence state of cobalt and the reduced coordination of cobalt sites. Moreover, a heterostructure comprising sandwich-like Ni,Fe layered double hydroxides/$Co_{1-x}S$ (Ni,Fe-LDH/$Co_{1-x}S$) was synthesized through the electrodeposition of $Co_{1-x}S$ onto the surface of NiFe-LDH[80]. In this system, the strained heterostructure significantly reduces the adsorption energy barriers.

In addition to the vacancy and heterostructure engineering, Yao *et al*[4] introduced N hetero atoms via the reaction with NH_4HCO_3 as well as sublimed sulphur as ions doping to construct N-CoS_2 (**Fig. 2.15 a**). In this case, the nitrogen doping influences the electronic states of Co towards a positive shifting in binding energy which facilitate the OER (overpotential of 300 mV at a current density of 10 mA cm^{-2}). DFT calculations further suggests this positively charged of Co atoms is beneficial for adsorption of water molecules as water molecules are typical polar molecules with negative O atoms (**Fig 2.15 f**). Moreover, the Mulliken charge analysis further indicates an increase in the charges in the Co sites as well as a lower free energy for the adsorption of water molecules.

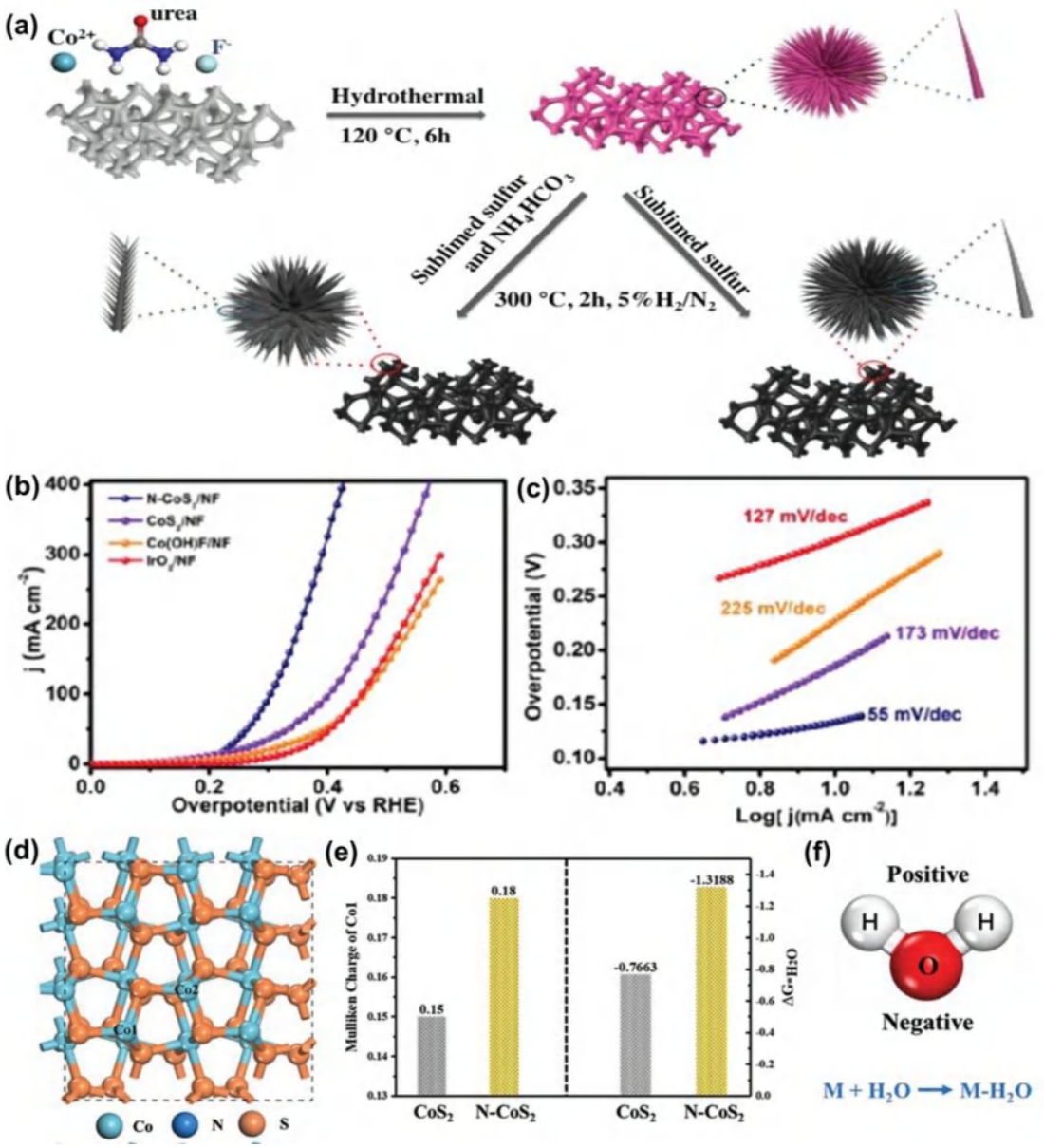

Fig. 2.15 (a) The synthetic process of N-CoS_2 and CoS_2; (b) Linear sweep voltammetry (LSV) plots of Co(OH)F, N-CoS_2, CoS_2, and IrO_2 ; (c) The corresponding Tafel slope plots; (d) Top view of the optimized structure of CoS_2 (001) surface; (e)**.** The Mülliken charge analysis of Co1 site in CoS_2 (001) and N-CoS_2 (001) (left panel), and the adsorption free energies of water on Co1 top sites of CoS_2 (001) and N-CoS_2 (001) surfaces (right panel; (f) The schematic diagram of polarity water molecule and the water adsorption equation[4].

Instead of strategies Co site engineering, Zhou *et al*[81] systematically investigated the anion effects (O, S, Se) on the NiCo bimetallic MOFs, the post treatments via sulfurized vapor, oxidation and selenidation of prepared MOFs, they realized the electrons transfer from Ni and Co due to different electron affinity of anions. Among them, S treated samples shows best OER performance (251 mV at 10 mA cm^{-2}) which is contributed by the lowest required formation energy of HOO*, moreover, they further demonstrated the Se treated samples with strongest electron affinity facilitates the HER.

2.4 Cobalt-based photocatalysts for photocatalytic HER

TiO_2 is the first discovered photocatalysts by Fujishima *et al*[82]. that show potentials in utilization of solar energy, especially the UV region (band gap of 3.0-3.2 eV). Extensive studies have been devoted to improving its photocatalytic performance. In this section, we mainly focus on the construction and loading of cocatalysts onto semiconductors, especially transition metal-based cocatalysts. Instead of TiO_2, we may pay efforts to those semiconductors (e.g., CdS, Iron oxides, C_3N_4, $BiVO_4$) exhibiting visible light absorption. The combination of cocatalysts onto semiconductors have been regarded with several advantages as follows: (1) Extend the light harvest region; (2) Provide active sites; (c) Facilitate the charge-hole separation; and (4) Improve the system stability. Under this circumstance, we are interested in the design principles of cocatalysts onto the semiconductors.

2.4.1 Cobalt-based photocatalysts on CdS

Cadmium sulphide, as mentioned, possesses the narrow band gap (~ 2.4 eV), which can utilize ~38% of the visible region. To load cocatalysts, surface modification of the semiconductor can be regarded as one possible way to construct the heterostructure,

decoration of cocatalysts. Li et al[83] reported that the CdS quantum dots capped with 3-mercaptopropionic acid can directly react with inorganic Ni and cobalt aqueous solution. The mercaptopropionic acid will directly coordinate with the Ni/Co ions to form the real catalytic unit under mild dark medium. More recently, Su et al[84] systematically investigated the Ni-S interactions between cadmium zinc sulphide quantum dots and capping agent. The stoichiometric amount Ni is carefully considered in the system by exploring the surface state of CZS. The distinguished automatically dispersed Ni sites in the system contributes to the sufficient charge separation, owing to the built-in electric field and optimized surface H_2 adsorption site (Ni stie). Shao *et al*[85] directly mix the $Cd_{0.9}Zn_{0.1}S$ powders with Co/Fe solution. In this case, metal ions are physically adsorbed by CZS semiconductor, followed by calcination at 200℃. The obtained $CoFe_2O_4$ loaded on multi-armed CZS composites show a PHE rate of 350 μmol h^{-1}. However, such post calcination process causes the random distribution of CFO nanoparticles, which may result in insufficient electron hole separation.

It should be noticed photo-corrosion is a common phenomenon of CdS photocatalysts, which can be regarded as the photogenerated-hole-induced instability ($CdS + 2h^+ \rightarrow Cd^{2+} + S$). The solutions to improve CdS's stability under Xenon lamp have attracted extensive attention in an effort to effectively avoid the photo-corrosion of CdS photocatalyst. Metal sulphide and phosphide, which are typical electrocatalysts for water splitting reaction, have been modified and incorporated into semiconductor system. The introduction of abovementioned transition metal atoms doping can, to some extent, facilitates the electron-hole separation. Hence, the generated holes will be continuously consumed by sacrificial agent. While more efforts have been devoted to the design and synthesize semiconductor/cocatalyst composites to achieve

distinguished electron pathways. In most cases, the loading of metal compounds is achieved by one step-calcination, hydrothermal method or ion-exchange method. Additionally, CoP[86] has been reported to incorporate into the CdS system, using a wet impregnation-phosphorization process. It is found that the CoP nanoparticles directly grown on the CdS spheres with random distribution. The obtained cocatalysts exhibit a PHE rate of 745 umol h^{-1} g^{-1}. Cobalt-based MOFs, as typical precursors Fang *et al*[87] synthesized the CdS hollow cages coated with ZIF-67. It is reported that the ZIF-67 will be easily converted to the layered double hydroxides with the existence of metal salt aqueous solution. The as prepared Co-LDHs are highly defective, with abundant active sites. Hence, the catalysts illuminated with visible light and under sonication exhibit a PHE activity of 109.46 μmol h^{-1}. It should be noticed that the top-down assembling method usually denote to a low crystallinity and random morphology, hence hider the catalytic performance.

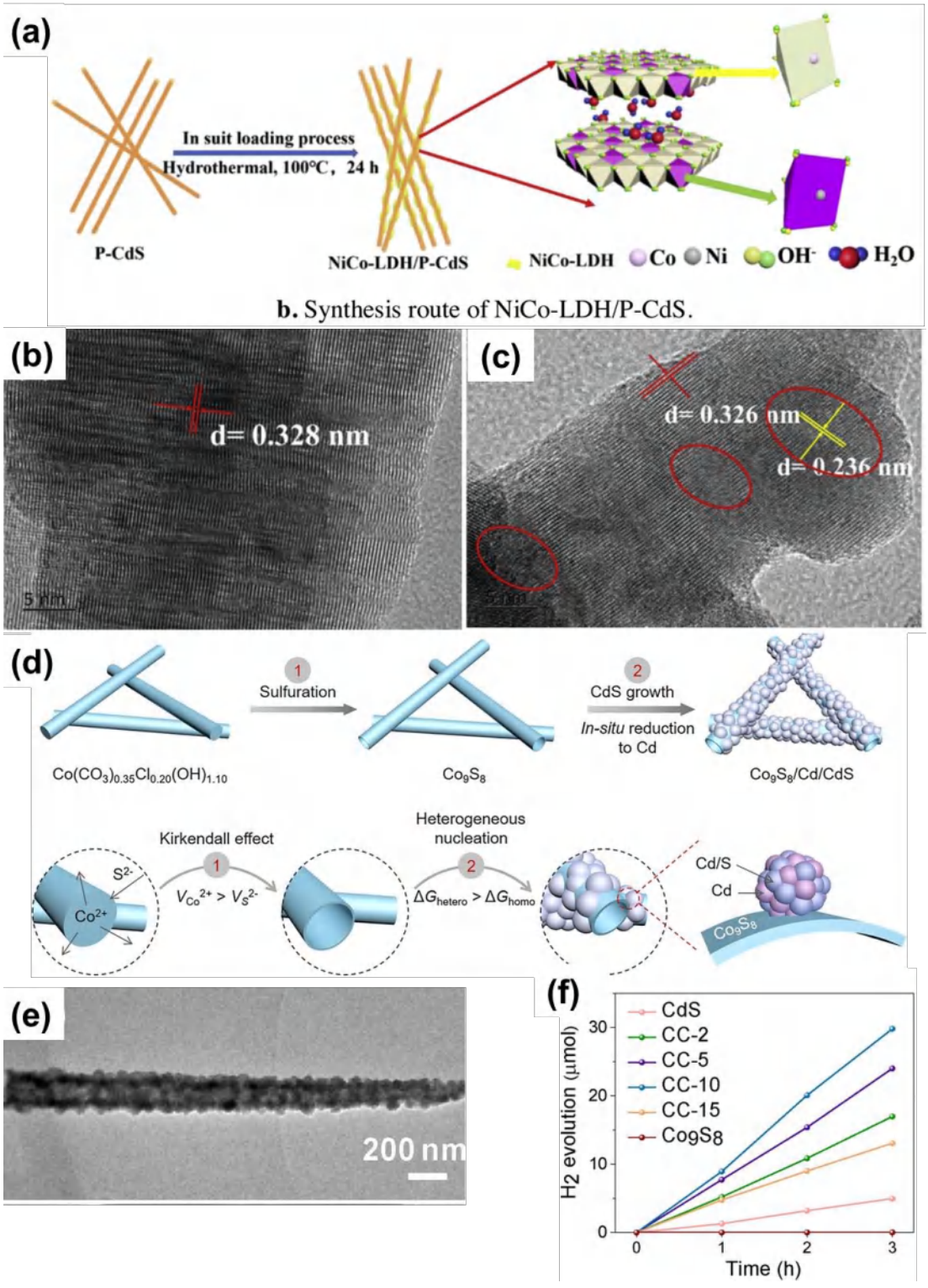

Fig. 2.16. (a) Schematic illustration of the synthetic process of hierarchical NiCo-LDH/P-CdS. HRTEM of (b) P-CdS and (c) NiCo-LDH/P-CdS composites. (d) Synthetic process of Co_9S_8/Cd/CdS Z-heterojunction; (e) TEM image of Co9S8/Cd/CdS nanorods; and (f) PHE course plot of various CdS based photocatalysts

[80].

More recently, Li *et al*[88] reported the in-situ loading process by a hydrothermal reaction (**Fig.2.16 a-b**). The nickel-cobalt salts were mixed with phosphorus doped CdS nanorods, followed by hydrothermal 100℃ reaction. As shown in **Fig.2.16 c**, the lattice spacing of 0.328 nm is attributed to CdS (101) plane, while fringe of 0.236 nm refers to NiCo layer double hydroxides. Zhang *et al.*[89] proposed a twostep process to fabricate Co_9S_8 based cocatalysts (**Fig.2.16 d-f**), by a sulfidation of precursor and in-situ reduction of Cd. The as-obtained heterostructure promotes the PHE reaction with a evolution rate of 10.42 $umol^{-1}$ h^{-1}. The optimized cocatalysts greatly enhance the redox activity, due to the abundant active sits. Moreover, MOF is also developed to show the application of PHE, Li *et al.*[90] introduce the hybrids between carbonized ZIFs and CdS as the potential candidates for PHE. The metallic Co, owing to the reducing ability of carbons, receive the photoexcited electrons from CdS and act as the active sites, boosting the HER (3.8 mmol h^{-1} g^{-1}).

2.4.2 Cobalt-based photocatalysts on g-C_3N_4

The graphitic C_3N_4 (g-C_3N_4) possesses a narrow band gap of 2.7 eV which can be regarded as another candidate for photocatalysis, however, it is reported to give the poor PHE rate with only 6.5 μmol g^{-1} h^{-1}[91]. Instead, the sheet like structure has been attracting interests. The most common way to load cocatalysts onto C_3N_4 sheet including several ways: 1. electrostatic absorption of metal ions, 2. Two step calcination process, 3. Hydrothermal method, 4. Ion-exchange methods. Dong *et al*[92] reported the synthesis Co dispersed g-C_3N_4 cocatalyst for efficient PHE under visible light illumination by mixing Co salts into C_3N_4 powders, followed by the hydrothermal

method. Zhang *et al*[93] synthesized $Co(OH)_2$ onto CdS@g-C_3N_4 heterostructure by physically adsorption of Ni ions, followed by the same hydrothermal reaction. The obtained catalysts possess a PHE rate of 115.18 μmol g^{-1} h^{-1}. More recently, Vu and co-workers[94] proposed the chemically bonded Ni-S cocatalysts onto C_3N_4 sheets by calcination of dicyanamide and a subsequent sulfidation process. The PHE activity of proposed catalyst reaches to 3628 umol g^{-1} h^{-1} which is 1.5 folds of Pt loaded g-C_3N_4 samples. In theory, the chemically bonded cocatalysts show superior catalytic performance due to the rapid charge transfer ability, compared with that of electrostatic samples. It is further reported that the defect engineering of g-C_3N_4 show potential improvements in PHE. Shen *et al*[95] proposed the N-vacancy in C_3N_4 can facilitate the electron transfer in PHE, the copper atoms are atomically dispersed in the polymerized carbon nitride precursor solution, followed by a calcination process. In this case, Cu atom occupies the N-vacancy position, and further serve as electron channels to promote the electron/hole separation process. The as-obtained catalysts (SA-Cu-CN-600) exhibit a 11.23 mmol h^{-1} g^{-1}. Similarly, Pan et al[96] also utilize the MOFs as metal precursor to prepare the metal phosphide/g-C_3N_4 composites. Due to the tunability of MOFs, heteroatoms such as Ni, Mn and Fe can be easily incorporate into the MOFs. The precursors further experience oxidation to facilitate the active sites (M doped CoP) formation. More recently, Su and co-workers[97] prepared 2D NiCo-LDHs loaded onto the C_3N_4 nanosheets. The LDHs over g-C_3N_4 is favour for the light absorption and electron migrations to show a PHE rate of 3.58 mmol g^{-1} h^{-1}. Zhu *et al*[98] further convert the LDHs on C_3N_4 to phosphide by chemical vapor deposition method. The NiFeCo hydroxides are converted to nanoparticles with the diameter smaller than 10nm, which further facilitates interfacial electron transfer, produce hydroxyl radicals. The as-prepared catalyst possesses a high PHE rate of 3.549 mmol h^{-1} g^{-1}. Qi *et al*[99] reported

the load of nickel-cobalt sulphides and phosphides by 3 steps: Ni-Co MOFs mixed with melamine, sulphur precursors, followed by 550℃ calcination process. Further phosphorization process partially converts the Ni_3S_4 to Ni_2P. Such strategy manually creates abundant defects, and interface, contributing to a high PHE rate of 14.49 mmol g^{-1} h^{-1} in dye sensitization system.

2.5 Electrochemical devices for wearable application

The rapid evolution of wearable devices has paved the way for innovative solutions catering to personalized functions, enhancing user experience, and addressing diverse needs. One notable exploration involves the development of self-power devices, exemplifying a shift towards energy autonomy. These devices harness ambient energy sources, such as human motion[100], breath or solar power, reducing dependency on external charging.

Another crucial application is electro/biochemical sensors that enabling real-time monitoring of various physiological and environmental parameters (e.g. composition in sweat)[101]. These sensors empower wearable devices to gather data including the concentration of ions, small molecules in sweat, pulse rate, electrocardiograph signal and so on for personalized health and safety applications, fostering a new era of proactive healthcare.

Additionally, wearable devices take account in the comfort of wearer in different situations. For examples, the wearable dehumidifiers utilizing air convection technology contribute to enhanced comfort by regulating the microclimate around the user. This novel approach mitigates moisture-related discomfort and creates a

conducive environment within the wearable device. The employment of this air convection technology further contributes to the heat management of human body. Engineered with specialized materials, these garments actively regulate body temperature, providing personalized thermal comfort.

In summary, the multifaceted developments in self-power devices, wearable batteries, electrochemical sensors, wearable dehumidifiers for heat management collectively underscore the transformative potential of wearable technologies in personalized functionality. Specifically, these wearable technologies differ with each other by working principles, e.g., the ions gradients in energy harvest devices; redox potentials in electrochemical sensors, and cross-ventilation in heat management device. Within the scope of this thesis topic, we aimed to explore potentials in electrochemical water splitting, combined with wearable technologies.

2.5.1 Device design principle

Electrochemical devices for wearable application, depending on their purpose, need to accurately measure substances and be stable and safe for the body. Addressing the requisites for lightweight, compact dimensions, portability, and skin comfort, each unit within electrochemical-based devices should exhibit flexibility and stretchability. Simultaneously, integration of electronic modules is essential to achieve specific objectives, such as real-time sweat analysis and breath capture. Meanwhile the power consumption should be considered, depending on the functionalities. This section provides a summary of the essential components necessary to fulfil these requirements, especially in textile-based wearable device.

2.5.1.1 Selection of substrates

Wearable devices, which contacts with the skin directly or are attached to the substrates, are required to collect the wearer's physiological information continuously, minimize interference of wearer's daily life. Hence, the fundamental prerequisite for wearable sweat sensors resides in their ability to adhere to the contours of the skin, necessitating compliance with the requirements of flexibility and stretchability. This imperative mandates the simultaneous preservation of optimal electrochemical and mechanical stability[102].

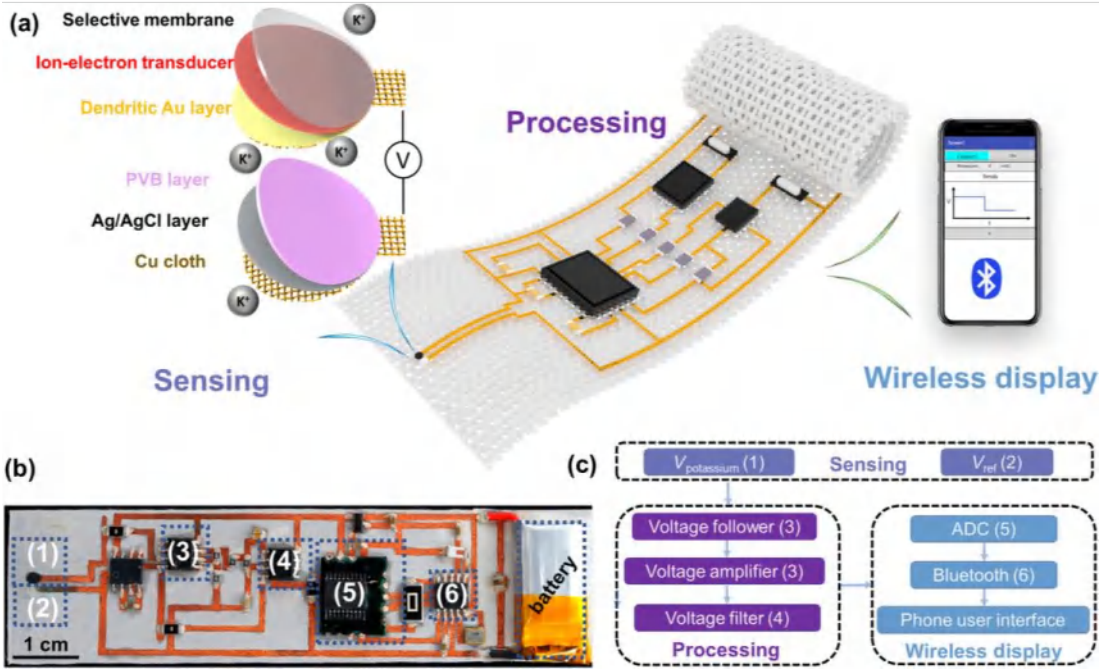

Fig. 2.17. (a) Illustration of wearable devices based on conductive textile substrates; (b) Electronic units in this wearable device; (c) Design of data processing procedures and wireless communication [94].

Textile-based platforms offer a natural breathability that promotes skin ventilation, allowing for natural sweating and evaporative cooling. They possess high flexibility, softness, and comfort. Currently, fabric-based wearable sensors are manufactured via two primary approaches. One involves printing readily designed sensors onto fabric

using a screen-printing process[103], enabling mass production of low-cost and reproducible approach. Another method involves creating thread-based sensors that can be integrated directly into fabrics. Additionally, there is a growing trend in using conductive fabrics directly (**Fig.2.17 a-c**)[104], providing ease in manipulating electrode size (screen printing), multifunction, demonstrating good stability compared to conventional metal-based electrodes.

2.5.1.2 Electronic components

Electronic components are very important components of wearable devices. The integration of these units is highly dependent on the targeted applications. For example, a wearable battery should contain capacitance unit, which stores the electricity. A wearable sensor should integrate sensing element to filter out the background noise. While a wearable dehumidifier should contain moisture sensitive substance.

2.5.1.3 Power components

In wearable devices, the support components are responsible for data processing and wireless data transmission necessitate power for operation. In practical terms, wearable devices should be capable of continuous operation over extended periods. Consequently, minimizing power consumption and devising efficient energy systems are pivotal considerations. Presently, wearable energy resources primarily fall into two types: lithium-ion batteries and energy harvesting devices. With respect to the water splitting reaction, whose initiated potential is 1.23 V, a lithium-ion batteries (3 V) is preferred.

2.5.2 Possible electron pathways at electrode surface

2.5.2.1 Electron pathways for sweat analysis

The typical electrochemical reactions in wearable devices are commonly covered in

biosensor, which utilizes catalyzed reactions to monitor the electron transfer at electrode surface. Based on such electron pathways, different generations of wearable electrochemical are developed. As illustrated, the enzyme (e.g., glucose oxidase, lactate oxidase), owing to its selectivity for specific molecules in sweat, is initially identified for generating oxygen. Subsequently, the electrochemical reduction of O_2 to H_2O_2, an alternative electron transfer pathway, can be continuously monitored (**Fig. 2.18**). However, enzyme-based sensors necessitate a high potential, requiring high electricity input. To address this, mediator molecules (e.g. Prussian blue) and catalysts are employed to reduce the required potential which are the next 2 generations. The latest generation tends to directly electrooxidize the small molecules with the assistance of electrocatalysts in sweat, whereas the reliability of this generation of electrochemical device is still suspicious.

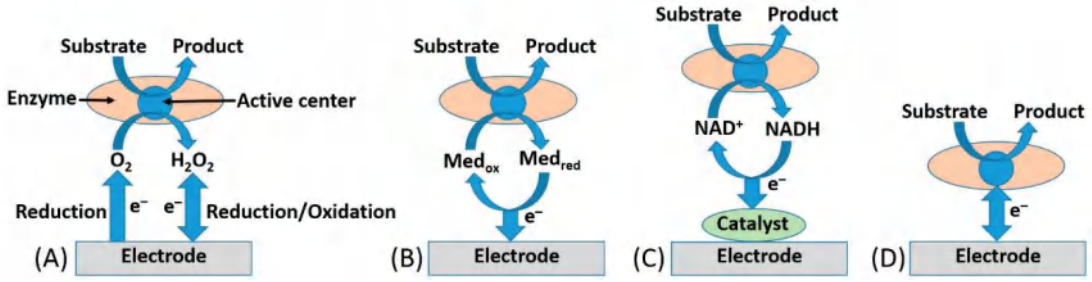

Fig. 2.18 Potential electron pathways for an electrochemical wearable device (a) enzyme based; (b) Mediator based; (c) NADH-catalyst based; and (d) non-enzyme-based reactions at electrode surface [105].

It should be noted that the concept of electrochemical biosensor is far beyond the scope of this thesis. Whereas, the device principle, including choice of electrode and energy input, and integration of whole device, is adopted in the following moisture digester device.

2.5.1.2 Electron pathways for human breath capture

Apart from the electrochemical reactions that are adjacent to human skin, the exhaled breath can also be utilized, especially the humid and carbon dioxides. In these cases, partial exposure to humidity to form an internal moisture gradient within the absorbents is the key to induce the known hydroelectric conversion (**Fig.2.19 a**). Tan *et al.*[106] summarized this first generation of hydroelectric device, however, the electricity generation is dependent on the accumulation of electrons at electrode surface, instead of electrochemical reactions. Beyond this device, the same group proposed a unique strategy by establishing a self-maintained moisture gradient within the nanowire film (**Fig.2.19 b**). With this film, ambient humidity gradient is no longer required, thus making the device less unrestricted to geographic location and external conditions. This advance is expected to profoundly improve the overall scalability and practicability of hydroelectric technologies. Unfortunately, these challenges would remain in the future given that related research studies are still very limited.

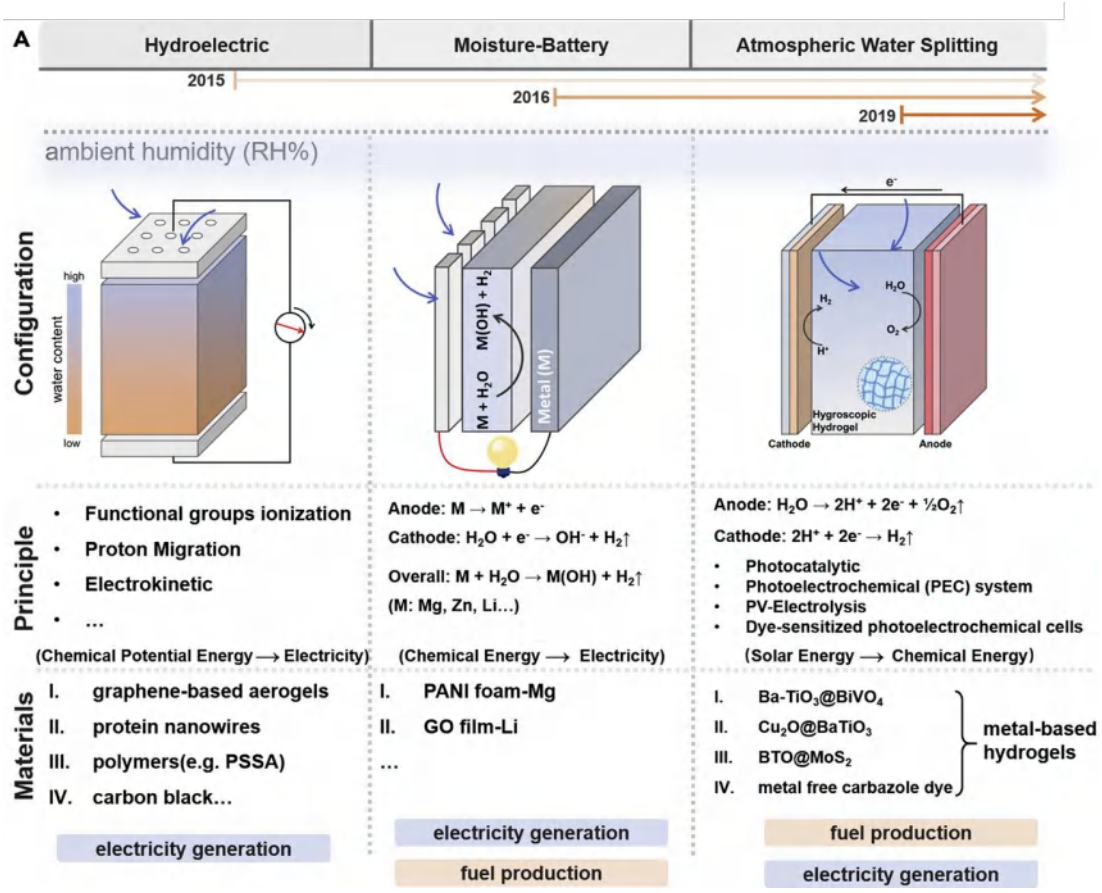

Fig. 2.19. Basic descript of humidity digestion framework (HDF) for energy generation. (a) Three main HDF technologies and their mechanisms.[96]

The development of atmospheric water splitting for next generation device was further brought forward by Tan's group[107,108]. As illustrated in the atmospheric water splitting device, the involved metal-based hydrogel that of high-water absorption capacity can directly splitting vapor molecules at the surface electrode. Therefore, the protons can be directly electrochemical reduced to green hydrogen gas. This reaction is within the scope of this thesis, since the integration of wearable device and electrochemical HER in the personalized device has not been proposed yet.

2.5.3 Customized electrochemical devices for gas capture

As discussed above, customized electrochemical cell depending on specific application

has shown potential interests. Many attentions have been paid to those electrodes that employed in aqueous medium, while those cells utilize other water source (e.g. vapor, moisture, carbon dioxides) seem to be another solution. Upton localized exposure to CO_2, Trevor *et al.*[109] adopt the concept of reverse electrodialysis, which generates ion gradients in a single initial solution. By selecting carbon capture agent (monoethanolamide), CO_2 from exhaled breath can be selectively captured. Furthermore, the prototype encompasses a configuration comprising a gas direction tube, CO_2 capture agent, and output electrode units, (**Fig.2.21 b**) making it well-suited for integration into the design framework of wearable technologies.

Similarly, Tan *et al*[108] tend to utilize the atmospheric moisture, instead of carbon dioxides by sandwiching hygroscopic materials that absorb environmental water molecules between electrodes (**Fig.2.21 c-e**). Additionally, the utilization of solar light facilitates the heat accumulation and water condensation at hydrogel interface, which further contribute to the water splitting reaction. The same group further demonstrates a moisture-sensitive hydrogel, which contains cobalt salts and dye molecules. This hydrogel with a water absorption capacity > 400%, can ideally transform from dry status to wet status after exposed to moisture **(Fig.2.21 f**). The employment of electrocatalyst (FeOOH) and semiconductor ($BiVO_4$) on ITO glass substrate further allow the harvest solar light into electricity, which functions as energy input. However, it is noticed that the above-mentioned devices are lack of flexibility and stretchability, which are not suitable for wearable applications.

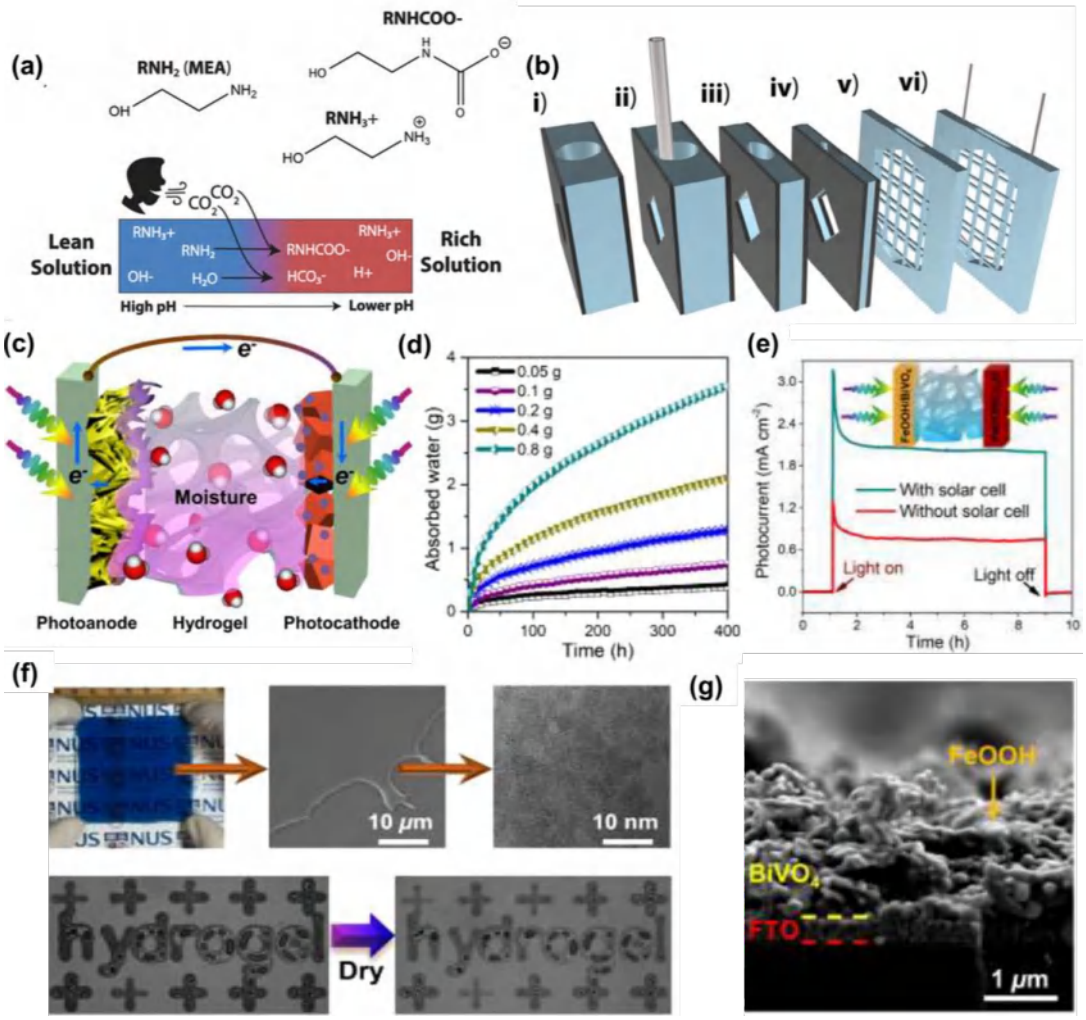

Fig. 2.20. (a) Design principles of breath-driven (CO_2) ion gradients to energy harvest system, (b) Illustration of device part (i: low-power geometry, ii: tube for direct application of breath iii: gaskets, iv: gaskets. v: increased cross-sectional area allows for increased current using this high-current geometry, vi: high-current geometry for the diffusion of pure CO_2 across the tubing wall[102]; (c) Schematic illustration of moisture converting device based on hydrogel; (d) Water absorption capacity of hydrogel; (e) Photocurrent response with the assistance of solar cell as electricity input; (f) Digital images of dehydrated hydrogel and printed hydrogel by 2D electrohydrodynamic printer, including the (left) hydrous and (right) dehydrated hydrogel; (f) SEM image of $FeOOH/BiVO_4$ on ITO substrate[101].

Baik and co-workers[110], instead of solar light, employed electricity to remove environmental moisture by constructing flexible and porous PE film. The high voltage (10 V) input can directly consume the moisture, by depositing catalysts on electrode with a consumption rate of 0.6 mL/h. However, limited studies have been conducted to directly utilize the moisture as water source, as well as the customization of electrochemical cell according to practical application. This unexplored field which may be interesting for sustainable development.

2.6 Conclusion and summary of research gap

In conclusion, combination of catalysts' designing principles and theoretical calculations have been well established for the exploring/understanding the cobalt oxides, sulphides and phosphides catalysts towards electro/photocatalytic HER and OER. By choosing proper earth abundant elements as the state-of-art materials, catalytic improvements can be achieved by morphology design (e.g. 2D nanosheets, nanotube arrays, hierarchical foam), phase control, electronic state modulations (e.g. anion and cation doping), interface engineering. In this review, cobalt and its derivatives including oxides and sulphides are mainly covered. This is due to the earth abundance of cobalt element and potential application for water splitting reactions. Moreover, compared with other candidates (e.g. MoS_2, which is only suitable for HER), cobalt based catalysts with tunable valence states are suitable for both HER and OER.

The exploration of cobalt based-electrocatalysts using different precursors towards high current density is still imperative. Only be understanding the initial states of metal precursors, people can design efficient electrocatalysts via post modulations. In addition to the catalytic performance, the stability (continuous operation for more than

20 hours at large current density) of the catalysts should be considered. Meanwhile, the concept of electrolyzer has been already extent to the wearable application by adopting the moisture sensitive substances. As a result, we have summarized the research gap, identified from the literature review, as follows: 1. The effect of heteroatoms on carbon support for the cobalt oxides' activity optimization has rarely been investigated; 2. Direct fixation of metal elements into biomass for electrocatalysts' fabrication is still challenging, without the extraction of active materials; 3. Difficulties lie in the synthesis of photocatalyst with semiconductor covered by electrocatalysts and exploration of corresponding electron transfer pathway; 4. The miniaturized electrolyzer for wearable application has not been fabricated.

Table 2.1 Summary of the synthesis conditions, precursors, morphology of catalysts and their performance in HER

MoS_2 Confined $Co(OH)_2$	MoS2 sheets; $Co(OH)_2$ particles	Lithiation; Ion Exchange	Nanoparticle confined in Sheets	1.0 M KOH	89	20 h	[111]
N-doped Mo carbide	Melamine; Molybdae ion; PEG	Self-interlink; Pyrolysis	Nano belts, Nano rods and Nano particles	1.0 M KOH	110	1000 cycles	[112]
CoP_3 Nanowire/TM	Co phosphide; MnO_2	Acid Etching	Nanowires	1.0 M KOH	76	60 h	[3]
$Zn_{0.1}Co_{0.9}Se_2$	ZIF-8; Se powders; Cobalt nitrate	Hydrothermal treatment	Hollow polyhedrons	0.5 M H_2SO_4	340	30 h	[113]
Fe-Ni@NC-CNTs	MIL-88 framework ;DCDA	Hydrothermal treatment; Pyrolysis	MOF-porous	1.0 M KOH	202	40,000s	[48]
R-MoS_2	Melamine-PMo_{12}; Thiourea	Reduction under H_2 condition	Nanoparticles	1.0 M KOH	111	5000 cycles	[114]
$CoNiSe_2$/NF	Nickle Foam; $NaBH_4$; Se powder	Hydrothermal; Selenylation	Nanorods	1.0 M KOH	74	10,000 cycles	[61]
Ru-N-S-$Ti_3C_2T_X$	$TiAlC_2$ sheet; Thiourea	Anneal @ Ar atm	Sheet like	1.0 M KOH	90	16h	[115]
Ni_4Mo/MoOx	Cu foam; Ni and MoOx	Induced codeposition	Nanosheets	1.0 M KOH	105	24h	[116]
$MoSe_2$	MoSe-10	Reduction and Etching	Nanosheets	0.5 M H_2SO_4	/	1000 cycles	[117]
CuS at $Ni(OH)_2$	Cu_2O sphere; CuS;$Ni(OH)_2$	Sulfidizing	Nanoshelled	1.0 M KOH	95	1000 cycles	[118]

$TaSe_2$	2H-$TaSe_2$	Direct synthesis; exfoliation	Flakes	0.5 M H_2SO_4	120	More than 1000cycles	[119]
Mo-Ni-Co selenides	Ni-Co Foam; Na_2MoO_4	Plasma treatment; Hydrothermal synthesis	Nanorod	1 M KOH	30	100 hours	[120]
N-doped carbon materials	ZIF-8	Pyrolysis	Porous structure	0.5 M H_2SO_4	155	/	[121]
N-doped carbon	Cu-BTC, carbon	Solvothermal reaction	Porous structure	0.5 M H_2SO_4	/	8000 cycles	[122]
Ni-doped Fe P/C	MIL-88A	Pyrolysis	Porous structure	0.5 M H_2SO_4	117	Over 12 hours	[123]

Table 2.2 Summary of the synthesis conditions, precursors, morphology of catalysts and their performance in OER

CoOx	Cu_2O nanowire; Co^{2+} etching	Fehling's reaction, ion exchange	Hollow rod	1.0 M KOH	320	8000 s	[74]
N-doped CoS_2	Cobalt; Urea; NH_4HCO_3; S	Hydrothermal & sulfidation process	Dandelion-Flower structure	1.0 M KOH	200	2000 cycles	[58]
$Co_{3-x}O_4$	Co^{2+}; glycerol	Hydrothermal & pyrolysis process	Nanoparticles	1.0 M KOH	268	10,000s	[59]
CoP_x@FeOOH	Co^{2+}; NaH_2PO_2; $FeSO_4$	Hydrothermal & Phosphidation &Electrodeposition	Nanorods	1.0 M KOH	222	30 hrs	[60]
Fe-Ni@MIL-53	MIL-53, $FeSO_4$, $NiSO_4$	Solvothermal	MOF-porous	1.0 M KOH	232	50,000s	[61]
NH_2-MIL-88B	$Ni(NO_3)_2$; $FeCl_3$; H_2BDC-NH_2	Solvothermal	MOF-porous	1.0 M KOH	240	30 hrs	[62]
NiFe(OH)x/(Ni,Fe)Se_2	Nickle Foam; $NaBH_4$; Se powder	Hydrothermal; Selenization; Electrodeposition	Nano sheets	1.0 M KOH	180	3,000 cycles	[63]
Ni-Fe$(OH)_x$/Defect graphene	NiFe-CO_3-LDH; graphene	Exfoliation; Self assembly	Sheet like	1.0 M KOH	210	10 hrs	[64]
[Fe]pyrazine[$Ni(CN)_4$] MOF	[Fe]pyrazine[$Ni(CN)_4$] MOF	Solvothermal; Pyrolysis	Nanosheets; Nanoflowers; Nano tubes	1.0 M KOH	249	24hrs	[65]
M-MNS	H_4dobdc ligand; Ni; Fe;Co;Cu	Hyrdrothermal; Oriented growth	Nanosheets	0.1 M KOH	298	50,000s	[66]

$NiCoS_4/Se_4$	NiCo-MOF	Sulfidation; Selenidation	Nanosheets	1.0 M KOH	251	1,200 min	[67]
$CeO_2/Ni(OH)_2$	Ni; CeO_2	Chemical bath deposition; Electrodeposition	Nanoparticles	1 M KOH	240	6 hrs	[68]
$V\text{-}NiS/NiS_2$	Ni, V, Urea, S	Hydrothermal; Sulfidation	Nanosheets	1 M KOH	220	50 hours	[124]
$Ni(OH)_2$	Ni, P, Se, S	Hydrothermal; Post treatments	Porous structure	1 M KOH	223	/	[125]

Table 2.3 Summary of the synthesis conditions, precursors, morphology of catalysts and their performance in photocatalytic HER

CZS@NiCoLDHs nanoflowers	300W Xe lamp (λ>420nm)	20v% TEOA	NiCo-LDHs	Hydrothermal	16 hrs	18.75 mmol h^{-1} g^{-1}	This Work
d$Zn_{0.15}S$-$Ni_{0.05}S$	225W Xe lamp (320 nm-780 nm)	0.3M Na_2S and Na_2SO_3	$Ni_{0.05}S$	Hyrothermal	16 hrs	604.4 μmol h^{-1} 10mg^{-1}	[126]
0.06wt%Pt/CdS	300W Xe lamp (λ>400nm)	10v% Lactic acid	Pt nanoparticle	Hydrothermal	20 hrs	10.28 mmol h^{-1} g^{-1}	[127]
L-NiCo	300W Xe lamp (1.5 AM filter)	No agent	$Ni_{0.83}Co_{0.17}$ hydroxides	Laser ablation	16 hrs	34 μmol h^{-1} g^{-1}	[128]
$CoFe_2O_4/Cd_{0.9}Zn_{0.1}S$	300W Xe lamp (λ>400nm)	0.7M Na_2S and 0.5M Na_2SO_3	$CoFe_2O_4$ nanoparticle	Hydrothermal synthesis	16 hrs	350 μmol h^{-1} g^{-1}	[85]
$Ni(OH)_2$–CdS/g-C_3N_4	300W Xe lamp (λ>420nm)	0.7M Na_2S and 0.5M Na_2SO_3	$Ni(OH)_2$	Hydrothermal synthesis	40 hrs	115.18 μmol h^{-1} g^{-1}	[129]
Ag_2S@CdS/ZnS	300W Xe lamp (800nm>λ>420nm)	0.1M Na_2S/ Na_2SO_3	Ag_2S	Solvothermal; Template	24 hrs	3.76 mmol h^{-1} g^{-1}	[130]
NiCo-LDH/40wt%P-CdS	300W Xe lamp (λ>420nm)	10v% Lactic acid	NiCo-LDH	Solvothermal; Phosphorization	12 hrs	8.67 mmol h^{-1} g^{-1}	[88]
Co_9S_8/Cd/CdS	300W Xe lamp (λ>420nm)	0.35M Na_2S and 0.25M Na_2SO_3	Co_9S_8	Hydrothermal synthesis	8 hrs	10.42 mmol h^{-1} g^{-1}	[80]
HCNs@HD-CoNi-LDH	300W Xe lamp (λ>420nm)	10v% TEOA	CoNi-LDH	Hydrothermal; Etching	25 hrs	10.95 mmol h^{-1} g^{-1}	[87]

CdS/WC (3wt.%)	300W Xe lamp (λ>420nm)	10v% Lactic acid	Tungsten carbide nanoparticle	Solvothermal; Mixture	20 hrs	9.18 mmol h^{-1} g^{-1}	[131]
NC@Co-CNTs/CdS	300W Xe lamp (λ>400nm)	10v% Lactic acid	Metallic cobalt	Hydrothermal carbonization	16 hrs	3.8 mmol h^{-1} g^{-1}	[81]

Chapter 3. Research methodology

3.1 Materials

All materials and chemicals in this thesis are used as received, without further purification. Detail list of employed materials is covered in the following Chapter 4, 5 and 6.

3.2 Synthesis of electro/photocatalysts

3.2.1 Hydrothermal synthesis

In general, the hydrothermal synthesis indicates the synthetic process that crystallizes the target materials from high temperature aqueous solution at high pressure in a Teflon-lined reactor. This is the most common way to prepare different phases of materials, especially for inorganic substances. The inorganic salts are dissolves in aqueous solution (if organic solvent, then it is devoted to solvothermal synthesis). Then, the solution is transferred to a reactor, which is further sealed in a stainless-steel autoclave. The temperature will subsequently raise above boiling point of solion to initiate aggregation of metal cluster and start the crystallization process.

3.2.2 Pyrolysis

The pyrolysis process is a typical carbonization reaction, involving complex reactions, where organics will be vaporized, and inorganic metal ions will aggregate to form particles. More specifically, the carbon-containing compounds undergo the uncompleted conversion to graphited carbons, which will further function as the supporting substance for metal catalysts. Therefore, the design of carbonization process (e.g. target temperature, rising rate, duration) is unique to different precursors, upon

whose molecular structure.

3.3 Experimental setups

3.3.1 Cleaning of glassware

In general, the standard procedure for glassware includes 2 steps: 1. Preparation of chromic mixture: 40 mL ultrapure water (conductivity = 0.26 µS cm^{-1}, T= 22±2 ℃) was slowly added into 20 g potassium permanganate powder under stirring. Subsequently, 360 mL H_2SO_4 acid (96%) was slowly added into above solution under stirring. The chromic mixture was ready to be used after natural cooling down. 2. All electrochemical cells were immersed into above chromic mixture (~ 100 mL), and underwent ultrasonication for 20 minutes, followed by rinsing in ultrapure water, ethanol. Finally, cleaned glassware were obtained by drying at 60℃.

3.3.2 Preparation of electrodes and electrolyte

In this study, we used four types of electrodes: 1. Carbon cloth; 2. Nickel foam; 3. Fluorine-doped tin oxide glass (FTO glass); 4. Glassy carbon. The first two electrodes were cut into 0.5 x 1.5 cm^2 (A_{geo} =1 cm^2, the electrode is half immersed into the electrolyte), while the rest one was used as received (1x1.5 cm^2). All electrodes are washed by ethanol, acetone, and ultrapure water under sonication for 15 mins (note: Ni foam requires extra cleaning in 0.1 M HCl) to remove any containments, oxides, and organics, followed by drying at 60℃.

All electrolyte was prepared using ultrapure water. 1M KOH (99.99%,)/ NaOH (99.9%) and 0.5M H_2SO_4 (ACS grade) were employed as electrolyte. The pH value of prepared electrolyte was measured using pH meter (HM-20R, DK-TOA, Japan), prior to use.

3.3.3 Setups of electrochemical cells

Typically, we used three-electrode system (**Fig.3.1**) for electro-catalytic measurements, which is consisting of working electrode, counter electrode, and reference electrode. The counter electrode should be noble materials, which means the potentials of it does not change when there is current passing through. This is because the recorded potential difference should between reference electrode and working electrode. In this study, we use platinum planar electrode (1x2 cm^2, 0.1 mm in thickness).

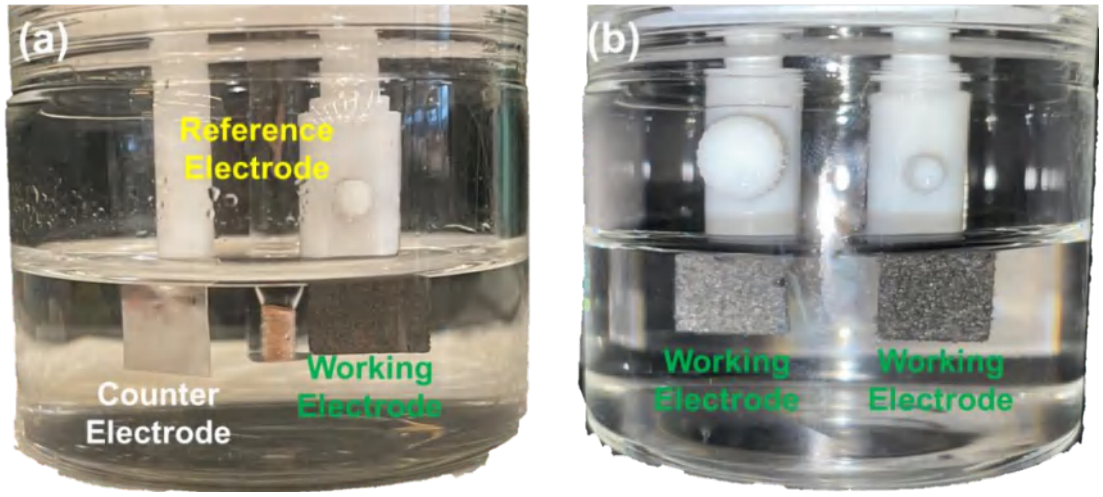

Fig.3.1. Illustration of setup for (a) three-electrode electrochemical cell (note: for alkaline and acid medium, the counter electrode was changed to graphite electrode), (b) two-electrode cell in this thesis.

The reference electrode is made of a standard electrochemical redox potential (e.g., Ag/AgCl, $Hg/HgSO_4$, Hg/HgO electrode). In this study, we used Ag/AgCl for the neutral medium, and Hg/HgO electrode for alkaline medium. The changes in potential of working electrode is recorded with respect to the reference electrode. Basically, there are two separate circuits in the three-electrode system: 1. Polarising current in WE-CE, and 2. No current is passing through WE-RE to precisely record the potential change.

3.4 Characterizations

3.4.1 X-ray diffraction analysis (XRD)

XRD is the fundamental non-destructive analytical method to study the samples' phase composition, crystal structure, plane orientations, etc. As indicated in Fig.3.2, the incident X-ray will be scattered by atoms in the lattice plane. One can obtain the lattice the lattice spacing and its Miler indices (h, k, l) according to the following Bragg equation:

$$2dsin\theta = n\lambda$$

Where d is the lattice spacing, θ is the angle between the incident beam and lattice plane, λ is the wavelength of incident X-ray (e.g. λ of Cu kα= 1.54 Å).

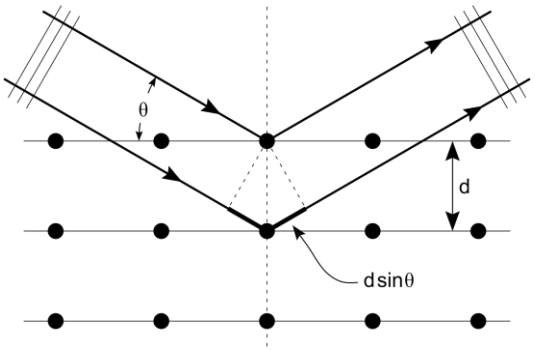

Fig.3.2. Illustration of X-ray diffraction in crystal sample. (Source: https://en.wikipedia.org/wiki/X-ray_crystallography).

Specifically, by comparing the standard card of one material (e.g., database from international center of diffraction data), one can distinguish the phase composition in the sample. Moreover, by analyzing the Bragg's law, one can also predict the crystal plane, which is related to the specific structure in the samples. In general, powder samples are grounded into the XRD holder (made of polycrystalline silicon) to form an unfirm plane, using Bragg-Brentano (BB) mode. For the film samples (e.g., textiles), it

is suggested to use Parallel beam mode of X-ray to reduce the X-ray intensity. The scanning angle usually starts from 10° to 70° at 10 °/min.

3.4.2 Scanning electron microscope (SEM) and energy-dispersive X-ray spectroscopy (EDX)

SEM is widely used to investigate the morphological information of various samples. It utilizes incident electrons (accelerate voltage = 10/20 kV) to emit the electrons from samples, and detector will collect the secondary electrons to give the morphological information. It is suitable for various samples including metals, semiconductors, and organics. For those insulators or poor conductive samples, gold sputtering is required to enhance the sample conductivity. For those nanoparticles, they are dispersed in ethanol under sonication, and further drop-casted onto silica wafer for SEM session.

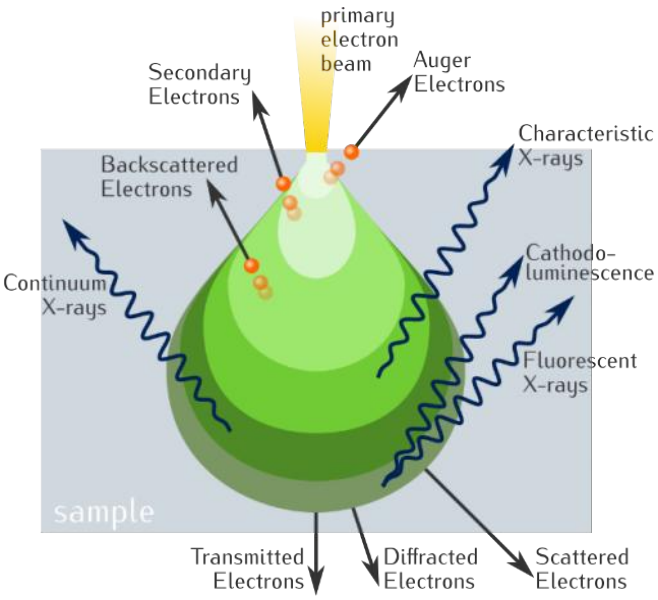

Fig.3.3. Working principles of SEM and EDX mapping (Source: https://en.wikipedia.org/wiki/Scanning_electron_microscopy).

EDX mapping is another crucial technique for the determination of elements based on SEM. It collects the characteristic X-rays that emitted from the higher-energy shell

electrons fall downs to the holes in lower-energy orbitals.

3.4.3 Transmission electron microscope (TEM)

TEM is the advanced techniques to investigate the structure of samples in an atomic resolution. Typically, the electrons are ejected and accelerated by a field electron emission gun at a high voltage (100 kV -300 kV). The emitted electrons are further focused by a series of condenser, object apertures to the specimen, which electrons will transmit the samples (**Fig.3.3**). The electrons further experience the projector lens and reaches the detector for imaging. While for the diffraction mode, a selected area aperture upon the objective lens. The whole process requires the specimen to be thin enough for observation. For the powder samples, very little amounts of samples are dispersed in ethanol under sonication and drop-casted onto the carbon mesh.

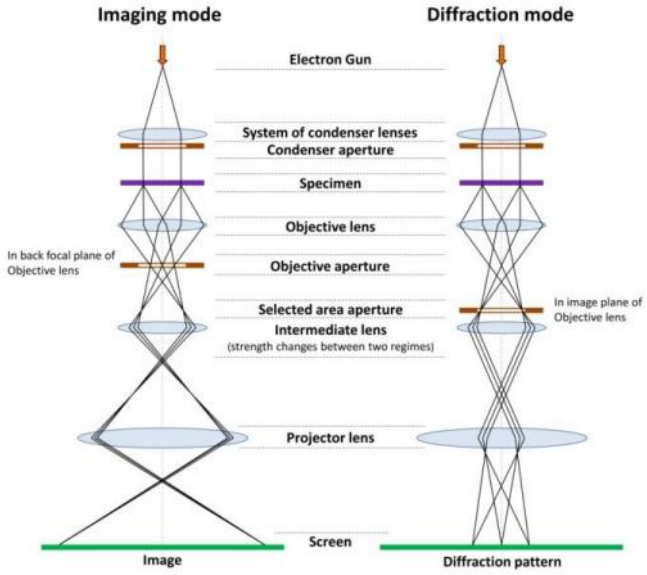

Fig. 3.4. Schematic illustration of imaging and diffraction modes in TEM (Source: https://en.wikipedia.org/wiki/Transmission_electron_microscopy).

TEM also has the dark-field mode by selecting diffracted electrons using the back focal aperture. The dark-field mode possesses a clearer contrast compared with the bright-

field images, where electron intensity will be reduced due to the thickness of samples. TEM also contains diffraction mode, to obtain a diffraction pattern in TEM, a selected area aperture is used to limit the region of the sample that is illuminated by the electron beam. This creates a focused electron beam that interacts with a specific area of the sample, producing a corresponding diffraction pattern.

3.4.4 Thermogravimetric analysis (TGA)

TGA is a thermal characterization technique that investigates the thermal phenomena of samples, including absorption, desorption, vaporization, sublimation, reduction, oxidation, and decomposition. By quantifying the weight changes of specimens when they undergo controlled heating, TGA enables the comprehensive exploration of these thermal activities. The samples are usually contained in crucible, which are further places on a holder. The holder is connected to the micro balance (**Fig. 3.4**).

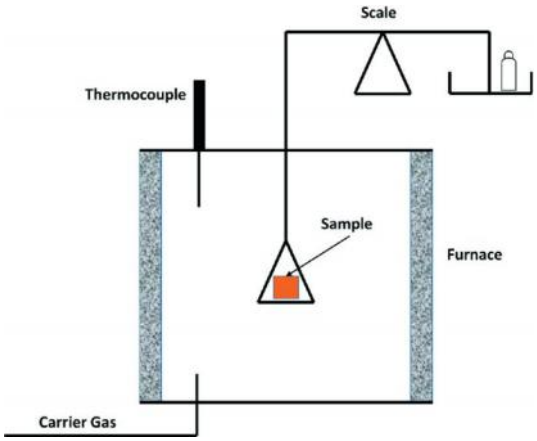

Fig.3.5. Schematic illustration of TGA instrument. (Source: https://link.springer.com/chapter/10.1007/978-3-030-11599-9_7).

Its utility is particularly pronounced in the analysis of volatile products that are susceptible to evaporation or loss during the thermal degradation of materials. Typically, TGA was employed to examine the composition of organic and inorganic samples. To

this end, fine sample powders/ chopped fibers with masses ranging between 1 and 5 mg were subjected to TGA, utilizing a temperature range of 100–900 °C and a heating rate of 10 °C min^{-1} under N_2 environment.

3.4.5 Fourier transform infrared (FTIR) spectroscopy

FTIR spectroscopy facilitates the acquisition of molecular information by subjecting the sample to infrared light, thereby enabling the identification of functional groups and molecular fingerprints. Infrared spectroscopy encompasses two primary approaches, namely diffuse reflection and attenuated total reflection (ATR). In these concepts, the utilization of a mathematical system known as Fourier Transform enables the conversion of raw signals into an optical spectrum, representing infrared wavelength-dependent information (**Fig. 3.5.**). The spectrum range can cover the region from near-infrared to far-infrared.

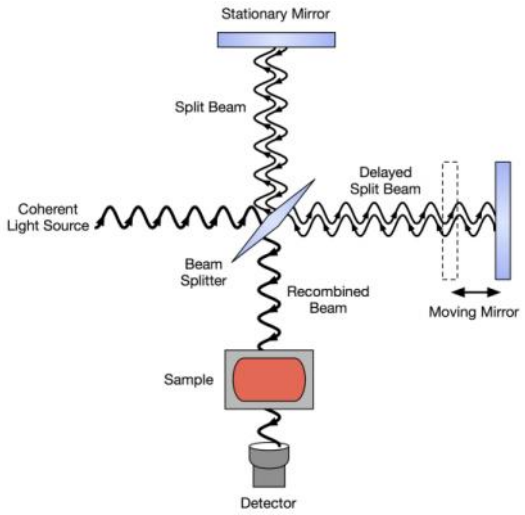

Fig.3.6. Schematic illustration of FTIR (Source: https://en.wikipedia.org/wiki/Fourier-transform_infrared_spectroscopy).

The present study emphasizes the utilization of ATR-FTIR for direct measurement of powder samples and fibers. The conventional KBr pellet method is employed as the

classical sample preparation technique. Typically, 200mg KBr powder are mixed with ~ 1 mg of samples in a motor. The mixture is further extruded into pellet, forming a light color. During the measurements, the infrared light will pass through the sample, giving the information of chemical bonds.

3.4.6 Ultraviolet–visible diffuse reflectance spectrometer (UV–vis DRS) spectroscopy

UV-vis DRS spectrometer is employed to determine the absorption and transmittance of powder sample. (e.g., band gap, absorption edges). In this case, the sample is irradiated by laser with wavelength in the range between 200 nm to 800 nm. One part of light will be absorbed the sample, while the remaining diffuse-reflected light will be collected and integrated in a sphere coated with $BaSO_4$ powders for further detection (Fig. 3.6). In order to achieve a reflectance close to 100%, the $BaSO_4$ reference is employed as background, which is adjacent to the samples.

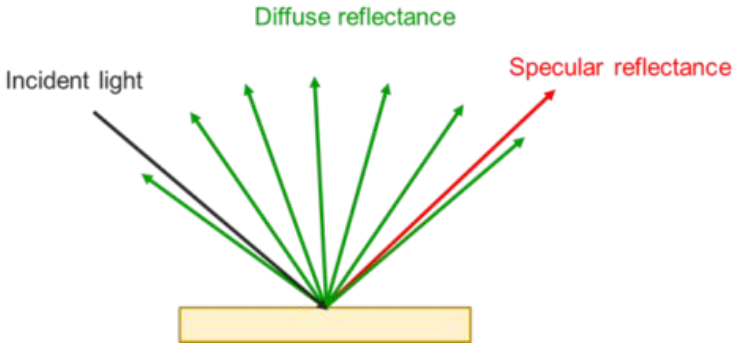

Fig. 3.7. Schematic illustration of diffuse reflectance in UV-vis spectroscopy.

The Tauc plot, which then is derived from UV-vis DRS spectrum, are calculated by using the following equation:

$$\alpha hv = C_1(hv - E_g)^n \quad (3.1)$$

Where α is the absorption coefficient of the materials, C_1 is constant, hv is the energy

of incident beam at different wavelengths,.

3.4.7 Raman spectroscopy

Raman spectroscopy is a common technique to investigate the vibration mode in the samples. It relies on the inelastic scattering of photons, which is also known as Raman scattering. In general, the incident beam interacts with molecular vibrations, phonon in the system, resulting in the energy shift of the vibrations (Stokes, Anti-Stokes scattering). This shift gives the information of vibrational modes in the samples. Similar to XRD measurements, powder samples are required to be grounded onto glass slide to ensure the perpendicular incident laser.

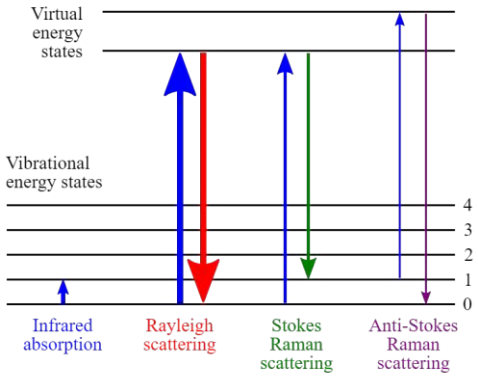

Fig. 3.8. Mechanism illustration of Raman spectroscopy.

3.4.8 Brunauer-Emmett-Teller (BET) surface area measurement

BET surface area measurements were conducted by N_2 adsorption-desorption isotherm at 77 K. Typically, N_2 gas molecules serves as the adsorption molecules in the samples, which gives the information of sample topology. BET theory is constructed on the basis of Langmuir theory (monolayer adsorption). It extends the monolayer adsorption to multilayers by adapting the following assumptions: 1. No chemical interaction between molecules and substrates; 2. Gas molecules only interact physically with the adjacent layer, 3. The enthalpy of adsorption for the first layer constant and greater than the

second layer.

$$\frac{P}{V(P_0-P)} = \frac{1}{V_m C} + \frac{(C-1)}{V_m C} \times \frac{P}{P_0} \quad (3.2)$$

Where P is the pressure, P0 is the saturated vapour pressure of N2, Vm is the measured adsorbed gas molecule per unit mass (STP cm^3 g^{-1}), C is the adsorption heat related to the gas molecule.

3.4.9 X-ray photoelectron spectroscopy (XPS)

XPS is commonly used in the analysis of electronic environment, elemental composition at the sample surface (~ 10 nm). Basically, it relies on the photoelectric effect of the sample. In specific, X-ray source (Al kα, hv = 1486.3 eV) generate the incident beam, which further transfer its energy to the core-level electrons of the samples. The electrons of the sample then are emitted outside the sample with kinetic energy. One can calculate the binding energy by determining the kinetic energy of emitted electrons by following equation:

$$E_{Kin} = hv - E_{bin} - \varphi_{analyzer} \quad (3.3)$$

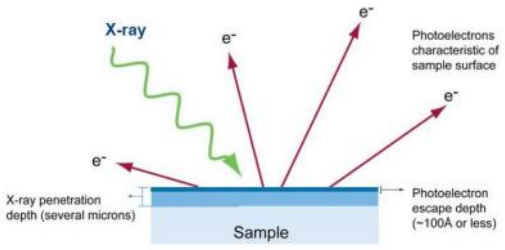

Fig. 3.9. Mechanism illustration of X-ray photoelectron spectroscopy.

Moreover, XPS also provides the information of oxidation state of one element, since the kinetic energy of electrons is highly dependent on the local electronic environment.

3.4.10 Ultraviolet photoelectron spectroscopy (UPS)

UPS is a well-known and convenient technique to measure the Fermi level and valence band maximum of semiconductors. The UPS spectra exhibit the second energy cut-off region and valence band region, revealing the work function of the material and its valence band versus to Fermi level.

Fermi level (Ef) was calculated using the equation:

$$E_f = \Phi_m = E_{cut-off} - h\nu \quad (3.4)$$

Where Φ_m is the work function of material; hν is the irradiation energy; $E_{cut\text{-}off}$ is the onset energy in the cut-off region; $h\nu$ is the He I source (21.22 eV).

In the valence band region of UPS spectra, the relative position of the valence band (VB) to the Fermi level is measured as VBedge by extrapolating the leading edge of the VB spectrum to the baseline. Thus, the valence band maximum (E_{VB}) is estimated by the equation:

$$E_{VB} = E_f - VB_{edge} \quad (3.5)$$

Meanwhile, the conduction band minimum (E_{CB}) is calculated by:

Therefore, the band structure of the sample could be built based on the above calculations.

$$E_{CB} = E_{VB} + E_g \quad (3.6)$$

3.4.11 Photoluminescence (PL) spectrophotometer and PL lifetime (τ_{ave})

PL is a widely used methodology for the characterization of optoelectronic properties of semiconductor. It is related to the fluorescence and phosphorescence properties of samples. These optoelectronic properties encompass various aspects, including bandgaps, photoelectronic activity, emission intensity, quantum yield,

absorption/emission characteristics, luminescence energy transfer, decay time, as well as chemical and physical stability. Specifically, in this thesis, we focus on the PL emission spectra, which is directly related to electron-hole recombination. Moreover, by comparing spectrum of various samples, the dynamics of electron can be studied, shedding light on the photocatalytic activity, point defects, and optical properties of as-obtained catalysts. In a typical trial, powder samples are sandwiched in between two quartz glass, by choosing the solid PL accessories.

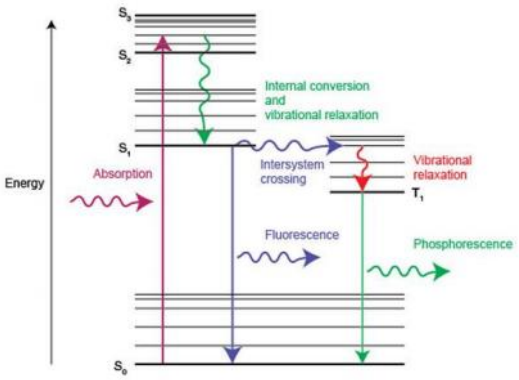

Fig. 3.10. Mechanism illustration of Photoluminescence spectroscopy.

PL electron lifetime, related to the carrier separation dynamics, was fitted and calculated according to the equations below:

$$A(t) = A_1 e^{\frac{-t}{\tau 1}} + A_2 e^{\frac{-t}{\tau 2}} + A_3 e^{\frac{-t}{\tau 3}} \quad (3.6)$$

$$A_{(ave)} = \frac{(A_1 {\tau_1}^2 + A_2 {\tau_2}^2 + A_3 {\tau_3}^2)}{(A_1 \tau_1 + A_2 \tau_2 + A_3 \tau_3)} \quad (3.7)$$

Where A and τ indicate the amplitudes and emission lifetimes of each component.

3.4.12 Inductively Coupled Plasma Optical Emission spectroscopy (ICP-OES)

ICP-OES technology is employed as the precise detection of chemical elements. Unlike XPS and EDX mapping, which only give the information of surface elemental composition, ICP-OES is a destructive technique, requiring the dissolution of samples

in the strong acid. The sample is then aspirated into an argon plasma generated by an inductively coupled plasma source. The plasma consists of a high-temperature ionized gas, which excites the atoms or ions in the sample to emit characteristic light. By comparing the intensity of emitted light from standard solution, we can tell the concentration of specific element in the samples. In this study, we dissolve 5mg samples into a mixture of concentrated HNO_3 and HCl (1:3 in v%). The solution is further diluted to 100 mL, which is further transferred to the machine.

3.5 Electrochemical measurements

3.5.1 Cyclic voltammetry (CV)

CV is an electrochemical technique for electrocatalytic characterization. It is consisting of sweeping potential along a triangular between two values at certain time (the slope between two value is determined as the scan rate dU/dt). Meanwhile, the electrochemical station will record the current response at a specific potential during the scan.

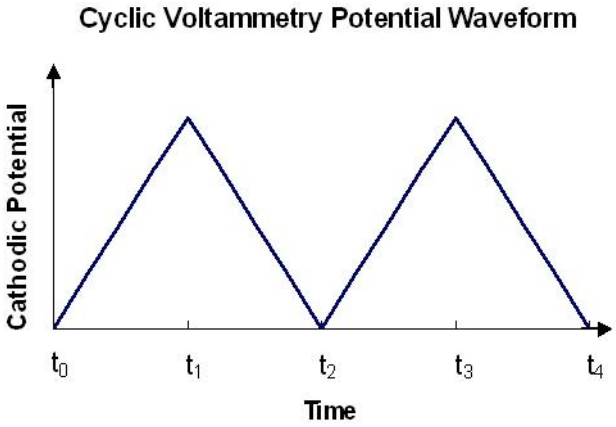

Fig. 3.11. Cyclic voltammetry- potential waveform. (The slope between two cathodic potentials is scan rates, for example: 10 mV/s)

A positive recorded current if the process at the working electrode assumes net shuffling

of electrons in direction from the working electrode to the counter electrode. Consequently, the negative current recorded by CV means the reactions taken at the working electrode indicates transfer of electrons from its surface. It should be noticed that the positive or negative value of current does not mean the oxidation/reduction (e.g., metals, molecules) process taken at the electrode. These values also have the meanings of electrolyte adsorption, changes in the double layer capacitance. In our study, we used CV to do the activation process, where catalysts will undergo reconstruction to expose more active sites. Moreover, ECSA values are also determined by CV technique.

3.5.2 Linear sweep voltammetry (LSV) and Tafel slope

LSV, similar to CV technique, the potential recorded between working electrode and a reference electrode is swept linearly in time. Based on the obtained current, we can determine the Tafel slope of samples, which is directly related to the reaction kinetics taken at electrode surface.

Generally, the Tafel plot consists of a linear relationship between the logarithm of the current and the overpotential, where the slope of the line can be related to the electron transfer kinetics according to the following equation:

$$\eta = \pm A log_{10}(\frac{i}{i0}) \quad (3.8)$$

where η is the overpotential in mV, A is the Tafel slope in mV/Dec, I the current density in mA/cm^2 and i_0 is the exchange current density in mA/cm^2.

3.5.3 Double Layer Capacitance (C_{dl}) and Electrochemical active surface area (ECSA)

ECSA was derived from the measurement of double layer capacitance by assuming the case of planar electrode. In order to obtain C_{dl}, CV at different scan rates in the non-

faradic region are conducted.

$$ECSA = \frac{C_{dl}}{C_s} \quad (3.9)$$

Where C_{dl} is double layer capacitance, C_s is the specific capacitance, which has a value of 40 uF cm^{-2} for planar electrode.

3.5.4 Electrochemical impedance spectroscopy (EIS)

EIS is a powerful technique to investigate the electron dynamics at the electrode surface, by giving small potential difference. Generally, by applying small potential altitude at fixed overpotential (e.g., 5mV at η=100 mV) will give the information of electron transfer of the catalyst layer deposited on the electrode.

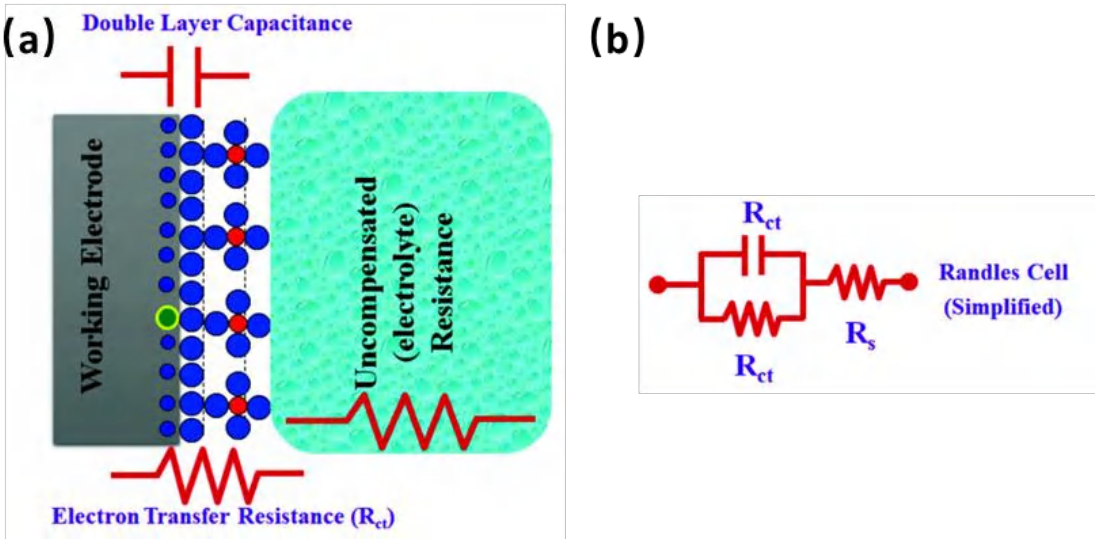

Fig. 3.12. (a) A scheme illustrates the EIS circuit and the redox reactions taken at the surface of working electrodes in a traditional three-electrode cell. (b) A simplified Randles cell, where Rct is the charge transfer resistance, Rs is the solution resistance and C_{dl} is the capacitance.

Based on the simple Randle cell, the composition of equivalent circuit at electrode/electrolyte interface can be regarded as tandem series between a solution

resistance and parallel double layer capacitance with electron transfer resistance.

3.5.5 Mott-Schottky curve

Mott–Schottky plot is a plot of 1/C2 vs applied potential at a fixed frequency. The flatband potentials (*E*fb) of the semiconductors can be calculated by extrapolation to the *x*axis of plots of 1/*C*2 *vs.* potential (V). The capacitance measurements are presented as an M-S plot following the equation below (Mott–Schottky equation):

$$\frac{1}{C^2} = 2(N_D e\varepsilon\varepsilon_0)^{-1} \times (E - E_{fb} - \frac{KT}{e}) \quad (3.10)$$

Where, C is the space charge capacitance per unite area (i.e., the capacitance of the semiconductor depletion layer), ND is the density per cm3 of donors/acceptors in the semiconductor, e is the electron charge (1.6×10^{-19} C), ε is the dielectric constant of the material, ε_0 is the permittivity of free space (8.85×10^{-12} F m^{-1}), E is the applied potential, E_{fb} is the flat band potential, k is the Boltzmann constant (1.38×10^{-23} J K^{-1}) and T is the absolute temperature (298 K).

3.6 Photochemical measurements

3.6.1 Photocatalytic hydrogen evolution and stability test

The photocatalytic hydrogen evolution was conducted in a 50 mL quartz vessel. Before each measurement, the quartz experienced the same procedures in the previous glass cleaning part. In this study, the Pyrex vessel possess a V-shape, where two sides allow the flow of N_2 to remove the air content in the quartz. While the upper part is sealed by plug avoiding the leakage of H_2. In a typical trial, 10 v% of TEOA hole sacrificial agent, 5 mg of Eosin Y dye sensitization system are dissolve in DI H_2O. Additional 2.5 mg of catalysts are dispersed into the above solution under sonication. The dispersion will

further undergo 20 min stirring, experience an adsorption-desorption equilibrium. Every 30 min, 100 uL of gases will be withdrawn, and injected into the gas chromatography to analyze the composition.

For the photostability test, the measurement is extent to 4hrs as one cycle, and every 1 hr, 100 ul of gas will be withdrawn and injected into the analyzer. Between each cycle, additional 1 ml TEOA will be replenished into the above system. In total there are 3 cycles to finish the stability test.

3.6.2 Chopped I-t curves

The chopped I-t curve was conducted by drop-cast sample/nafion dispersion onto the FTO glass. The xenon lamp was cut on and off by chopping at a 30s interval. The photo-induced electron-hole separation will be detected by electrochemical station. Therefore, the photocurrent is directly related to the charge separation ability of samples.

3.7 Theoretical simulations

Density functional theory (DFT) is a computational approach to investigate the electronic structure and interfacial reactions of atoms, molecules and bulk materials. DFT is the in concept of quantum theory, where electron density is described by time resolved electron wavefunction. While the older quantum mechanical methods that focus on solving the complex many-body Schrödinger equation, the development of DFT simplify the equations by substituting the wavefunction with electron density. The foundation of DFT lies in the Hohenberg-Kohn theorems, which state that the electron density determines the potential energy of a system and, consequently, all other properties. These theorems establish the link between the ground-state electron density

and the ground-state properties of a system, making it possible to calculate various properties using only the knowledge of the electron density.

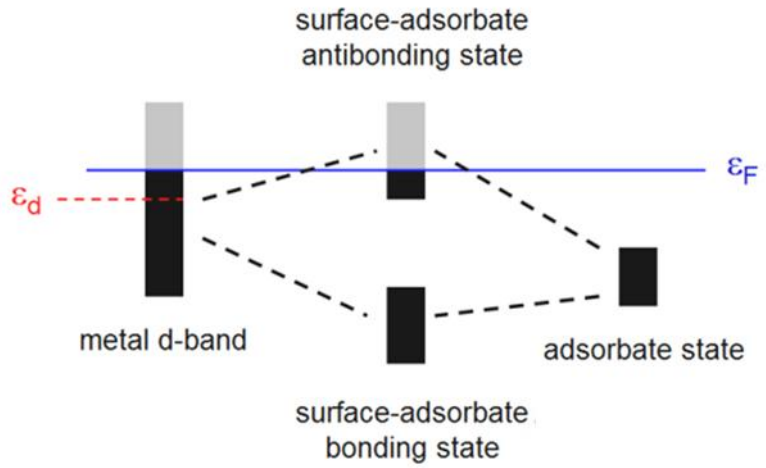

Fig. 3.13. Schematic illustration of the formation of a chemical bond between an adsorbate valence level to the s and d states of a transition metal.

DFT plays an important role in the photo/electrocatalytic area by giving the mechanism understanding, predicting the catalytic performance coupled with machine learning. More specifically, DFT calculations can be employed in following aspects related to this thesis's work:

1. Gibbs free energy for reaction mechanism exploration: as mentioned int above fundamental principles for HER and OER, scientists have explored several reaction pathways. DFT, under this circumstance, can be calculated for each intermediate by comparing the adsorption energy.
2. Interaction between electrocatalyst and substrate (**Fig. 3.5**): catalysts are usually supported by carbon frameworks, or semiconductors in photocatalysis. The choice of substrate material and its interaction with the catalyst can significantly influence the catalytic activity and stability. DFT can predict the adsorption energies, charge transfer, and electronic coupling between the catalyst and substrate, aiding in the

design of efficient catalyst-electrode systems.

3. Catalyst Design and Screening: DFT calculations allow for the screening and evaluation of potential catalysts for determined reaction pathway. By calculating the adsorption energies of molecules/intermediates on different catalyst surfaces, DFT can identify promising candidates with desirable properties, such as high activity, selectivity, and stability. This aids in the development of efficient catalysts for specific electrochemical processes.

By combining experimental techniques with DFT calculations, researchers can gain a deeper understanding of electrocatalysis, accelerate catalyst development, and provide guidance for the design of more efficient and sustainable electrochemical devices.

Chapter 4. Cobalt oxides-based catalysts with tunable Co valence states for electrochemical water splitting

4.1 Introduction

Electrocatalytic water splitting to generate hydrogen and oxygen has attracted intensive attention as an effective solution to the global warming[6,133]. Among various candidates, transition metal-based materials derived from earth-abundant elements have been regarded as one of promising catalysts to boost the water splitting reaction. Nevertheless, strategies such as heteroatom doping[22,134], defects engineering[7,23], atom intercalation[135,136] and topographical control[137] were designed to significantly increase the number of accessible active sites and modulate the corresponding electronic environment of metallic atoms.

Zeolitic imidazolate frameworks (ZIFs) comprise these strategies by facile one-pot synthesis with ordered crystal structure, modular versatility such as tunable atoms and organic linkers as well as low cost of synthesis[61,138,139]. Moreover, spontaneous coordination between Zn/Co and organic linkers at moderate conditions comes to ours interests, due to the easy heteroatom doping. Typically, cobalt element has been reported as a promising candidate due to the medium adsorptive energy to the reaction intermediates according to density function theory calculations[140]. While the low intrinsic conductivity of ZIFs limits their applications as electrocatalysts. As a solution, high temperature carbonization is commonly employed to improve the intrinsic conductivity of ZIFs. Moreover, Co element will facilitate the graphitization of the

frameworks by the formation of carbon nanotubes (CNTs) at high pyrolysis temperature[9,141,142] to enhance the conductivity of samples. Therefore, scientists have designed core-shell structure like ZIF-67@ZIF-8[66,143] to selectively functionalize the metallic Co located in carbons while Zn will evaporate at similar temperature (> 905 ℃) to avoid the particles aggregations. However, under such harsh condition, the organic linkers will break down causing the collapse of whole framework due to the weak coordination force. This collapse hinders the available active sites in the inner part. To tackle this problem, protective/confinement pyrolysis has been proposed: for instance, ZIF-8 was mixed with surfactants such as polyvinylpyrrolidone (PVP)[144] or cetyltrimethylammonium bromide (CTAB)[145] to establish the cohesive interaction between interfaces. Or the construction of rigid interface such as pyrolyzing ZIF8@SiO_2[146] also achieved significant improvements in the maintenance of pore system and original surface area of ZIFs. As a result, the maintenance of pore systems or the construction of hierarchical structure can facilitate the electrolyte diffusion and mass transfer.

However, to best of our knowledge, few attentions have been paid to reveal the electronic modulation on the active sites of these protective carbonized samples from post treatment. As mentioned, most ZIFs carbonized at this harsh temperature will lose their original specific surface area, which finally lies in the range of S_{BET}~100-200 m^2g^{-1}. The resultant products sluggish the overall catalytic performance due to the low possibility of active sites exposed to electrolyte. Moreover, PVP polymer, as reported which will incorporate into MOF system, can also contribute to the formation of graphitized carbons. In this case, the post phosphine treatments induces the P doping into such carbon frameworks, instead of formation of CoP nanoparticles [66,143,147].

Ultimately, our studies confirm that the introduction of P element can effectively influence the electronic environment of Co elements. As a result, the kinetics of overall water splitting reaction can be improved. In this study, we firstly manifested a high specific surface area (645.7 $m^2 g^{-1}$) and constructed a micro-mesoporous system of PVP assisted bimetallic ZIF-8/ZIF-67 (PVP-$Zn_{0.2}$@ZIF-67) at a pyrolysis temperature of 920℃. Then we confirmed the introduction of P into the carbon frameworks by taking advantage of larger pores sizes to reveal optimized electronic state interaction. Moreover, we also investigated the effect among different Co valence states, where synergetic effect between Co^0 and Co^{2+} boosts the water reduction and Co^{2+} and Co^{3+} facilitate the water oxidation respectively. The as-synthesized catalysts were employed as bifunctional electrocatalysts towards hydrogen evolution reaction (HER) and oxygen evolution reaction (OER).

4.2 Experimental Section

4.2.1 Materials

All materials were purchased and used without further purification. Zinc nitrate hexahydrate ($Zn(NO_3)_2 \cdot 6H_2O$, ≥98.0%), 2-methylimidazole (2-MeIM, ≥97.0%), sodium hypophosphite monohydrate (NaH_2PO_2) and 20wt% Pt/C were purchased from Alfa Aesar. Cobalt nitrate hexahydrate ($Co(NO_3)_2 \cdot 6H_2O$, ≥98.0%) and polyvinyl pyrrolidone (PVP, Mw = 13 kDa) were purchased from Aladdin. Methanol and ethanol (ACS grade) were purchased from Anaqua Co Ltd..

4.2.2 Synthesis of ZIF-8/ZIF-67 and PVP assisted ZIF-8/ZIF- 67

In a typical synthesis of ZIF8/ZIF67[20], $Zn(NO_3)_2 \cdot 6H_2O$ (0.36 g) and $Co(NO_3)_2 \cdot 6H_2O$ (1.45 g) was completely dissolved in 50 mL of methanol to form a purple solution A.

2-Methylimidazole (2-MeIM, 4.49 g) was dissolved in 93.3 mL of methanol to form a homogeneous solution B. Then the solution B was poured into solution A under stirring for 1 hour (in total 143.3 mL of methanol). The resultant powders were collected under 5000 rpm centrifuge and washed with methanol three times to remove unreacted materials and dried in vacuum at 60℃ for 8 hours.

To fabricate PVP assisted ZIF-8/ZIF-67, an additional methanolic PVP solution (1.8 g of PVP dissolved in 30 mL methanol) was poured into abovementioned metal precursor and organic linker contained methanolic solution (ZIF8/ZIF67) after 20 minutes' nucleation of ZIFs. Finally, the obtained PVP assisted ZIF8/ZIF67s underwent washing with methanol for three times and were dried in vacuum at 60℃ overnight.

4.2.3 Synthesis of phosphine treated CoO_x/ nitrogen doped Carbons (P-CoO_x/NCs)

The synthesized PVP assisted ZIF8/ZIF67 further experienced carbonization process at 920 ℃ for 150 minutes with a ramp rate of 5℃/min under N_2 atmosphere and was naturally cool down. The resultant products were denoted as CoO_x/N-doped carbons (CoO_x/NCs). In this work, all the carbonizations were employed on the PVP assisted ZIF-8/ZIF-67 samples. Otherwise, the direct carbonization of ZIF8/ZIF67 at 920℃ for 150 minutes denotes CoO_x/NCs without PVP. Additionally, PVP assisted ZIF8/ZIF67s also experienced different carbonization temperatures (800℃, 900℃) which further denote CoO_x/NCs@800℃/900℃.

After the carbonization, different amounts of NaH_2PO_2 (x = 600, 900, 1200 mg) were employed as phosphine precursors to conduct the surface treatment of CoO_x/NCs. In a typical treatment, 5 mg of CoO_x/NCs was placed in the downstream of a porcelain boat and x (600, 900, 1200) mg of NaH_2PO_2 was put in the upstream of the boat under N_2

atmosphere. The temperature of tube furnace was elevated with a ramp rate of 3℃/min to 350℃ and maintained for 120 minutes, allowing the decomposition of NaH_2PO_2 (Equ. 1, Notice: the tail gas of NaH_2PO_2 is extremely toxic requiring saturated $CuSO_4$ solution as exhaust converters). The final products were collected after the naturally cool down of the furnace which were denoted as m P-CoO_x/NCs where m = 0, 600, 900, 1200.

$$2\ NaH_2PO_2\ (s) \rightarrow PH_3\ (g) + Na_2HPO_4\ (s) \qquad (4.1)$$

4.2.4 Synthesis of Co/NCs and oxidized CoO_x/NCs (O-CoO_x/NCs)

To prepare Co/NCs, CoOx/NCs powders (100 mg) were dispersed into 5M HCl (50 mL) for 2 days[45,46] by undergoing following Equ. 2 and 3. These processes transform cobalt oxide to soluble $CoCl_2$. The resultant products were washed with DI water and methanol three times to wash away $CoCl_2$ and denote Co/NCs.

$$Co_3O_4(s) + 8HCl(l) \rightarrow 3CoCl_2(l) + 4H_2O(l) + Cl_2(g) \qquad (4.2)$$

$$CoO(s) + 2HCl(l) \rightarrow CoCl_2(l) + H_2O(l) \qquad (4.3)$$

To obtain oxidized CoO_x/NCs (O-CoO_x/NCs), CoO_x/NCs powders (100 mg) were put into the crucible in a tube furnace in air. The temperate was risen to 550℃ with a ramp rate of 5 ℃/min and kept for 2 hours. During this process, the metallic Co will be transformed to the Co^{2+} and Co^{3+}. The final products were collected after naturally cooling down of the furnace.

4.2.5 Preparation of catalysts on the carbon paper

The as-synthesized xP-CoO_x/NCs (5 mg) was dispersed in a mixture of 2-proponal (250 μL) and DI water (750 μL, conductivity = 0.26 μS cm^{-1}). At the meantime, Nafion solution (30 μL, 5wt%) was dropped into the above solution. After 1 hour sonication to

achieve a uniform dispersion, 20 μL of prepared ink was drop-cast onto the 0.5 x 0.5 cm^2 carbon paper and dried under infrared irradiation for 30 minutes to yield a mass loading ~ 0.2 mg/cm^2.

4.2.6 Physical Characterization

Scanning electron microscopy (SEM) images and Energy Dispersive X-ray spectrometer (EDX) of composition analysis were obtained from a Tescan VEGA3, Czech (accelerating voltage = 20kV). Transmission electron microscopy was conducted on JEOL 2100F, Japan (operating voltage = 200 kV). X-ray diffraction (XRD) patterns were collected on a Rigaku SmartLab 9kW-Advance, Japan using monochromate Cu kα radiation (λ = 0.154 nm) at a scan rate of 7°/min. Raman spectroscopy was taken using a NomadicTM 3-in-1 microscope, America with He-Ne laser excitation (λ = 532 nm) and OLYMPUS MPlanFLN 10x objective lens. Brunauer-Emmett-Teller (BET) surface area measurements were taken by N_2 adsorption-desorption isotherm at 77 K using NOVA touch LX4, Austria. X-ray photoelectron spectroscopy (XPS) was recorded on a Thermo Scientific Nexsa using a monochromatic and focused Al Kα source (1486.6 eV).

4.2.7 Electrochemical measurements

The electrochemical measurements were carried at the electrochemical workstation (CHI660D, Shanghai Chenhua Science Technology Corp., Ltd.) at room temperature. A typical three-electrode configuration including Pt plate (1 x 1 cm^2, 0.1 mm) as counter electrode; Ag/AgCl (saturated KCl solution) as reference electrode, carbon paper (0.5 x 0.5 cm^2) as working electrode was employed for both HER and OER half reaction evaluations. In this case, N_2 saturated 1M NaOH (pH =13.6) was functioned

as electrolyte. The linear sweep voltammetry (LSV) was measured at a scan rate of 5 mV/s with 85% iR compensation. All recorded potentials were converted to the reversible hydrogen electrode (RHE) according to the Nernst equation (Equ. 4):

$$E_{RHE}(\mathrm{V}) = E_{working} + 0.059\mathrm{pH} + E^{0}_{Ag/AgCl} \quad (4.4)$$

Where E_{RHE} is the calculated potential vs. RHE, $E_{working}$ is the recorded potential against Ag/AgCl, and $E^{0}_{Ag/AgCl}$ equals to 0.197 V which is the standard equilibrium potential at 25 °C.

The Tafel slope has been plotted according to the equation below (Equ. 5) to investigate the reaction kinetics:

$$\eta = a + \beta \log(j) \quad (4.5)$$

Where η and j are overpotential (V) and current density (mA cm^{-2}) respectively, and other symbols represent their usual meanings.

Double layer capacitance (C_{dl}) was taken by employing cyclic voltammetry (CV) at scan rates varying from 2 mV/s to 50 mV/s. The C_{dl} was calculated by figuring out the potential difference in the non-Faradaic region.

Electrochemical Impedance Spectroscopy (EIS) measurements were conducted at an overpotential of 20 mV for HER and 100 mV for OER with an amplitude of 5 mV from 100 KHz to 0.1 Hz to investigate the charger transfer resistance and solution resistance at high- and low-frequency region respectively.

The stability test was conducted by the chronoamperometric curves (I-t) at a current density of 10 mA cm^{-2}, and the CV testing with a scan rate of 50 mV s^{-1} for 2000 cycles. The electrolyzer for overall water splitting reaction was composed of two same

electrodes where both cathode and anode are made of carbon paper (1 x 1 cm^2) with 900 P- CoO_x/NCs (mass loading ~ 0.2 mg cm^2, 900P- CoO_x/NCs || 900P- CoO_x/NCs).

4.3 Results and Discussion

4.3.1 Morphology and Composition characterizations of CoOx/NCs

As illustrated in **Fig. 4.1 a**, the precursors are firstly prepared by incorporating cobalt ions into the ZIF-8 frameworks. A subsequent high temperature to evaporate Zn element, leave Co atoms interacting with O element in PVP agent. The obtained carbonized samples further experience the phosphine post treatments to modulate the electronic environment of cobalt atoms. The morphology of ZIF-8 and $Zn_{0.2}$@ZIF-67 nanoparticles were examined by TEM (**Fig.4.1 b-c**). The resultant products show a well-constructed rhombic structure with an average size of 82 ± 15 nm[12,66]. Moreover, a lighter purple colour of $Zn_{0.2}$@ZIF-67 can be noticed due to the introduction of cobalt ions into ZIF-8, compared with that of pure ZIF 67, proving the efficient incorporation of Co^{2+} into ZIF-8 frameworks. After introduction of PVP, the morphology of PVP assisted $Zn_{0.2}$@ZIF-67 shows a distortion, which may originate from the incorporation of polymers into frameworks (**Fig.4.1 d**)[148,149]. From the X-ray diffraction pattern (XRD), it confirms the crystal structure of PVP assisted $Zn_{0.2}$@ZIF67 (**Fig.4.1 e**). In consistent with the peaks of ZIF-8s, when PVP and cobalt salts were introduced, those intensive peaks occurring at 7.3°, 10.4°, 12.7°, 14.7° and 17.9° are attributed to the (011), (002), (112), (022) and (222) facet, respectively[16,66].

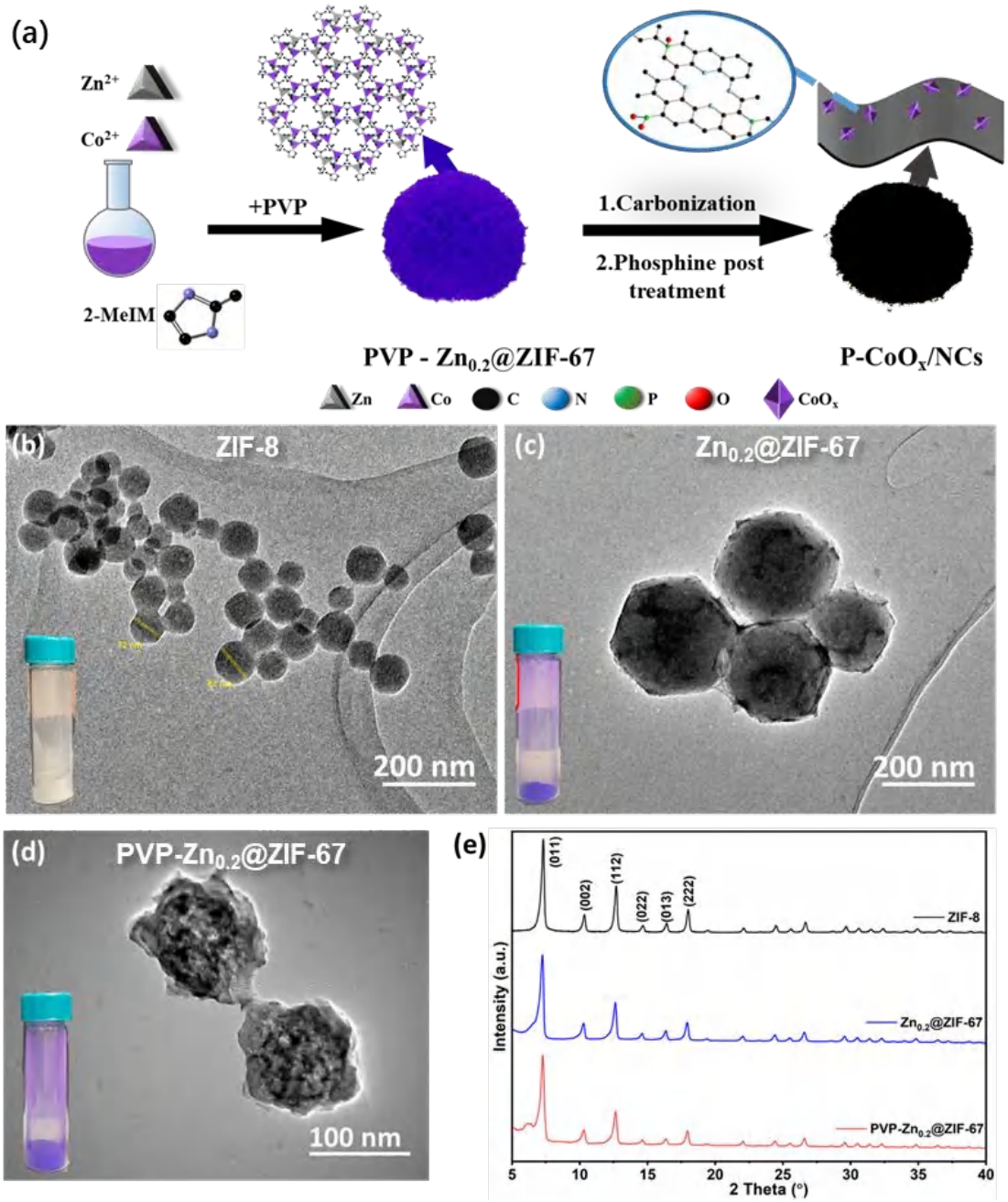

Fig. 4.1. (a) Schematic illustration of synthetic process of P-CoOx/NCs; (b-d) TEM images of ZIF-8 and $Zn_{0.2}$@ZIF-67 and PVP-$Zn_{0.2}$@ZIF-67, (f) Corresponding XRD patterns.

It is reported that the introduction of PVP polymer may induce the substitution of intercalated 2-MeIM, with slight distortion of ZIFs crystal structure[149,150].

Additionally, a small broad peak at ~6° is observed in both $Zn_{0.2}$@ZIF-67 and PVP-$Zn_{0.2}$@ZIF-67 samples. This peak suggests that both doping and PVP assisted synthesis may induce certain phase distortion, while the major phases of ZIF-8s still remain. Therefore, PVP polymers are assumed to be attached on ZIF surface, as well as incorporated into frameworks. After high temperature carbonization (920℃) of PVP - $Zn_{0.2}$@ZIF-67, all crystal structures in ZIFs are destroyed where organic linkers denote to the nitrogen doped carbons (NCs). While for Zn element, it will vaporize at this temperature to prevent the aggregation of metallic particles[151], due to the low boiling point (905℃)[152], which was further confirmed by EDX mapping (**Fig.4.3**). The resultant XRD pattern (**Fig.4.2 a)** of CoO_x/NCs shows the presence of the mixture of CoO (35.8°, 41.8° and 60.5°, PDF#15-0806), metallic Co (44.9° and 50.8°, PDF#43-1003), and Co_3O_4 (19.2°, 30.9°, 37.1° and 65.5°, PDF#48-1719)[153], indicating that the Co atoms interact with the O elements from the organic linkers and PVP chains[154]. The Raman spectra also proves the existence of CoO and Co_3O_4, the intensive peak locating at 665 cm^{-1} (**Fig.4.2 b**) is related to the A_{1g} vibrational mode of Co-O bonds. Another two peaks are accredited to F_{2g} (509.2 cm^{-1}) and E_g (470.5 cm^{-1}) mode corresponding to the combined vibrations of tetrahedral cobalt sites in the Co_3O_4 lattice[150,155]. In addition to the formation of CoO, it is noticed that the intensity of peaks representing Co_3O_4 is decreased in the carbonized samples without PVP polymers. Therefore, it can be deducted that release of oxygen element from PVP polymer increases the cobalt oxidation states. SEM (**Fig.4.2 d**) image indicates that CoOx/NCs@920℃ possesses a rough surface, and a porous structure when looking at the sheet structure.

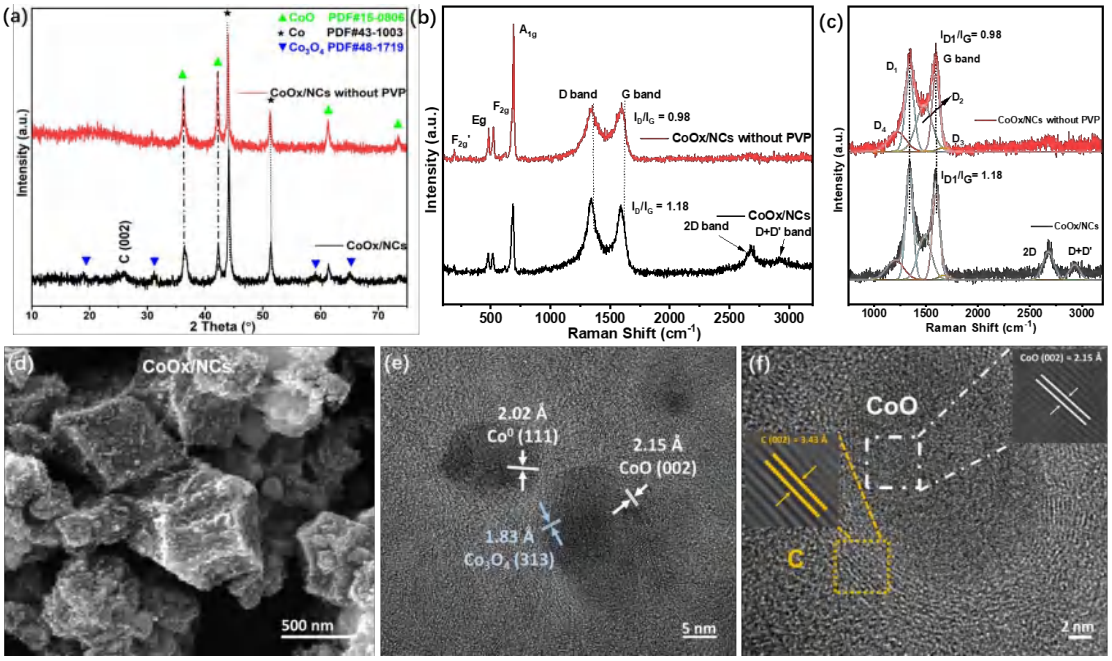

Fig. 4.2. (a) XRD patterns, (b) Raman spectra of CoOx/NCs with and without PVP polymer at 920℃; (c) Deconvoluted peaks for D and G band in Raman spectra; (d) TEM image of CoOx/NCs@ 920℃; (e-f) corresponding HRTEM images (Enlarged: inverse FFT image of C and CoO lattice plane).

Furthermore, it is noticed that the large PVP-$Zn_{0.2}$@ZIF-67 particles survive after harsh carbonization process, due to the role of PVP agent. From HRTEM images (**Fig.4.2 e,f**) of CoO_x/NCs @920℃, the existence of CoO surrounded by the graphite layer as well as the formation of CNTs due to the catalytic effect of metallic Co nanoparticles can be observed. The d-spacing values of metallic particles indicate the presence of mixture of CoO and Co_3O_4 where CoO metallic particles are more abundant. Such co-existence of metallic and metal-oxide particle can enhance the conductivity of final products, compared with that of pure metal oxides.

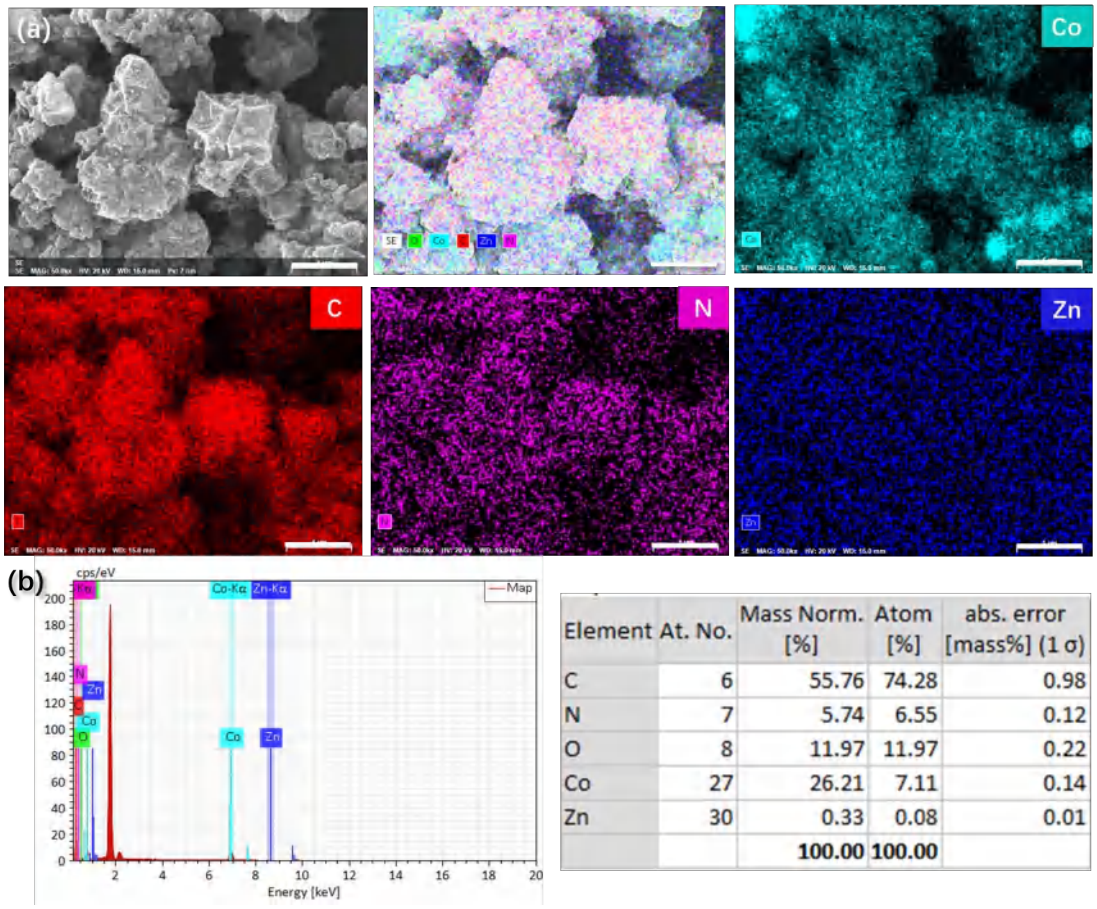

Element	At. No.	Mass Norm. [%]	Atom [%]	abs. error [mass%] (1 σ)
C	6	55.76	74.28	0.98
N	7	5.74	6.55	0.12
O	8	11.97	11.97	0.22
Co	27	26.21	7.11	0.14
Zn	30	0.33	0.08	0.01
		100.00	**100.00**	

Fig. 4.3 (a) SEM image of CoOx/NCs, and corresponding EDS mapping of Co, C, N, Zn element; (b) EDS spectrum and corresponding compositional table summary.

Apart from the Co characteristic peaks in XRD pattern, the peak located at 25.0° also proves a higher graphitization degree (**Fig.4.2 a**) at higher carbonization temperature, which may arise from the incorporation of PVP polymer into ZIFs. Similarly, Raman spectra to investigate the graphitization degree of carbons are shown in **Fig.4.2 b**. The carbonized PVP-ZIF-8/ZIF67s reveals two graphite characteristic peaks located at 1260 cm^{-1} and 1580 cm^{-1}. In general, these peaks relate to the D band and the G band of graphite[151]. Specifically, D band arises from the defects and disordered atoms in the graphite atomic structure while G band originates from the hybridized sp2 carbon atoms. Further deconvolution of D and G band was conducted to compare the graphitization

degree in the sample (**Fig.4.2. c**) [156]. As indicated, the I_{D1}/I_G for CoO_x/NCs without and with PVP are 0.98 and1.18 respectively. The higher I_{D1}/I_G value indicates more defects in the carbonized samples, however, additional 2D and D+D' band, located at 2670 cm^{-1} and 2930 cm^{-1}, indicate the formation of multilayer graphene in the samples. Hence a better conductivity can be achieved in CoOx/NCs @ 920℃.

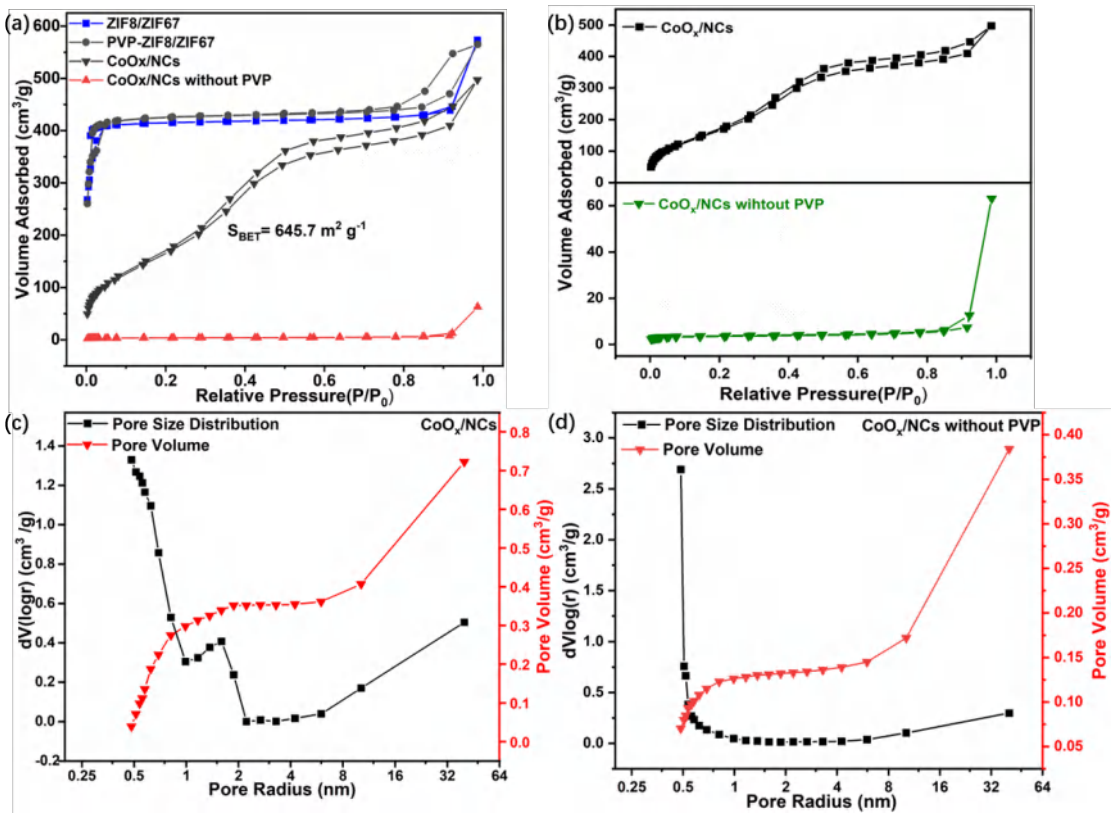

Fig. 4.4. (a) N_2 adsorption and desorption isotherms of ZIFs before and after carbonization @920℃; (b) Comparison in N_2 adsorption-desorption isotherms of CoO_x/NCs with and without PVP assistance; corresponding pore size distribution and pore volume curves of (c) PVP assisted and (d) without PVP assisting CoOx/NCs.

The calculated Brunauer–Emmett–Teller (BET) surface area (642.2 m^2 g^{-1}) of PVP assisted CoO_x/NCs has been retained well after high temperature carbonization (**Fig.4.4**). This value is significantly larger than those ZIF derived carbons without PVP

assistant (51.28 m^2 g^{-1}). Moreover, the pore size distribution indicates that the carbonized sample with PVP assistant generates a mesoporous structure (~ 3.2 nm in radius, **Fig.4.4 c**), while those samples without PVP assistance is hard to bear with the breakage of organic linkers at high pyrolysis temperature, only leaving pore system with lower pore volume and smaller pore size (< 0.5 nm in radius, **Fig.4.4 d**). During the carbonization process, the PVP is supposed to be carbonized firstly[143]. With increasing temperature causing the break-down of organic linkers of PVP-$Zn_{0.2}$@ZIF-67, a strong confinement pyrolysis effect will be achieved due to the strong cohesive interaction from PVP derived carbons and ZIFs[150]. Thus, the assistance of PVP contributes to the formation of a mesoporous structure and prevents the aggregation of active sites in the samples for further optimization with phosphine.

4.3.2 Characterization of phosphine treated CoOx/NCs

The post phosphine treatments were conducted to manipulate the cobalt electronic environment. SEM images (**Fig.4.5 a-c**) reveals that few amount (600 and 900 mg) of phosphine treatment exhibit limited morphology changes, while the high input of phosphine gases cause the surface corrosion, leading to a smooth surface in 1200 P-CoOx/NCs.

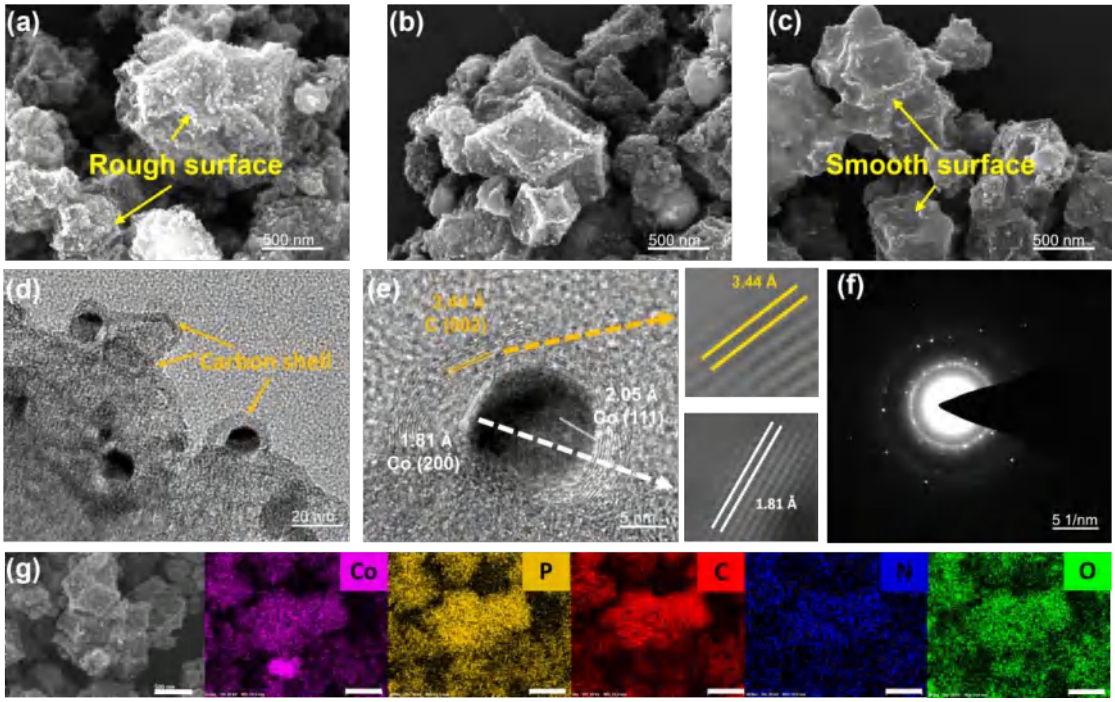

Fig. 4.5. (a-c) SEM images of CoO_x/NCs treated with different amounts (600mg; 900mg and 1200mg); (d) TEM image, (e) HRTEM (adjacent: inverse FFT images), (f) Selected area diffraction and (g) EDS mapping of 900 P-CoO_x/NCs (Scale bar: 500 nm).

TEM image (**Fig.4.5 d and 4.6 a**) of 900 P-CoO_x/NCs indicate abundant carbon shells existed in sample surface, where cobalt nanoparticles are wrapped. HRTEM (**Fig.4.5 e, Fig.4.6 b-c**) exhibited a clear multilayer graphene structure outside the exposed cobalt nanoparticles, as a result, preventing the formation of CoP nanoparticles. The SAED pattern (**Fig.4.5 f**) shows a polycrystalline structure of 900 P-CoO_x/NCs. Further EDS mapping (**Fig.4.5 g and Fig.4.6 e**) of 900 P-CoO_x/NCs confirms the unfirm of P element with an atomic concentration of 2.21% into the carbon frameworks.

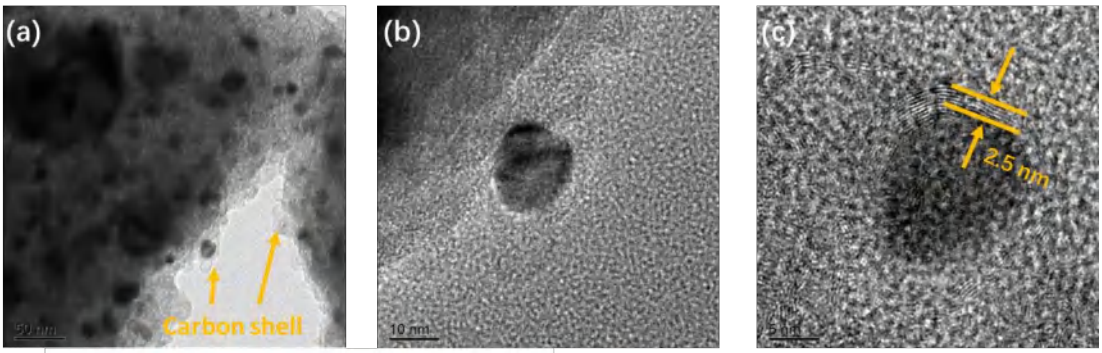

(d)

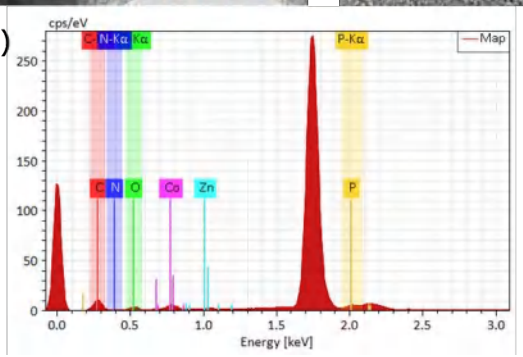

(e)

Map

Element	At. No.	Mass Norm. [%]	Atom [%]	abs. error [mass%] (1 σ)
C	6	50.86	68.19	0.67
N	7	4.11	4.73	0.10
O	8	18.74	18.86	0.25
P	15	4.25	2.21	0.03
Co	27	21.54	5.88	0.10
Zn	30	0.50	0.12	0.02
		100.00	**100.00**	

Fig. 4.6 (a) TEM; (b-c) HRTEM; (d) EDS spectrum and (e) Table summary of 900 P-CoOx/NCs.

XRD patterns (**Fig.4.7 a**) of P-CoOx/NCs samples indicate little changes in the CoO and metallic Co phases after phosphine treatment. Raman spectra of corresponding P-CoO_x/NCs (**Fig.4.7 b**) reveal that the decreased intensity of A_{1g}, F_{2g} and E_g vibration of Co tetrahedral site, arising from the surface corrosion effect of phosphine gases. The X-ray photoelectron spectroscopy (XPS) was employed to investigate the surface chemical states, proving the interfacial charge transfer from Co to P and confirm the P doping into the carbon framework instead of the direct interaction with Co element. In the whole XPS spectrum, it is noticed that there is still little amount of Zn in the samples and the most abundant part is graphite carbons. Typically, in **Table 4.1**, the atomic amount of Zn accounts for 0.11% and 69.86% of signals arise from carbons. When considering the phosphine treatment, it can be revealed that with increasing amounts of

phosphate precursor, the atomic percentage of P at the surface of m P- CoO_x/NCs shows the similar trend by increasing from 6% to 11.26% indicating the successful phosphine post treatment. It is also noticed that the P 2p spectrum is deconvoluted into P-O (133.9 eV) and P-C (132.2 eV). With respect to C 1s spectrum, the relevant C-P is attributed to 286.5 eV (**Fig. 4.8 c,d**)[157,158].

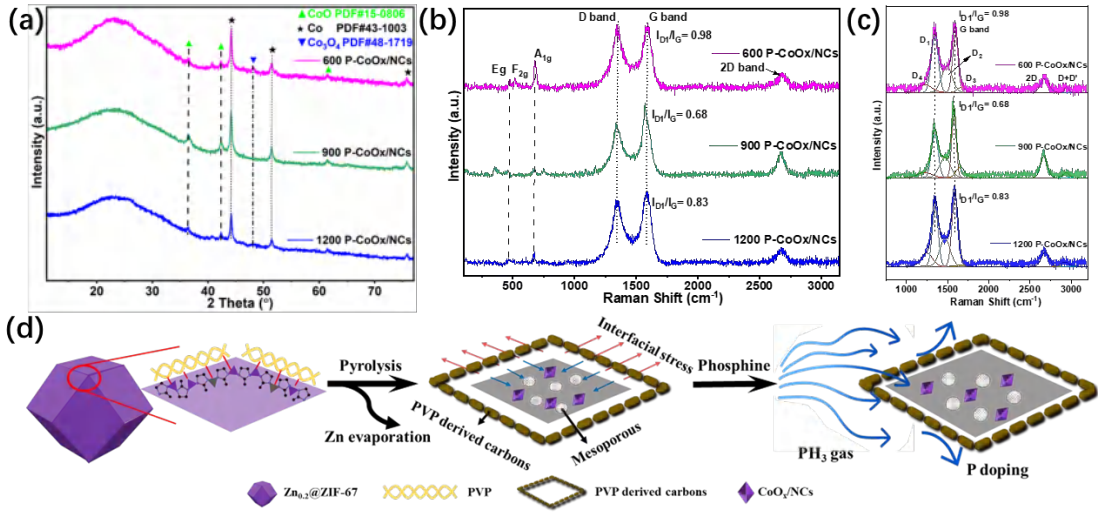

Fig. 4.7. (a) XRD patterns, (b) Raman spectra of 600 P, 900 P, 1200 P-CoOx/NCs; (c) Corresponding deconvoluted D and G band; (d) Schematic illustration of PVP role in carbonization and phosphine post treatment.

In addition to the surface chemical composition analysis, the interfacial charge transfers between Co and P atoms are confirmed by comparing the high-resolution Co 2p peaks and P 2p spectrum (**Fig.4.8 d.e**). It is noticed that the spectrum of 900P-CoO_x/NCs is predominant of spin–orbit doublets (Co $2p_{3/2}$ and Co $2p_{1/2}$) as well as shakeup satellites, characteristics of mixed valence of Co^{2+}/Co^{3+}[159,160]. The spectrum is further deconvoluted into Co^{3+} (781.1 eV), Co^{2+} (783.2eV), Co^{0}(780.3eV) with a Co^{3+} to Co^{2+} to Co^{0} ratio of 1:1.17:0.91. The peaks located at 780.3 eV and 796.2 eV are attributed to the Co^{0}. Interestingly, the 900P-CoO_x/NCs possesses highest Co^{2+} fraction among

all prepared samples (shown in **Table 4.1**), arising from the reducing ability of phosphine gas. Several studies[160–162] have shown that excessive amount of PH_3 gas during phosphorization proves will further reduce CoP to Co_2P[163], forming heterojunctions. Compared with the Co 2p spectrum of 1200P-CoO_x/NCs, a positive shift towards higher binding energy from 600P-CoO_x/NCs was observed (~0.8 eV). Accordingly, high resolution of P 2p spectrum shows a negative shift (134.7 eV to 133.6 eV) due to the increase in the electron density. This shift arises from the electronic transfer from Co to P atom, due to the stronger electron affinity of P[164]. To further reveal P doping effects in carbon shells, UPS was conducted to investigate the Fermi level of 900 P-CoO_x/NCs. As indicated (**Fig.4.8 c**), the cut-off energy of CoO_x/NCs and 900 P-CoO_x/NCs are 12.21 eV and 12.56 eV, respectively. By using following equation: $E_f = \varphi_m = hv - E_{cut-off}$, the Fermi levels of samples were determined to be 9.01 eV and 8.66 eV, correspondingly. Further plot (**Fig.4.8 f**) shows that the Fermi level of 900 P-CoO_x/NCs shifts towards higher level, compared with that of CoO_x/NCs. This shift can be attributed to the P doping at carbon frameworks, which further redistribute the electronic environment of cobalt elements. Moreover, when samples are contacted with electrodes, electrons can be more easily transferred to 900 P-CoO_x/NCs, facilitating further catalytic reactions.

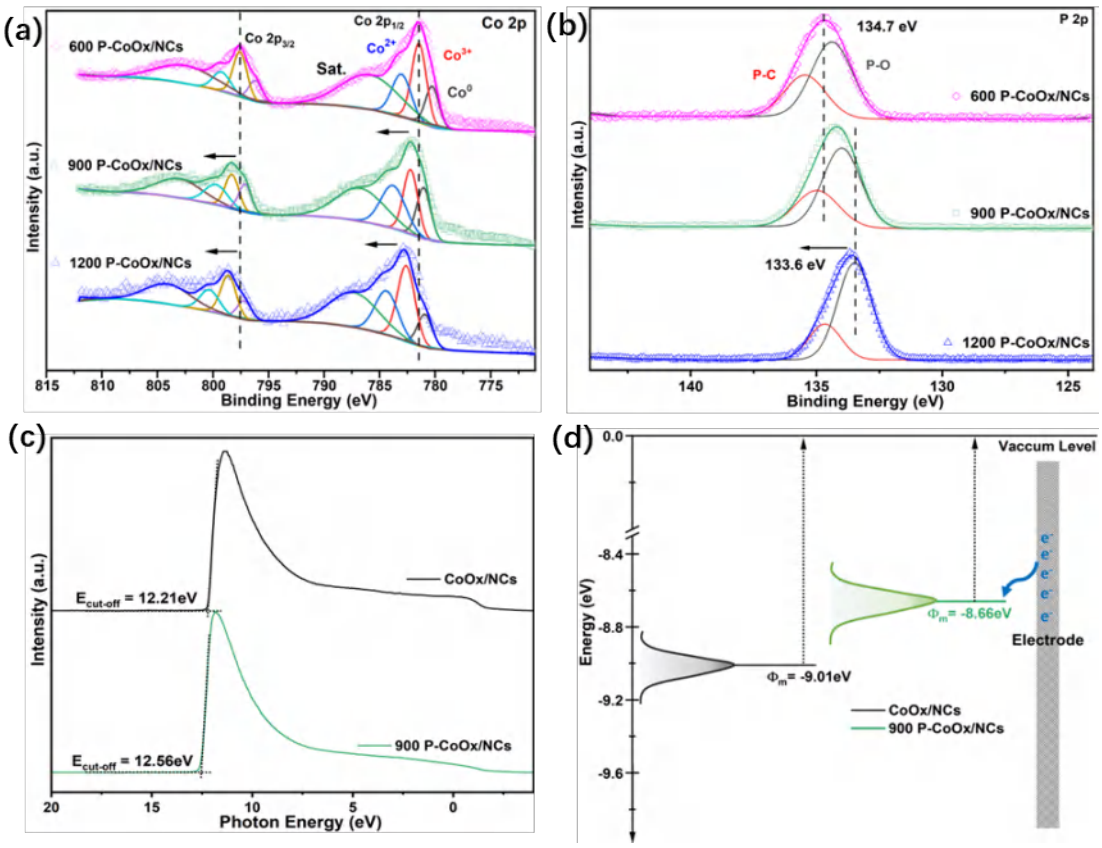

Fig. 4.8. XPS results of (a) Co 2p and (b) P 2p spectra of 600 P, 900 P, 1200 P-CoOx/NCs; (c) Ultraviolet photoelectron spectroscopy (UPS) of CoOx/NCs and 900 P-CoOx/NCs; (d) Corresponding work function relative to the electrode.

As shown in O1s spectrum (**Fig.4.9 b**), the peak representing the Co-O bond (528.7 eV) vanishes after the P vapor treatment. This phenomenon could be the excessive P element on the surface of sample hindering the signal of Co-O. Combined with the information from P 2p spectrum (**Fig.4.9 d**), it can be concluded that phosphorus atoms are introduced to carbon frameworks instead of having direct interactions with Co to form CoP as no spin-orbital doublets are observed in all x P-CoO_x/NCs. While for those O elements in cobalt oxide, it cannot be substituted by P to form CoP due to the strong ionic bonding of cobalt oxide. When considering the configurations of N atom of CoO_x/NCs, its 2p spectrum is divided into three configurations[165,166]: pyridinic N

(398.0 eV), pyrrolic N (403.2 eV) and N oxide (405.5 eV) with an atomic percentage of 46.6%, 45.2%, and 8.2% respectively. When introducing phosphorus atoms into carbon frameworks, it can be noticed (**Fig.4.9 c)**, an increase in the amount of pyrrolic N and correspondingly a decrease in the percentage of pyridinic N suggesting P atoms are introduced into carbon frameworks with similar configuration of pyridinic N[167]. The presence of different nitrogen configurations also provides the possibility to coordinate with metallic actives forming M-N_4 structure which has been reported to facilitate the OER[168].

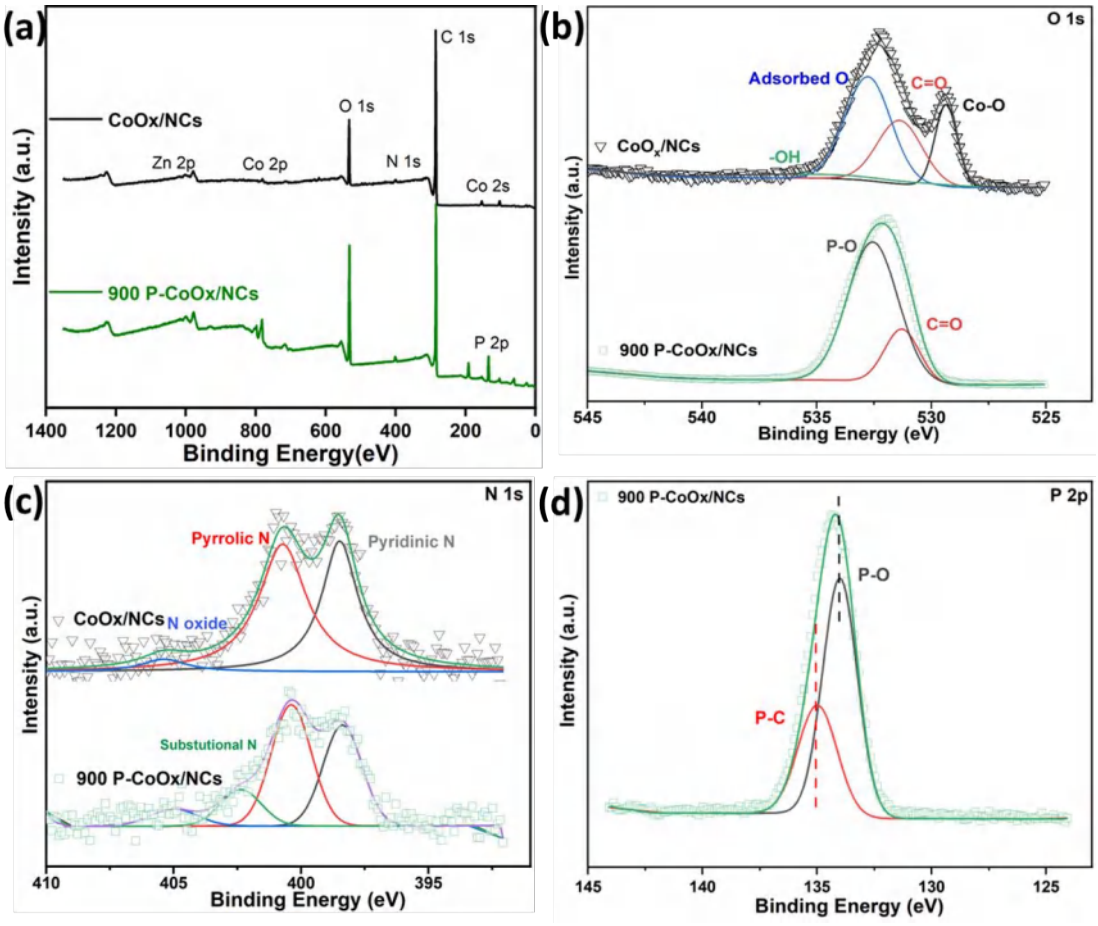

Fig. 4.9. (a) XPS surveys of CoO_x/NCs and 900P-CoO_x/NCs; (b) N 1s and (c) C 1s spectra of CoO_x/NCs and 900P-CoO_x/NCs and (d) P 2p spectrum from 900P-CoO_x/NCs.

For comparison, we conducted the same phosphorization process on CoO_x/NCs samples without PVP assistance. As shown in **Fig.4.10**, the large particles are observed at CoO_x/NCs framework surface. Moreover, XRD pattern confirms the crystal phase. Those peaks observed at 31.3°, 36.3°, 45.8°, 47.9°, 51.8° 56.4° are assigned to cobalt phosphide phase (PDF# 29-0497). Combined with XPS results, it is confirmed that PVP derived carbons may function as protective shell, which further prevents the phosphorization of metallic cobalt and cobalt oxide.

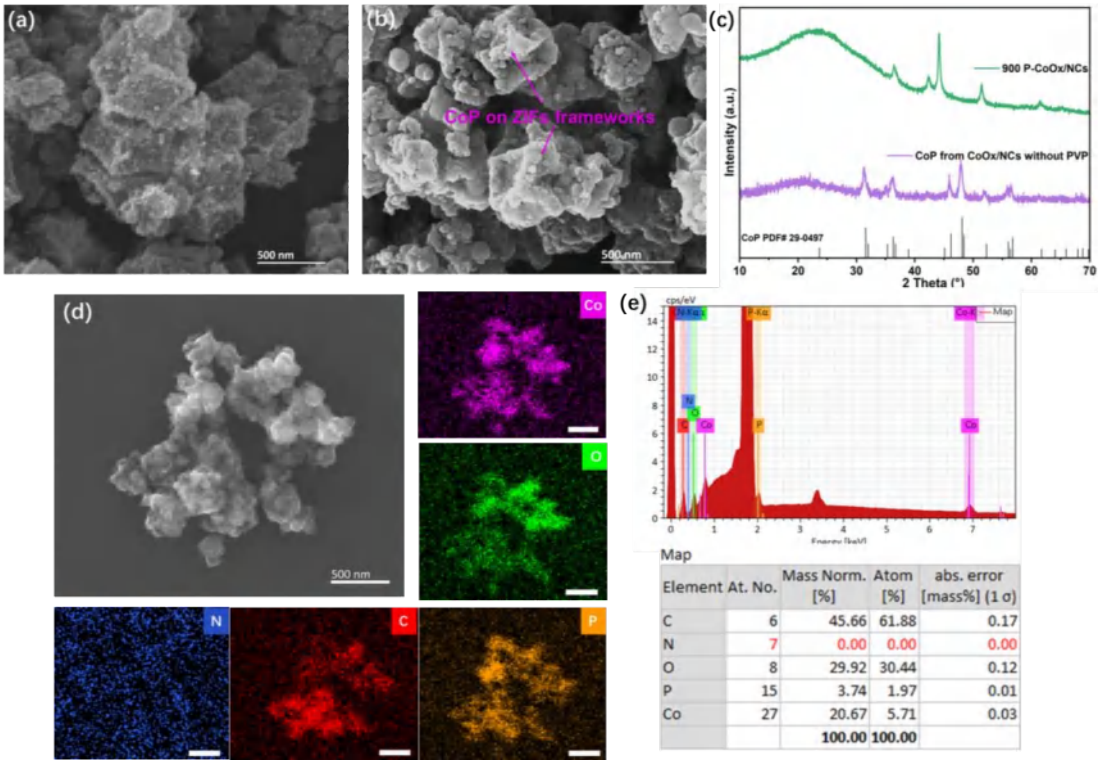

Fig. 4.10. SEM images of (a) CoOx/NCs and (b) CoP nanoparticles derived from CoOx/NCs without PVP, (c) Corresponding XRD patterns; (d) EDS mapping of CoP nanoparticles (Scale bar: 500 nm); and (e) Corresponding EDS spectrum and table summary of composition.

Table 4.1. Surface Element Composition (XPS) of the P treated ZIF derivates.

Sample	XPS atomic % (at. %) [a]						
	C	N	O	Zn	Co	P	$Co^{3+}/Co^{2+}/Co^{0}$
CoO_x/NCs	69.86	2.41	25.59	0.11	2.03	-	1: 056: 0.53
600 P-CoO_x/NCs	66.08	2.48	22.96	0.15	2.33	6.00	1: 0.63: 0.47
900 P -CoO_x/NCs	62.56	2.49	24.39	0.12	3.12	7.32	1: 1.17: 0.91
1200 P- CoO_x/NCs	58.58	2.45	27.36	0.17	3.05	8.39	1: 0.71: 0.39

[a] Surface atomic percentage derived from high-resolution C 1s, O 1s, N 1s, Zn 2p, Co 2p and P 1s core-level peaks.

As indicated in **Fig.4.7. d,** it can be concluded that the excessive amount of PVP is incorporated into ZIF frameworks. Meanwhile, PVP polymers form layers on surface of ZIFs, due to their affinity to metal atoms. The role of PVP polymer is further summarized as follows: 1. The PVP layer contributes to the formation of carbon layers (2-3 nm) during pyrolysis process. The PVP derived carbons not only increase the graphitization degree of final products, but also provide interfacial stress, preventing the inward collapse of ZIF frameworks. 2. The carbon out layers further function as protective shells/ active shells, which are responsible for the P doping during phosphorization. Combined with XRD and XPS results the P atoms mainly substitutes the C and N atoms, forming P-C bonds and PO_4^{3-} species in the carbon frameworks. Meanwhile, such N doped carbons, compared with the activity of cobalt oxides, are usually inert for water splitting. This means the protective carbon shells are not a solid "wall", which may prevent the penetration of water molecules.

4.3.3 Electrocatalytic Evaluation

Based upon above explanation of PVP role in carbonization and phosphorization, we further optimized the Zn/Co ratios in ZIF precursors for water splitting application (**Fig.4.11**). As indicated in XRD pattern, pristine ZIF-67 are converted to the mixture of metallic Co and cobalt monoxide. With increased amounts of Zn dopant, the intensity

of metallic cobalt peaks decreases gradually, indicating a loss of cobalt content. Interestingly, the peaks representing Co_3O_4 and CoO remain stable. Similarly, Raman spectrum (**Fig.4.11 c**) of corresponding carbonized bimetallic ZIFs shows a similar trend, where the intensity of peaks representing Co-Co interacting decreases gradually. While peaks located at ~500 cm^{-1} remain stable until the amount of input dopant reaching 0.8 (ratio in molar). It is noticed that CoO is rather stable at 920℃ and retain well in all samples. It can be deducted that cobalt element firstly interact with O atom released from PVP polymer forming cobalt oxides. Subsequently, the cobalt oxide is reduced to metallic Co at high temperatures, due to the reducing ability of carbons.

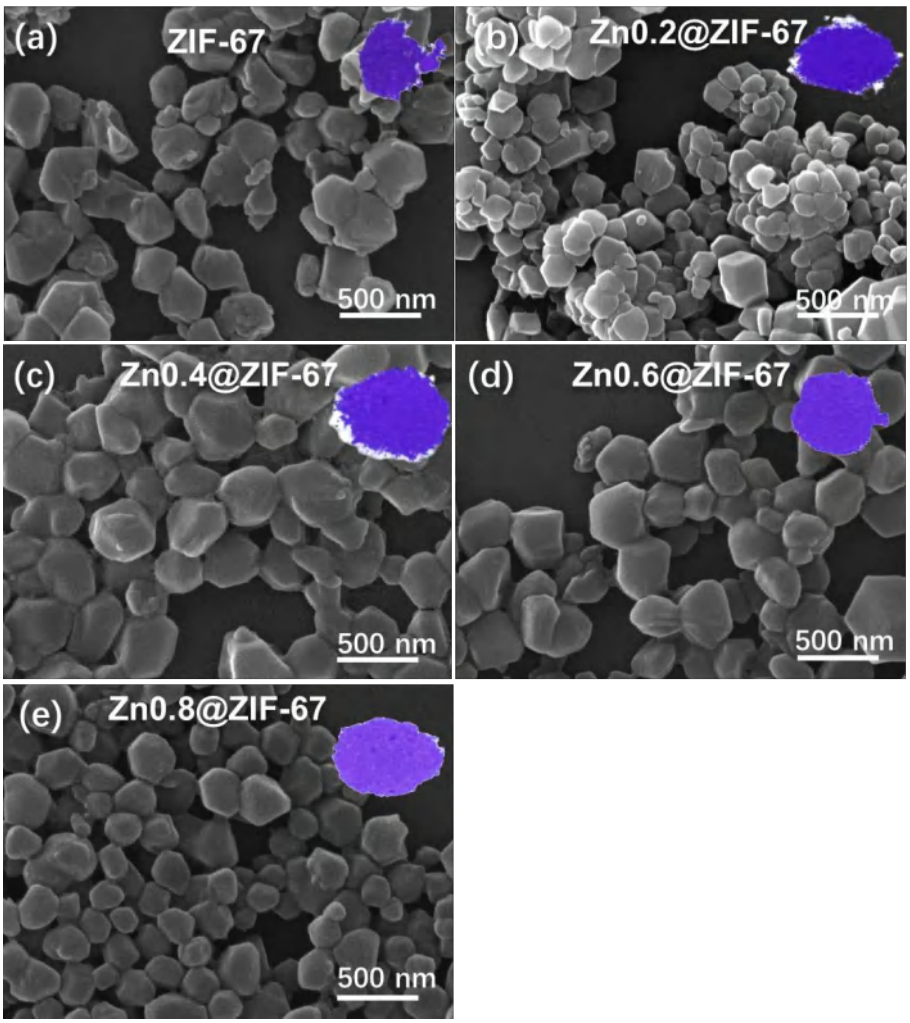

Fig. 4.11. (a-e) SEM and corresponding digital images of PVP-Zn_x@ZIF-67 (x= 0, 0.2, 0.4, 0.6, 0.8).

Under this circumstance, optimization of HER based various of PVP-Zn_x@ZIF-67-920 samples was conducted (**Fig.4.12 d**). As indicated, $Zn_{0.2}$@ZIF-67-920 outperforms other candidates. The pristine ZIF-67 possesses certain catalytic performance, originating from the catalytic effect of metallic cobalt and cobalt monoxide. After introducing Zn dopant, $Zn_{0.4}$@ZIF-67-920 and $Zn_{0.2}$@ZIF-67-920 The pristine ZIF-8-920 sample exhibits lowest catalytic performance, due to the limited exposed active sites.

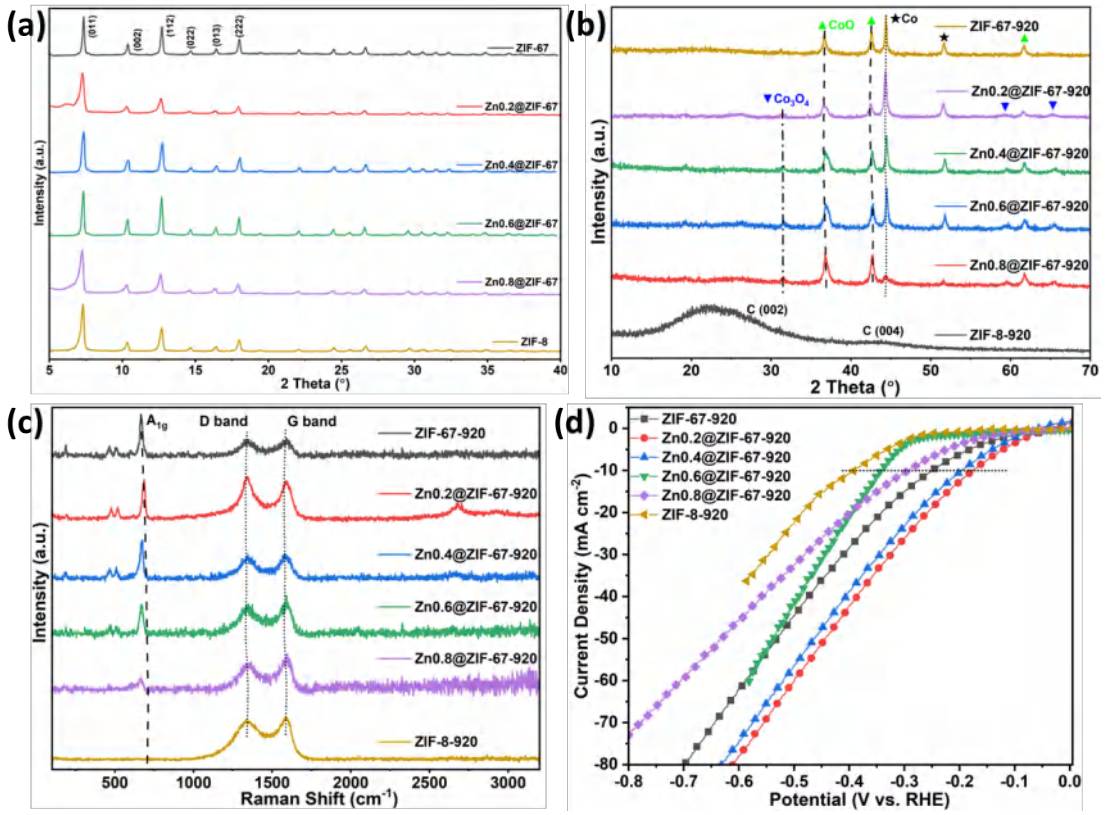

Fig. 4.12. XRD patterns of (a) PVP-Zn_x@ZIF-67, and (b) Carbonized PVP-Zn_x@ZIF-67; (c) Raman spectra and (d) HER polarization curves of carbonized PVP-Zn_x@ZIF-67.

With well-constructed pore systems based on carbonized PVP assisted $Zn_{0.2}$@ZIF-67, the electrocatalytic activities of phosphine treated CoO_x/NCs were evaluated in N_2 saturated 1 $_M$ NaOH at ambient conditions with a sweep rate of 5mV/s. The reference Pt/C (20 wt%) catalyst was evaluated as benchmark for HER. It possesses an overpotential of 20 mV at current density of 10 mA cm^{-2} and a Tafel slope of 35 mV/dec in 1 $_M$ NaOH (**Fig.4.13 a**), due to its fast proton absorption and hydrogen desorption. Among all samples, CoO_x/NCs possess the poorest catalytic performance, while 900P-CoO_x/NCs present low overpotential and low Tafel slope. Due to its optimized electronic environment, Co element exhibit outperforming activities in 900P-CoOx/NCs with an overpotential of 82 mV at 10 mA cm^{-2} and a Tafel slope of 79 mV/Dec. This Tafel slope of 79 mV/Dec indicates the rate-determining step (RDS) as Volmer-Heyrovsky step, where electron transfer and hydrogen desorption sluggish the whole reaction pathway[143]. Nyquist plot was conducted at an overpotential of 100 mV to investigate the electron transfer ability (R_{CT}). As indicated in **Fig.4.13 c**, commercial Pt/C exhibits a low R_{CT} of 12.5 Ω, followed by 900 P-CoO_x/NCs (R_{CT} =18.2 Ω), 1200 P-CoO_x/NCs (R_{CT} = 23.0 Ω), 600 P-CoO_x/NCs (R_{CT} =27.7 Ω). The smaller value of 900 P-CoOx indicates the easier electron transferability towards adsorbed hydrogen atoms.

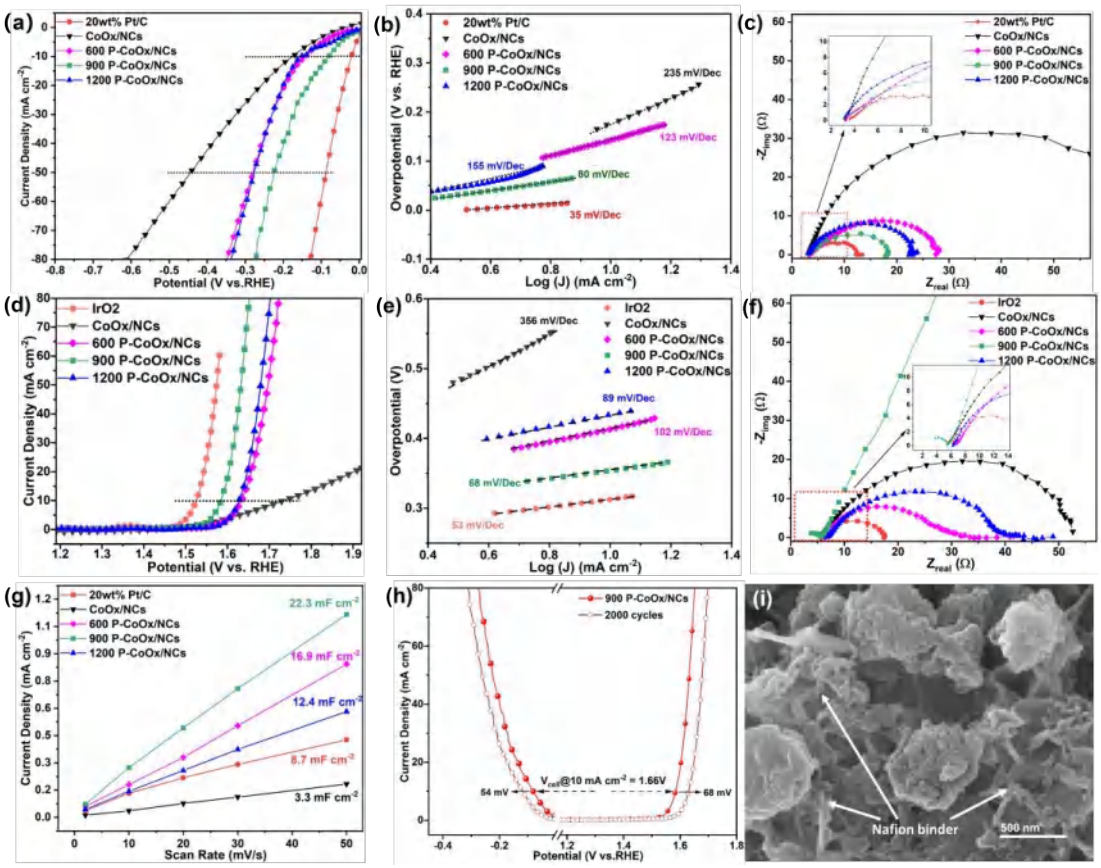

Fig. 4.13. (a) HER polarization curves, (b) Corresponding Tafel slopes and (c) Nyquist plots of CoO_x/NCs treated with 0, 600, 900, 1200 mg of P precursors and 20 wt% Pt/C benchmark at a sweep rate of 5mV/s; (d) OER polarization curves, (e) Corresponding Tafel slopes and (f) Nyquist plots of CoO_x/NCs treated with 0, 600, 900, 1200 mg of P precursors and IrO_2 benchmark at a sweep rate of 5 mV/s in 1_M NaOH; (g) Double layer capacitance; (h) LSV curves of 900 P-CoO_x/NCs after cycling; (i) SEM image of 900 P-CoO_x/NCs after cycling.

Similar to the HER results, the OER performance of 900P-CoO_x/NCs also outperforms those samples treated with 600 mg and 1200 mg of P precursors. As shown in **Fig.4.11 d**, its overpotential required to achieve a current density of 10 mA cm^{-2} is 343 mV and a 383 mV to achieve the current density of 50 mA cm^{-2}, while others exhibit higher

overpotentials (η_{10} =390mV and 400 mV for 600P and 1200P-CoO_x/NCs correspondingly**.** The Tafel slope of 900P-CoO_x/NCs possesses lowest value of 68 mV/Dec (**Fig.4.11 e**), indicating the highest kinetics in OER. The Nyquist plot was then conducted at an overpotential of 100 mV to demonstrate the resistance of electron transfer, where a lower value indicates a faster electron transfer process[169]. All the semicircles in **Fig.4.11 f** deviate the origin point with a value of ~6.5 Ω, caused by the electrolyte resistance (R_S). Among all samples, 900P-CoO_x/NCs possess the lowest electron transfer resistance (2.5 Ω). This value suggests 900P-CoO_x/NCs can facilitate the charge transfer (R_{CT}) at the interface towards oxygen evolution, due to a moderate electronic environment of Co elements. While other phosphine treated samples exhibit relatively larger resistance to the charge transfer (27.5Ω for 600P-CoO_x/NCs; 39.2 Ω for 1200P-CoO_x/NCs). The larger resistance can be contributed to the weaker or stronger interaction between Co and P with undesired electronic environment of Co element. However, compared with the R_{CT} of CoO_x/NCs (49.5 Ω), the treatment with phosphine vapor improves the electron transfer resistance as well as exposed active sites in the carbonized sample.

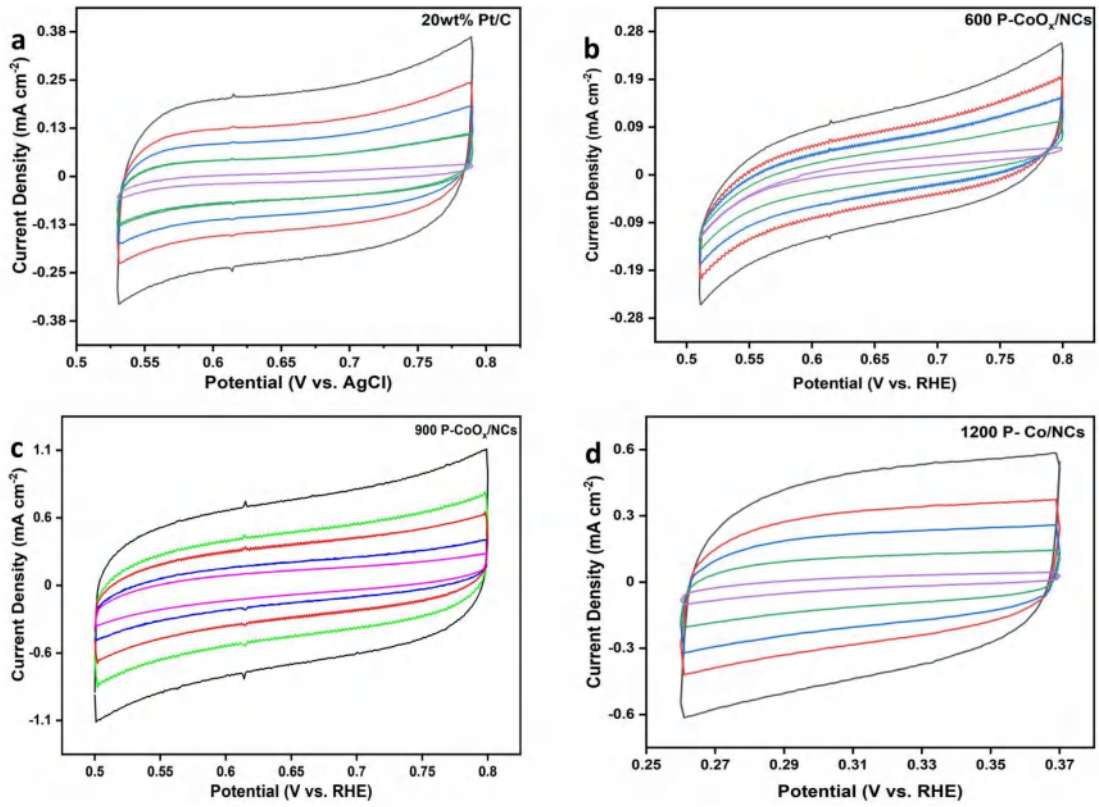

Fig. 4.14. CV scans at different scan rates for (a) 20 wt% Pt/C; (b) 600P-CoO_x/NCs; (c) 900P-CoO_x/NCs and (d) 1200P- CoO_x/NCs.

Double layer capacitance (C_{dl}) measured at non-faradic region was employed to investigate the possible active sites in the samples (**Fig.4.11 g and 4.12)**. The calculated values of C_{dl} are 3.3 mF cm^{-2}, 16.9 mF cm^{-2}, 22.3 mF cm^{-2}, 8.7 mF cm^{-2} for CoO_x/NCs, 600P-CoO_x/NCs, 900P-CoO_x/NCs, 1200P-CoO_x/NCs and commercial Pt/Cs respectively. Among them, 900P-CoO_x/NCs present the highest C_{dl} value, suggesting more active sites exposed for the proton adsorption. Compared with the C_{dl} of CoO_x/NCs, all values of P-CoO_x/NCs are larger, suggesting the P treatment is an effective strategy to expose the available active sites. Since our P-CoO_x/NCs (~ $2.5x10^{-7}$ mol/cm^2) has higher active site density than even Pt/C product (~ $2.1x10^{-7}$ mol/cm^2), the catalyst carbon matrix in our samples would be obviously superior to the carbon substrate of Pt/C. This advantage is attributed to its mesoporous pore size (rather than

micro pore of Pt/C). As a result, this post phosphorus doping strategy significantly improves the reaction kinetics of samples. In addition, it is noticed that the higher Co^{2+} fraction in the sample boosting the overall reaction suggesting the Co^{2+} are the active sites towards water splitting[150,153]. The polarization curves towards HER and OER after 2000 CV cycles (**Fig.4.11 h**) also prove a good stability of as-synthesized samples with a deterioration of 54 mV (HER) and 68 mV (OER) at the current density of 10 mA cm^{-2}. Meanwhile, SEM (**Fig.4.11 i**), XRD and Raman spectrum (**Fig.4.13 c,d**) confirms the morphological and structural stability after the cycling test.

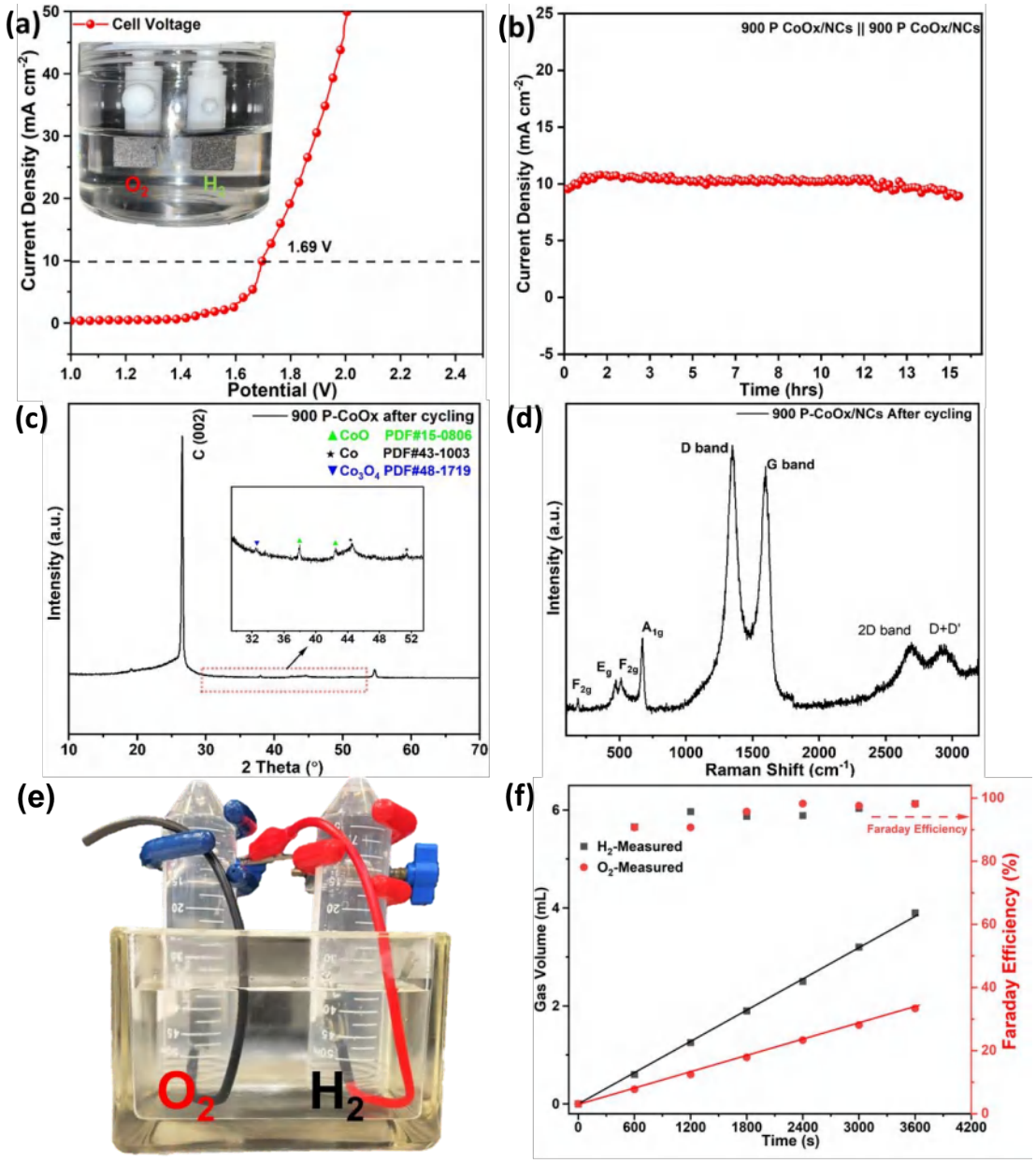

Fig. 4.15. (a) Cell voltage of overall water splitting reaction (900 P-CoO_x/NCs || 900 P-CoO_x/NCs); (b) Chronopotentiometry curve for 900P-CoO_x/NCs at 1.69 V vs. RHE; (c) XRD pattern and (d) Raman spectrum of 900 P-CoOx/NCs after cycling test; (e) Digital image of water splitting device; (f) Collected gas volume and calculated Faraday efficiency of 900 P-CoOx/NCs.

The overall water splitting reaction was conducted by drop-casting catalysts on the carbon paper as cathode and anode. As demonstrated in **Fig.4.13 a**, the fabricated two-electrode cell requires a rather low voltage (1.69 V) to achieve a current density of 10 mA cm^{-2}. The stability of this cell was further tested at 1.69 V for 15 hours. It is noticed that a 4.7% of current density decay, which is likely attributed to the protective graphite layers around the cobalt oxides (**Fig.4.13 b**). To further explore the catalytic performance of 900 P-CoO_x/NCs, the production of H_2 and O_2 as a function of reaction time was collected and has a good consistence with theoretical calculated amount H_2 and O_2 production at the current density of 9.5 mA cm^{-2}. The water splitting reaction based on 900P-CoO_x/NCs achieves an average Faraday Efficiency above 95% with a ratio of H_2 to O_2 equalling to 2 (**Fig.4.13 e,f and Table 4.2**). Moreover, the production rate for H_2 and O_2 are calculated to be 0.048 μmol s^{-1} and 0.024 μmol s^{-1} respectively. What's more, our 900 P-CoOx/NCs exhibits a good position in both HER and OER catalytic performance compared with other cobalt based catalysts.

Table 4.2. Summary of the measured amount of H_2 and O_2 and their corresponding Faraday Efficiency

Time/s	H_2			O_2		
	$V_{measured}$/mL	$V_{theoritical}$/mL	$\eta_{efficiency}$/%	$V_{measured}$/mL	$V_{theoritical}$/mL	$\eta_{efficiency}$/%
0	0	0	0	0	0	0
600	0.6	0.6616	90.85	0.3	0.3308	90.69
1200	1.25	1.3233	94.22	0.6	0.6617	90.68
1800	1.9	1.9849	95.72	0.95	0.9925	95.72
2400	2.5	2.6466	94.46	1.3	1.3233	98.24
3000	3.2	3.3083	96.73	1.61	1.6542	97.58
3600	3.9	3.9698	98.24	1.95	1.9849	98.14

Note: The Faraday efficiency (η) is the ratio between the measured volume and theoretical volume of produced H_2 and O_2 at different time.

The theoretical volume is calculated from the following equation:

$$V_{theoretical} = I \times t \times V_{mole}/(n \times F)$$

Where I is the current measured during the electrolysis, t is the time, V_{mole} is molar volume of H_2 and O_2 at standard conditions, n is the number of electrons to produce 1 molecule of H_2 and O_2, and F is the Faraday's constant (96485 C/mol)

4.3.4 Investigation of catalytic performance of multivalence Co

To reveal the role of different valence states of cobalt in P-CoO_x/NCs, a series of post treatments have been conducted: (1) Employ acid to remove cobalt oxide denoting Co/NCs; (2) Anneal CoO_x/NCs at 550°C to transform metallic Co to cobalt oxide, referring to O-CoO_x/NCs. As shown in **Fig.4.14 a-b**, the acid treated CoOx/NCs exhibits an open-structure, caused by the strong acid leaching effect. While the oxidized samples reveal random particle distribution. Moreover, the carbon content of O-CoOx/NCs is rarely observed, due to the open-air calcination. Further XRD pattern (**Fig.4.14 c**) and Raman spectrum (**Fig.4.14 d**) confirm the observation. The new peaks in O-CoOx/NCs represent the existence of Co_3O_4, indicating a higher oxidation fraction of Co. For acid leached sample, only characteristic peaks of metallic cobalt are identified, proving a lower oxidation state. When considering HER performance (**Fig.4.14 e**), CoO_x/NCs requires the lowest overpotential (219 mV) compared with that of oxidized CoO_x/NCs (302 mV), and metallic Co/NCs (235 mV) to achieve a current density of 10 mA cm^{-2}. This phenomenon indicates the presence of metallic Co (Co^0) cooperating with higher valence state of cobalt (Co^{2+}) lowers the energy barrier of hydrogen generation. However, all Tafel slopes of corresponding samples towards HER are above 150 mV/Dec (**Fig.4.15 a**) suggesting the desorption of H_{ads} are the rate-determining steps[170] in the alkaline medium. Nevertheless, Co/NCs at higher current density exhibits a faster reaction kinetics, which can be attributed to the open structure of carbon frameworks and more exposed metallic active sties.

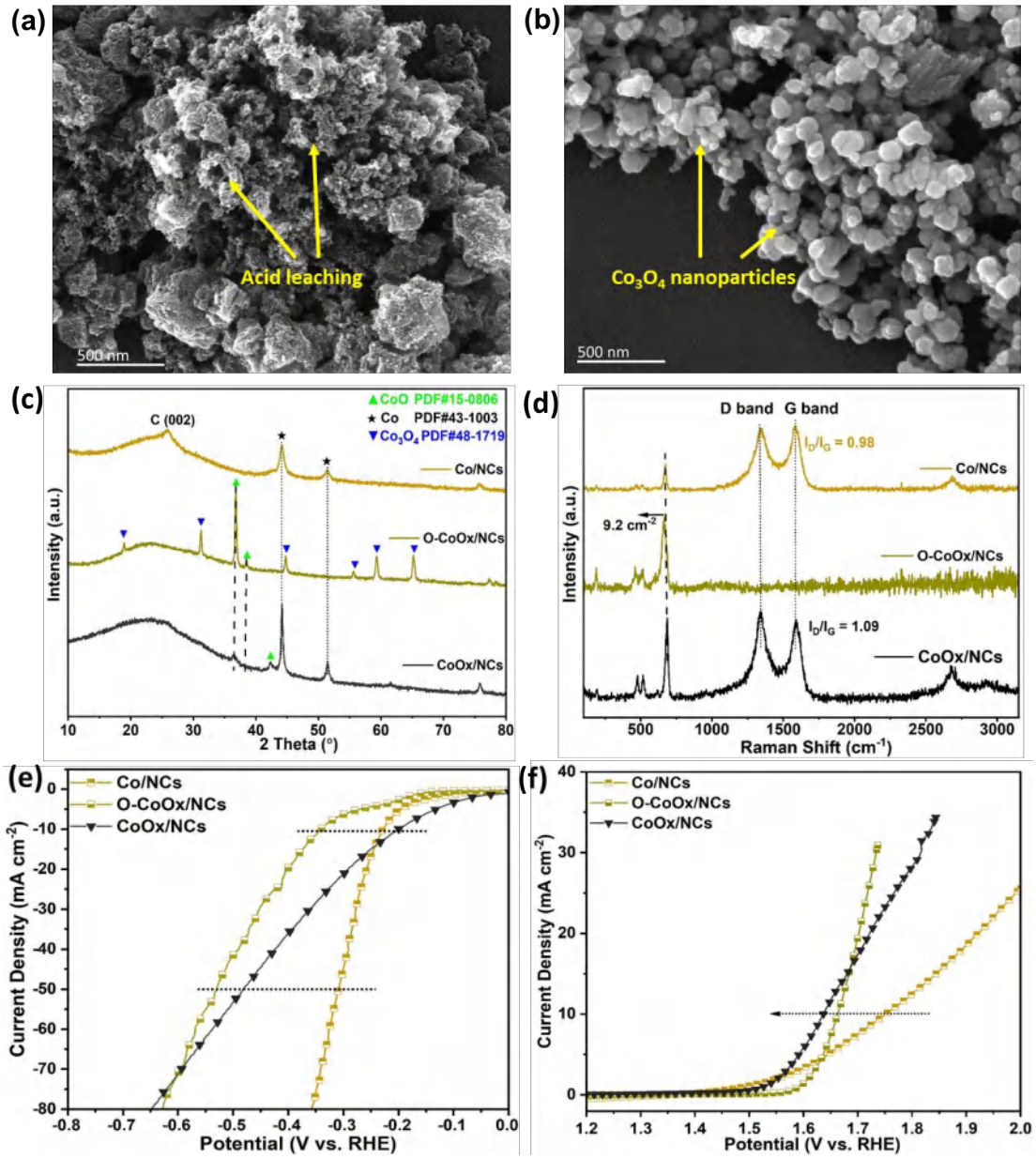

Fig. 4.16. (a-b) SEM images of Co/NCs and O-CoOx/NCs; (c) XRD patterns; (d) Raman spectrum; (e)HER; and (f) OER polarization curves of Co/NCs, O-CoO_x/NCs and CoO_x/NCs.

When considering OER performance (**Fig.4.14 f, 4.15 b**), both acid-treated and oxidized CoO_x/NCs (Co/NCs and O-Co/NCs) requires a higher overpotential to achieve the current density of 10 mA cm^{-2} (470mV and 427 mV respectively). This higher

overpotential prove the synergetic effects between Co^{2+} and Co^{3+} to boost the water splitting reaction. Interestingly, the C_{dl} value of Co/NCs shows the highest value among all three batches (6.75 mF/cm^2, **Fig.4.15 c**) which may arise from the removal of excessive metal oxide and amorphous carbons. This acid leaching process provides more possibilities with active sites exposed to electrolyte. It is also noticed that the reaction kinetics of O-CoOx/NCs has been improved for both HER and OER. This enhancement may be attributed to the oxidation of Co^{2+} to Co^{3+} firstly then followed by the formation of key intermediate Co-OOH by OH^- adsorption during the water oxidation reaction[171]. When considering electron transfer resistance of multivalent Co elements. The existence of various states of cobalt in CoO_x/NCs shows the lowest value (49.5 Ω, **Fig.4.17 d**) suggesting the synergetic effects between cobalt elements and the as-prepared CoO_x/NCs can be employed as a promising candidate for post phosphine treatment. Therefore, due to the higher fraction of Co^{2+} (Co^{3+}: Co^{2+} = 1: 1.17) in 900P-CoOx/NCs, the adsorption energy of H_2O molecule can be minimized, which further facilitates the conversion of adsorbed OH^- groups to oxyhydroxides intermediates.

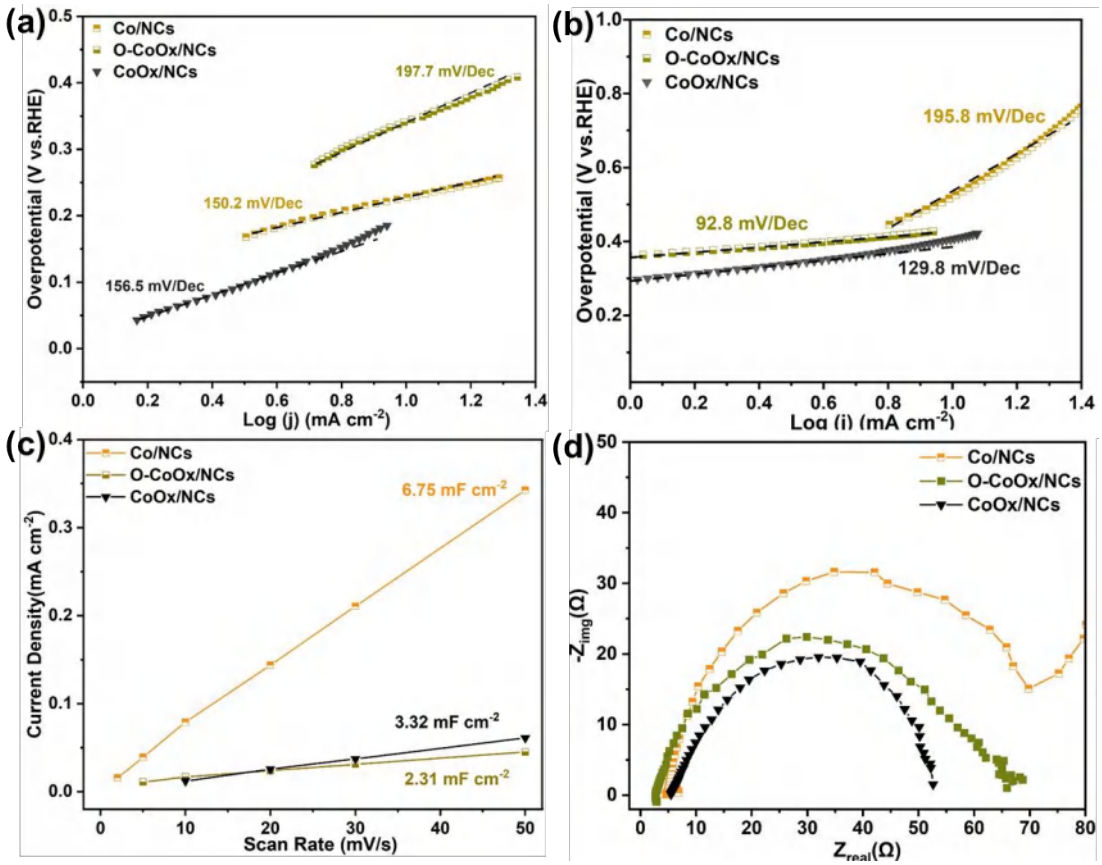

Fig. 4.17 Tafel slopes of (a) HER; (b) OER; (c) ECSA; and (d) Nyquist plots of Co/NCs, O-CoOx/NCs and CoOx/NCs.

4.4 Chapter Conclusion

In conclusion, we fabricated the N/P codoped cobalt oxides based electrocatalyst to boost water splitting reaction, the N and P atoms were doped into the carbon frameworks, where nitrogen and phosphorus elements originated from organic linkers and phosphine vapor, respectively. By further optimizing the phosphine precursor's amount, the electronic environment of cobalt element can be regulated, which further contributes to an optimized intermediate adsorption/desorption energy, and enhanced catalytic performance. Moreover, the PVP assisted carbonization treatment equipped the catalyst with a high specific surface area of 645.7 m^2 g^{-1} and micro-mesoporous

topologies. The final electrocatalyst can drive the HER and OER at an overpotential of 89 mV and 343 mV udner a current density of 10 mA cm^{-2}, respectively. Overall, our findings included the following: 1) The carbonization of ZIFs assisted by PVP polymer can avoid the collapse of pore system under harsh carbonization, contributing to active sites exposure and N doping into the carbon frameworks; 2) The mesoporous system and PVP functionalization promotes the surface interaction between phosphine vapor and carbons to allow P doping. The optimized electronic environment of cobalt oxides tuned by N and P heteroatoms towards boosting water splitting reaction; 3) Phosphine post treatment also enhances the accessible electrochemical active surface area as well as the electron transfer kinetics shedding lights on the electronic modulation of ZIFs assisted by PVP.

The post acid and oxidation treatment reveal that the synergetic effect between Co^0 and Co^{2+} facilitates HER kinetic, meanwhile, effect between Co^{2+} and Co^{3+} improve the OER kinetics. In addition, the constructed electrolyzer based on 900P-CoO_x/NCs possesses a cell voltage of 1.69 V to achieve the current density of 10 mA cm^{-2}. We believe that our study provides a robust way to construct mesoporous system in carbonized ZIFs, and an electronic modulation strategy of cobalt oxides electrocatalysts for water splitting reaction.

Chapter 5. Biomass derived cobalt sulfide for electrochemical water splitting and its all-flexible moisture digester

5.1 Introduction

Electrocatalytic water splitting to generate hydrogen and oxygen has attracted intensive attention as an effective solution to alleviate the global warming[133]. The transition metal-based catalysts are explored to substitute the noble metal catalysts[6]. Notably, the transition metal-based catalyst is usually supported by carbon frameworks, due to their advanced stability, diversity, and tunability. Therefore, the utilization of biomass as natural carbon sources to decorate metal active sites has been attracting increasing interests[172-173]. It is originated from the easy reproducibility, accessibility, and low-cost of such biomass derived carbons. Willow catkin[174], as cellulose based biomass, can be easily converted to active carbons using pyrolysis approach. However, due to the rare amount of metal fixing atoms (e.g., M-N_4) in the carbon skeleton, such conversion is reported to employ excessive ammonia gas as the nitrogen source to load the metal-based catalysts. More recently, researchers utilized silk fibroin[175], a protein-based biomaterials rich in amino groups, as the precursor to load the metal active sites. Such in-situ fixing strategy, to some extent, allows interactions between metal and nitrogen atoms during carbonization process. Nevertheless, the transition metal atoms will easily aggregate at high temperature, leading to the elemental metal. Moreover, efficiency of N doping in such carbon frameworks are low, as the evaporation of organic bonds at high temperature are more sever [3]. Herein, we modified wool keratin structure to selectively fix cobalt active sites into fibres before carbonization process, and

successfully converted biomass as support for electrocatalysts.

Among several fibre-based candidates, wool fiber, as a fundamental raw material in textile industry, is chosen as a promising candidate for the electrochemical applications (e.g. sensors, capacitors, and catalysts) [176–179]. The structure of wool is distinctive from that of silk, where α-helix structures containing amino groups are further connected by disulphide bonds (-S-S-) to form macro fibre structure. Specifically, the outermost layer of wool fibre has certain level of disulphide bonds[180]. Meanwhile at the nano scale, a sulphur rich region exists in the intercellular place, which can also be engineered by either oxidation or reduction[181,182]. By adopting the click chemistry method, the cleavage of disulphide bonds in these regions via reductive treatments contributes to cysteine groups, where the fixation of metal atoms such as gold can be achieved [183,184]. Such metal fixation strategy starts from the treatments of natural precursors shows a more efficient loading. Compared with that of in-situ fixation and carbonization process, the metal active sites are already fixed tightly by coordinative bonds before carbonization process.

In this work, we firstly engineered the wool fibre at a mesoscale to encapsulate the cobalt-based nanoparticles for the application of water splitting reaction for the first time. The fixation was achieved by selectively reducing disulphide bonds to cysteine groups in the keratin by $NaBH_4$, allowing further coordinative interaction between thiol groups and cobalt ions. Such fixation strategy facilitates the formation of Co_9S_8 during carbonization process, by avoiding the interaction between cobalt ions and oxygen element in the keratin. In comparison, the physical adsorption of cobalt ions was conducted by manually denaturing the wool structure with NaOH. Instead of forming

Co_9S_8, CoO and metallic Co were generated during pyrolysis, arising from the release of O element in organics, reducing ability of carbons and aggregation of metal ions at high temperature. The obtained catalysts supported by biochar, experiencing further activations process, are denoted to the Co_9S_8 supported by N/P co-doped carbons (Fix-920-A). The as-prepared catalyst boots the electrocatalytic water splitting reaction (η_{10} = 90.7 mV for HER, and η_{10} = 295 mV for OER). A low cell voltage (η_{10} = 1.62 V) can be achieved when the as-obtained catalysts are employed in an alkaline water electrolyzer. Based on this superior catalytic performance, an all-flexible device is designed and fabricated by adopting the strategy of hydrogel separator and moisture sensitive salts, which possess a stable working current at 20 mA for 2 hrs. Therefore, we not only demonstrate a reduction-carbonization-activation strategy for the utilization of natural biomass, but also provides a concept of personalized wearable device for human health improvement.

5.2 Experimental Section

5.2.1 Materials

Wool felts with average fibre diameter of 30 μm were purchased from Tianmei Felt Factory, China. Wool felts were further washed with a mixture of ethanol/acetone (50/50 v%) to remove dusts, grease, which were further dried in the oven at 80℃. All silver fabrics were purchased from Kazhtex Co. China. Elastic 50A for 3D printing was provided by the 3D printing machine supplier (Formlabs Forms 3, UK).

All other chemicals were used as delivered: Sodium borohydride $NaBH_4$ (99%); sodium hydroxide (97%), potassium hydroxide (99%), and sodium chloride (90%) were purchased from J&K Chemicals Co., Ltd. China. Cobalt (II) acetate (99%) and

Phosphoric acid (≥ 85 wt.% in H_2O) were purchased from Fisher Scientific UK. Commercial Pt catalyst (20 wt%, Pt/C) was purchased from Alfa Aesar Chemicals Co., Ltd., USA. Agar-agar (Biological grade) and urea (99%) were purchased from Shanghai Aladdin Biochemical Technology Co., Ltd.

5.2.2 Synthesis of Wool-Fix/Ads

Precleaned wool felts (0.4 g, 2 x 2 x 0.5 cm^3) were immersed in the solution of $NaBH_4$ (5g/L; liquor ratio = 1: 50) under vigorous stirring for 4 hours at room temperature, which is denoted as Wool-R (Note: pH of solution is tuned to ~8 by drop adding of 1_M NaOH to avoid the reformation of disulphide bonds). The treated samples were then separated and centrifuged under 10,000 rpm for 10 minutes to remove excessive solution. The pre-dried samples were subsequently immersed into cobalt acetate solution (10 mL, 10 mM) under shaking for 8 hours, allowing the diffusion and fixation of cobalt ions into the wool fibers. Afterwards, samples were rinsed by DI H_2O, centrifuged under 10,000 rpm for 10 minutes, and dried in a vacuum oven at 60℃ overnight. The as prepared sample denotes to Wool-fix.

With respect to the adsorption samples (Wool-Ads), the $NaBH_4$ was substituted by 10 mM NaOH (pH ~ 10), whereas other procedures remain the same. In addition, the alkaline destroyed wool samples without immersing into cobalt precursor solution were denoted to Wool-D (NaOH treated).

5.2.3 Synthesis of Fix/Ads-920, and Fix-920-A/K

Wool-fix/ads samples (0.5 g) were put into a tube furnace with N_2 inert environment, where a two-step carbonization approach was conducted. The temperature was firstly elevated to 350 ℃ with a ramp rate of 5 ℃/min and maintained for 1 hour to form

conjugate carbon frameworks. Subsequently, the temperature was risen to 920 ℃ with a rate of 3 ℃/min and held for 2 hours. The samples collected after naturally cooling down were denoted to Fix-920. For carbonized Wool-Ads sample, it was marked as Ads-920.

To activate the Fix-920; the obtained samples (0.1 g) were immersed into phosphoric acid solution (2 ml; 5wt%) under vigorously stirring for one day. The samples were collected and washed with DI H_2O by centrifuging at 10,000 rpm, which then dried at 80℃ overnight. Afterwards, the phosphorus acid impregnated Fix/Ads-920 samples experienced 550℃ activation process for 2 hours with a ramp rate of 5℃/min under N_2 inert atmosphere. The collected electrocatalyst supported by biochar was denoted to Fix-920-A. To fabricate Fix-920-K, 0.1 g Fix-920 was thoroughly ground with 0.2 g K_2CO_3, where other procedures remain the same. The K_2CO_3 activated Fix-920 further denotes to Fix-920-K.

5.2.4 Preparation of catalysts onto the carbon cloth/silver fabrics

The obtained electrocatalysts (5 mg) were dispersed into a mixture of iso-propanol (200μL); ethanol (200μL) and DI H_2O (580 μL, conductivity = 0.26 μS cm^{-1}) with extra addition of Nafion dispersion (20 μL, 5wt%). After achieving uniform dispersion of catalyst under sonication for 1 hour in an ice bath, 10 μL of dispersion was drop-casted onto two sides of a 0.5 x 1 cm^2 carbon cloth ($A_{geometric}$= 1 cm^2)/ silver fabrics ($A_{geometric}$= 20 cm^2). The casted carbon cloth/silver fabric was dried under infrared irradiation for 30 minutes to yield a mass load ~ 0.2 mg/cm^2.

5.2.5 Synthesis of moisture sensitive hydrogel

To prepare moisture sensitive hydrogel, 0.25 g of agar, 0.75 g urea and 0.15 g sodium

chloride were dissolved in 9 g H_2O. The temperature was then elevated to 85℃ to obtain transparent solution, which was further poured into 3D printed separator, and cross-linked in a 4℃ fridge for 24 hrs.

5.2.6 3D printing of resin separator for wearable device

All 3D printed separators were conducted on Formlabs Forms 3, UK, using stereolithography method. Each layer was set to be 0.2 mm, while 3 layers were deposited for final separator. The as-deposited separator was cured under 365 nm UV light for 15 min, and further washed/cleaned by ethanol for 30 min to remove residuals.

5.2.7 Physical characterizations

Scanning electron microscopy (SEM) images and Energy Dispersive X-ray spectrometer (EDX) were obtained from a Tescan VEGA3, Czech (accelerating voltage = 20kV). Transmission electron microscopy (TEM) and high-resolution TEM (HRTEM) were conducted on JEOL 2100F, Japan (operating voltage = 200 kV). X-ray diffraction (XRD) patterns were collected on a Rigaku SmartLab 9kW-Advance, Japan using monochromate Cu kα radiation (λ = 0.154 nm) at a scan rate of 5°/min. Raman spectroscopy was taken using a NomadicTM 3-in-1 microscope, America with He-Ne laser excitation (λ = 532/785 nm) and OLYMPUS MPlanFLN 10x objective lens. (Note: for all measurements on organic wool fibers, 785 nm laser was selected using a laser power of 1% and expose time: 10s.) Brunauer-Emmett-Teller (BET) surface area measurements were taken by N_2 adsorption-desorption isotherm at 77 K using NOVA touch LX4, Austria. The quantitative analysis of cobalt was obtained by the Agilent 5100 synchronous vertical dual view inductively coupled plasma–optical emission spectrometer (ICP–OES). X-ray photoelectron spectroscopy (XPS) was recorded on a Thermo Scientific Nexsa, UK using a monochromatic and focused Al Kα source

(1486.6 eV).

5.2.8 Electrochemical measurements

The electrochemical measurements were carried at the electrochemical workstation (CHI660E, Shanghai Chenhua Science Technology Corp., Ltd.). A typical three-electrode configuration including Pt plate (2 x 1 cm^2, 0.1 mm) as counter electrode; Hg/HgO (1_M KOH) as reference electrode, carbon paper (0.5 x 1 cm^2) as working electrode was employed for both HER and OER evaluations. In this case, carbon paper was washed with ethanol and DI H_2O under sonication for several times, and N_2 saturated 1_M KOH (pH =13.8) was functioned as electrolyte. The linear sweep voltammetry (LSV) was measured at a scan rate of 5 mV/s with iR compensation, where electrolyte resistance was determined by electrochemical impedance spectroscopy (EIS) at open circuit voltage. All recorded potentials were converted to the reversible hydrogen electrode (RHE) according to the Nernst equation (Equ. 1):

$$E_{RHE}(\mathrm{V}) = E_{working} + 0.059\mathrm{pH} + E^{0}_{Hg/HgO} - iR \qquad (1)$$

Where E_{RHE} is the calculated potential vs. RHE, $E_{working}$ is the recorded potential against Hg/HgO, and $E^{0}_{Hg/HgO}$ equals to 0.098 V, which is the standard equilibrium potential at 25 ℃. The Tafel slope has been plotted according to the equation below (Equ. 2) to investigate the reaction kinetics:

$$\eta = a + \beta \log(j) \qquad (2)$$

Where η and j are overpotential (mV) and current density (mA cm^{-2}) respectively.

Double layer capacitance (C_{dl}) was taken by employing cyclic voltammetry (CV) at scan rates varying from 5 mV/s to 100 mV/s. The C_{dl} was calculated by figuring out the potential difference in the non-Faradaic region. Electrochemical Impedance Spectroscopy (EIS) measurements were conducted at an overpotential of 50 mV for

HER and 150 mV for OER with an amplitude of 5 mV from 100 KHz to 0.1 Hz to investigate the charger transfer resistance and mass transfer at high- and low-frequency region respectively. The stability test was conducted by the chronoamperometric curves (I-t) at a current density of 10 mA cm^{-2}, and the CV testing with a scan rate of 100 mV s^{-1} for 1000 cycles.

5.2.9 Theoretical simulations

Density functional theory calculations were conducted, using projector augmented wave (PAW) pseudopotential and the Perdew-Burke-Ernzerhof (PBE) exchange-correlation functional implemented in the Vienna Ab-initio Simulation Package (VASP). Calculations were made by a plane wave kinetic energy cut-off energy of 450 eV. The Gamma k-point meshes of 2 x 2 x 1 was set for the structural relaxation. The convergence criterion for the force and energy was set to be 10^{-5} eV and 0.01 eV A^{-1}, respectively. The structures were spin-polarized and under relaxation until reaching the convergence tolerance of force on each atom (< 0.05 eV). The Brillouin-zone integration was sampled by a Γ-centered 6 × 6 × 1 Monkhorst–Pack k-point. To better describe the electron stats of 3d orbital in cobalt element, DFT+U method was employed, where U= 4.5 eV for Co_9S_8 [185], and U = 3.5 eV for CoO.[46]

The adsorption energy is calculated as follows:

$$\Delta G_0 = \Delta E + \Delta ZPE - T\Delta S \quad (3)$$

Where ΔE is the total energy difference between slab model and adsorbate A, ΔZPE is the zero point energy of adsorbate (H_2, O_2 and H_2O), and $T\Delta S$ is achieved by the thermal correction of intermediate model using T = 298.15 K in a VASPKIT module [186].

5.2.10 Moisture uptake and device performance measurement

The measurement of all-flexible moisture digester was conducted in a temperature humidity chamber (HD-100T, HaiDa Co., China). The condition was set to be 37℃, 80% RH and maintained for 2 hrs. The working current was recorded on a CHI660E (Chenhua Co. China) electrochemical station, using a working voltage of 3V.

5.3 Results and discussion

5.3.1 Morphology and composition characterization of catalysts supported by biochar

As illustrated in **Scheme 1**, the modification of wool felts starts from a mesoscale level, where the cuticle layer (0.5 μm in thickness) will experience a reduction (Wool-R) or denaturation (Wool-D) treatment.

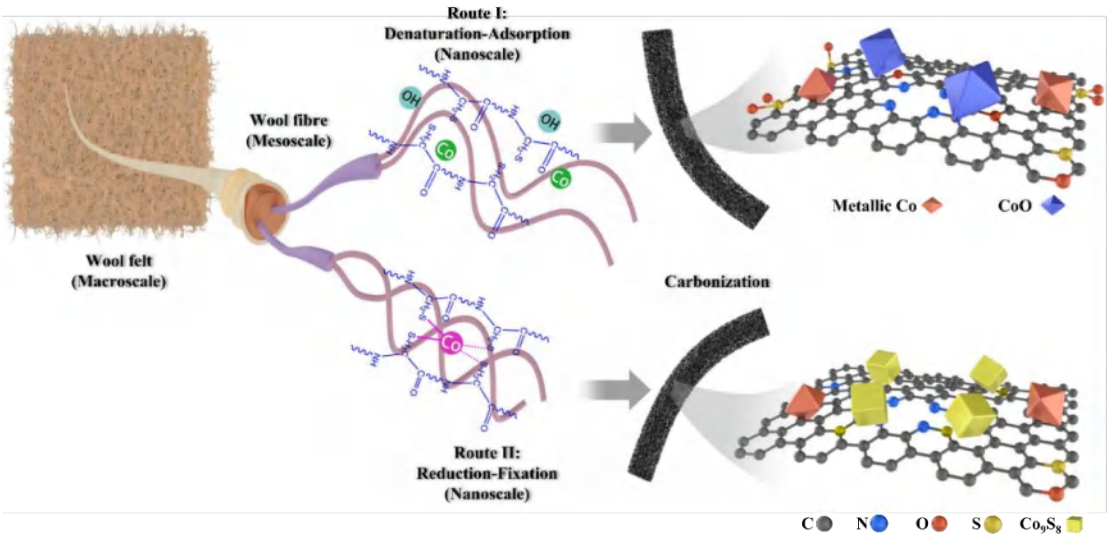

Scheme 5.1. Fabrication process of reduced/destroyed wool felt for Co-based (metallic Co, CoO and Co_9S_8) electrocatalysts supported by biochar frameworks.

The **Fig.5.1** indicates that little changes in the dimensions can be noticed after reductive/denaturalize treatments, since reactions major take place at mesoscale of fibers.

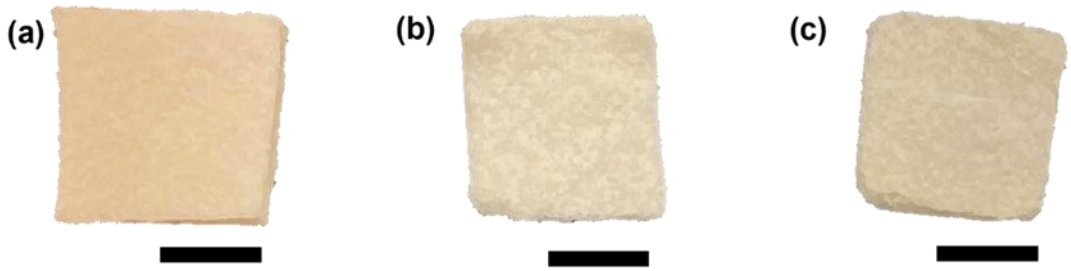

Fig. 5.1. Digital images of (a) Wool, (b) Wool-R, and (c) Wool-D (Scale bar: 1 cm).

The subsequent diffusion of cobalt ions will be selectively fixed or simply adsorbed in a nanoscale, depending on the chemical treatments. Such fixation/adsorption strategy further contributes two distinctive cobalt-based catalysts (Co_9S_8/CoO based) after carbonization process. Compared with diameter of original wool fibre (30.2 ± 5 μm), both diameters of reduced and denatured wool fibers show a slight decrease by 0.4 μm and 0.6 μm, respectively. Moreover, the epicuticle layer become smooth after alkaline treatment, arising from the hydrolysis of wool fibers. The XRD pattern (**Fig.5.2 d**) was then recorded to investigate the crystal changes. Notably, Wool-R sample exhibits a decreased crystallinity in keratin I region, proving the selective disruption of disulphide bonds. Since keratin I structure is composed of intermediate filaments, where α-helix structure is connected by disulphide linkages. Such selectively reductive treatment decreases the periodic arrangements between helix structure, causing a decrease in crystallinity. The Raman spectrum was subsequently collected to identify changes of chemical bonds in wool fibers before and after treatments, due to the good sensitivity to disulphide bonds and thiol groups[187–189]. As shown in **Fig.5.2 e,** peaks located at 507.3 cm^{-1},1451.1 cm^{-1}; 1670.5 cm^{-1} and 2980.6 cm^{-1} were attributed to the disulphide bonds, Amide I and II groups, and CH groups [190,191], correspondingly. After reducing/ denaturing treatment, peaks indicating amide groups (C-N, -C=O) still can be observed. The remaining amide peaks suggest that the wool skeleton mostly survives after both

reductive and denatured treatments. The denaturation process does not change the peptide linkages (primary structure) after removing the scale layer, but alters the secondary, and tertiary structures in the keratin, contributing to the remaining peaks in Raman (Amide I and II groups). However, the peak intensity of disulphide bond decreases significantly after both treatments, showing the selectively destroy/ reduction of the bond. Notably, the reduced thiol groups can be detected from the peak at 2585 cm^{-1} in Wool-R sample [2], proving the selective reduction of disulphide bond.

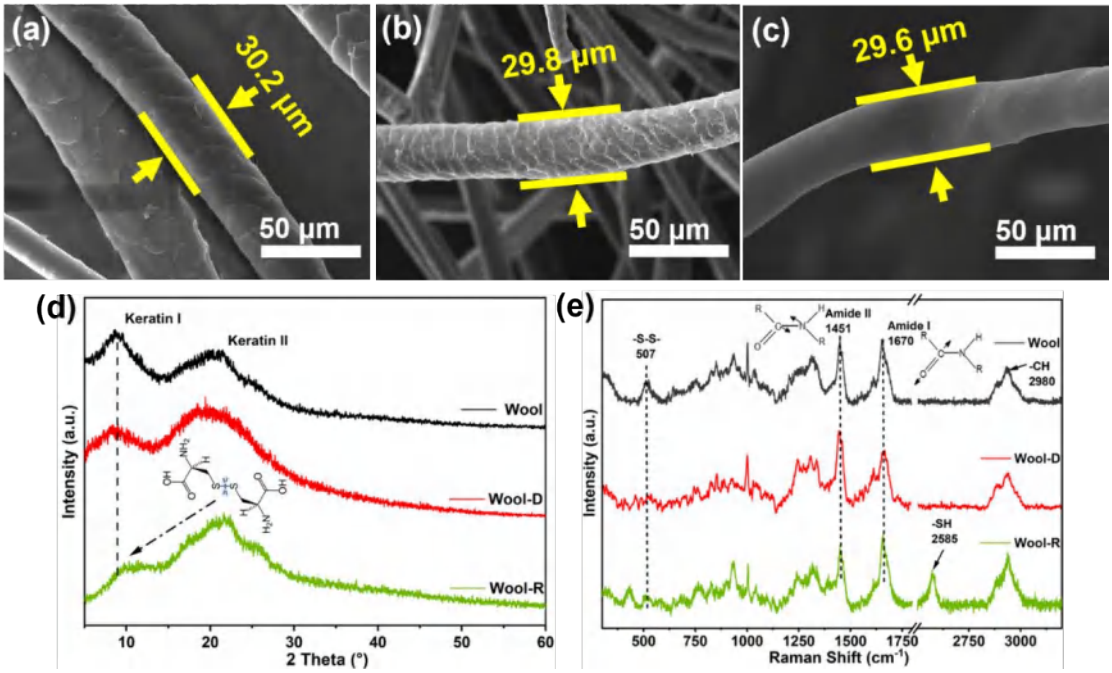

Fig. 5.2. (a-c) SEM images, (d) XRD patterns and (e) Raman spectra of original wool felt, denatured wool fibers (Wool-D), and reduced (Wool-R), respectively.

After immersing the treated wool felt into cobalt solution, the cobalt ions are expected to diffuse into wool surface firstly and are further fixed by thiol groups by coordinative bonds (Wool-Fix). As indicated in **Fig.5.3 a-c**, a clear colour change of reduced wool felt from yellow to light brown can be observed. This change indicates diffusion and subsequent fixation of cobalt ions into wool skeleton (**Fig.5.3 d-f**). However, such evidence of cobalt ion diffusion cannot be observed in alkaline treated samples, due to

the low diffusion kinetics, and limited adsorption sites for cobalt atoms (Wool-Ads).

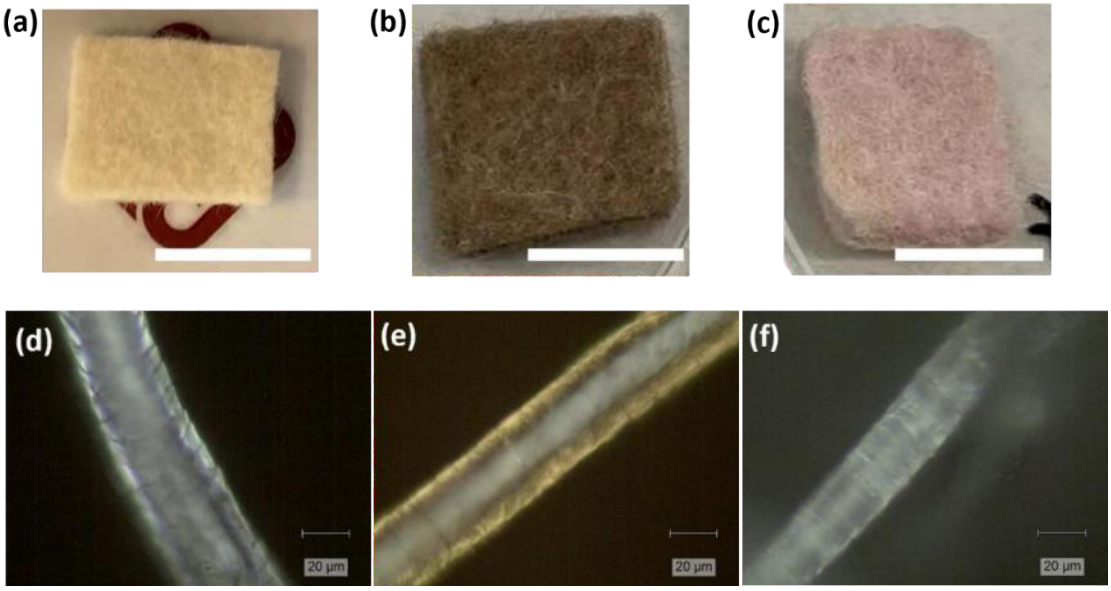

Fig. 5.3. (a-c) Digital images (scale bar: 1 cm), (d-f) optical microscopy of original wool felt, Wool-fix; and Wool-ads, respectively.

Raman spectrum of the subsequent fixation/adsorption of cobalt ions shows (**Fig.5.4 a**) 2 characteristic peaks of Co-S complex and $Co(OH)_2$. Specifically, peaks located at 263.9 cm^{-1} and 289.8 cm^{-1} are attributed to Co-S complex [192], whereas the peaks observed at 474.1 cm^{-1} and 521.4 cm^{-1} are regarded as the signal of $Co(OH)_2$ [193]. The formation of cobalt hydroxide can be considered as the interaction between remaining hydroxyl groups and cobalt atoms once diffusing inside the wool fibre. Therefore, we conclude the whole reductive process at wool felt as follows: the sodium borohydride, a common strong reducing agent, will be firstly hydrolysed into boron hydroxide (Equ. 4). The disulphide bonds are then reduced to thiol anions (Equ. 5), where cobalt cation ions will be fixed by forming coordination bonds (Equ. 6). [182]

$$NaBH_4 + 4H_2O \rightarrow B(OH)_4^- + Na^+ + 3H_2 + 2H^+ + 2e^- \quad (4)$$

$$K\text{-}S\text{-}S\text{-}K + 2H^+ + 2e^- \rightarrow 2\ K\text{-}SH \quad (5)$$

$$4K\text{-}SH + Co^{2+} \rightarrow [Co^{2+}\ (S\text{-}K)_4] + 4H^+ \quad (6)$$

Where K indicates the amino, carboxyl groups in keratin structure.

As indicated in TGA curve (**Fig.5.4 b**), the formation of carbon skeleton is supposed to take place when temperature is above 350 ℃ by decomposing amino groups, carboxylic groups in wool keratin [194]. When temperature is further evaluated to 700 ℃, ~70% weight of Wool-fix is lost due to the cleaving of surface ether/carbonyl groups on carbon frameworks[195]. Moreover, more amounts of residuals (~26%) at 900℃ can be observed in Wool-fix sample, indicating a high loading of cobalt elements by fixation strategy.

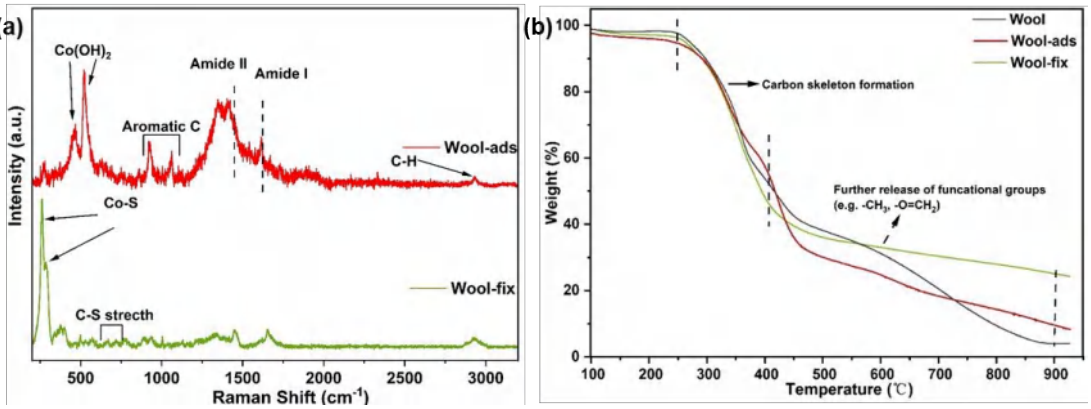

Fig. 5.4. (a) Raman spectra of Wool-ads and Wool-fix, (b) TGA curves of Wool fibers, Wool-ads and Wool-fix.

As observed in EDS mapping of carbonized wool fiber (**Fig.5.5 a, 5.6 d,e**), the EDS result confirms the uniform dispersion of Co and sulphur elements along one single carbonized wool fibre (Fix-920), and further suggesting an cobalt atomic composition of 0.17%. During activation process, H_3PO_4 acid acts as activation reagent by attacking the remaining phenolic and carbonyl groups firstly. Such interaction is then supposed to introduce C-O-P configuration into the carbon skeleton during post decomposition process, leading to a porous biochar. After carbonization and activation process, the

Fix-920-A remains fibre structure, but possesses rough surface and spongious structure in SEM images (**Fig.5.5 e**). Further TEM images (**Fig.5.5 f**) of Fix-920-A show that particles are decorated in carbon skeleton, and determined as a mixture of metallic Co ($d_{\{111\}}$ = 0.204 nm) and Co_9S_8 ($d_{\{440\}}$ = 0.248 nm) under HRTEM (**Fig.5.5 g**).

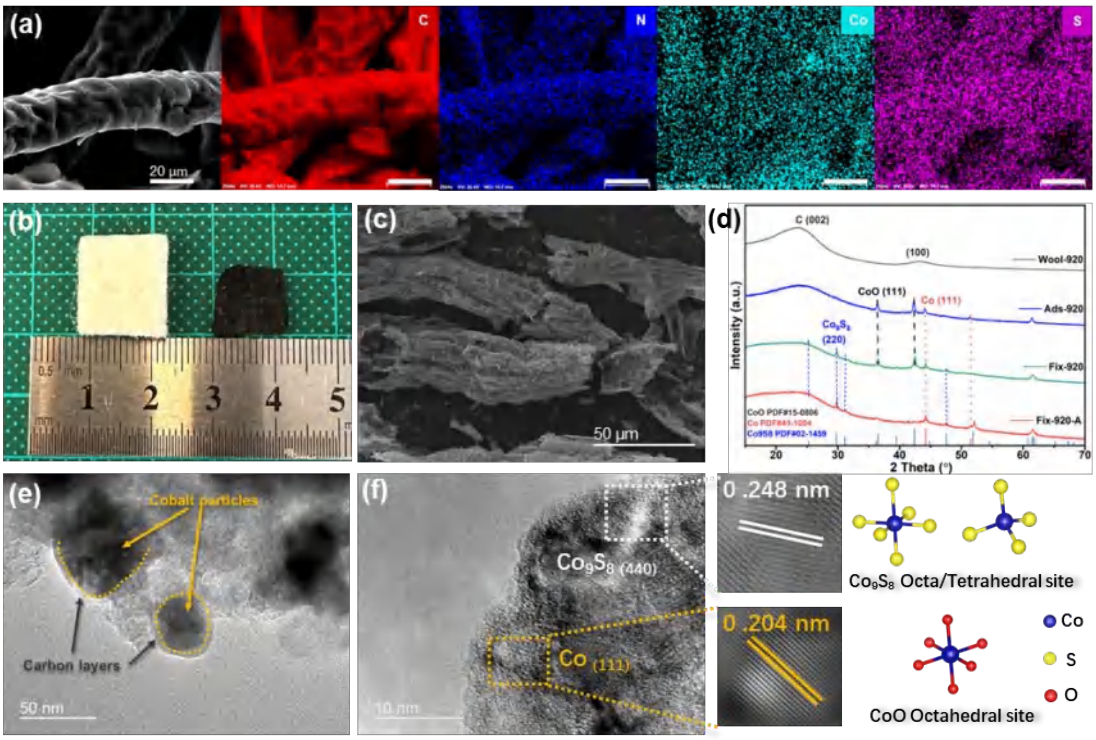

Fig. 5.5. (a) EDX mapping of Fix-920; (b) Digital image of original wool felt and Fix-920-A electrode; (c) SEM image, (d) XRD patterns, (e) TEM and (f) HRTEM images of Fix-920-A.

Moreover, the formation of carbon nanotubes was identified, which is attributed to the catalytic effect of metallic cobalt particles for CNT growth at high temperature. [167,196] The composition of cobalt element, further determined by ICP-OES, in Ads-920 and Fix-920 was 2.50 wt.% and 4.76 wt.%, respectively. The X-ray diffraction pattern (**Fig.5.5 d**) was then recorded to investigate the crystal structure of various samples. After carbonization at 920℃, all samples possess a broad peak at 25.2°, indicating the graphite {002} facet [197]. Meanwhile, those peaks indicating existence of CoO, Co, and

Co_9S_8 were observed. Specifically, peaks located at 36.4°, 42.3° and 61.4° are attributed to the {111}, {200}, and {220} facet of CoO (PDF#15-0806) in Ads-920 sample. Peaks at 44.1° and 51.3° shows the existence of metallic Co {111} and {200} plane (PDF#43-1003) in both Ads-920 and Fix-920-A samples. The formation of metallic cobalt particles can be attributed to the reducibility of active carbons at high carbonization temperature [198,199], which also in turn facilitates the growth of CNTs. In contrast to the Ads-920, the sample prepared by coordinating the thiol groups (Fix-920 and Fix-920-A) contributes the formation of cobalt sulphide (25.3°, 30.1°, 31.3°, 39.6° and 47.6°, respectively, PDF#02-1459). Meanwhile, the existence of cobalt sulfides and porous morphology is observed in SEM and TEM images (**Fig.5.6. a-c**)

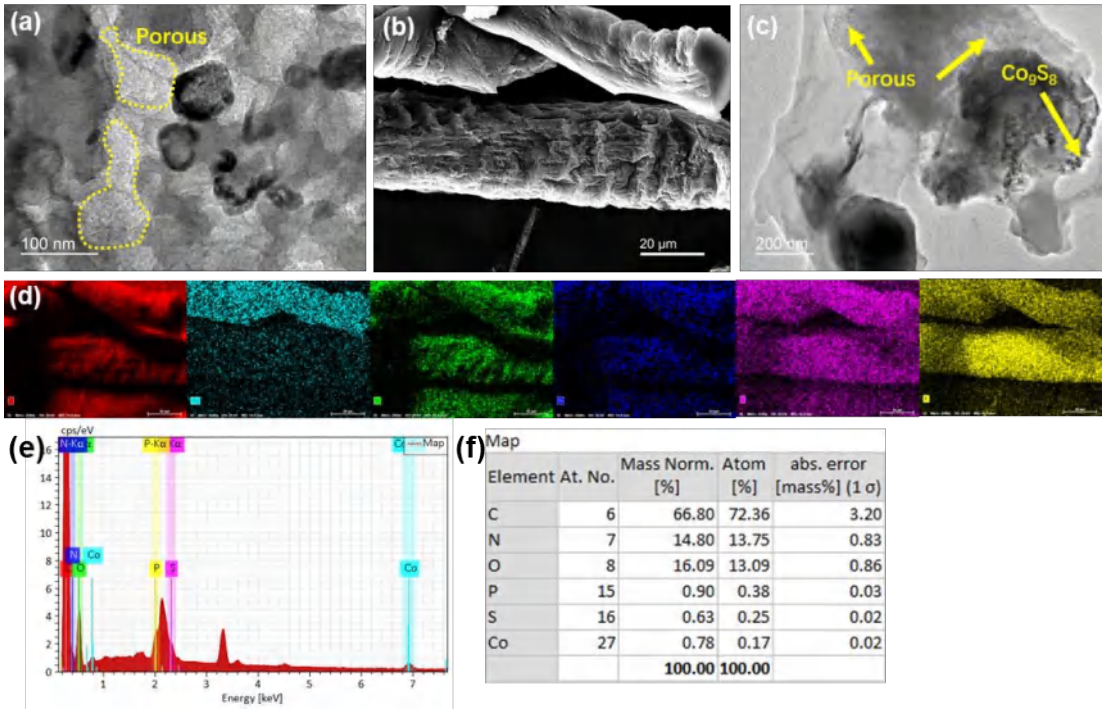

Element	At. No.	Mass Norm. [%]	Atom [%]	abs. error [mass%] (1 σ)
C	6	66.80	72.36	3.20
N	7	14.80	13.75	0.83
O	8	16.09	13.09	0.86
P	15	0.90	0.38	0.03
S	16	0.63	0.25	0.02
Co	27	0.78	0.17	0.02
		100.00	100.00	

Fig. 5.6. (a,c) TEM and (b) SEM image of Fix-920-A; (d) corresponding EDS mapping; (e,f) EDS spectrum and table summary of compositions in Fix-920-A sample.

The Raman spectrum (**Fig.5.7 a**) of carbonized samples also indicates the existence of Co-O/ Co-S bonds in range of 190 cm^{-1} to 750cm^{-1}.[200–202] Peaks located at 195 cm^{-1},

510cm^{-1} and 610 cm^{-1} are attributed to $F_{2g\ (1)}$ and $F_{2g\ (2)}$ mode metallic Co.[203] The intensive peaks at 474 cm^{-1} and 688 cm^{-1} indicate the E_g and A_g mode of Co-O/S tetrahedral structure [204]. Meanwhile, the broad peaks at 1350 cm^{-1} and 1650 cm^{-1} indicate the D and G mode of graphite structure, respectively (**Fig.5.7 b**). The ratio between peak intensity of G and D band (I_G/I_{D1}) is an indicator of graphitization degree in the samples[12]. All values ($I_G/I_{D1} < 1$) show a relative low graphitization degree. For Fix-920 sample, it possesses highest graphitization degree ($I_G/I_{D1} = 0.64$). While after acid activation process, the graphitization degree decreases to 0.59 suggesting more defects of carbon frameworks in the Fix-920-A.

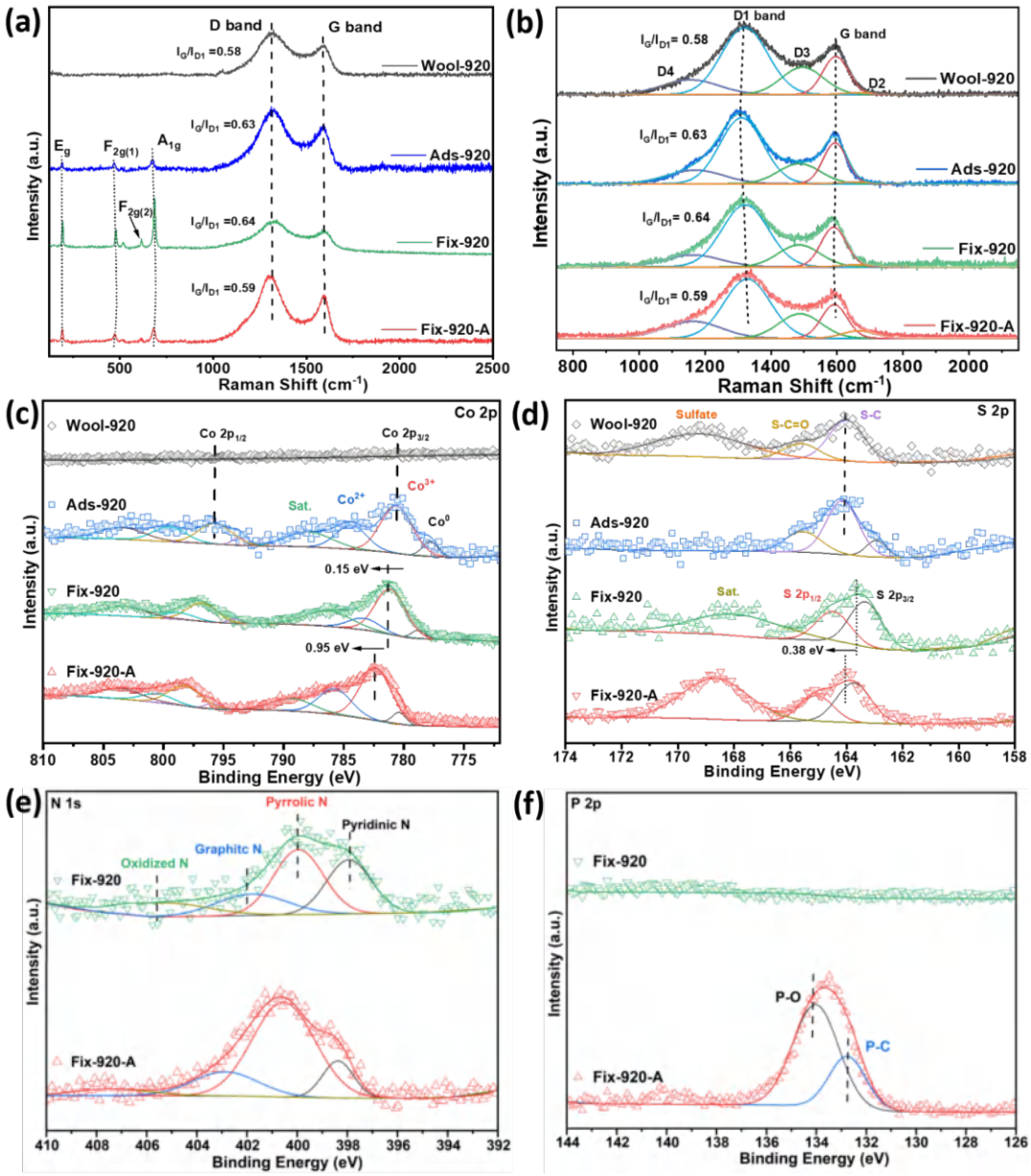

Fig. 5.7. (a) Raman spectra; (b) Corresponding deconvoluted D and G band; (c) Co 2p and (d) S 2p spectra of Wool-920, Ads-920, Fix-920 and Fix-920-A, respectively; (e) N 1s and (f) P 2p spectra of Fix-920 and Fix-920-A.

In addition to the morphology and composition analysis, the topological measurements of various samples were investigated by N_2 adsorption-desorption analysis. Compared with the inactivated samples (**Fig. 5.8 a**), the phosphorus acid activated samples shows a typical Type III hysteresis loop, characteristics of mesoporous structure [205]. The Fix-

920-A sample possesses a BET surface area of 439.3 m^2/g and an average pore size of 3.4 nm (**Fig. 5.8 b**), which is a typical mesoporous system and comparable with the pore system of those $ZnCl_2$ and K_2CO_3 activated carbon samples [206–208].

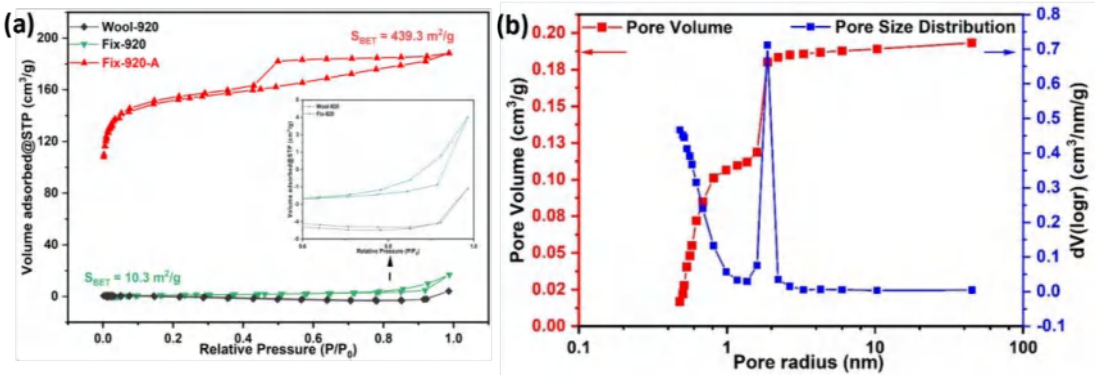

Fig. 5.8. (a) N_2 adsorption-desorption isotherms; (b) Pore size distribution and cumulative pore volume of Fix-920-A derived from N_2 adsorption-desorption isotherm.

The high-resolution X-ray spectroscopy (XPS) was conducted to investigate the surface chemical states, prove the changes in the cobalt electronic environment, and doping of phosphorus atoms in carbon matrix. As shown in **Fig.5.9 a & b**, direct carbonization of wool felt at 920℃ introduces sulphate (SO_4^{2-}) configurations in carbon matrix with an atomic percentage of 0.48% (**Table 5.1**). [17, 18] The peaks located at 780.5 eV and 796.3 eV are attributed to the Co $2p_{3/2}$ and $2p_{1/2}$ respectively. The peaks are further deconvoluted into mixed valence states of Co^{2+} (780.5 eV)/Co^{3+} (784.3 eV) [209]. In addition, the small peak identified at 778.5 eV in Fix-920-A samples is attributed to metallic cobalt (Co^0), in consistence with TEM and XRD results (observation of cobalt particles and characteristic peaks). Compared with the Co $2p_{3/2}$ of Ads-920 sample, a positive shift toward higher binding energy of both Fix-920 (0.15 eV) and Fix-920-A (0.95 eV, compared with Ads-920) can be noticed (**Fig.5.7 c,d**) [210], proving the charge transfer from cobalt core level to sulphur atoms.

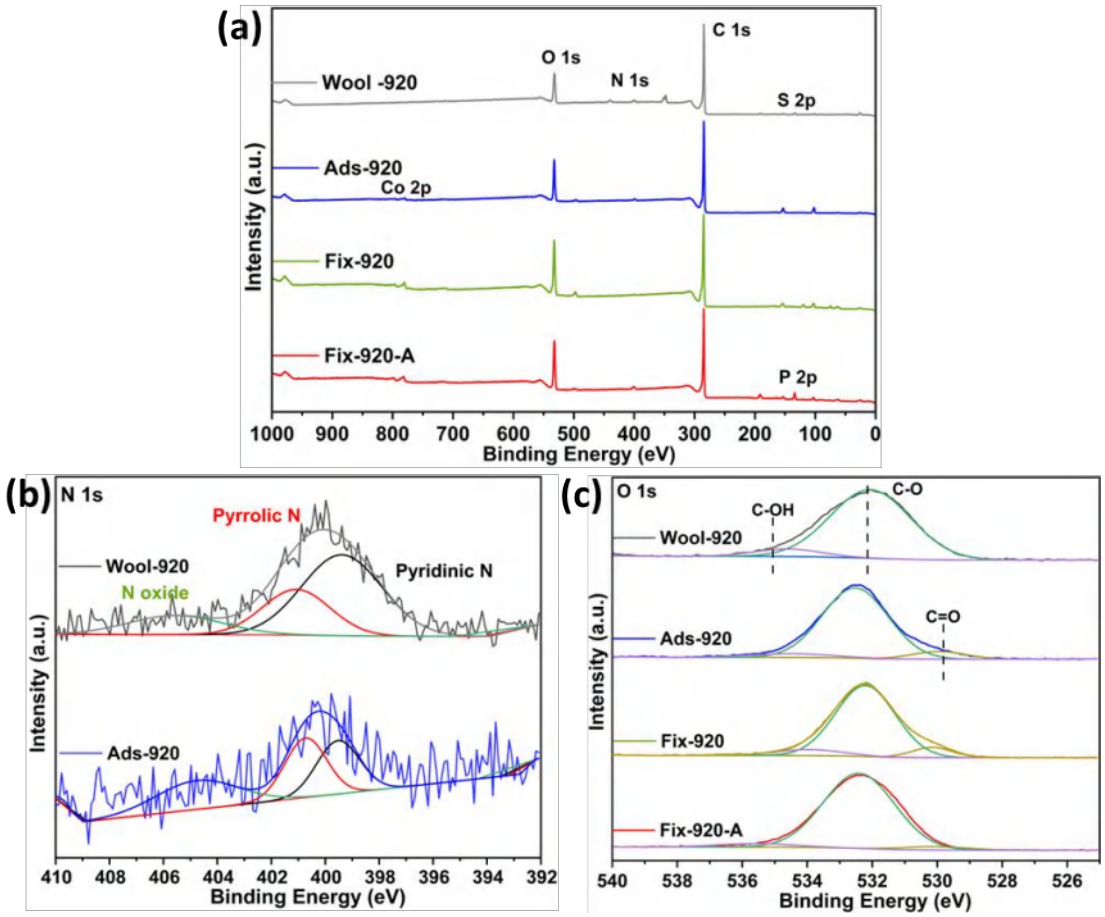

Fig. 5.9. (a) XPS spectra of Wool-920, Ads-920, Fix-920 and Fix-920-A, respectively. (b) N 1s spectra and (c) O 1s spectra of corresponding wool candidates.

This transfer may arise from the stronger electron affinity of S than that of cobalt atoms. [211,212] The further phosphorus activation (**Fig.5.7 d**) also influences cobalt electronic, causing a further positive shift of Co 2p to 782.5 eV. Apart from the electronic environment variations, both S 2p spectrum of wool-920 and Ads-90 indicate the spontaneous doping of sulphur content (S-C, and S-C=O) into the graphitized carbons. However, after fixing cobalt atoms, the formation of cobalt sulphide (Co_9S_8) during carbonization process causes the double split of spectrum into S $2p_{3/2}$ (163.1 eV) and S $2p_{1/2}$ (164.2 eV) in the spectrum. Moreover, a positive shift to higher binding energy by 0.38 eV is observed, due to the phosphorus doping in the carbon matrix (P-C, **Fig.5.7**

f). Interestingly, the fraction of pyridinic N to pyrrolic N of Fix-920-A decreased dramatically from 2.11 to 0.19. This decrease indicates the phosphorus atom substitutes the pyridinic N in carbon frameworks during activation process. In addition to the electronic environment analysis, a higher fraction of Co^{3+} to Co^{2+} in Fix-920-A (1.75, **Table 5.1**) in Co 2p spectrum is noticed, which can contribute to the oxidation process in OER.

Table 5.1 Surface Element Composition analysis on various carbonized and activated wool samples.

Sample	XPS atomic % (at. %) [a]							
	C	N	O	S	Co	P	$Co^{3+}/Co^{2+}/Co^{0}$	Pyridinic N/ Pyrrolic N
Wool-920	79.16	2.63	16.74	0.48	-	-	-	2.11
Ads-920	79.17	2.02	17.74	0.41	0.65	-	1.38/ 1.0 / 0.31	0.92
Fix-920	75.22	2.92	21.17	0.73	1.42	-	1.16 /1.0 /0.32	0.75
Fix-920-A	72.09	2.81	20.9	0.51	1.53	1.16	1.75 /1.0 / 0.20	0.19

[a] Surface atomic percentage derived from high-resolution C 1s, N 1s, O 1s, Co 2p, S 2p and P 1s core-level peaks.

5.3.2 Electrocatalytic Water Splitting Evaluation

With optimized topology and distinctive electronic environment of samples, the corresponding electrocatalytic activities for HER and OER are recorded in a N_2 saturated alkaline medium, shown in **Fig.5.10 a-c**. The reference Pt/C (20 wt%) catalyst was evaluated as benchmark for HER. It possesses an overpotential of 35 mV at current density of 10 mA cm^{-2} and a Tafel slope of 43.9 mV/dec in 1 M KOH. Among all candidates, direct carbonization of wool felt exhibits the lowest catalytic performance. While after the introduction of cobalt elements and activation, all remaining samples exhibit enhanced catalytic activity. Specifically, Ads-920 and Fix-920 require an overpotential 695.1 mV, 509.5 mV at 10 mA cm^{-2} with a Tafel slope of 277.9 mV/dec and 142.6 mV/Dec respectively. These values indicate an unfavourable HER catalytic performance and poor reaction kinetics in cobalt oxide/sulphide-based biochar.

Contrarily, with well-constructure pore systems and phosphorus doping based on Fix-920, Fix-920-A lowers the overpotential to 90.7 mV at 10 mA cm^{-2}, and a Tafel slope of 83.7 mV/Dec. This slope, determined by polarization curve, indicates the Volmer (M + H_2O + e^- ↔ M-H_{ads} + OH^-) -Heyrovsky (M-H_{ads} + e^- + H_2O ↔ H_2↑ + M + OH^-) step as rate-determining step (RDS). This value suggests the electron transfer and hydrogen desorption sluggish the whole reaction pathway[21,16,213]. Potassium carbonate activated Fix-920 also exhibits an enhanced catalytic performance (η10 =209.5 mV) compared with that of carbonized wool fibers without pore system. Both activation processes suggest that the mesoporous system facilitates the electrolyte diffusion, further improving the catalytic activity of carbonized wool fibers.

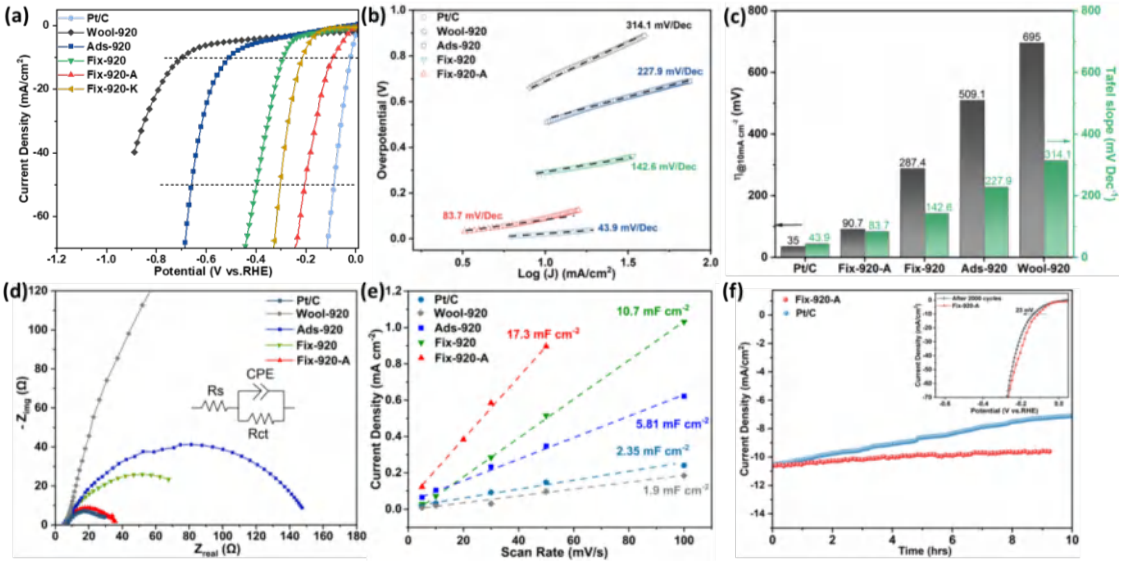

Fig. 5.10. (a) HER polarization curves with 100% iR corrected, (b) Tafel plots, (c) Table summary, (d) Electrochemical impedance spectra, (e) Double layer capacitance of commercial Pt/C, Wool-920, Ads-920, Fix-920, Fix-920-A, Fix-920-K; (f) HER stability test of Fix-920-A.

The Nyquist plot of Fix-920-A, obtained at an overpotential of 100 mV, suggests a low charge-transfer resistance (R_{ct} = 25.3 Ohm, **Fig.5.10 d**), which is much lower than that

of Fix-920 (85.4 Ohm), Ads-920 (145.5 Ohm) and Wool-920 (257.5 Ohm). Compared with the R_{ct} of commercial Pt/C (10.5 Ohm), the Fix-920-A exhibit a comparable value, attributed to the high conductivity from carbon frameworks, doping of hetero atoms, and Co_9S_8 as active sites. Further double layer capacitance (C_{dl}, **Fig.5.10 e and 5.11**) measured at non-faradic region (-0.2 – 0.15 V vs. $Hg/HgCl_2$) was to investigate the available electrochemical active sites in the samples. The calculated values of C_{dl} are 1.9 mF cm^{-2}, 2.35 mF cm^{-2}, 5.81 mF cm^{-2}, 10.7 mF cm^{-2}, 17.3 mF cm^{-2} for wool-920, commercial Pt/Cs, Ads-920, Fix-920 and Fix-920-A, respectively. Among them, Fix-920-A again exhibits the highest C_{dl} value with an electrocatalytic active surface area (ECSA) of 432.5 cm^2. This advantage can be attributed to its mesoporous pore size by post activation. Moreover, the HER catalytic performance of Fix-920-A (**Fig.5.10 f**) outperforms many other cobalt-based candidates and achieves remarkable results in those catalysts supported by biochar.

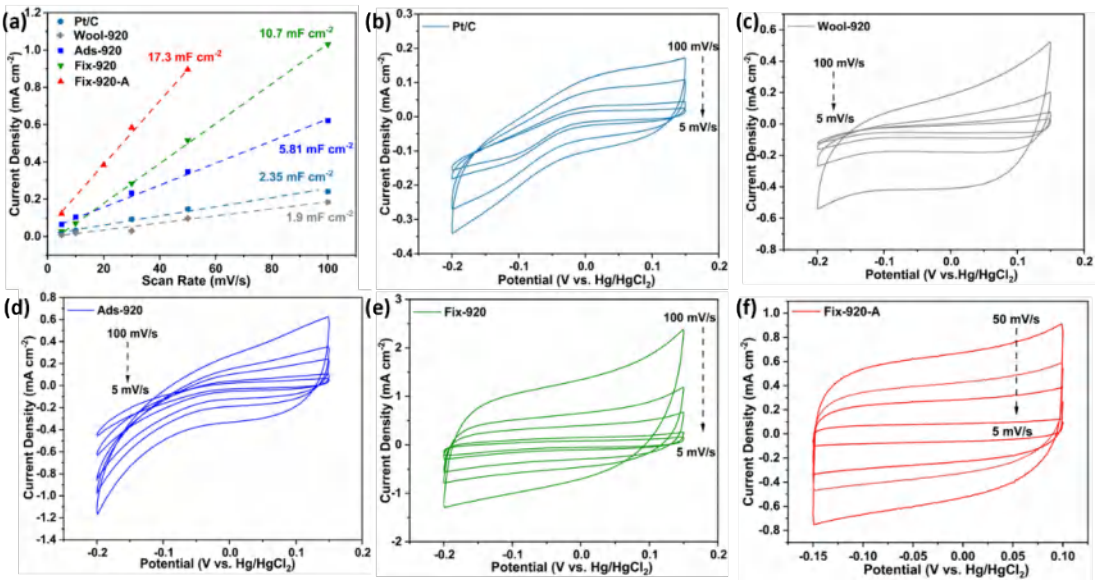

Fig. 5.11. (a) Double layer capacitance of Pt/C, Wool-920, Ads-920, Fix-920 and Fix-920-A; (d-f) Corresponding cyclic voltammetry curves at the potential range of -0.2 – 0.15 V vs. $Hg/HgCl_2$ with scan rates varying from 5 mV/s to 100 mV/s

Similar to HER performance, the OER performance in the same condition of Fix-920-A also outperforms other prepared candidates (**Fig.5.12 a-c**). The Fix-920-A exhibits an overpotential of 295 mV to achieve the current density of 10 mA cm^{-2} with a Tafel slope of 53.7 mV/Dec, proving a favourable catalytic OER performance and accelerated kinetics on active sites. Moreover, further EIS results prove the lowest electron transfer resistance of Fix-920-A (28.7 Ohm for OER, **Fig.5.12 d**) than that of Fix-920 (44.6 Ohm), Ads-920 (76.1 Ohm), and Wool-920 (300.5 Ohm). This lowest value can be originated from the 3D porous structure with phosphorus doping, which not only accelerates the interfacial charge transfer, but also the mass transfer with electrolyte.[39] Similarly, the OER catalytic performance of Co_9S_8-N,P/ACs (**Fig.5.12 e**) lies in the merit region of low overpotentials and Tafel slope, which is also compare with that of commercial IrO_2 electrocatalysts. In addition to powder sample, the blackish biochar remains felt structure after both carbonization and activation, leaving open structures (**Fig.5.12 f**). We directly employ the felt as anode for OER. Owing to the abundant active sites and open structure, the felt can continuously release the O_2.

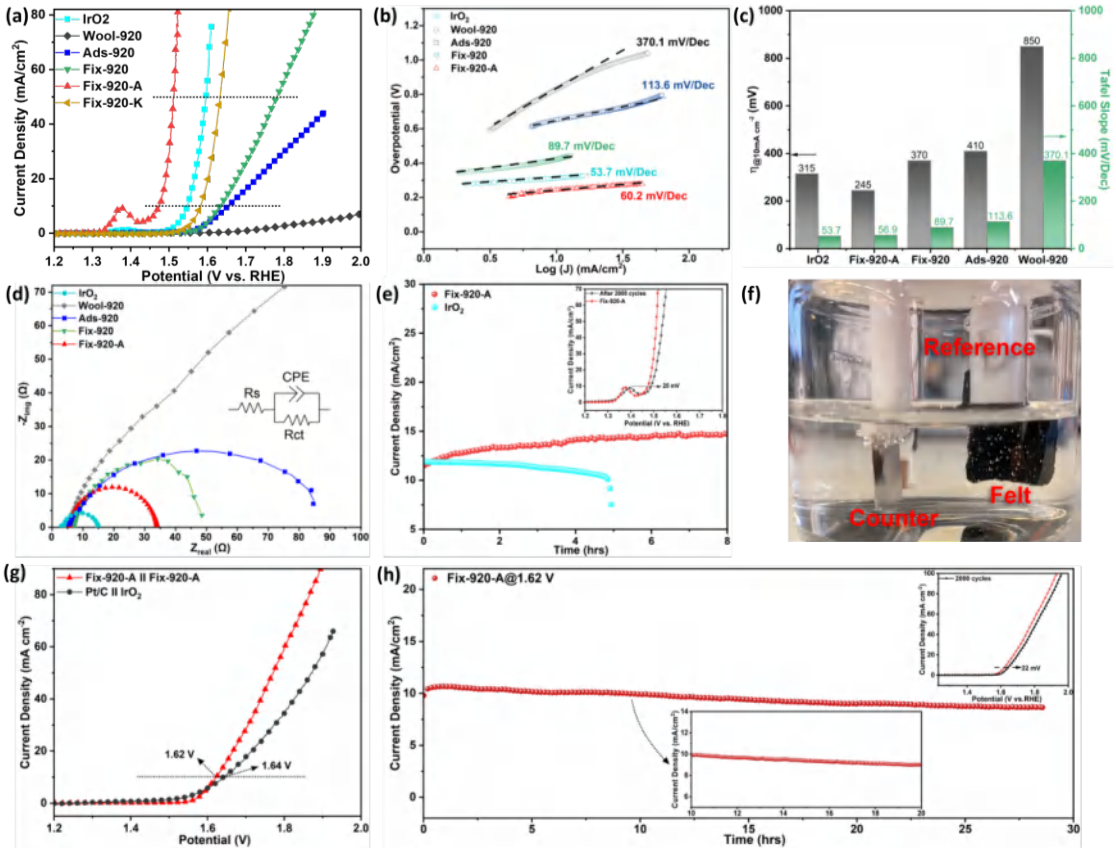

Fig. 5.12. (a) OER polarization curves with 100% iR corrected, (b) Tafel plots, (c) Table summary, and (d) Electrochemical impedance spectra of Wool-920, Ads-920, Fix-920, Fix-920-A and Fix-920-K; (e) OER stability test of Fix-920-A; (f) Digital image of free-standing Fix-920-A electrode for OER in a typical three-electrode configuration; (g) Cell voltage of overall water splitting reaction (Fix-920-A||Fix-920-A); (h) Chronopotentiometry curve for Fix-920-A at 1.62 V (Insert: LSV curve after 2500 cycles; 100 mV/s).

The overall water splitting reaction was then conducted by drop-casting grounded catalysts on the carbon paper as cathode and anode. As shown in **Fig.5.12 g**, the required potential to drive overall splitting reaction is 1.62 V Moreover, it is noticed (**Fig.5.12 h**) that the constructed two-electrode cell was run at 10 mA cm^{-2} for more than 24 hours. It can be noticed that there is only 9.8% of current density decay in the samples. Further

polarization curve shows a 22-mV distortion after 2500 CV cycles, proving a good stability of the whole device.

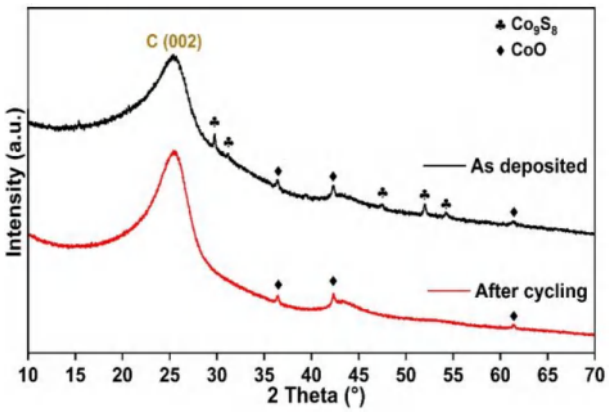

Fig. 5.13. XRD pattern of Fix-920-A after cycling test.

By comparing the XRD pattern of Fix-920-A before and after cycling test (**Fig.5.13**), those peaks indicating the Co_9S_8 (25.3°, 31.3°, 47.6°, 47.5°, 52.6° and 54.3°, respectively) vanish after 1,000 cycling. While those peaks located at 36.4°, 42.3° and 61.4° remain after the stability test, which suggests the CoO are not catalytic favourable compared with cobalt sulphide, but more stable in the redox reaction.

5.3.3 Identification of active sites

As aforementioned, the prepared electrocatalysts are composed of metallic cobalt, cobalt monoxide, and cobalt sulphide. As indicated in **Fig.5.14 a&b**, the Co $2p_{3/2}$ peaks exhibit slight shifts after HER (− 0.59 eV) and OER (+0.61 eV) stability test. It is well-documented that Co 2p peaks tend to shift towards higher binding energy, attributed to the formation of higher valence states of Co^{3+} (~67.5 %). Contrarily, in the S 2p spectra, Sulphur signals vanish after OER, indicating the surface oxidation of Co_9S_8 to active CoOOH species, while sulphur remains stable after HER stability test. In this case, Co_9S_8 {440} and CoO {111} slabs (**Fig.5.14 c**) were optimized for further calculations. In order to figure out the active sites among these two candidates, DFT calculations

were further made to clarify the Gibbs free energy of each reaction coordinates during water splitting reactions. (**Fig5.14 d,e; Table 5.2**) Specifically, Co octahedral site (Co_{octa}) in Co_9S_8 and CoO were chosen as both active sites for the intermediate adsorption. As a result, in HER side, the adsorption energy of proton on Co octahedral site in Co_9S_8 possesses a lower value (-0.94 eV), which is a comparable value in the literature (-0.9 eV). While CoO exhibits a more negative value of -2.36 eV, causing a strong adsorption energy of H, and as a result, hindering the further desorption of hydrogen gases. This result again supports the Volmer- Heyrovsky mechanism is adopted in HER half reaction. With respect to the OER side, the adsorption free energy of OH^- (ΔG_{OH*}) on tetrahedral site on CoO {111} and Co_9S_8 {440} are -1.61 eV and -0.68 eV respectively [214]. While for the third step (G_{O*} to G_{OOH*}) requires a larger energy barrier, increasing to 1.67 eV and 2.98 eV for Co_9S_8 {440} and CoO {111}. The 3rd step hence is regarded as the rate determining step (**Fig.5.15**). Therefore, it can be concluded that in the water splitting reaction, the Co_9S_8 are more energetically favourable, and can be regarded as the true active sites.

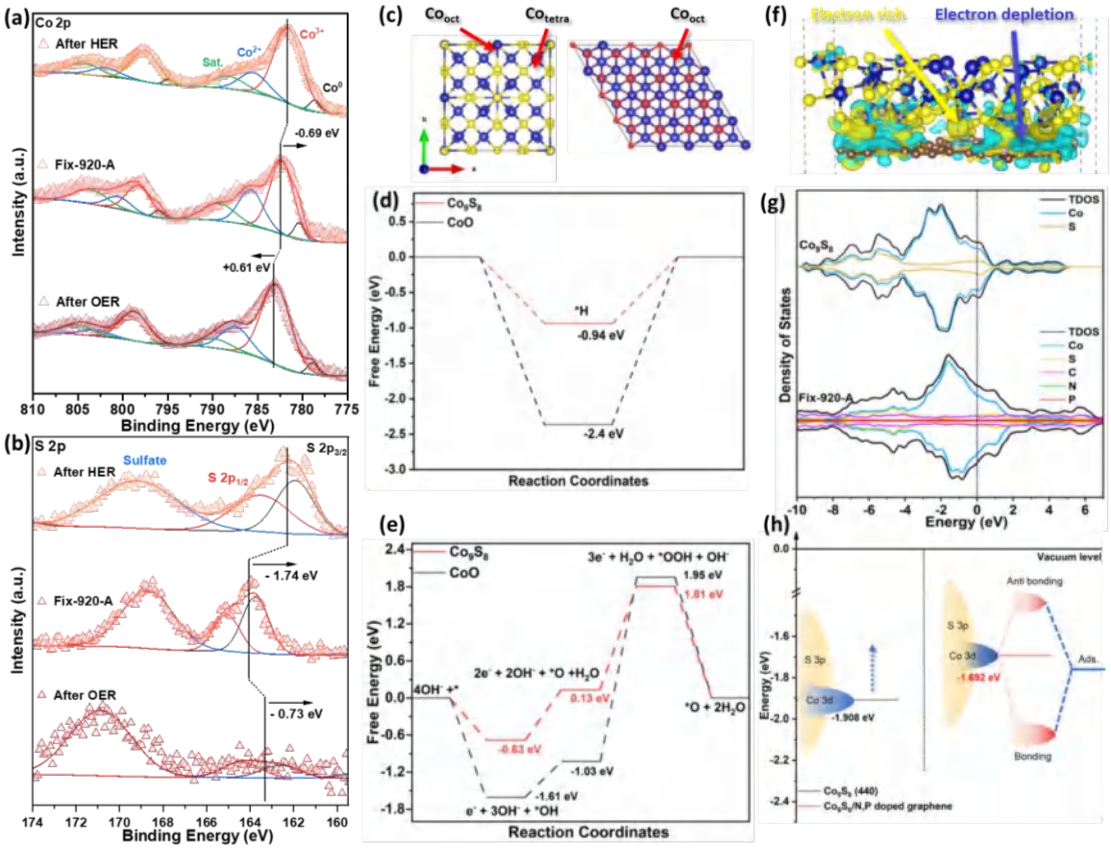

Fig. 5.14. (a) Crystal structure of optimized Co_9S_8 {440} (left) and CoO {111} (right) from c direction (blue: cobalt, yellow: sulphur atom, red: oxygen atom); Calculated adsorption free energy for reaction coordinates in (b) HER, and (c) OER; (d) Charge density difference plot of Co_9S_8/N, P doped graphene heterostructure; (e) Calculated density of states plot and (f) Derived d-band center of Co_9S_8 and heterostructure.

Further charge density difference plot (**Fig.5.14 f**) of Co_9S_8/N,P doped carbons indicates an uniform electronic redistribution at interface after introducing one layer of N,P doped graphene. The electron accumulation is noticed at the region of Co-N and Co-P bonds, proving the electronic interactions after doping. Such interaction is in consistent with the results from XPS, where the P doping into carbon frameworks leads to an electron decrease in Co 2p spectrum. Further DOS plot (**Fig.5.14 g**) confirms that the introduction of N,P doped carbon layer improves the electronic accumulation

(especially Co atoms) at Fermi level, which, as a result, facilitates the electronic transfer at interface. Besides DOS calculations, d-band center of corresponding Co_9S_8 and heterostructure suggests a favourable hydrogen atom adsorption. As indicated, an upshift of d-band center from -1.908 eV to -1.692 eV suggests a favourable adsorption of intermediates (*H), which further facilitates the overall catalytic kinetics[215]. During the whole catalytic process, the formation of intermediates mainly on Co_{oct} of Co_9S_8, leading to the bond breakage of Co-S [202]. While the CoO will still provide certain level of catalytic effect, even all Co-S bonds are consumed.

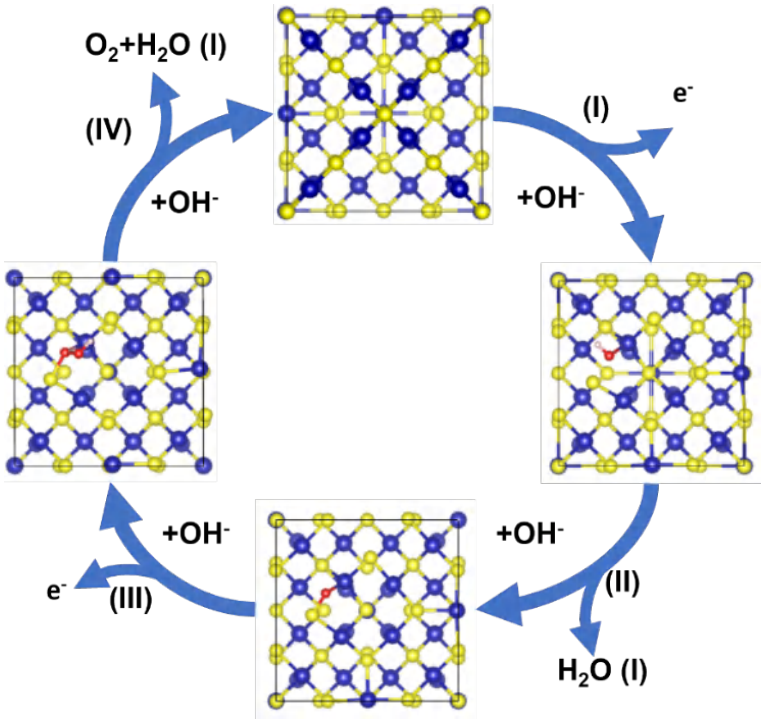

Fig. 5.15. Proposed adsorptive hydroxyl groups on cobalt tetrahedral site in alkaline medium.

Therefore, it can be concluded that in the water splitting reaction, the Co_9S_8 are more energetically favourable, and can be regarded as the true active sites. Moreover, after the construction of heterostructure between Co_9S_8 and N,P co doped carbons, the electronic structure of cobalt is regulated by Co-P bond at interface. The adsorption

energy for intermediates on Co_{oct} thereby can be further influenced, resulting in an improved catalytic performance.

Table 5.2. Density functional theory simulations of water splitting reaction on Co_9S_8 {100}

HER simulation

	Initial energy	Thermal correction		ZPE	Final Energy	U = 0V
Slab	-414.1822	0	-414.1822	H2	-420.9822	0
H	-418.68296	0.163533	-418.519427	1/2 H2	-421.919427	-0.93723
Slab	-414.1822	0	-414.1822	H2	-420.9822	0

OER simulation

	Initial energy	Thermal Correction		ZPE	Final energy	U=0
Slab	-294.26157	0	-294.2616	$2H_2O$	-322.70157	0
OH	-306.08925	0.325497	-305.7638	$H_2O+1/2H_2$	-323.383753	-0.68218
O	-301.60779	0.057132	-301.5507	H_2O+H_2	-322.570658	0.130912
OOH	-311.04975	0.35442	-310.6953	$3/2\ H_2$	-320.89533	1.80624
Slab	-294.26157	0	-294.2616	$2H_2O$	-322.70157	0

Table 5.3. Density functional theory simulations of water splitting reaction on CoO {111}

HER simulation

	Initial energy	Thermal correction		ZPE	Final Energy	U = 0V
Slab	-294.26157	0	-294.26157	H_2	-301.06157	0
H	-300.23814	0.214035	-300.024105	$1/2H_2$	-303.424105	-2.36253
Slab	-294.26157	0	-294.26157	H_2	-301.06157	0

OER simulation

	Initial energy	Thermal Correction		ZPE	Final energy	U = 0 V
Slab	-414.1822	0	-414.1822	$2H_2O$	-442.6222	0
OH	-426.95572	0.345279	-426.6104	$H_2O+1/2H_2$	-444.2304	-1.60824
O	-422.68867	0.056678	-422.632	H_2O+H_2	-443.652	-1.02979
OOH	-430.78672	0.317571	-430.4691	$3/2\ H_2$	-440.6691	1.953051
Slab	-414.1822	0	-414.1822	$2H_2O$	-442.6222	0

5.3.4 All-flexible Wearable device based on Co_9S_8 electrocatalyst

Electrochemical water splitting for hydrogen production, serving as a sustainable and environmentally friendly means of generating hydrogen, has garnered increasing

academic and industrial attention in recent years. Moreover, it is noticed H_2 gas as a therapy shows interesting potentials in personalized medical field. Nevertheless, the current porotypes of water electrolysis system predominantly entail liquid electrolytes, necessitating the incorporation of fluid reservoirs alongside periodic deionized water replenishment. These configurations, further enforced by the introduction of membrane separators between electrodes, impose spatial constraints that impede the downscaling of electrolysis devices, consequently precluding direct integration into medical apparatuses.

In contemporary research, a novel electrolytic approach has emerged as a promising solution, notably the utilization of solid polymer electrolytes. The electrolyte frequently manifest as perfluorosulfonic acid proton (Nafion) exchange membranes. However, the cost-intensive nature of Nafion membranes limit their application in personalized area. It is worth noting that hydrogels owing to their intricate three-dimensional polymeric network, exhibit pronounced water retention capacities and structural resilience. These attributes, coupled with their cost-effectiveness, favorable physical attributes, mechanical robustness, and biocompatibility, have conferred upon hydrogels versatile utility across diverse domains, encompassing environmental engineering and advanced material sciences.

In the primary research, the composition of breath is studied and consisting of 5% water vapor, which can be captured and utilized by hydrogel (**Fig. 5.16**). Further calculations are made based on several assumptions: 1. The rate of breath for one adult is 6 L/min, in which moisture is 0.15 L/min. 2. 2 electron reactions for the generation of 1 H_2 gas molecule, the Vmole of H_2 at 25 ℃ is 24.0 L/mol, 3. The area of electrode is 4 cm^2 and

electron density if 10 mA cm^{-2}.

$$V_{theoretical} = I \times t \times V_{mole}/(n \times F)$$

$$= \frac{0.04\ A \times 60\ s \times 24.0\ L/mol}{2 \times 96485}$$

$$= 0.298\ mL\ H_2$$

As indicated in the calculations, the moisture that caputred by one adult in 1 minute can produce 0.298 mL H_2 at standard conditions.

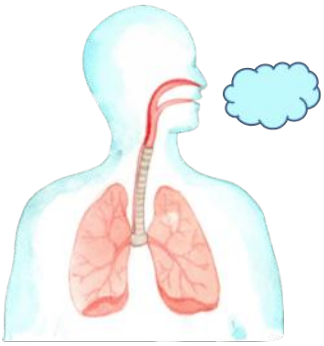

Category	Composition (%)
N_2	78
O_2	13
CO_2	~4
Vapor	~5
Other (Ar)	0-1
Total	~100

Fig. 5.16 Composition of human's breath.

5.3.5 Flexible moisture digester design and potential applications

To construct the all-flexible attachable device, the anode is consisting of carbon cloth, which is stable in oxygen evolution reaction. The catalysts are chosen to be IrO_2 for OER process. The cathode is made of silver fabrics, deposited with Co_9S_8 N/P-ACs (**Fig. 5.17 a**). Moreover, the application of this attachable device can be in both facial mask (**Fig. 5.17 b**) and googles (**Fig. 5.17 c**), to capture the moisture between face and device.

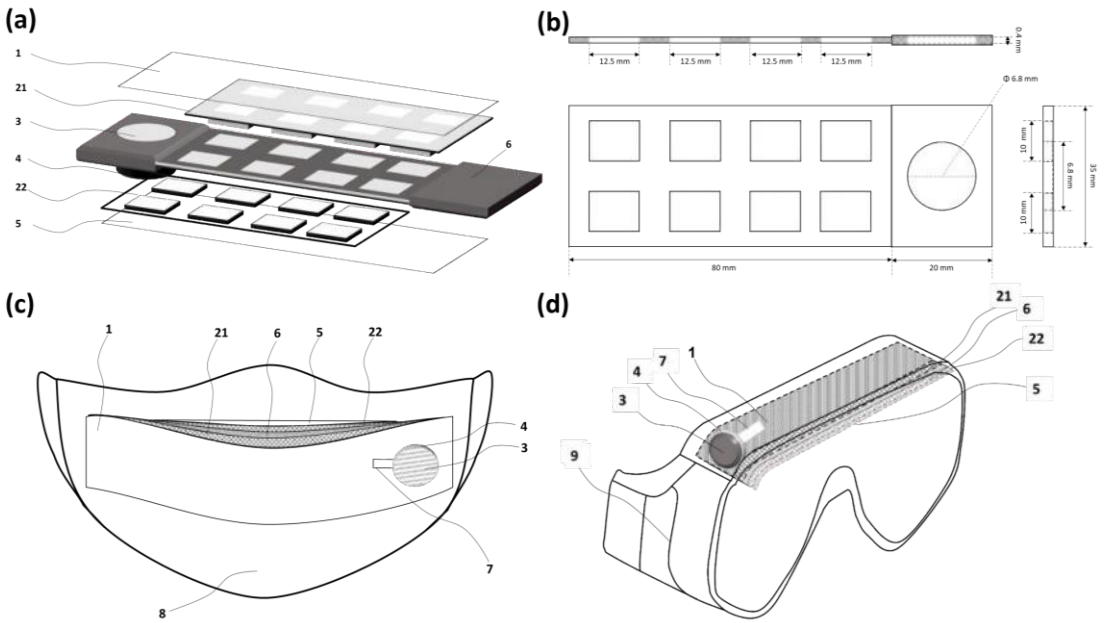

Fig. 5.17 (a) Desing of all-flexible wearable device; (b) Dimensional properties of flexible spacer; Potential applications for (c) facial mask; (d) submersible goggles. (1. Flexible porous cathode, 21. Up layer of hydrogel with hygroscopic salt, 22. Down layer of hydrogel with hygroscopic salt; 3. Patch switch, 4. Coin battery, 5. Flexible porous anode 6. Flexible porous support and spacer, 7. Conductive copper tape, 8. Facial mask, 9. Goggles)

5.3.6 Optimization of electrodes and device integration

The anode is set to be carbon cloth, which should resist harsh condition. While the cathode can be flexible silver clothes which provide both softness and good electricity. In this case, 5 candidates are chosen, including Ag coated nonwovens, warp and weft knitted, woven and blend woven Ag fabrics (**Fig. 5.18**). As indicated, the nonwoven fabrics are sputtered with Ag elements, while the remaining are silver fabrics. For blend woven samples, only weft yarns are made of silver fibres.

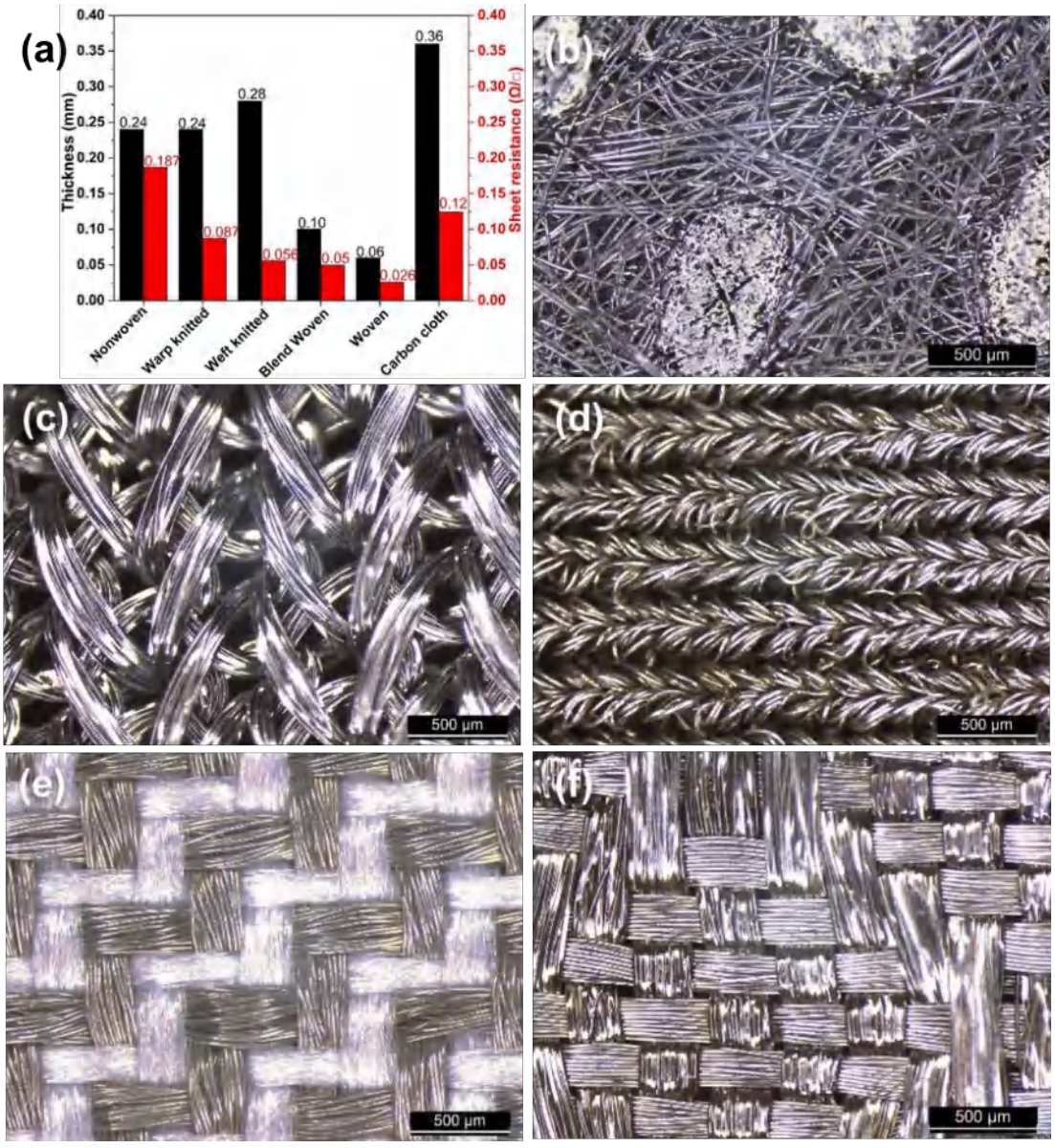

Fig. 5.18 (a) Basic properties of various candidates; Optical images of various silver fabrics (b) nonwoven based; (c) warp knitted; (d) weft knitted; (e) blend woven; and (f) woven based.

To reveal the influence of different candidates on HER performance, sheet resistance indicates that nonwoven silver fabrics possesses highest resistance (0.187 Ω, **Fig.5.18 a**), while woven silver fabrics indicates lowest sheet resistance, proving the best conductivity. Not surprisingly, warp knitted, and woven fabrics show the superior catalytic performance in LSV measurements. It can be noticed that carbon cloth as a

commercial substrate possess a highest catalytic performance, while nonwoven based Ag fabrics exhibits a lowest HER performance. This poorest performance indicates the coating of Ag element is not suitable for wearable application, due to the poor conductivity of substrate. Among other candidates, the HER performance of commercial Pt/C is quite similar, which suggest suitable application in wearable field.

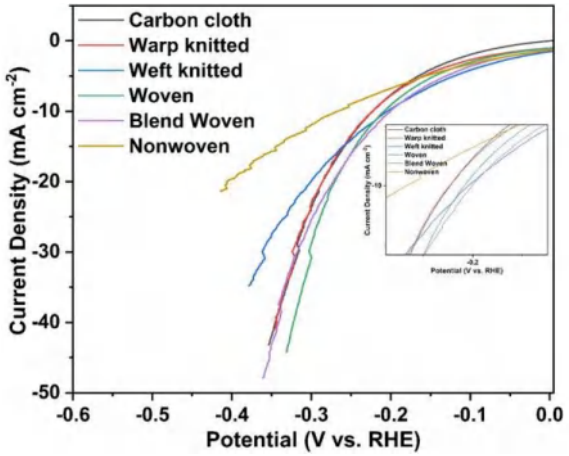

Fig. 5.19 Optimization of various electrodes with loading of 0.5mg cm^{-2} (20 wt% Pt/C).

Further double layer capacitance (**Fig.5.20**) and electrochemical active surface area measurement indicate that the superior performance of warp knitted fabrics is originated from higher C_{dl} (9.29 mF cm^{-2}, 4.82 mF cm^{-2} for woven fabrics; 3.65 mF cm^{-2} for weft knitted, 3.1 mF cm^{-2} for carbon cloth; 2.54 mF cm^{-2} for blend woven; and 2.21 mF cm^{-2} for nonwovens) and ECSA. This higher value provides more active sites even though the load of commercial Pt/C is the same. However, due to the nature of knitted sample, whose edge will be curly under natural conditions, we choose woven silver fabrics as the candidate for cathode.

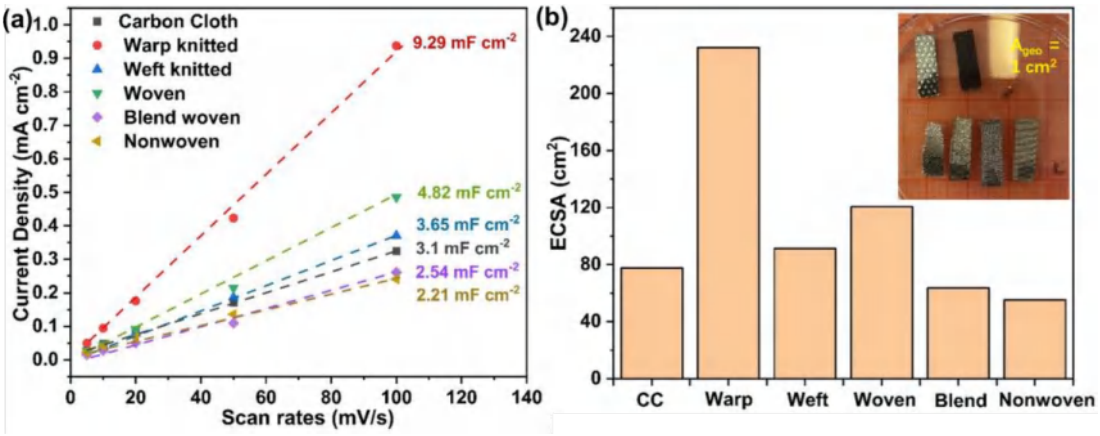

Fig. 5.20 (a) Double layer capacitance and (b) Electrochemical active surface area of various candidates.

To reveal the moisture sensitivity of hydrogel, metal salts (20 wt%) including cobalt nitrate, sodium chloride are added to improve the capturing ability of membrane. As indicated in **Fig.5.21 a**, the salt will separate out of the agar skeleton after vacuum drying, indicating the moisture sensitivity of hydrogel membrane. Further comparison between hydrogel and nafion membrane indicates hydrogel with moisture sensitive salts has a certain level of moisture uptake (5.15 wt% increase in 45 min). Whereas the nafion membrane shows limited weight change.

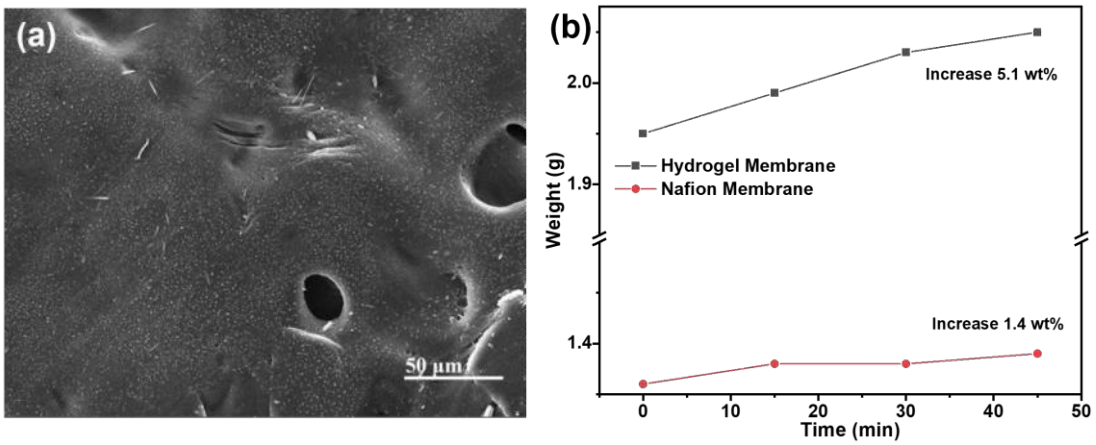

Fig. 5.21 (a) SEM image of hydrogel spacer; (b) Weight changes of hydrogel membrane and nafion membrane at different time slots.

5.3.7 Performance of device

Figure 5.22 indicates the final porotype of flexible device, which is in consistence with the original design. Moreover, a controller will be attached to give 3 V input, driving the water splitting reaction.

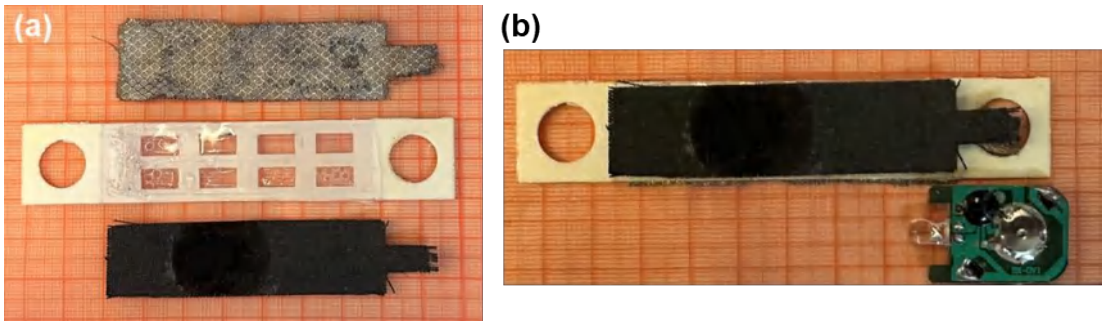

Fig. 5. 22 Optical images of (a) components of all flexible device; (b) Device with electricity controller.

As indicated in **Fig. 5.23 a**, under an externally applied voltage of 3 volts, the device registers a current of approximately 25 milliamperes in a humid environment, while concurrently maintaining stability for a duration of 4800 seconds. It is further determined that under these specified conditions (25℃, 85% relative humidity), utilizing a 200 milliampere-hour lithium-ion button cell as the power source, the device can sustain operations for a duration of 13 hours. This empirical evidence substantiates the effective moisture-absorbing capacity of the hydrogel material, which concurrently serves as a proton conductor, facilitating the efficient electrolysis of ambient moisture.

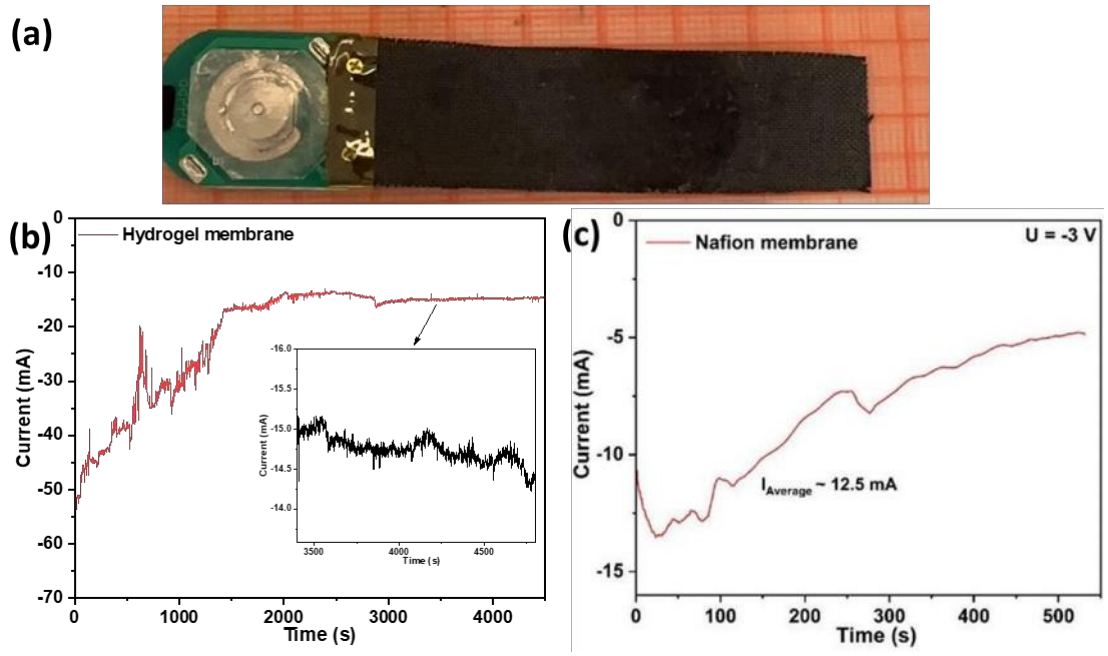

Fig. 5. 23 (a) Digital image of assembled moisture digester; Stability test using (b) hydrogel separator and (c) Nafion membrane at 3 V input (30°C, 80% relative humidity).

5.4 Chapter Conclusion

Through reduction-carbonization-activation treatments, the wool felt has been successfully converted into electrocatalysts for water splitting reaction. By taking advantages of natural disulphide bonds in wool keratin, we selectively fixed the cobalt atoms in the wool fibers with a high loading of 4.76 wt% after carbonization. The as-obtained cobalt sulphide supported by N, P-doped carbons further contributed to the water splitting reaction. The Fix-920-A catalysts possessed a favourable HER ($\eta 10$= 90 mV)/OER ($\eta 10$= 295 mV) activity in 1_M KOH. The as-fabricated electrolyser exhibited a low cell voltage of 1.62 V at 10 mA cm^{-2} with low current decay (~ 9.8%) after 25 hrs operation. Compared with that of physically adsorbed cobalt ions (Ads-920), the superior electrochemical activity of Fix-920-A originated from the well-constructed pore system, synergistic effect between Co_9S_8 and phosphorus doping, and good

conductivity of carbon frameworks. Specifically, the negatively charge P atoms can trap the positively charged proton like a base. Moreover, combined with the accumulated electrons at Fermi-level from DOS calculation, the P doping will regulate the Co atoms' electronic environment to lower down the energy barrier for OH- oxidation process.

Apart from the electrochemical measurement, a flexible and attachable device based on Co_9S_8 N/P-ACs catalysts has been designed and constructed. By adopting the concept of hydrogel spacer and moisture capturing salts, the attachable device can effectively adsorb humid, and convert moisture to hydrogen gas with a stable working current under a 3 V input. This work demonstrated a strategy to utilize the natural content in keratin as precursors for the synthesis of transition-metal based electrocatalysts and personalized device.

Chapter 6. Cobalt-nickel layered double hydroxides-based catalyst for photocatalytic hydrogen evolution reaction

6.1 Introduction

Utilization of solar energy towards the production of hydrogen and oxygen is a promising way for realizing carbon-neutral society[82,216–218]. Hence, efficient visible-light-induced photocatalytic hydrogen evolution (PHE) is currently attractive, which requires suitable cocatalysts that possess high light absorption capability, abundant exposed catalytic active sites, and efficient charge transfer capability. Cadmium zinc sulfide (CZS), as typical semiconductor with a narrow band gap (2.5 eV), shows promising potentials towards visible-light-driven PHE[219,220]. However, the serve photocorrosion, electron-hole recombination in CZS system impedes its application, which is in urgent demands on cocatalyst loading. Chen et al[221] successfully instructed the integration of CuS cocatalyst by carefully injecting Cu-S seeds into cationic (Cd/Zn) precursor solution, followed by the solvothermal reaction. However, the selective decoration of CuS onto CZS nanorods is ultimately realized by controlling all experimental factors, including temperatures, feeding amount and ratios between copper and CZS. More recently, Ma et al[126] reported the incorporation of NiS nanoparticles into CZS system, by one-pot hydrothermal synthesis. The distribution of cocatalysts, however, is highly dependent on the mixture status during the synthetic process, as the trapped NiS particles inside composites are rarely exposed to water molecules. Herein, surface modifications of CZS surface at mild condition are successfully conducted by adopting small molecules with strong metal affinity. This

engineering contributes to the full coverage of CZS by nickel-cobalt layered double hydroxides, with distinguished interface, and abundant active sites.

As indicated, most cocatalysts decorated onto semiconductor system are fabricated by one pot method[222–224]. While disorderly introducing transition metal atoms may cause the distortion of heterostructure, further limiting the PHE activity. Interfacial/surface engineering, as a result, sheds light on the construction of electron tunnel for improving electron-hole separation in semiconductor and facilitating charge transfer from CZS to cocatalysts. Obviously, the poor interfacial interaction between semiconductor and cocatalyst acts like a "wall", hindering the efficient transportation of charge flow. Therefore, the core-shell structure is more expected to be a promising solution, by growing shell layer with electron acceptors and active sites. By investigating the ligand-nanoparticles interactions, research have been reported that the ligand capping agent (e.g. oleyl amine[225], DDT[226]) on CZS can significantly influence products' morphologies and band structures. The impact of surface capping agents is further confirmed to have little impact when particle size is larger than several nanometers, since crystal domain has been formed and stabilizes the whole semiconductor system. However, it is believed that capping agent although has little effects on particles' band structure, does changes the semiconductor's surface micro-environment, where one can manifest this situation for constructing heterostructure. Moreover, transition metal-based catalysts such as metal dichalcogenide[214], metal oxides[227], have been intensively investigated for water splitting reactions. Recently, metal hydroxides have been attracting interests, due to their easy fabrication in a moderate situation and potentials in large-scale industrial applications. However, no such study has been reported to construct a truly core shell structure of semiconductor and hydroxides

heterostructure.

This study presents a facile synthesis method to prepare a core-shell CZS@NiCo layered double hydroxide (NiCo-LDHs) cocatalyst with a distinguished interfacial structure and complete coverage on CZS semiconductor. The synthesis process involves surface modification of CZS with thioglycolic acid (TGA), followed by hydrothermal loading of electrocatalyst. The successful surface modification is firstly confirmed by simulation. Further experimental zeta potential (-2.96 mV) of modified CZS surface facilitates strong ionic interaction between M^{2+} ions and carboxyl groups (in TGA site). Consequently, a CZS@NiCo-LDHs cocatalyst with an average diameter of 105±5 nm and a firm LDH shell thickness of ~20 nm is obtained. The close contact core-shell structure possesses a hierarchical topology (S_{BET}= 87.69 m^2/g), allowing for easy diffusion of electrolyte, rapid electron-hole separation, and efficient transfer of photogenerated electrons. The NiCo-LDHs act as active water splitting electrocatalysts, receiving separated electrons from CZS. The high coverage of LDHs on CZS results in a high PHE rate of ~18.75 mmol g^{-1} h^{-1}, with favorable photostability in 5 cycles under visible light irradiation. Density function theory calculations show an apparent redistribution of electron density after introducing LDHs, and DOS states of the heterostructure possesses an improved electron conductivity, facilitating the electron transfer, and charge separation. This work opens a new avenue by adopting capping agent to change the surface electronic environment, which is further employed for the construction of heterostructure.

6.2 Experimental Section

6.2.1 Materials

Cadmium acetate dihydrate (98%), Zinc acetate dihydrate (98%), Cobalt acetate dihydrate (98%-102%), Nickel chloride tetrahydrate were purchased from Alfa Aesar (United States); Thiourea (99%+), Ammonia persulfate (98%+), Thioglycolic acid (TGA, 98%), Ammonia hydroxide (28 -30 wt%), Eosin Y (water soluble, 99%) were purchased from ACROS organics (UK); Potassium hydroxides pellets (99%+, ACS grade), Sodium sulfide (99%, ACS grade) were purchased from Aladdin (China). PVP (Mw = 58,000, K30), Ethylene glycol (99%+) were purchased from MACKLIN; Cd standard (1 mg/mL), Zn standard (1 mg/mL), Ni standard (1 mg/mL), Co standard (1 mg/mL) in 1% HNO_3 solution were purchased from Aladdin. Triethanolamine (99%) was obtained from Shanghai Chemical Reagent Co., Ltd. All chemicals were purchased and used without further purification.

6.2.2 Synthesis of $Cd_{0.75}Zn_{0.25}S$ and surface modification of CZS nanospheres

To obtain CdZnS nanospheres, cadmium acetate dihydrate (0.84 g), zinc acetate dihydrate (0.19 g; Cd: Zn= 0.75:0.25 in molar ratio), and PVP (2 g, Mw = 54,000) are dissolved in 40 mL EG to form a clear solution A. Thiourea (0.80 g) as sulfur precursor is dissolved in 20 mL ethylene glycol to form solution B. The solution B is then drop added into pre-hot solution A to initiate the nucleation. The whole reaction takes place at 150℃ for 3 hrs. The samples were then precipitated by adding acetone and collected under centrifugation at 13,000 rpm for 10 min. The final products were obtained by vacuum drying at 60℃ overnight.

To modify the surface of CZS nanospheres, 100 μL of N_2 saturated thioglycolic acid (pH of acid is further tuned to 10) is added in to 10 mL of 20 mg/mL of CZS aqueous

dispersion. The modification accounts for 3 hrs under vigorous stirring. The TGA-modified CZS nanospheres was collected under centrifugation at 10,000 rpm and redispersed into 10 mL DI H_2O for further use.

6.2.3 Synthesis of CZS@Ni-LDHs and CZS@NiCo-LDHs core-shell structure

To obtain core-shell structure, nickel chloride hexahydrate (1.02 g), cobalt chloride hexahydrate (0.35 g, Ni^{2+}: Co^{2+} = 3:1 in molar mass), and ammonia persulfate (0.34 g) were dissolved in 30 mL DI H_2O to form a clear solution C. Subsequently, 1mL, 4.5 mL and 13.5 mL of solution C was poured into above 10 mL TGA-modified CZS dispersion under stirring for 1 hour to achieve an adsorption equilibrium of metal ions. For pure Ni-LDHs, 1.304 g of nickel chloride tetrahydrate instead of mixture of nickel and cobalt salts was employed.

Subsequently, 0.7 mL of ammonia solution (28-30 wt%) is quickly injected into the above adsorption steady state solution. The whole solution is further transferred into a 50 mL Teflon kettle, and underwent 120℃ hydrothermal reactions for 8 hrs. The final CZS@Ni-LDHs, and CZS@NiCo-LDHs powders are separated, washed by centrifuging at 10,000 rpm using ethanol and DI H_2O respectively, which are further dried at 60℃ in a vacuum oven.

6.2.4 Synthesis of CZS/NiCo-LDHs composites

To obtain CZS/NiCo-LDHs composites, 7 mL of above solution C is directly added to 10 mL of CZS aqueous dispersion, while other procedures remain the same.

6.2.5 Preparation of catalysts on Ni foam and FTO glass electrode

The obtained photo/electrocatalysts (5 mg) were dispersed into a mixture of iso-

propanol (200μL); ethanol (200 μL) and DI H_2O (580 μL, conductivity = 0.26 μS cm^{-1}) with extra addition of Nafion dispersion (20 μL, 5wt%). After achieving uniform dispersion of catalyst in an ice bath under sonication for 1 hour, 10 μL of dispersion was drop-casted onto two sides of a 0.5 x 1.5 cm^2 Ni foam or one side of 1 cm^2 FTO glass ($A_{geometric}$= 1 cm^2). In all cases, FTO glasses and Ni foam were washed with acetone, ethanol and DI H_2O under sonication for several times, The casted electrode was dried under infrared irradiation for 30 minutes to yield a mass load ~ 0.2 mg/cm^2.

6.2.6 Physical characterizations

Scanning electron microscopy (SEM) images were obtained from Tescan MIRA 3, Czech (accelerating voltage = 20kV). Transmission electron microscopy (TEM) and high-resolution TEM (HRTEM) were conducted on JEOL 2100F, Japan (operating voltage = 200 kV). High-angle annular dark-field scanning TEM (HADDF-STEM) and EDX mapping were conducted on FEI TF20-super X, Thermo Fisher, United States (operating voltage = 200 kV). X-ray diffraction (XRD) patterns were collected on a Rigaku SmartLab 9kW-Advance, Japan using monochromate Cu kα radiation (λ = 0.154 nm) at a scan rate of 5°/min. Raman spectroscopy was taken using a NomadicTM 3-in-1 microscope, America with He-Ne laser excitation (λ = 532/785 nm). Brunauer-Emmett-Teller (BET) surface area measurements were taken by N_2 adsorption-desorption isotherm at 77 K using NOVA touch LX4, Austria. The quantitative analysis of cobalt was obtained by the Agilent 5100 synchronous vertical dual view inductively coupled plasma–optical emission spectrometer (ICP–OES). X-ray and ultraviolet photoelectron spectroscopy (XPS & UPS) were recorded on a Thermo Scientific Nexsa, UK using a monochromatic and focused Al Kα source (1486.6 eV) and He I source (21.2 eV). The surface morphology and surface potential were investigated by atomic

force microscopy (AFM) using Asylum MFP3D Infinity with Kelvin Probe Photoluminescence spectrum (FSL-980, Edinburgh, UK) and time resolved PL spectrum, related to the carrier separation dynamics, was fitted, and calculated according to the equations (2-3) below:

$$A(t) = A_1 e^{\frac{-t}{\tau 1}} + A_2 e^{\frac{-t}{\tau 2}} + A_3 e^{\frac{-t}{\tau 3}} \quad (2)$$

$$A_{(ave)} = \frac{(A_1 {\tau_1}^2 + A_2 {\tau_2}^2 + A_3 {\tau_3}^2)}{(A_1 \tau_1 + A_2 \tau_2 + A_3 \tau_3)} \quad (3)$$

Where A and τ indicate the amplitudes and emission lifetimes of each component.

UV-vis diffuse reflection spectrum (UV-vis DRS) was obtained by UV Cary-300, Shimadzu, UK equipped with an integrating sphere in the wavelength of 250 nm – 800nm, in which white $BaSO_4$ was employed as reference. The band gap, valence band and conduction band of the prepared catalysts can be calculated according to the following equation (4-7):

$$\alpha(hv) = A(hv - E_g)^{\frac{1}{2}} \quad (4)$$

$$E_g = VB_{potential} - CB_{potential} \quad (5)$$

$$\phi = 21.22eV - E_{cut-off} \quad (6)$$

$$VB_{potential} = VB_{xps} - E_f \quad (7)$$

$$CB_{potential} = VB_{potential} + E_g \quad (8)$$

6.2.7 Photo/electrochemical measurements

The photocatalytic hydrogen evolution measurements were carried out at in a 50 mL quartz reaction vessel at atmospheric pressure. A 300W Xe lamp equipped with a wavelength filter (λ≥ 420nm, PLS-SXE300, Beijing PerfectLight Tec. Co., Ltd.) was placed at the distance of 5 cm from vessel. In a typical trial, photocatalysts (2.5 mg)

were dispersed into a mixture of DI H_2O and TEOA (10 v% of DI H_2O), where TEOA functions as the sacrificial agent. The suspension then underwent sonication for 5 min and was purged with N_2 to remove the air before reaction. The photocatalytic H_2 evolution reaction was quantified by a gas chromatograph (Fuli, GC9790-II, China) equipped with a thermal conductivity detector (TCD), using ultra-high purity N_2 (99.999%) as carrier gas. The photocatalytic stability test was extended to 3 cycles for a total of 12 hrs. After each cycle, extra 1 mL TEOA were added into above dispersion, where the vessel underwent N_2 purgation before next cycle. (Note: Eosin Y is employed for pure NiCo-LDHs, which function as the visible light absorption agent)

The electrochemical measurements were carried out at the electrochemical workstation (CHI660E, Shanghai Chenhua Science Technology Corp., Ltd.). A typical three-electrode configuration including Pt plate (2 x 1 cm^2, 0.1 mm) as counter electrode; Ag/AgCl (Saturated KCl solution) as reference electrode, Fluorine doped tin oxide conductive glass (FTO, cut with 1 x 1 cm^2) or Ni Foam (0.5 x 1.5 cm^2) as working electrode was employed for photo/electrochemical measurements. N_2 saturated 0.1_M Na_2SO_4 (pH =7.1) was functioned as electrolyte. The linear sweep voltammetry (LSV) was measured at a scan rate of 5 mV/s with 100% iR compensation, where electrolyte resistance was determined by electrochemical impedance spectroscopy (EIS), using Ni foam. All recorded potentials were converted to the reversible hydrogen electrode (RHE) according to the Nernst equation (Equ. 9):

$$E_{RHE}(\mathrm{V}) = E_{working} + 0.059\mathrm{pH} + E^0_{Ag/AgCl} - iR \qquad (9)$$

Where E_{RHE} is the calculated potential vs. RHE, $E_{working}$ is the recorded potential against Ag/AgCl, and $E^0_{Ag/AgCl}$ equals to 0.197 V, which is the standard equilibrium potential

at 25 ℃. The Tafel slope has been plotted according to the equation below (Equ. 10) to investigate the reaction kinetics:

$$\eta = a + \beta \log(j) \quad (10)$$

Where η and j are overpotential (mV) and current density (mA cm^{-2}) respectively.

Chopped light current-time (i-t) curves were obtained at open circuit potential vs. Ag/AgCl reference electrode (OCP) with 30s light on and off interval. Electrochemical Impedance Spectroscopy (EIS) measurements on Ni foam electrode were conducted at an overpotential of 100 mV for HER with an amplitude of 5 mV from 100 KHz to 0.1 Hz to investigate the charger transfer resistance and mass transfer at high- and low-frequency region respectively. EIS measurement using FTO glass electrodes with the same configurations were conducted at open circuit potential under visible light illumination. Mott-Schottky plot was measured at a fixed frequency of 1 Khz.

6.2.8 Theoretical Simulations

Density functional theory calculations were conducted, using projector augmented wave (PAW) pseudopotential and the Perdew-Burke-Ernzerhof (PBE) exchange-correlation functional implemented in the Vienna Ab-initio Simulation Package (VASP). Calculations were made by a plane wave kinetic energy cut-off energy of 400 eV. The Gamma k-point meshes of 2 x 2 x 1 was set for the structural relaxation. The convergence criterion for the force and energy was set to be 10^{-6} eV and 0.01 eV A^{-1}, respectively. The structures were spin-polarized and under relaxation until reaching the convergence tolerance of force on each atom (< 0.05 eV). To better describe the electron stats of 3d orbital in cobalt element, DFT+U method was employed, where U= 3 eV for

Co and Ni atoms. The adsorption energy of small molecules was obtained according to the equation 10 below:

$$E_{adsorp} = E_{hetero} - E_{molecule} - E_{slab} \quad (11)$$

Where E_{hetero} is the energy after adsorption, $E_{molecule}$ and E_{slab} are the energies of individual system.

6.3 Results and discussion

6.3.1 Surface modification of CZS nanospheres

As indicated in **scheme 6.1**, the CZS nanospheres with exposed Cd/Zn atoms at surface are synthesized by a solvothermal method. The as synthesized cadmium zinc sulfide nanospheres possess an average diameter of 83.5±7 nm (**Fig.6.1 a; 6.3 a**). The selected area electron diffraction ring (**Fig.6.3 a,b**) of CZS refers to lattice fringe of CZS (111), (220), and (311), respectively in the bulk[228].

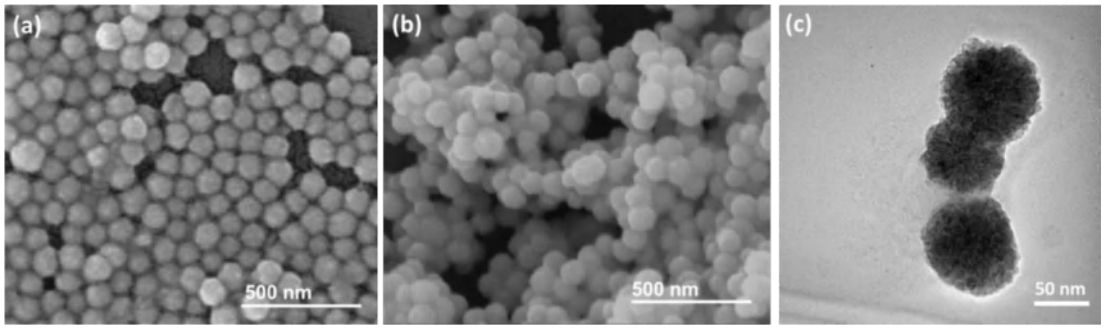

Fig. 6.1 SEM image of (a) CZS nanospheres; (b) SEM and (c) TEM image of TGA modified CZS.

High-resolution TEM image (**Fig.6.3 b**) at surface edge indicates the polycrystalline structure of CZS nanosphere, where surface lattice fringes of 0.208 nm and 0.324 nm are attributed to CZS (220) and (101) plane[228], respectively. It is noticed the as-synthesized spheres possess a pomegranate-liker morphology. This phenomenon can be

related to the fact that Cd/Zn-S seeds are supposed to aggregate firstly, and then form nanocluster as the seed center, where more Cd and Zn-S bonds attach onto the cluster center forming larger nanosphere. Moreover, from the HRTEM results, it is assumed that the surface layer of CZS is covered by Cd and Zn atoms from (101) plane. ICP-OES was then employed to reveal the stoichiometric ratio between Cd and Zn, which is determined to be $C_{0.768}Z_{0.232}S$ (**Table 6.1**) and is similar to the input ratio.

Table 6.1 ICP-OES results of corresponding samples

Element / Sample	Cd 226.502 (ppm)	Co 238.892 (ppm)	Ni 221.648 (ppm)	Zn 202.548 (ppm)	Input amount (mg/100mL)
NiCo-LDHs	-	16.1001	52.2362	-	7.75
CZS@NiCo-LDHs	7.22642	11.6549	36.2048	0.90556	13.94
CZS/NiCo-LDHs	6.98453	16.1001	52.2362	1.18556	16.03

In order to calculate the molar amount of employed thioglycolic acid in surface modification, we conducted calculations by identifying inorganic part and surface Cd/Zn atoms ratio based on several assumptions [226] (**Fig.6.2**).

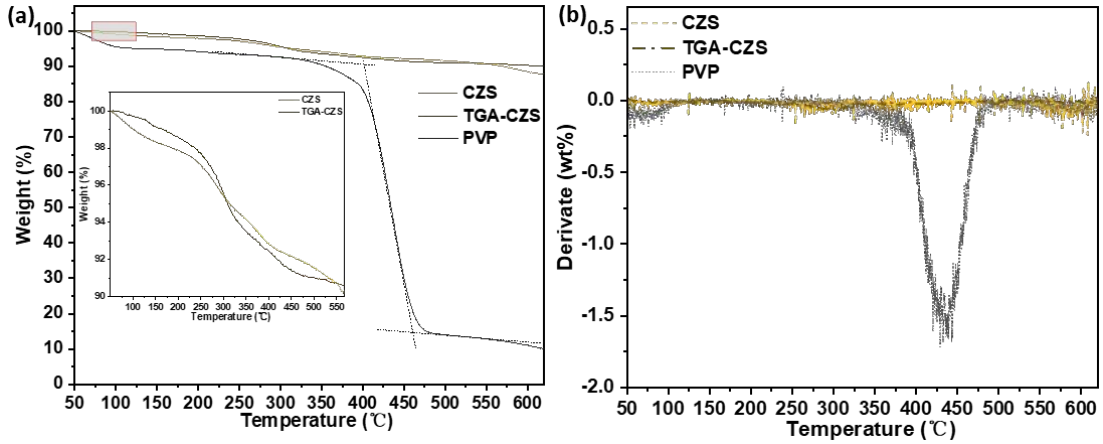

Fig. 6.2 (a) Thermogravimetric analysis of obtained PVP capped CZS nanoparticles and PVP polymer; (b) Corresponding differential thermal analysis.

To determine the amount of thioglycolic acid employed in the surface modification of

CZS nanospheres, thermal gravimetric analysis was employed to investigate the ratio between PVP organic part and CZS inorganic part. As shown in the **Fig.6.2 b**, a significant decomposition of PVP starts from 398.5℃ and end at 500℃. During this region, we observed that the weight of CZS nanospheres decrease from 92.78% to 91.82%, which may arise from the decomposition of PVP polymer. Hence, we dedicate that 99% of products are composed of CZS inorganic part.

We also assume that each thioglycolic acid molecule will attach to one Cd atom at surface, and the average bond length between Cd-S and Zn-S is 2.53 Å for simplicity. We assume the molecular density of $C_{0.75}Z_{0.25}S$ is 132.73 g/mol. The density of CZS is 4.82 g/cm^3.

For example, to calculate the amount of thioglycolic acid for 5 mg CZS nanoparticles with a diameter of 80 nm:

Step I: Number of individual particles (N_{part}) in 5 mg sample:

$$Volume\ of\ \ Individual\ NPs = \frac{4}{3}\pi r^3 = \frac{4}{3} \times \pi \times 40nm^3 = 2.68 \times 10^{-16} cm^3$$

$$N_{part} = \frac{Total\ Inorganic\ Volume\ of\ Sample}{Volume\ of\ Individual\ NP} = \frac{5mg \times 99\%}{4.82g/cm^3 \times 2.68 \times 10^{-16} cm^3}$$

$$= 3.83 \times 10^{12}$$

Step II: Total surface sites in mole in 5 mg CZS sample:

$$Volume\ of\ \ Individual\ NPs\ excluding\ surface\ layer = \frac{4}{3}\pi(r - 0.253nm)^3$$

$$= 2.63 \times 10^{-16} cm^3$$

$$Volume\ of\ \ Individual\ NPs\ suface\ layer = 2.68 \times 10^{-16} - 2.63 \times 10^{-16}$$

$$= \ 5.83 \times 10^{-18} cm^3$$

$$Moles\ of\ CZS\ at\ surface\ for\ individual = \frac{5.83 \times 10^{-18} cm^3 \times 4.82 g/cm^3}{132.73\ g/mol}$$

$$= 2.11 \times 10^{-19} mol$$

$$Total\ surface\ site\ of\ CZS\ in\ mole = 2.11 \times 10^{-19} mol \times 3.83 \times 10^{12}$$

$$= \sim 0.81\ \mu mol$$

Step III: Calculation of volume of thioglycolic acid:

Given that the density, molecular weight of thioglycolic acid is 1.326 g/mL, 92.11 g/mol and 98%.

$$The\ volume\ of\ TGA = \frac{0.81 \mu mol \times 92.11\ \text{g/mol}}{1.326\ \text{g/ml} \times 0.98} = 0.57 \mu l$$

So, for 500 mg of CZS nanoparticles, we may add 57μl of thioglycolic acid. While in practical, we added 100μl of thioglycolic acid for excessive modification.

Moreover, the feasibility of small molecule modification was firstly examined by density function simulations. The optimized bond length of Cd-S and Zn-S are 2.57 Å and 2.49 Å (**Fig.6.3 d**), which are close to the crystal Cd-S (2.55 Å) and Zn-S bond length (2.41 Å). Subsequently, the adsorption energy of thioglycolic acid molecules (TGA) onto the CZS surface were calculated. The adsorption energy of acid molecules on top of Cd and Zn atoms are -2.03 eV and -1.09 eV, respectively, suggesting a favorably spontaneous adsorption on CZS (101) surface. Besides, the molecule tends to be adsorbed onto Cd atom firstly, followed by Zn atom. Additionally, ζ-potential technique was conducted to explore the surface electronic environment of CZS before and after modification. As illustrated in **Fig.6.3 e,f**, the measured ζ-potential of TGA-CZS shift more negative from 7.3 mV to -19.7 mV, leading to a stronger cation ion attraction ability. This positive effect contributes to the subsequent loading of LDHs, in

consistent with simulation results that carboxyl group provides a more negative electronic environment. The pure NiCo-LDHs in ethanol dispersion possess a positive potential (14.3 mV), showing that NiCo-LDHs exhibit relative fewer chances to be physically adsorbed on the CZS surface, without surface modification. Meanwhile, the morphology of CZS after thioglycolic acid modification were examined by TEM with little distortion (**Fig.6.1 c**).

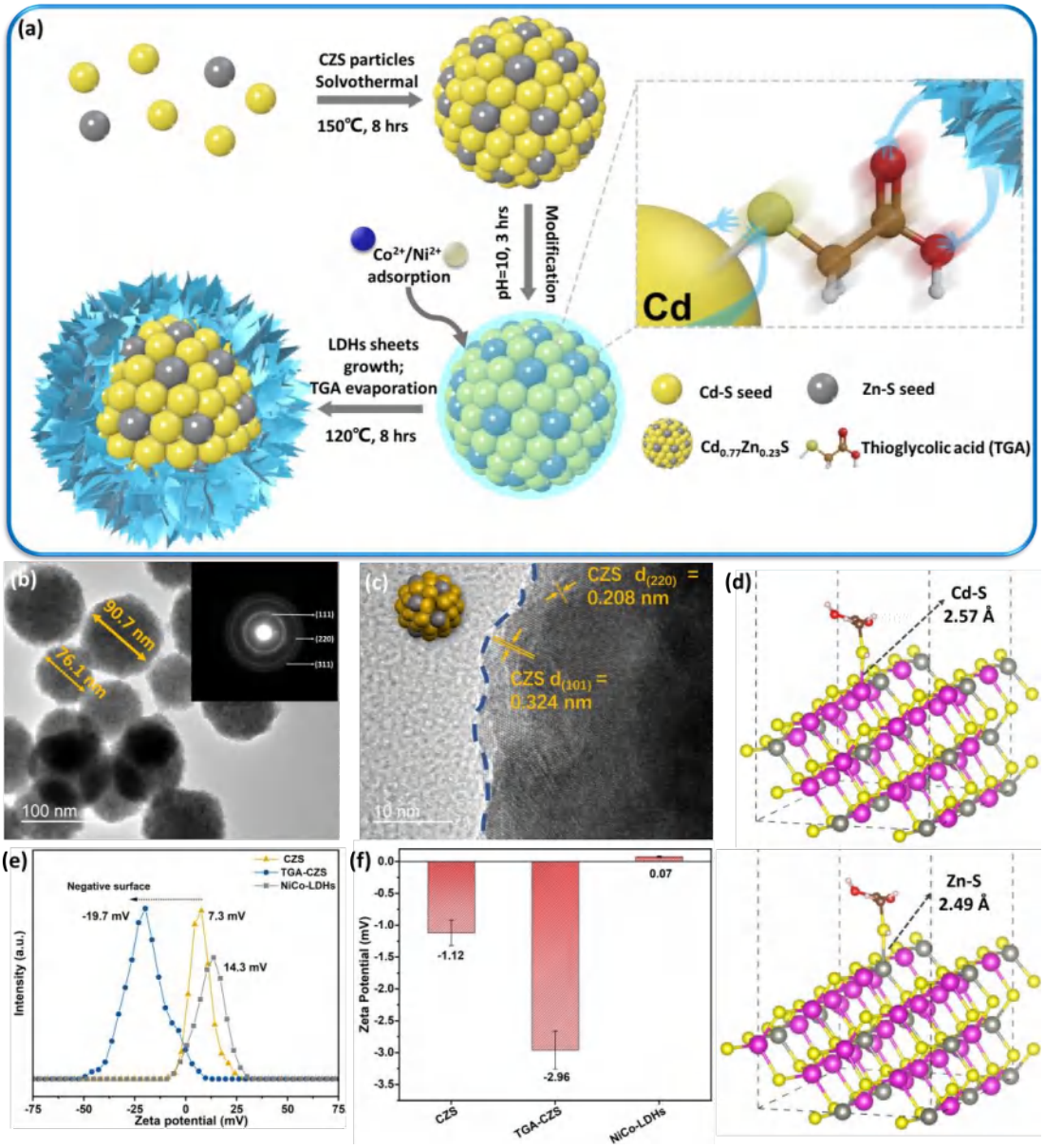

Fig. 6.3. (a) Schematic illustration of synthesis of CZS@NiCo-LDHs; (b) TEM and (c) High-resolution TEM image of cadmium zinc sulfide (CZS) nanospheres, (d)

Optimized geometry of one TGA molecule on the CZS (101) plane (upper: on top site of Cd atom, lower on top site of Zn atom, purple: Cd atom, grey: Zn atom, yellow: S atom, brown: carbon atom, red: oxygen atom, light pink: hydrogen atom), (e-f) ζ-potential plot of CZS, Thioglycolic acid modified CZS (TGA-CZS) and NiCo-layered double hydroxides dispersed in ethanol.

6.3.2 Morphological and physical characterization of cocatalysts

The NiCo-LDHs cocatalysts, as depicted in **Fig.6.4a, Fig.6.5a** exhibit a nanoflower morphology with a diameter of 273.5±26 nm after hydrothermal treatment, in consistence with literature[87]. Thereby, this structure demonstrates a capability for complete coverage on the CZS nanosphere surface. Meanwhile, ICP-OES results suggest the stoichiometric ratio of LDHs is $Ni_{0.752}Co_{0.248}$-LDHs (**Table 6.1**), close to the designed ratio. As a result of successful surface modification, TEM images and high-angle annular dark-field scanning TEM (HADDF-STEM) of CZS@NiCo-LDHs illustrate the well-constructed core-shell structure (**Fig.6.4 b,c; Fig.6.5 b**), with an average shell thickness of ~20 nm. (**Fig.6.4 c**). Again, the ICP-OES results suggest a loading of 65.2 wt% of LDHs in the composites. Further high-resolution TEM images (HRTEM, **Fig.6.4 d**) confirm the interfaces between CZS nanospheres and NiCo-LDHs. The lattice fringes of 0.208 nm and 0.150 nm are attributed to the (220) facet of CZS nanospheres, and (001) facet of NiCo-LDHs, respectively[84]. Besides morphologies, EDS elemental mapping (**Fig.6.4 f-k**) were recorded to show the distribution of elements. As illustrated, the core of nano-flower is composed of CZS semiconductor, meanwhile, the shell is made of Ni and Co elements with a thickness ~25 nm, in good coordination with HRTEM image.

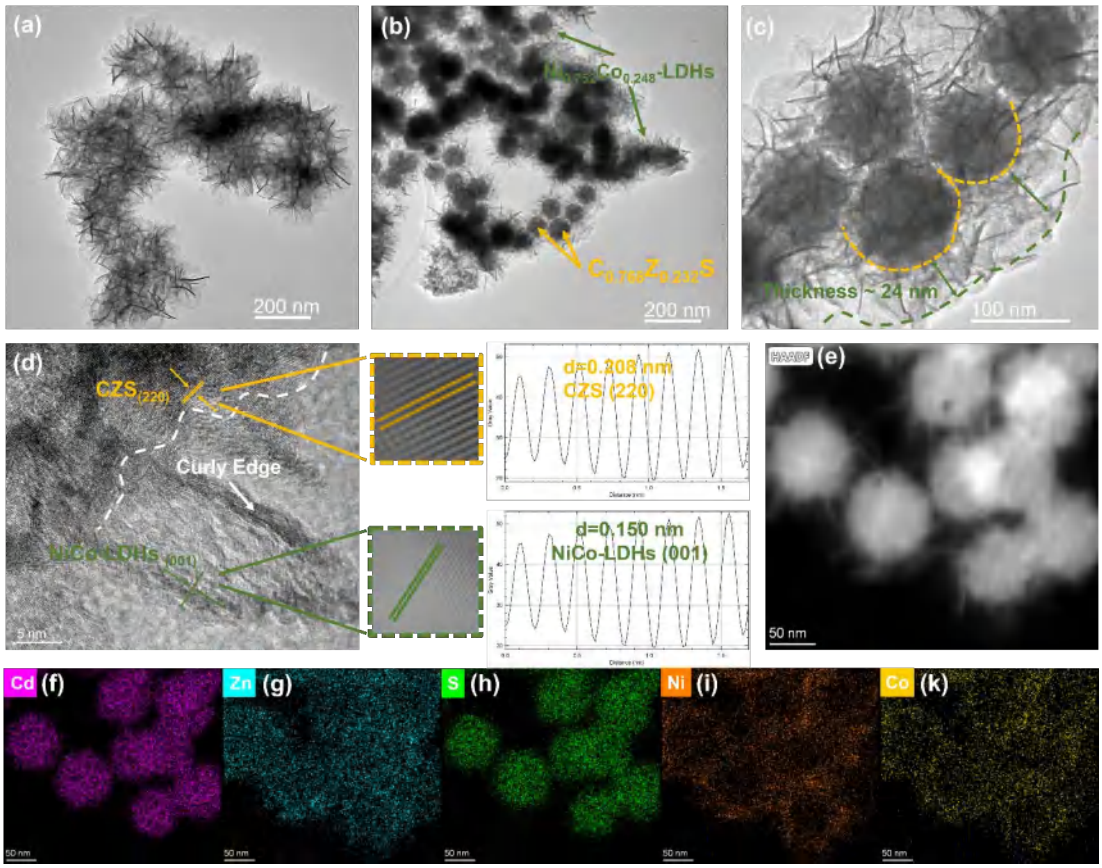

Fig. 6.4. TEM images of (a) NiCo-LDHs, CZS@NiCo-LDHs core-shell structure at (b) low and (c) high magnification, (d) HRTEM image of selected area (enlarged figure: inverse FFT image of corresponding CZS and NiCo-LDHs lattice spacing), (e) HADDF-STEM image and (f-k) corresponding EDS elemental mapping of Cd, S, Ni, Co and overlayed elements.

Such well-defined structure is also observed in CZS@Ni-LDHs sample but possessing thinner shell thickness (**Fig.6.5 c,d**). The CZS/NiCo-LDHs composites (**Fig.6.5 e,f**), however, exhibits random structure of a mixture of CZS semiconductor and LDHs. Such mixture causes a loose interfacial interaction between semiconductors and catalysts, which may further lead to poor electron transfer.

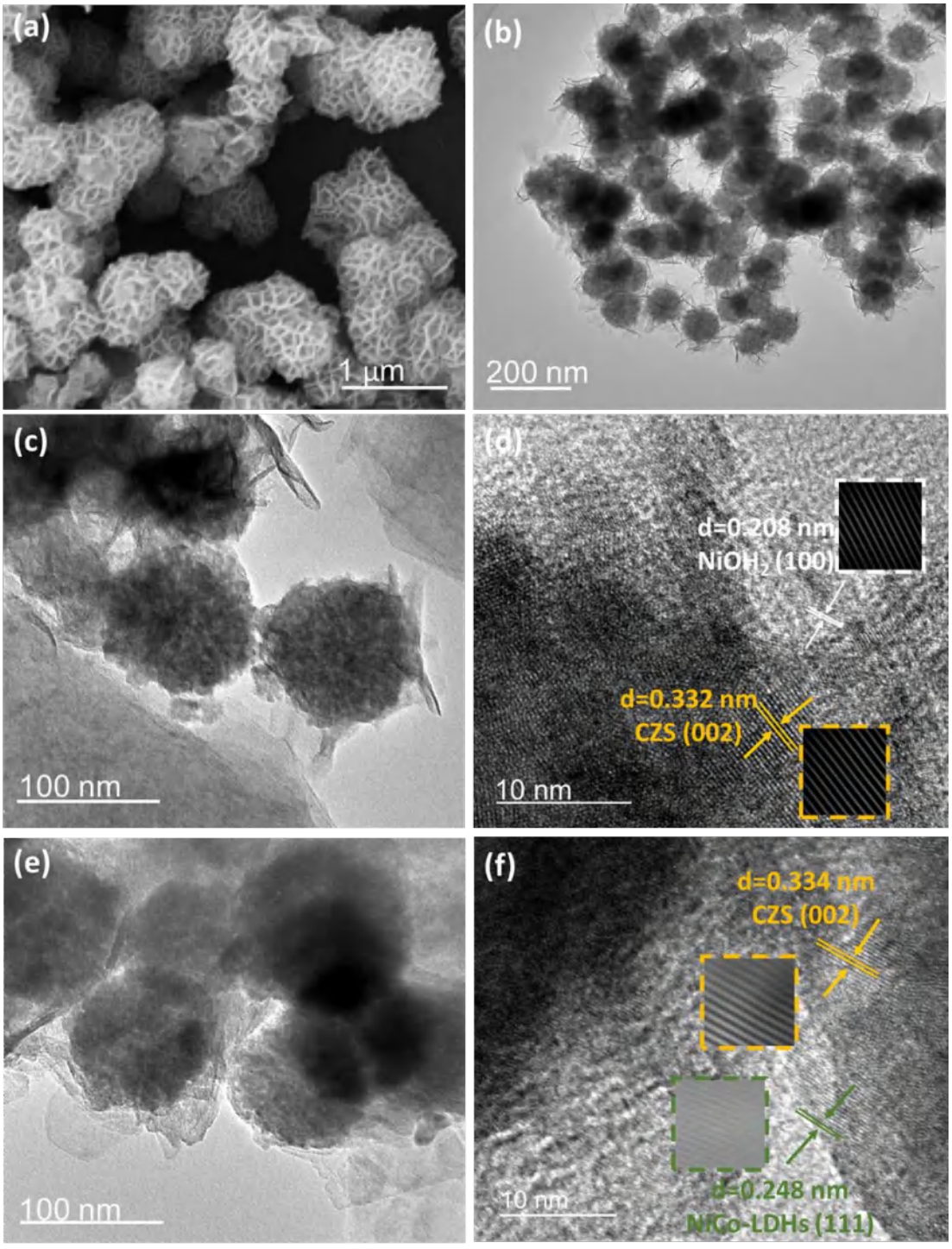

Fig. 6.5. SEM image of (a) pure NiCo-LDHs nanoflower; TEM image of (b) CZS@NiCo-LDHs sample; (c) CZS@Ni-LDHs and corresponding (d) HRTEM image (insert: inverse FFT image of CZS@Ni-LDHs); (e) TEM image and (f) HRTEM image of CZS/NiCo-LDHs composites (insert: inverse FFT image of composite).

XRD patterns (**Fig.6.7 a**) were recorded to investigate the crystal structures of each component. The XRD pattern of CZS shows a typical sphalerite diffraction pattern, where characteristic peaks of 26.5°, 43.9° and 52.2° are attributed to the cadmium zinc blende (111), (220), (311) lattice plane[84,229], respectively. After introducing Ni hydroxides and NiCo-LDHs into CZS system, new peaks representing β-$Ni(OH)_2$ (JPCDS: 14-0117) are observed at 19.1°, 32.9°, 39.4°, 51.8°, 58.8°, and 63.5°, correspondingly[88,230]. Notably, the incorporation of cobalt ions into Ni LDHs (NiCo-LDHs) results in a negative shift towards lower degree (~0.4°). This can be attributed that the introduction of cobalt ions leads to a larger lattice space. Moreover, according to the Bragg's law, the lattice spacing of this pure NiCo-LDHs is 0.46 nm along (001) plane. While in the core-shell sample, a clear shift of (001) plane by 0.25° was observed in NiCo-LDHs. This shift further denotes to an enlarged lattice plane of LDHs (0.47 nm) in core-shell structure, due to the mismatch of lattice and formation of strongly coupled interface. Additionally, two peaks at 34.3° and 38.5° are determined as β-$Co(OH)_2$ phase (JCPDS: 74-1057)[231]. Notably, the XRD pattern of the CZS@NiCo-LDHs sample demonstrates a significant decrease in the intensity of β-$Ni(OH)_2$ peaks, which can be attributed to the strongly coupled interfaces. More specifically, the LDHs in CZS@NiCo-LDHs are predominantly adhered to the CZS core surface in the form of thin layer, rather than being as separate entities in the composite sample (CZS/NiCo-LDHs). Raman spectrum (**Fig.6.6 a**) was then conducted to double confirm the chemical bonds in samples. The peak identified at 321.6 cm^{-1} and 623.1 cm^{-1} are recognized as 1 and 2nd plasmon-optical phono mode of CZS[232]. While peaks located at 529.8 cm^{-1} are recognized as Ni-O bonds in Ni hydroxides[233,234], which are in consistence with results from XRD pattern.

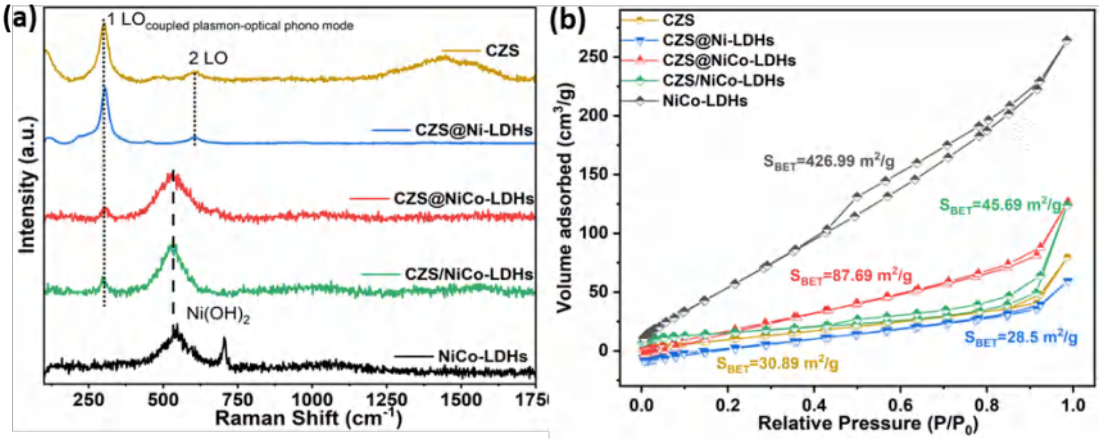

Fig. 6.6. (a) Raman spectra; (b) N_2 adsorption and desorption isotherms of CZS; CZS@Ni-LDHs; CZS@NiCo-LDHs; CZS/NiCo-LDHs and pure NiCo-LDHs.

The N_2 adsorption and desorption isotherms (**Fig.6.6 b**), followed by pore size distribution (**Fig.6.7 b**) analysis were employed to investigate the topography of various photocatalysts. The NiCo-LDHs synthesized in this work possessed a high BET surface area (S_{BET} = 426.99 m^2/g), originating from the macroscopical flower-like structure and periodic interlamellar space at microscale[235]. The core-shell sample (CZS@NiCo-LDHs) benefits from the high surface area of LDHs and a well-defined interface, which result in the highest surface area (S_{BET} = 87.69 m^2/g), compared to that of CZS@Ni-LDHs (S_{BET} = 28.5 m^2/g) and CZS/NiCo-LDHs (S_{BET} = 45.69 m^2/g). The property of high surface area, as a result, can facilitate the electrolyte diffusion in the core-shell sample. Notably, the original CZS nanosphere has a surface area of 30.89 m^2/g, which is likely due to the aggregation of Cd/Zn-S seed during synthesis and finally leads to the formation of micropores within the semiconductor. What's more, a clear hierarchical topology in pore size distribution is identified in CZS@NiCo-LDHs, where both micropores (r ~ 0.5 nm) and mesopores (r ~ 1.2nm) exist. Moreover, we also conduct the water contact angle analysis (**Fig.6.7 c**) by dispersing the powders onto the FTO glass. The original glass possesses a relative more hydrophobic surface (θ =

106.46°) compared with that of CZS powder covered surface (45.87°). After loading of CZS@NiCo-LDHs and pristine NiCo-LDHs, the contact angles further decrease to 40.32° and 41.51°, proving the hydrophilic structure of core-shell sample.

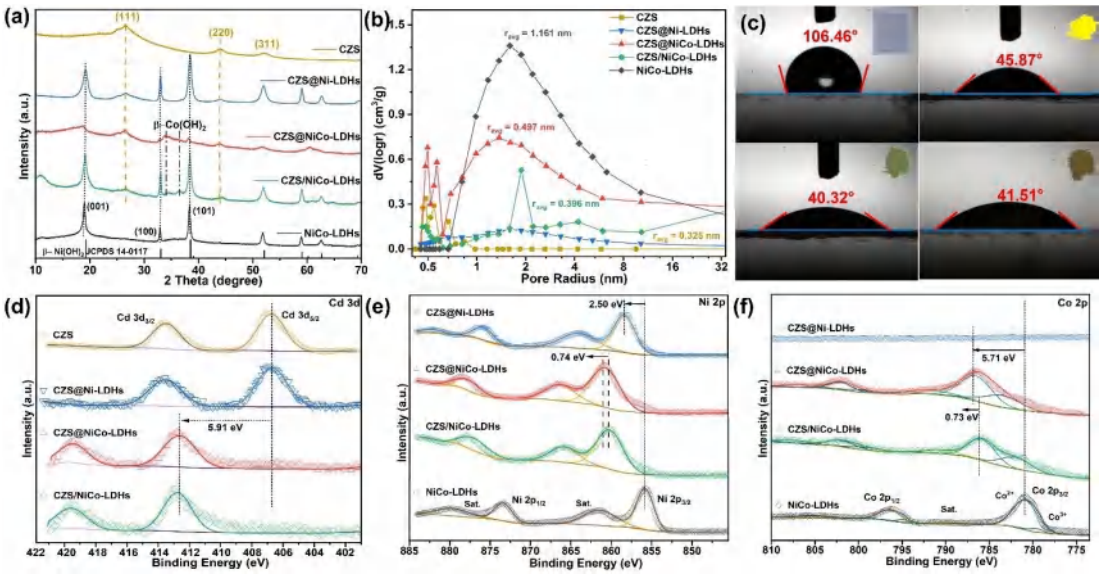

Fig. 6.7. (a) X-ray diffraction patterns, (b) Pore size distributions of CZS, CZS@NiCo-LDHs, NiCo-LDHs, CZS/NiCo-LDHs, and NiCo-LDHs; (c) Water contact angles of FTO glass substrate, CZS, CZS@NiCo-LDHs, NiCo-LDHs, CZS/NiCo-LDHs, and NiCo-LDHs; X-ray photoelectron spectroscopy of (d) Cd 3d, (e) Ni 2p, (f) Co 2p of corresponding samples.

XPS analysis was then conducted to investigate the surface chemical states, composition, proves the changes in Ni and cobalt electronic environment. It should be noted that XPS spectrum of Cd 3d (**Fig.6.7 d**) possess a significant positive shift (~5.91 eV) for both core-shell and composite samples, indicating a strong interfacial interaction. However, it is interesting that the signal of Zn 2p (**Fig.6.8 a**) for CZS@ Ni-LDHs and NiCo-LDHs decrease, compared with that of pristine CZS and composites. This weakening effect may be attributed to the fact that XPS is a surface sensitive technique with a resolution ~10nm. Meanwhile in the core-shell sample, the shell of

LDHs is up to 20 nm. In addition, a slight shift (~0.5 eV) towards higher binding energy is noticed, suggesting a weak interaction of Zn atom, compared to surface atoms. With respect to Ni and Co 2p spectrum, the deconvoluted peaks are assigned to the electron spin doublet and satellite. Specifically, peaks in NiCo-LDHs (**Fig.6.7 e-f**) located at 780.91 eV and 796.18 eV are attributed to Co $2p_{3/2}$ and $2p_{1/2}$, respectively[143,230]. The peaks observed at 855.89 eV and 873.37 eV are assigned to Ni $2p_{3/2}$ and $2p_{1/2}$, accordingly[236]. Additionally, Co^{3+} valence state (779.54 eV) is identified in Co 2p spectrum of pure NiCo-LDHs, while a shift towards higher binding energy is observed in core-shell (5.71 eV) and composite samples (4.98 eV). It should be noticed that Co^{2+} state is more stable than Co^{3+}, which requires more energy to excite the core-level electrons in Co^{3+} orbital. The ration between Co^{3+} and Co^{2+} in CZS@NiCo-LDHs is 0.53 and 0.59 for CZS/NiCo-LDHs, with similar oxidized Co^{2+} ions into LDHs frameworks. Furthermore, the negative shift (1.65 eV) of S 2p spectrum (**Fig.6.8 b**) towards lower binding energy is observed[127,129]. This corresponding movement in Co, Ni and S 2p spectrum indicates a strong interfacial interaction, compared with that of composites. Meanwhile, it can be deducted that the S atoms are the electron acceptor, due to the high electron affinity.

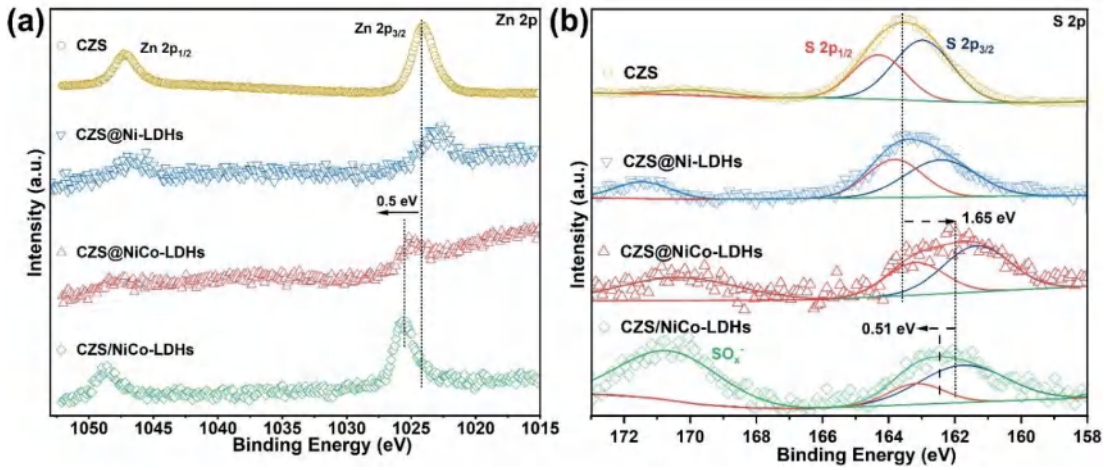

Fig. 6.8. (a)Zn 2p and (b) S 2p spectra of CZS; CZS@Ni-LDHs; CZS@NiCo-LDHs;

CZS/NiCo-LDHs and pure NiCo-LDHs.

6.3.3 Photocatalytic performance

The photocatalytic hydrogen evolution measurements of all samples were conducted under visible light region (λ>420 nm) using 10 v% TEOA aqueous solution as hole sacrificial agent and Eosin Y as dye sensitization system for pure NiCo-LDHs. As illustrated in **Fig.6.9 a**, the original CZS semiconductor exhibits low photocatalytic activity (1.31 mmol g^{-1} over 4 hrs), even though the adsorption region of CZS semiconductor lays under visible region. The low activity can be attributed to the limited catalytic sites on CZS surface. It has been reported that the (most possible active sites are Zn vacancies-V_{Zn}) [237]. Due to the dye sensitization system as visible light absorber[238], NiCo-LDHs shows surprisingly high PHE activity, which is beyond 10 mmol g^{-1} in 4 hrs irradiation. Nevertheless, H_2 accumulated evolution test of CZS@Ni-LDHs, CZS @NiCo-LDHs, and CZS/NiCo-LDHs compounds are 11.52 mmol g^{-1}, 69.85 mmol g^{-1} and 29.87 mmol g^{-1}, respectively. The PHE rate of each sample normalized to mass was summarized in **Fig.6.9 b**, which clearly shows the activity enhancement of core-shell samples. The PHE rate of CZS@NiCo-LDHs reaches to 18.75 mmol g^{-1} h^{-1}. Such outstanding catalytic performance is around 34 times better than pristine CZS system (0.42 mmol g^{-1} h^{-1}), 3 times higher than that of pure NiCo-LDHs (7.94 mmol h^{-1} g^{-1}). We also investigated the performance of $Ni(OH)_2$@CZS and NiCo-DLHs/CZS composites. The CZS/NiCo-LDHs shows a moderate PHE activity of 8.75 mmol h^{-1} g^{-1}, indicating that the electron-hole separation is insufficient. Moreover, the stability test of CZS@NiCo-LDHs shows a slight decrease in the accumulated amount of H_2 to 52.42 mmol h^{-1} g^{-1}, suggesting a superior electron transfer capability and abundant in active sites in the sample.

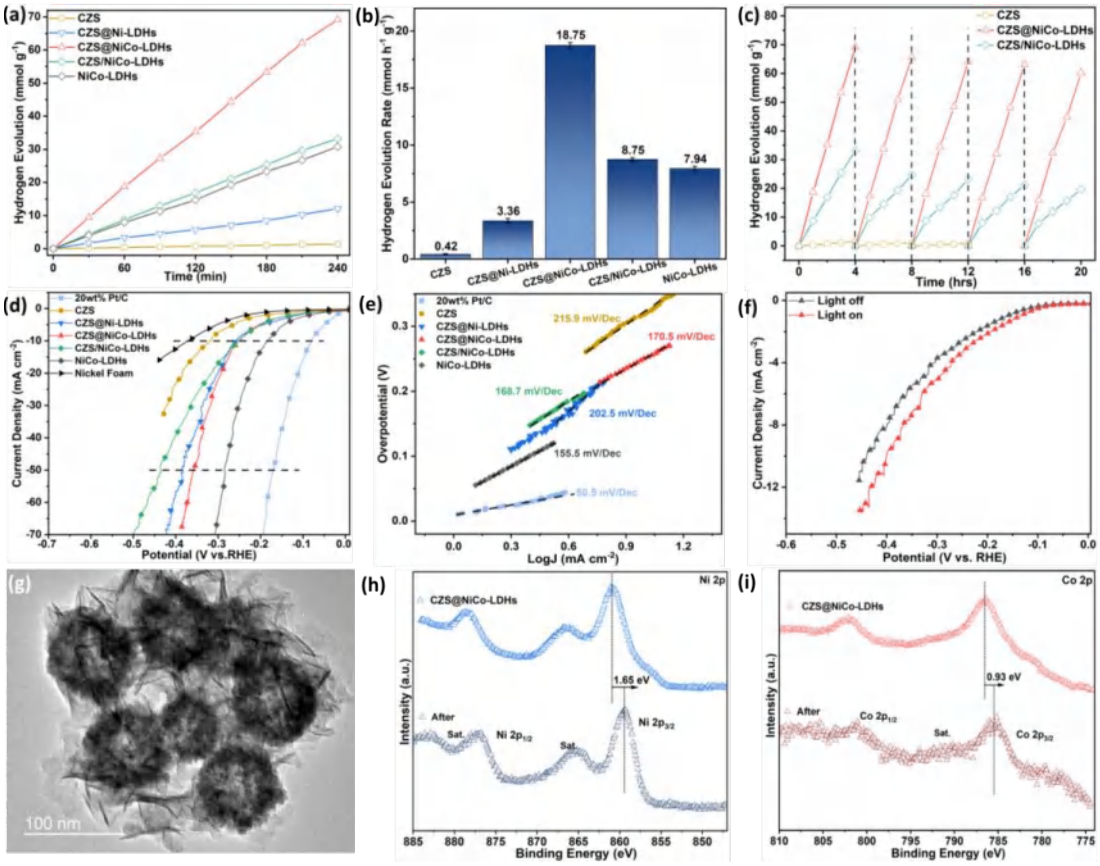

Fig. 6.9. (a) Time courses of photocatalytic H_2 evolution (PHE) and (b) PHE rate of CZS, CZS@Ni-LDHs, CZS@NiCo-LDHs, CZS/NiCo-LDHs, and NiCo-LDHs in 10 v% TEOA aqueous solution (note: Eosin Y sensitization is employed for pure NiCo-LDHs, which functions as semiconductor); (c) PHE stability test of CZS, CZS@NiCo-LDHs, and CZS/NiCo-LDHs over 12 hrs; (d) linear sweep voltammetry (5 mV/s), (e) Tafel slopes of commercial 20wt% Pt/C, CZS, CZS@Ni-LDHs, CZS@NiCo-LDHs, CZS/NiCo-LDHs, and NiCo-LDHs in 1_M KOH; (f) LSV curve of CZS@NiCo-LDHs on ITO substrate before and after light irradiation; (g) TEM; (h) Ni 2p; and (i) Co 2p spectra before and after PHE stability test.

Further electrochemical measurement (**Fig.6.9 d,e**) and analysis were conducted in typical three-electrode system. Not surprisingly, NiCo-LDHs as typical electrocatalysts requires lowest overpotential of 212.7 mV and 313.8 mV to reach 10 mA cm^{-2} and 50

mA cm^{-2}, respectively. Moreover, the low Tafel slope suggests the NiCo-LDHs possesses a faster proton adsorption, hydrogen desorption kinetics, compared with those samples coupled with semiconductor. However, it is noticed that compared with catalytic performance of commercial Pt/C, the NiCo-LDHs may experience post treatment to exhibit enhanced catalytic performance. Post TEM and XPS (**Fig.6.9 g-i** and **Fig.6.10 a-d**) analysis were conducted to examine the morphology distortion and electronic environment of samples after PHE cycle test.

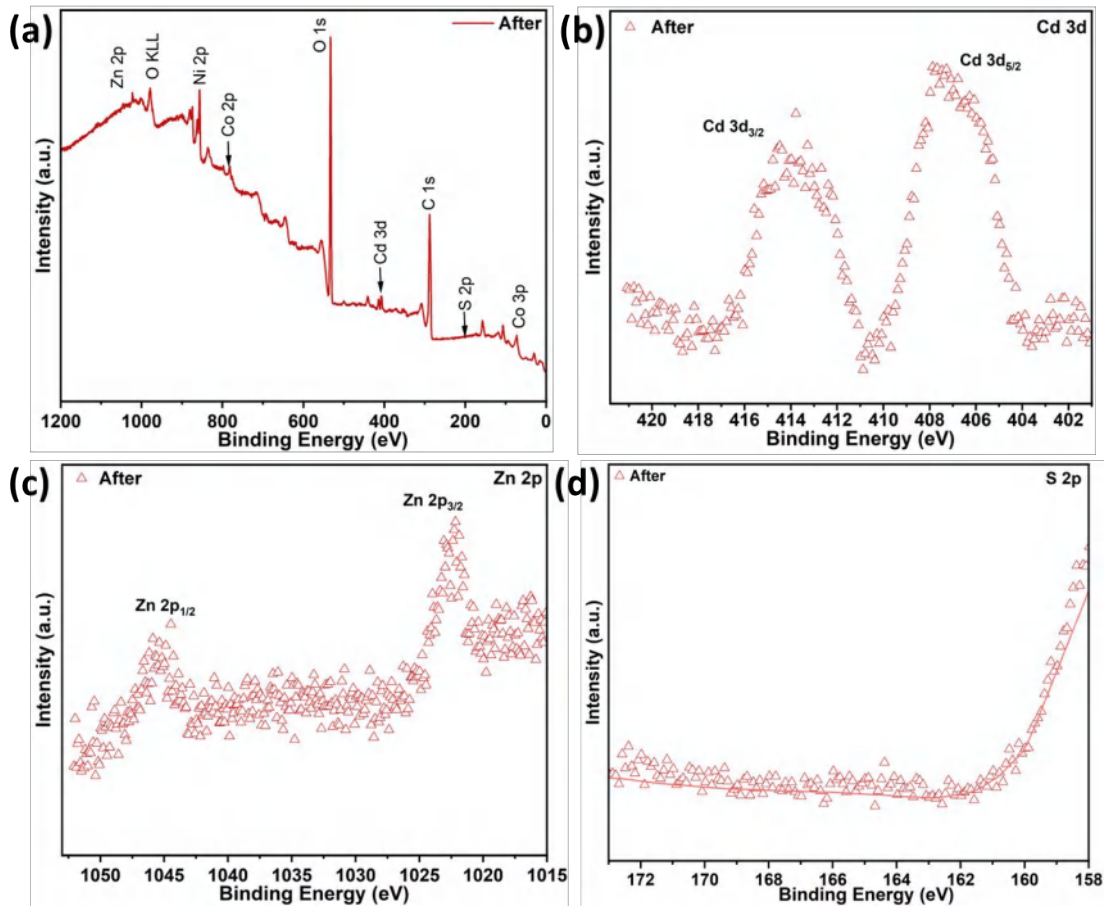

Fig. 6.10. (a) XPS survey, (b)Cd 3d spectrum, (c) Zn 2p spectrum, (d) S 2p spectrum of CZS@NiCo-LDHs after PHE stability test.

As indicated, the morphology of CZS@NiCo-LDHs maintains after 4 PHE cycles, with LDH shell and CZS nanospheres. It is further noticed that the photocorrosion still takes

place at the center of CZS core, leading to a hollow structure. This hollow structure has been reported to be the electron deficiency induced corrosion, due to the lack of efficiency in electron-hole separation of pristine CZS spheres. In comparison, the nanocomposite sample exhibits a morphological distortion (**Fig.6.11**) and separation between LDHs and CZS, indicating that the insufficient charge-hole separation causes the loss of catalytic efficacy.

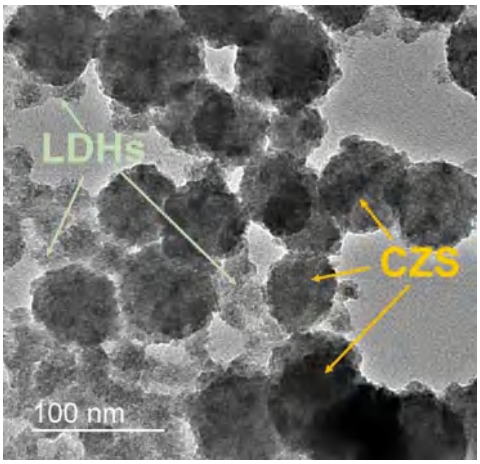

Fig. 6.11. Post TEM image of CZS/NiCo-LDHs composites after stability test.

From XPS results, the Ni and Co 2p spectrum shows little shift towards to lower binding energy slightly (1.65 eV and 0.93 eV, respectively). The Cd $3d_{5/2}$ and Zn $2p_{3/2}$ spectrum shift back to 407.08 eV and 1022.eV, respectively, suggesting the decrease in LDHs' thickness with improved XPS signal at CZS surface. Interestingly, the signals in S 2p spectrum of core-shell sample are rarely detected. This absence of S element, as reported[239,240], originates from the photooxidative dissolution of CZS particles by adopting the following equation:

$$CdZnS(s) + 2O_2 \xrightarrow{h\upsilon} Cd/Zn(aq)^{2+} + SO_4(aq)^{2-} \quad (1)$$

6.3.4 Optical and electrochemical study

The steady state photoluminescence spectrum was measured to investigate the photogenerated electron-hole pairs in CZS semiconductor, core-shell and composite

samples (**Fig.6.12 a**). The intensity of luminescence peaks is directly related to the carrier recombination capability. As indicated in excitation spectrum of CZS, we employed wavelength of 340 nm as incident light source, and all emission peaks are centered at ~ 480 nm. The original semiconductor possesses highest PL emission peak, followed by CZS/NiCo-LDHs and CZS@NiCo-LDHs. This decreasing trend indicates that most electrons and holes in CZS recombines. For core-shell samples, most photoinduced electrons are possibly transferred to LDHs, as well as the complete coverage of LDHs passive electron-hole recombination. Moreover, it is noticed that the PL peak of CZS@NiCo-LDHs exhibits triplet emission peaks at 471, 491 and 527 nm, accordingly. These emission peaks, originating from the emission peaks of intrinsic CZS, defects level of S and Zn[237,128,220], may arise from the post hydrothermal treatment, which are in consistent with literature[241]. Further time-resolved PL spectrum (**Fig.6.12 b**) indicates the lifetime of electrons in samples. The corresponding biexponential fitting illustrates the composition of each electron with acceptable χ^2(shown in the table). The extend τ_1 and τ_2 electron is related to the intrinsic properties of excited electrons/carriers. The τ_2 of CZS@NiCo-LDHs (3.807ns with a portion of 37.26%) and CZS/NiCo-LDHs (0.901ns with a portion of 49.46%) is significantly shorter than that of pristine CZS (4.049 ns with a portion of 82.55%), indicating a low fluorescence decay time of carries and possible transfer to cocatalysts. Meanwhile, τ_3 of core-shell samples (19.683 ns) exhibit obvious increases compared with that of composite sample (4.721 ns). This phenomenon suggests a sufficient electron-hole separation on the surface of core-shell sample[98], owing to the full coverage of LDHs and strongly coupled interface.

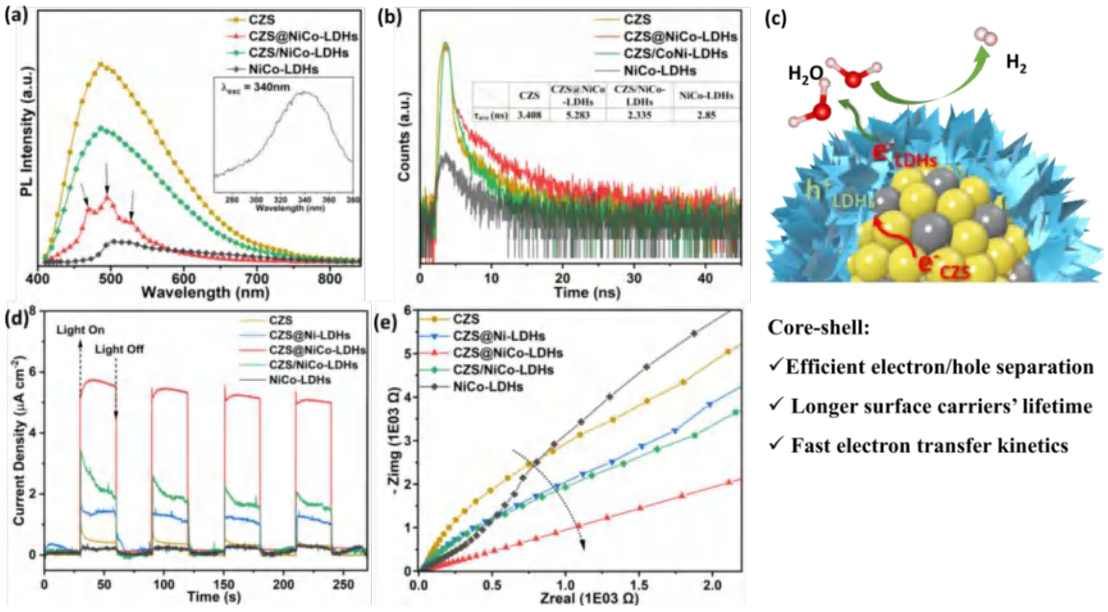

Fig. 6.12. (a) Photoluminescence (PL) spectra (insert: excitation spectrum of CZS, λ_{exc} = 340 nm), (b) Time-resolved PL decay spectra (insert table: summary of electron lifetime) of CZS, CZS@NiCo-LDHs and CZS/NiCo-LDHs; (c) Illustration of electron transfer pathways at interface; (d) Chopped i-t curves and (e) Electrochemical impedance spectrum (EIS) under illumination of CZS, CZS@Ni-LDHs, CZS@NiCo-LDHs, CZS/NiCo-LDHs in 0.1 M Na_2SO_4 (load 0.4 mg/cm^2).

Transient photocurrent response plot at open circuit potential under visible irradiation (**Fig.6.12 d**) was conducted to investigate the number of free electrons in samples, after irradiation which is directly related to PHE activity. In this case, all prepared samples possess an anodic current, proving the n-type characteristics of samples. Due to the server electron-hole recombination, CZS itself exhibits a low photocurrent (0.38 μA cm^{-2}). Such low photocurrent is also observed in pure NiCo-LDHs sample (0.25 μA cm^{-2}), which is originated from the low visible-light absorption. After loading $Ni(OH)_2$ and NiCo-LDHs onto CZS surface, the corresponding photocurrents indicate significant increase to 1.14 μA cm^{-2} and 5.05 μA cm^{-2}, respectively. Such enhancement can be

attributed to the fact that well-established interface leading more electrons transferred to electrode instead of recombination. Electrochemical impedance spectrum (**Fig.6.12 e**) was also measured under illumination, proving the interfacial charge transfer ability. As indicated, CZS, as typical semiconductor, shows poorest electron transfer kinetics. After incorporating the LDHs into CZS system, it should be noticed all transfer kinetics are improved to certain extent, owing to the established interface between CZS and LDHs, depended on the coverage. The CZS/NiCo-LDHs exhibited a significant larger semicircular arc than that of core-shell samples, indicating a larger charge transfer resistance. The CZS@NiCo-LDHs, as a result, possess an improved electron transfer resistance. This enhancement may be attributed to the abundant metal vacancies (V_{Zn}), which further promote the catalytic performance[237,242]. In a short summary (**Fig. 6.12 c**), the CZS@NiCo-LDHs exhibits an efficient electron-charge separation capacity, long lifetime of carries at LDHs surfaces, and improved electron transfer resistance.

6.3.5 Photocatalytic mechanism and simulation study

For in-depth analysis on the photocatalytic hydrogen evolution ability of each sample, the UV-vis DRS spectra were recorded. As shown in **Fig.6.14 a** CZS possesses a typical light-yellow color, while pure NiCo-LDHs exhibit a brown color. After loading/mixing LDHs on/with CZS, such yellow color turns to green with different shades. Consistent with this color change phenomenon, the spectrum of CZS show a typical absorption edge at 508 nm, lying under the visible light absorption region, which further suggests a band gap of 2.52eV for CZS sample. However, the pure NiCo-LDHs indicate an enhanced visible light absorption capability, with low capacity in visible region. Meanwhile, for both core-shell and composites, enhancement of absorption in visible light region is observed, whose band gap is calculated to be 2.28 eV and 2.55 eV,

respectively.

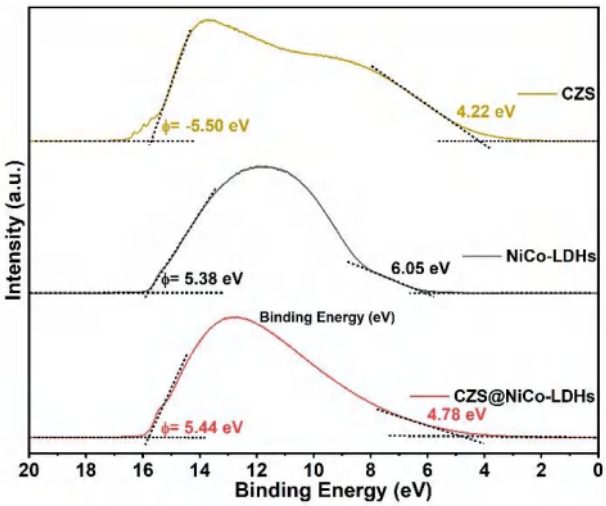

Fig. 6.13 UPS spectrum of CZS, NiCo-LDHs, and CZS@NiCo-LDHs.

Based on above optical measurement, further Valence-band XPS (**Fig.6.14 c**), UPS measurements (**Fig.6.13**) were conducted to identify the potential heterojunction between CZS and NiCo-LDHs. As indicated in Fig.6 d, the pristine CZS and NiCo-LDHs show an overlay in the band gap region, which will induce an electric field after the construction of interface. This heterojunction further contributes to a direct Z-scheme heterojunction, where the excited electrons in semiconductor will consume the holes remained in the valence band of NiCo-LDHs. Consequently, electrons at conduction band of NiCo-LDHs will facilitate the PHE reaction. Moreover, Mott-Schottky measurement at different frequencies was conducted to explore the band alignment, related to water splitting reaction potential. As indicated (**Fig.6.14 e**), the band structure of CZS@NiCo-LDHs exhibits a suitable region for both water reduction (0 V) and oxidation process (1.23 V).

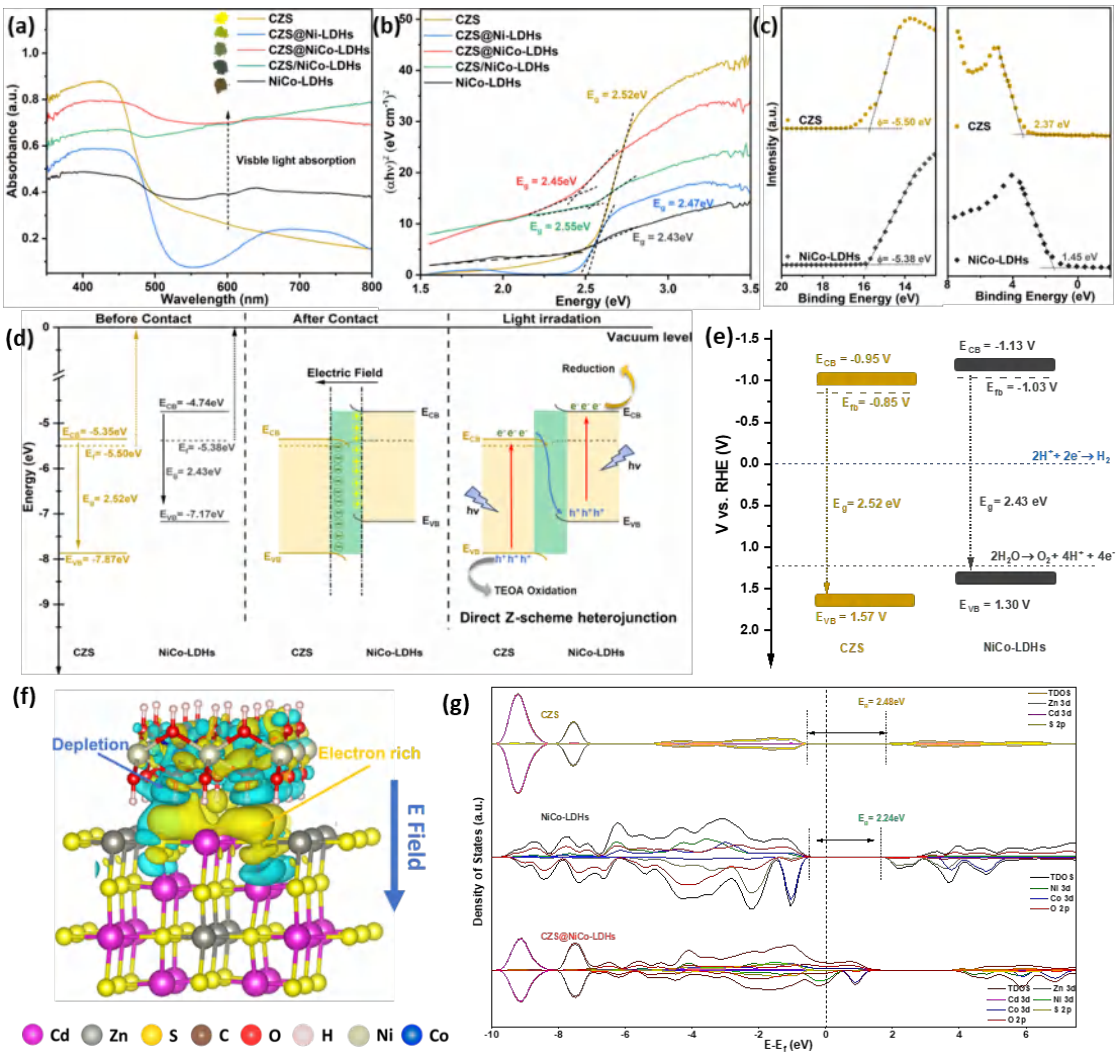

Fig. 6.14. (a) UV-visible absorption spectra, (b) Tauc plots of CZS, CZS@Ni-LDHs, CZS@NiCo-LDHs, CZS/NiCo-LDHs and NiCo-LDHs; (c) UPS and VB-XPS spectrum of CZS, NiCo-LDHs and CZS@NiCo-LDHs; (d) Band alignment between CZS and NiCo-LDHs under different conditions; (e) Band alignment of CZS and NiCo-LDHs, related to water splitting potentials; (f) Charge density plot and (g) Density of states of CZS, CZS@NiCo-LDHs and NiCo-LDHs.

Charge density difference plot (**Fig.6 14 f**) of CZS/NiCo-LDHs heterostructure indicates that S atoms are the electron rich region, whereas Co and Ni atoms are electron depletion region. This charge difference is in consistent with XPS results, where a

negative shift of S 2p spectrum to lower binding energy. Moreover, density of states plots of CZS, NiCo-LDHs and heterostructure indicate that more electrons are accumulated at the Fermi level of heterostructure, compared with the others. This accumulation suggests an improved electron conductivity through the interface. Density of states plot was then calculated to investigate the electron distribution after the construction of heterostructure. As indicated in **Fig.6.14 g**, CZS possesses a bang gap of 2.48 eV, close to the measured UV-vis spectrum results. After constructing the heterostructure, an increase in the electron density at the Fermi level can be observed, suggesting an improved electron conductivity. Such improvement contributes to better electron transport at interface, leading to an enhanced catalytic performance.

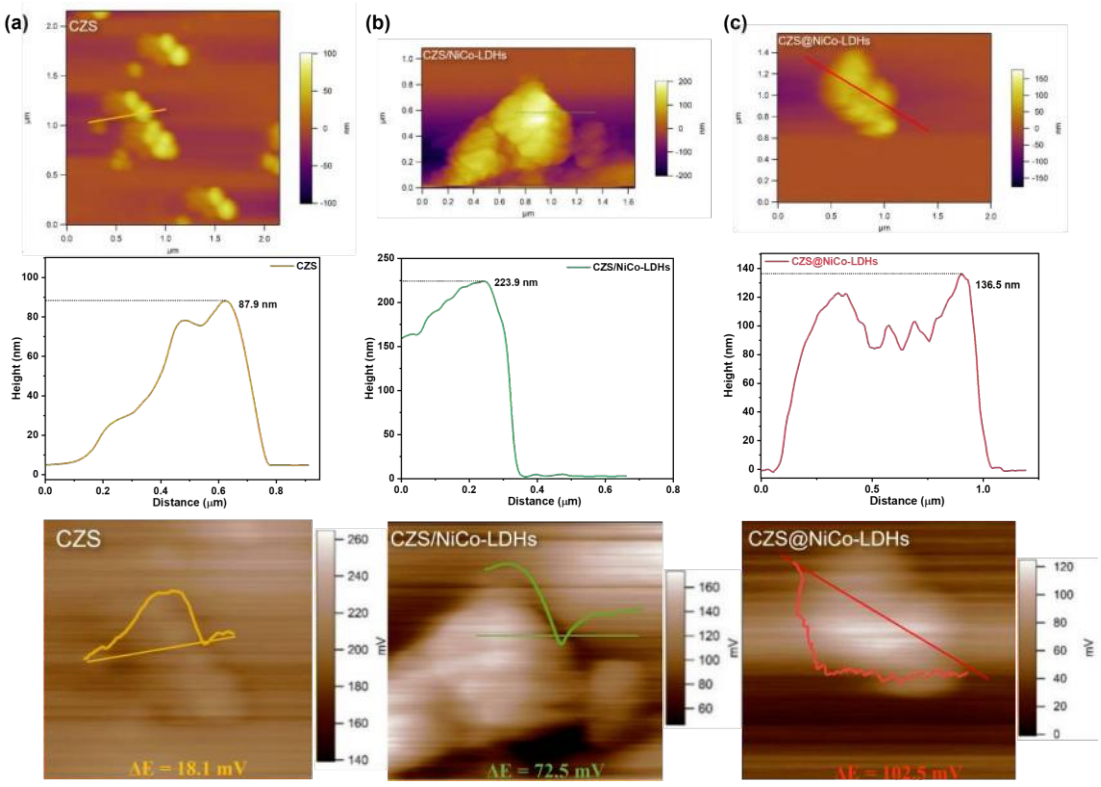

Fig. 6.15. AFM height profiles and corresponding kelvin-probe force microscopy of (a) CZS, (b) CZS/NiCo-LDHs, and (c) CZS@NiCo-LDHs.

To further evaluate the predicted electric field in charge density plot, we employed KPFM to measure the surface potential of pristine CdZnS, composite and core-shell samples. The as-measured potential, known as built-in electric field, greatly influences the charge-hole separation, and surface carrier time. As indicated in the AFM height profile (**Fig.6.15 a-c**), the height of CZS, CZS/NiCo-LDHs, and CZS@NiCo-LDHs are 87.9 nm, 223.9nm and 135.5 nm, respectively, which are consistent with those results from TEM images. Subsequent kelvin-probe measured surface suggest CZS@NiCo-LDHs exhibits highest potential (102.5 mV), indicating the strongest built-in electric effect. Both Zeta potential measurements and KPFM results (**Fig. 6.16**) confirms that the interface construction promotes a built-in electric field effect, which further facilitates the catalytic performance.

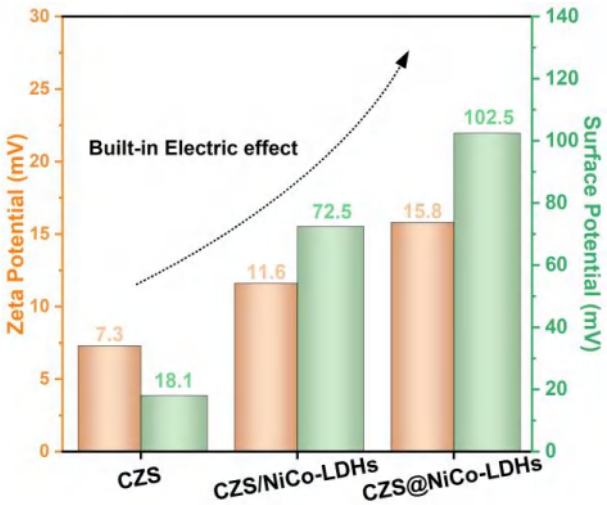

Fig. 6.16. Comparison between Zeta potentials and Kelvin probe measured surface potentials of CZS, CZS/NiCo-LDHs, and CZS@NiCo-LDHs.

6.4 Chapter conclusion

To conclude, a novel surface modification strategy based on cadmium zinc sulfide system was proposed by taking advantage of small molecules with strong metal-affinity.

The changes in surface micro-environment were identified and contributed to the full coverage of CZS by NiCo-layered double hydroxides. This heterostructure, which was further determined to be direct Z-scheme heterojunction, possessed an efficient charge-hole separation capability, longer surface carriers' lifetime, and faster electron transfer kinetics. Optical measurements and the Mott-Schottky plot again confirmed that suitable alignment existed between CZS and NiCo-LDHs, where excited electrons of CZS will consume the holes at the valence band left in NiCo-LDHs.

As a result, the obtained CZS@NiCo-LDHs exhibited a favorable catalytic performance (18.75 mmol $g^{-1}h^{-1}$) and good stability (5 cycles, 20hrs) for visible-light driven PHE reaction. DFT simulations and KPFM measurements suggested that a built-in electric field existed after constructing CZS@NiCo-LDHs core-shell samples. Meanwhile, an electron redistribution and improvement in electron conductivity can be identified in the samples. This idea inspired from the interfacial engineering and surface electronic environment modification, provides a new basis for further design of cocatalysts with distinguished heterojunctions.

Chapter 7. Conclusions and suggestions for future research

7.1 Conclusions

In this thesis, the cobalt oxides/sulfides/hydroxides electro/photocatalysts were investigated in water splitting reaction. To improve the catalytic performance and stability of catalysts, strategies including hetero-atom doping, micro-mesoporous system construction, carbon protective shell formation, and heterojunction design have been conducted. Moreover, a wearable moisture digester device was designed and developed.

The PVP polymers in MOFs contributed to the formation of carbon protective shells, which led to the heteroatom doping during phosphine treatments. Moreover, post treatments of phosphine treated CoOx/NCs revealed the role of synergistic effect between metallic Co^0 and Co^{2+} for HER, Co^{2+} and Co^{3+} for OER. Similarly, the P doping into activated carbons derived from wool fiber skeleton, significantly influenced the electronic environment of Co_9S_8, where electrons at Co sites are transferred to P sites. Such doping strategy lowered down the energy barrier and further facilitated the water splitting reaction. For cobalt hydroxides-based core-shell samples, the direct Z-scheme was identified in NiCo-LDHs/CZS heterostructure, by optical measurements. Meanwhile, from DFT simulations, the Co atoms in NiCo-LDHs, functioning as active sites for HER, further facilitated photocatalytic hydrogen evolution reaction. Apart from the electro/photocatalysts, a personalized and wearable device, based on above Co_9S_8 electrocatalysts has been designed and fabricated to consume the moisture, for the first time. This device provided a prototype of downsizing electrocatalytic splitting

reactor, which shows potentials in personalized application.

In summary, three catalysts including cobalt oxides, cobalt sulfide, and cobalt layered double hydroxides were successfully prepared from different precursors (either inorganic or organic templates) and utilized in the electro/photocatalytic water splitting reactions. The strategy of heteroatom doping into the protective carbon shell was found to be an effective approach to tune both CoOx and Co_9S_8 electronic environment. Meanwhile, the natural sulfur elements in protein were utilized for the preparation of cobalt sulfide electrocatalysts for the first time. Post strategies including acid treatments and pore system construction were adopted to identify the true active sites and improve the catalytic performance. These works not only shed light on the understanding of intrinsic properties of cobalt tetrahedral and octahedral sites (CoOx, Co_9S_8 and Co hydroxides-based catalysts) in water splitting reaction, but also provide strategy to customize the electrolyzer for wearable application.

7.2 Suggestions for future research

This thesis demonstrated three cobalt based electro/photocatalysts, and one application in wearable device. Although cobalt oxides, sulfides and layered double hydroxides have been prepared and studied, detailed analysis and further developments of these systems need to be done in the future. For example:

(1) Understanding reaction pathway at the molecular level is far beyond satisfaction. DFT simulations are considered to identify the active sites for reactions, the real-time monitoring of intermediate species is rarely conducted. This lack of monitoring may ignore some key reaction species, which can be further works.

(2) Although all as-obtained catalysts exhibit favorable catalytic performance, they are still in the lab level (e.g. hydrothermal synthesis, tube furnace carbonization). The exploration of repeatable, scalable synthetic methods is still under pursing.

(3) The long-time stability is another key indicator in all photo/electrocatalysts. This target is real dependent on the design, and structural information of catalysts, due to the possible structural evolution under harsh photo/electrochemical conditions. Further works can be explored to characterize the structural information (e.g. coordinative environment, valence states of active sties) of catalysts by techniques such as EXFAS.

Due to the appeal of carbon neutralization across the world, research that utilize solar energy and electricity have also been conducted in the carbon dioxide photo/electrochemical reduction reaction. Consequently, not only the generation of green hydrogen and oxygen is of significance, the electrochemical carbon dioxide reduction (CO_2ER) to C_2, C_3 products (e.g. alcohol, propanol) also show attractive research interests as well as industrial applications.

Chapter 8. References

(1) Luo, Y.; Li, X.; Cai, X.; Zou, X.; Kang, F.; Cheng, H. M.; Liu, B. Two-Dimensional MoS2 Confined Co(OH)2 Electrocatalysts for Hydrogen Evolution in Alkaline Electrolytes. *ACS Nano* **2018**, *12* (5), 4565–4573. https://doi.org/10.1021/acsnano.8b00942.

(2) Wang, F.; Hu, L.; Liu, R.; Yang, H.; Xiong, T.; Mao, Y.; Balogun, M. S.; Ouyang, G.; Tong, Y. Hybrid Implanted Hybrid Hollow Nanocube Electrocatalyst Facilitates Efficient Hydrogen Evolution Activity. *J. Mater. Chem. A* **2019**, *7* (18), 11150–11159. https://doi.org/10.1039/c9ta00931k.

(3) Ji, Y.; Yang, L.; Ren, X.; Cui, G.; Xiong, X.; Sun, X. Nanoporous CoP 3 Nanowire Array: Acid Etching Preparation and Application as a Highly Active Electrocatalyst for the Hydrogen Evolution Reaction in Alkaline Solution. **2018**, 8–11. https://doi.org/10.1021/acssuschemeng.8b01714.

(4) Yao, N.; Li, P.; Zhou, Z.; Meng, R.; Cheng, G.; Luo, W. Nitrogen Engineering on 3D Dandelion-Flower-Like CoS2 for High-Performance Overall Water Splitting. *Small* **2019**, *15* (31), 1–9. https://doi.org/10.1002/smll.201901993.

(5) Zhao, S.; Tan, C.; He, C. T.; An, P.; Xie, F.; Jiang, S.; Zhu, Y.; Wu, K. H.; Zhang, B.; Li, H.; Zhang, J.; Chen, Y.; Liu, S.; Dong, J.; Tang, Z. Structural Transformation of Highly Active Metal–Organic Framework Electrocatalysts during the Oxygen Evolution Reaction. *Nat. Energy* **2020**, *5* (November). https://doi.org/10.1038/s41560-020-00709-1.

(6) Wang, Q.; Astruc, D. State of the Art and Prospects in Metal-Organic Framework (MOF)-Based and MOF-Derived Nanocatalysis. *Chem. Rev.* **2019**. https://doi.org/10.1021/acs.chemrev.9b00223.

(7) Ma, S.; Sadakiyo, M.; Heim, M.; Luo, R.; Haasch, R. T.; Gold, J. I.; Yamauchi, M.; Kenis, P. J. A. Electroreduction of Carbon Dioxide to Hydrocarbons Using Bimetallic Cu-Pd Catalysts with Different Mixing Patterns. *J. Am. Chem. Soc.* **2017**, *139* (1), 47–50. https://doi.org/10.1021/jacs.6b10740.

(8) Zhou, T.; Xu, W.; Zhang, N.; Du, Z.; Zhong, C.; Yan, W.; Ju, H.; Chu, W.; Jiang, H.; Wu, C.; Xie, Y. Ultrathin Cobalt Oxide Layers as Electrocatalysts for High-Performance Flexible Zn–Air Batteries. *Adv. Mater.* **2019**, *31* (15), 1–8. https://doi.org/10.1002/adma.201807468.

(9) She, Z. W.; Kibsgaard, J.; Dickens, C. F.; Chorkendorff, I.; Nørskov, J. K.; Jaramillo, T. F. Combining Theory and Experiment in Electrocatalysis: Insights into Materials Design. *Science (80-.).* **2017**, *355* (6321). https://doi.org/10.1126/science.aad4998.

(10) Gong, L.; Zhang, D.; Lin, C. Y.; Zhu, Y.; Shen, Y.; Zhang, J.; Han, X.; Zhang, L.; Xia, Z. Catalytic Mechanisms and Design Principles for Single-Atom Catalysts in Highly Efficient CO2 Conversion. *Adv. Energy Mater.* **2019**, *1902625*, 1–9. https://doi.org/10.1002/aenm.201902625.

(11) Hu, Y.; Luo, G.; Wang, L.; Liu, X.; Qu, Y.; Zhou, Y.; Zhou, F.; Li, Z.; Li, Y.; Yao, T.; Xiong, C.; Yang, B.; Yu, Z.; Wu, Y. Single Ru Atoms Stabilized by Hybrid Amorphous / Crystalline FeCoNi Layered Double Hydroxide for Ultraefficient Oxygen Evolution. **2020**, *2002816*, 1–8. https://doi.org/10.1002/aenm.202002816.

(12) Zhao, X.; Pachfule, P.; Li, S.; Simke, J. R. J.; Schmidt, J.; Thomas, A. Bifunctional Electrocatalysts for Overall Water Splitting from an Iron/Nickel-

Based Bimetallic Metal–Organic Framework/Dicyandiamide Composite. *Angew. Chemie - Int. Ed.* **2018**, *57* (29), 8921–8926. https://doi.org/10.1002/anie.201803136.

(13) Zheng, Y. R.; Vernieres, J.; Wang, Z.; Zhang, K.; Hochfilzer, D.; Krempl, K.; Liao, T. W.; Presel, F.; Altantzis, T.; Fatermans, J.; Scott, S. B.; Secher, N. M.; Moon, C.; Liu, P.; Bals, S.; Van Aert, S.; Cao, A.; Anand, M.; Nørskov, J. K.; Kibsgaard, J.; Chorkendorff, I. Monitoring Oxygen Production on Mass-Selected Iridium–Tantalum Oxide Electrocatalysts. *Nat. Energy* **2021**. https://doi.org/10.1038/s41560-021-00948-w.

(14) Hochfilzer, D.; Chorkendorff, I.; Kibsgaard, J. Catalyst Stability Considerations for Electrochemical Energy Conversion with Non-Noble Metals: Do We Measure on What We Synthesized? *ACS Energy Lett.* **2023**, *8* (3), 1607–1612. https://doi.org/10.1021/acsenergylett.3c00021.

(15) Andersen, S. Z.; Čolić, V.; Yang, S.; Schwalbe, J. A.; Nielander, A. C.; McEnaney, J. M.; Enemark-Rasmussen, K.; Baker, J. G.; Singh, A. R.; Rohr, B. A.; Statt, M. J.; Blair, S. J.; Mezzavilla, S.; Kibsgaard, J.; Vesborg, P. C. K.; Cargnello, M.; Bent, S. F.; Jaramillo, T. F.; Stephens, I. E. L.; Nørskov, J. K.; Chorkendorff, I. A Rigorous Electrochemical Ammonia Synthesis Protocol with Quantitative Isotope Measurements. *Nature* **2019**, *570* (7762), 504–508. https://doi.org/10.1038/s41586-019-1260-x.

(16) Zhang, W.; Arramel, A.; Wong, P. K. J.; Zhang, L.; Zheng, J.; Zhang, W.; Zhang, H.; Yan, X.; Qi, J.; Li, J. Core-Shell Hybrid Zeolitic Imidazolate Framework-Derived Hierarchical Carbon for Capacitive Deionization. *J. Mater. Chem. A* **2020**, *8* (29), 14653–14660. https://doi.org/10.1039/d0ta05709f.

(17) Zhu, H.; Gao, G.; Du, M.; Zhou, J.; Wang, K.; Wu, W.; Chen, X.; Li, Y.; Ma, P.; Dong, W.; Duan, F.; Chen, M.; Wu, G.; Wu, J.; Yang, H.; Guo, S. Atomic-Scale Core/Shell Structure Engineering Induces Precise Tensile Strain to Boost Hydrogen Evolution Catalysis. *Adv. Mater.* **2018**, *30* (26), 1–9. https://doi.org/10.1002/adma.201707301.

(18) Dubouis, N.; Grimaud, A. The Hydrogen Evolution Reaction: From Material to Interfacial Descriptors. *Chem. Sci.* **2019**, *10* (40), 9165–9181. https://doi.org/10.1039/c9sc03831k.

(19) Simon, T.; Bouchonville, N.; Berr, M. J.; Vaneski, A.; Adrovic, A.; Volbers, D.; Wyrwich, R.; Döblinger, M.; Susha, A. S.; Rogach, A. L.; Jäckel, F.; Stolarczyk, J. K.; Feldmann, J. Redox Shuttle Mechanism Enhances Photocatalytic H2 Generation on Ni-Decorated CdS Nanorods. *Nat. Mater.* **2014**, *13* (11), 1013–1018. https://doi.org/10.1038/NMAT4049.

(20) Lee, J.; Kim, C.; Choi, K. S.; Seo, J.; Choi, Y.; Choi, W.; Kim, Y. M.; Jeong, H. Y.; Lee, J. H.; Kim, G.; Park, H. In-Situ Coalesced Vacancies on MoSe2 Mimicking Noble Metal: Unprecedented Tafel Reaction in Hydrogen Evolution. *Nano Energy* **2019**, *63* (April). https://doi.org/10.1016/j.nanoen.2019.06.042.

(21) Xiao, P.; Sk, M. A.; Thia, L.; Ge, X.; Lim, R. J.; Wang, J. Y.; Lim, K. H.; Wang, X. Molybdenum Phosphide as an Efficient Electrocatalyst for the Hydrogen Evolution Reaction. *Energy Environ. Sci.* **2014**, *7* (8), 2624–2629. https://doi.org/10.1039/c4ee00957f.

(22) Yang, J.; Xiao, Y.; Zhao, Q.; Zhang, G.; Wang, R.; Teng, G.; Chen, X.; Weng, M.; He, D.; Mu, S.; Lin, Y.; Pan, F. Synergistic Effect of Charge Transfer and Short H-Bonding on Nanocatalyst Surface for Efficient Oxygen Evolution Reaction. *Nano Energy* **2019**, *59* (January), 443–452. https://doi.org/10.1016/j.nanoen.2019.02.053.

(23) Zhang, X.; Yu, X.; Zhang, L.; Zhou, F.; Liang, Y.; Wang, R. Molybdenum Phosphide/Carbon Nanotube Hybrids as PH-Universal Electrocatalysts for Hydrogen Evolution Reaction. *Adv. Funct. Mater.* **2018**, *28* (16), 1–8. https://doi.org/10.1002/adfm.201706523.

(24) Wang, S.; Zhang, J.; Gharbi, O.; Vivier, V.; Gao, M.; Orazem, M. E. Electrochemical Impedance Spectroscopy. *Nat. Rev. Methods Prim.* **2021**, *1* (1). https://doi.org/10.1038/s43586-021-00039-w.

(25) Kibria, M. G.; Edwards, J. P.; Gabardo, C. M.; Dinh, C. T.; Seifitokaldani, A.; Sinton, D.; Sargent, E. H.; Kibria, G.; Edwards, J. P.; Gabardo, C. M.; Dinh, C. T.; Seifitokaldani, A.; Sinton, D.; Sargent, E. H. Electrochemical CO 2 Reduction into Chemical Feedstocks : From Mechanistic Electrocatalysis Models to System Design. *Adv. Mater.* **2019**, *1807166* (31), 1–24. https://doi.org/10.1002/adma.201807166.

(26) Wu, H.; Huang, Q.; Shi, Y.; Chang, J.; Lu, S. Electrocatalytic Water Splitting : Mechanism and Electrocatalyst Design. *Nano Res.* **2023**.

(27) Conway, B. E.; Tilak, B. V. Interfacial Processes Involving Electrocatalytic Evolution and Oxidation of H2, and the Role of Chemisorbed H. *Electrochim. Acta* **2002**, *47* (22–23), 3571–3594. https://doi.org/10.1016/S0013-4686(02)00329-8.

(28) Jeong, H. M.; Kwon, Y.; Won, J. H.; Lum, Y.; Cheng, M. J.; Kim, K. H.; Head-Gordon, M.; Kang, J. K. Atomic-Scale Spacing between Copper Facets for the Electrochemical Reduction of Carbon Dioxide. *Adv. Energy Mater.* **2020**, *1903423*, 1–12. https://doi.org/10.1002/aenm.201903423.

(29) Voiry, D.; Shin, H. S.; Loh, K. P.; Chhowalla, M. Low-Dimensional Catalysts for Hydrogen Evolution and CO2 Reduction. *Nat. Rev. Chem.* **2018**, *2* (1). https://doi.org/10.1038/s41570-017-0105.

(30) Pomerantseva, E.; Bonaccorso, F.; Feng, X.; Cui, Y.; Gogotsi, Y. Energy Storage: The Future Enabled by Nanomaterials. *Science* **2019**, *366* (6468). https://doi.org/10.1126/science.aan8285.

(31) Tang, J.; Salunkhe, R. R.; Liu, J.; Torad, N. L.; Imura, M.; Furukawa, S.; Yamauchi, Y. Thermal Conversion of Core-Shell Metal-Organic Frameworks: A New Method for Selectively Functionalized Nanoporous Hybrid Carbon. *J. Am. Chem. Soc.* **2015**, *137* (4), 1572–1580. https://doi.org/10.1021/ja511539a.

(32) Cherevko, S.; Geiger, S.; Kasian, O.; Kulyk, N.; Grote, J. P.; Savan, A.; Shrestha, B. R.; Merzlikin, S.; Breitbach, B.; Ludwig, A.; Mayrhofer, K. J. J. Oxygen and Hydrogen Evolution Reactions on Ru, RuO2, Ir, and IrO2 Thin Film Electrodes in Acidic and Alkaline Electrolytes: A Comparative Study on Activity and Stability. *Catal. Today* **2016**, *262*, 170–180. https://doi.org/10.1016/j.cattod.2015.08.014.

(33) Hahn, C.; Hatsukade, T.; Kim, Y. G.; Vailionis, A.; Baricuatro, J. H.; Higgins, D. C.; Nitopi, S. A.; Soriaga, M. P.; Jaramillo, T. F. Engineering Cu Surfaces for the Electrocatalytic Conversion of CO2: Controlling Selectivity toward Oxygenates and Hydrocarbons. *Proc. Natl. Acad. Sci. U. S. A.* **2017**, *114* (23), 5918–5923. https://doi.org/10.1073/pnas.1618935114.

(34) Li, C. W.; Ciston, J.; Kanan, M. W. Electroreduction of Carbon Monoxide to Liquid Fuel on Oxide-Derived Nanocrystalline Copper. *Nature* **2014**, *508* (7497), 504–507. https://doi.org/10.1038/nature13249.

(35) Ni, W.; Li, C.; Zang, X.; Xu, M.; Huo, S.; Liu, M.; Yang, Z.; Yan, Y. M. Efficient Electrocatalytic Reduction of CO2 on CuxO Decorated Graphene Oxides: An Insight into the Role of Multivalent Cu in Selectivity and Durability. *Appl. Catal.*

B Environ. **2019**, *259* (January). https://doi.org/10.1016/j.apcatb.2019.118044.
(36) Zhao, C.; Gao, Y.; Zhang, Z.; Ma, D. Functions of Phytic Acid in Fabricating Metal-Free Carbocatalyst for Oxidative Coupling of Benzylamines†. *Chinese J. Chem.* **2020**, *38* (11), 1292–1298. https://doi.org/10.1002/cjoc.202000145.
(37) Sun, M.; Ji, J.; Hu, M.; Weng, M.; Zhang, Y.; Yu, H.; Tang, J.; Zheng, J.; Jiang, Z.; Pan, F.; Liang, C.; Lin, Z. Overwhelming the Performance of Single Atoms with Atomic Clusters for Platinum-Catalyzed Hydrogen Evolution. *ACS Catal.* **2019**, *9* (9), 8213–8223. https://doi.org/10.1021/acscatal.9b02305.
(38) Jaramillo, T. F.; Jørgensen, K. P.; Bonde, J.; Nielsen, J. H.; Horch, S.; Chorkendorff, I. Identification of Active Edge Sites for Electrochemical H2 Evolution from MoS2 Nanocatalysts. *Science (80-.).* **2007**, *317* (5834), 100–102. https://doi.org/10.1126/science.1141483.
(39) Gao, R.; Yan, D. Recent Development of Ni/Fe-Based Micro/Nanostructures toward Photo/Electrochemical Water Oxidation. *Adv. Energy Mater.* **2020**, *10* (11), 1–19. https://doi.org/10.1002/aenm.201900954.
(40) Yang, Y.; Lin, Z.; Gao, S.; Su, J.; Lun, Z.; Xia, G.; Chen, J.; Zhang, R.; Chen, Q. Tuning Electronic Structures of Nonprecious Ternary Alloys Encapsulated in Graphene Layers for Optimizing Overall Water Splitting Activity. *ACS Catal.* **2017**, *7* (1), 469–479. https://doi.org/10.1021/acscatal.6b02573.
(41) Fan, X.; Zhou, H.; Guo, X. WC Nanocrystals Grown on Vertically Aligned Carbon Nanotubes: An Efficient and Stable Electrocatalyst for Hydrogen Evolution Reaction. *ACS Nano* **2015**, *9* (5), 5125–5134. https://doi.org/10.1021/acsnano.5b00425.
(42) Wang, J.; Hu, H.; Zhang, H.; Zhao, J.; Li, X.; Song, Z.; Ding, J.; Deng, Y.; Han, X.; Hu, W. Regulating the Catalytically Active Sites in Low-Cost and Earth-Abundant 3d Transition-Metal-Based Electrode Materials for High-Performance Zinc–Air Batteries. *Energy & Fuels* **2021**, *35* (8), 6483–6503. https://doi.org/10.1021/acs.energyfuels.1c00388.
(43) Li, X.; Yu, J.; Jaroniec, M. Hierarchical Photocatalysts. *Chem. Soc. Rev.* **2016**, *45* (9), 2603–2636. https://doi.org/10.1039/c5cs00838g.
(44) Guo, Y.; Tang, J.; Henzie, J.; Jiang, B.; Xia, W.; Chen, T.; Bando, Y.; Kang, Y.-M.; Hossain, M. S. A.; Sugahara, Y.; Yamauchi, Y. Mesoporous Iron-Doped MoS 2 /CoMo 2 S 4 Heterostructures through Organic–Metal Cooperative Interactions on Spherical Micelles for Electrochemical Water Splitting . *ACS Nano* **2020**. https://doi.org/10.1021/acsnano.9b08904.
(45) Zhu, B.; Zou, R.; Xu, Q. Metal–Organic Framework Based Catalysts for Hydrogen Evolution. *Adv. Energy Mater.* **2018**, *8* (24), 1–33. https://doi.org/10.1002/aenm.201801193.
(46) Ling, T.; Yan, D. Y.; Wang, H.; Jiao, Y.; Hu, Z.; Zheng, Y.; Zheng, L.; Mao, J.; Liu, H.; Du, X. W.; Jaroniec, M.; Qiao, S. Z. Activating Cobalt(II) Oxide Nanorods for Efficient Electrocatalysis by Strain Engineering. *Nat. Commun.* **2017**, *8* (1), 1–7. https://doi.org/10.1038/s41467-017-01872-y.
(47) Duan, X.; Pan, N.; Sun, C.; Zhang, K.; Zhu, X.; Zhang, M.; Song, L.; Zheng, H. MOF-Derived Co-MOF,O-Doped Carbon as Trifunctional Electrocatalysts to Enable Highly Efficient Zn–Air Batteries and Water-Splitting. *J. Energy Chem.* **2021**, *56*, 290–298. https://doi.org/10.1016/j.jechem.2020.08.007.
(48) Yang, Y.; Lun, Z.; Xia, G.; Zheng, F.; He, M.; Chen, Q. Non-Precious Alloy Encapsulated in Nitrogen-Doped Graphene Layers Derived from MOFs as an Active and Durable Hydrogen Evolution Reaction Catalyst. *Energy Environ. Sci.* **2015**, *8* (12), 3563–3571. https://doi.org/10.1039/c5ee02460a.

(49) Gao, X.; Zhang, H.; Li, Q.; Yu, X.; Hong, Z.; Zhang, X.; Liang, C.; Lin, Z. Hierarchical NiCo2O4 Hollow Microcuboids as Bifunctional Electrocatalysts for Overall Water-Splitting. *Angew. Chemie - Int. Ed.* **2016**, *55* (21), 6290–6294. https://doi.org/10.1002/anie.201600525.

(50) Jiang, S.; Zhang, R.; Liu, H.; Rao, Y.; Yu, Y.; Chen, S.; Yue, Q.; Zhang, Y.; Kang, Y. Promoting Formation of Oxygen Vacancies in Two-Dimensional Cobalt-Doped Ceria Nanosheets for Efficient Hydrogen Evolution. *J. Am. Chem. Soc.* **2020**, *142* (14), 6461–6466. https://doi.org/10.1021/jacs.9b13915.

(51) Baranton, S.; Coutanceau, C. Nickel Cobalt Hydroxide Nanoflakes as Catalysts for the Hydrogen Evolution Reaction. *Appl. Catal. B Environ.* **2013**, *136–137*, 1–8. https://doi.org/10.1016/j.apcatb.2013.01.051.

(52) Feng, Y.; Wang, X.; Huang, J.; Dong, P.; Ji, J.; Li, J.; Cao, L.; Feng, L.; Jin, P.; Wang, C. Decorating CoNi Layered Double Hydroxides Nanosheet Arrays with Fullerene Quantum Dot Anchored on Ni Foam for Efficient Electrocatalytic Water Splitting and Urea Electrolysis. *Chem. Eng. J.* **2020**, *390* (February), 124525. https://doi.org/10.1016/j.cej.2020.124525.

(53) Cao, J.; Sun, S.; Li, X.; Yang, Z.; Xiong, W.; Wu, Y.; Jia, M.; Zhou, Y.; Zhou, C.; Zhang, Y. Efficient Charge Transfer in Aluminum-Cobalt Layered Double Hydroxide Derived from Co-ZIF for Enhanced Catalytic Degradation of Tetracycline through Peroxymonosulfate Activation. *Chem. Eng. J.* **2020**, *382* (August 2019), 1–10. https://doi.org/10.1016/j.cej.2019.122802.

(54) Rajeshkhanna, G.; Singh, T. I.; Kim, N. H.; Lee, J. H. Remarkable Bifunctional Oxygen and Hydrogen Evolution Electrocatalytic Activities with Trace-Level Fe Doping in Ni- and Co-Layered Double Hydroxides for Overall Water-Splitting. *ACS Appl. Mater. Interfaces* **2018**, *10* (49), 42453–42468. https://doi.org/10.1021/acsami.8b16425.

(55) Feng, J. X.; Ding, L. X.; Ye, S. H.; He, X. J.; Xu, H.; Tong, Y. X.; Li, G. R. Co(OH)2@PANI Hybrid Nanosheets with 3D Networks as High-Performance Electrocatalysts for Hydrogen Evolution Reaction. *Adv. Mater.* **2015**, *27* (44), 7051–7057. https://doi.org/10.1002/adma.201503187.

(56) Jia, Y.; Zhang, L.; Gao, G.; Chen, H.; Wang, B.; Zhou, J.; Soo, M. T.; Hong, M.; Yan, X.; Qian, G.; Zou, J.; Du, A.; Yao, X. A Heterostructure Coupling of Exfoliated Ni–Fe Hydroxide Nanosheet and Defective Graphene as a Bifunctional Electrocatalyst for Overall Water Splitting. *Adv. Mater.* **2017**, *29* (17), 1–8. https://doi.org/10.1002/adma.201700017.

(57) Siegmund, D.; Blanc, N.; Smialkowski, M.; Tschulik, K.; Apfel, U. P. Metal-Rich Chalcogenides for Electrocatalytic Hydrogen Evolution: Activity of Electrodes and Bulk Materials. *ChemElectroChem* **2020**, *7* (7), 1514–1527. https://doi.org/10.1002/celc.201902125.

(58) Feng, L. L.; Li, G. D.; Liu, Y.; Wu, Y.; Chen, H.; Wang, Y.; Zou, Y. C.; Wang, D.; Zou, X. Carbon-Armored Co9S8 Nanoparticles as All-PH Efficient and Durable H2-Evolving Electrocatalysts. *ACS Appl. Mater. Interfaces* **2015**, *7* (1), 980–988. https://doi.org/10.1021/am507811a.

(59) Peng, S.; Li, L.; Zhang, J.; Tan, T. L.; Zhang, T.; Ji, D.; Han, X.; Cheng, F.; Ramakrishna, S. Engineering Co9S8/WS2 Array Films as Bifunctional Electrocatalysts for Efficient Water Splitting. *J. Mater. Chem. A* **2017**, *5* (44), 23361–23368. https://doi.org/10.1039/c7ta08518d.

(60) Ao, K.; Wei, Q.; Daoud, W. A. MOF-Derived Sulfide-Based Electrocatalyst and Scaffold for Boosted Hydrogen Production. *ACS Appl. Mater. Interfaces* **2020**, *12* (30), 33595–33602. https://doi.org/10.1021/acsami.0c04302.

(61) Yang, Y.; Zhang, W.; Xiao, Y.; Shi, Z.; Cao, X.; Tang, Y.; Gao, Q. CoNiSe 2 Heteronanorods Decorated with Layered-Double-Hydroxides for Efficient Hydrogen Evolution. *Appl. Catal. B Environ.* **2019**, *242* (July 2018), 132–139. https://doi.org/10.1016/j.apcatb.2018.09.082.

(62) Park, S. K.; Kim, J. K.; Chan Kang, Y. Metal-Organic Framework-Derived CoSe2/(NiCo)Se2 Box-in-Box Hollow Nanocubes with Enhanced Electrochemical Properties for Sodium-Ion Storage and Hydrogen Evolution. *J. Mater. Chem. A* **2017**, *5* (35), 18823–18830. https://doi.org/10.1039/c7ta05571d.

(63) Popczun, E. J.; Read, C. G.; Roske, C. W.; Lewis, N. S.; Schaak, R. E. Highly Active Electrocatalysis of the Hydrogen Evolution Reaction by Cobalt Phosphide Nanoparticles ** Angewandte. **2014**, 5531–5534. https://doi.org/10.1002/ange.201402646.

(64) Li, Y.; Dong, Z.; Jiao, L. Multifunctional Transition Metal-Based Phosphides in Energy-Related Electrocatalysis. *Adv. Energy Mater.* **2019**, *1902104*, 1–36. https://doi.org/10.1002/aenm.201902104.

(65) Chen, Z.; Wu, H.; Li, J.; Wang, Y.; Guo, W.; Cao, C.; Chen, Z. Defect Enhanced CoP/Reduced Graphene Oxide Electrocatalytic Hydrogen Production with Pt-like Activity. *Appl. Catal. B Environ.* **2020**, *265* (October 2019), 118576. https://doi.org/10.1016/j.apcatb.2019.118576.

(66) Pan, Y.; Sun, K.; Liu, S.; Cao, X.; Wu, K.; Cheong, W. C.; Chen, Z.; Wang, Y.; Li, Y.; Liu, Y.; Wang, D.; Peng, Q.; Chen, C.; Li, Y. Core-Shell ZIF-8@ZIF-67-Derived CoP Nanoparticle-Embedded N-Doped Carbon Nanotube Hollow Polyhedron for Efficient Overall Water Splitting. *J. Am. Chem. Soc.* **2018**, *140* (7), 2610–2618. https://doi.org/10.1021/jacs.7b12420.

(67) Pan, Y.; Sun, K.; Lin, Y.; Cao, X.; Cheng, Y.; Liu, S.; Zeng, L.; Cheong, W. C.; Zhao, D.; Wu, K.; Liu, Z.; Liu, Y.; Wang, D.; Peng, Q.; Chen, C.; Li, Y. Electronic Structure and D-Band Center Control Engineering over M-Doped CoP (M = Ni, Mn, Fe) Hollow Polyhedron Frames for Boosting Hydrogen Production. *Nano Energy* **2019**, *56* (October 2018), 411–419. https://doi.org/10.1016/j.nanoen.2018.11.034.

(68) Zhu, Y.; Zhang, L.; Zhang, X.; Li, Z.; Zha, M.; Li, M.; Hu, G. Double Functionalization Strategy toward Co-Fe-P Hollow Nanocubes for Highly Efficient Overall Water Splitting with Ultra-Low Cell Voltage. *Chem. Eng. J.* **2021**, *405* (July 2020), 127002. https://doi.org/10.1016/j.cej.2020.127002.

(69) Callejas, J. F.; Read, C. G.; Popczun, E. J.; McEnaney, J. M.; Schaak, R. E. Nanostructured Co2P Electrocatalyst for the Hydrogen Evolution Reaction and Direct Comparison with Morphologically Equivalent CoP. *Chem. Mater.* **2015**, *27* (10), 3769–3774. https://doi.org/10.1021/acs.chemmater.5b01284.

(70) Cao, B.; Hu, M.; Cheng, Y.; Jing, P.; Liu, B.; Zhou, B.; Wang, X.; Gao, R.; Sun, X.; Du, Y.; Zhang, J. Tailoring the D-Band Center of N-Doped Carbon Nanotube Arrays with Co4N Nanoparticles and Single-Atom Co for a Superior Hydrogen Evolution Reaction. *NPG Asia Mater.* **2021**, *13* (1), 1–14. https://doi.org/10.1038/s41427-020-00264-x.

(71) Sun, S.; Sun, Y.; Zhou, Y.; Xi, S.; Ren, X.; Huang, B.; Liao, H.; Wang, L. P.; Du, Y.; Xu, Z. J. Shifting Oxygen Charge Towards Octahedral Metal: A Way to Promote Water Oxidation on Cobalt Spinel Oxides. *Angew. Chemie - Int. Ed.* **2019**, *58* (18), 6042–6047. https://doi.org/10.1002/anie.201902114.

(72) Wang, H.; Xu, S.; Tsai, C.; Li, Y.; Liu, C.; Zhao, J.; Liu, Y.; Yuan, H.; Abild-Pedersen, F.; Prinz, F. B.; Nørskov, J. K.; Cui, Y. Direct and Continuous Strain Control of Catalysts with Tunable Battery Electrode Materials. *Science (80-.).*

2016, *354* (6315), 1031–1036. https://doi.org/10.1126/science.aaf7680.

(73) Zhang, R.; Zhang, Y. C.; Pan, L.; Shen, G. Q.; Mahmood, N.; Ma, Y. H.; Shi, Y.; Jia, W.; Wang, L.; Zhang, X.; Xu, W.; Zou, J. J. Engineering Cobalt Defects in Cobalt Oxide for Highly Efficient Electrocatalytic Oxygen Evolution. *ACS Catal.* **2018**, *8* (5), 3803–3811. https://doi.org/10.1021/acscatal.8b01046.

(74) Wang, Y.; Jiang, K.; Zhang, H.; Zhou, T.; Wang, J.; Wei, W.; Yang, Z.; Sun, X.; Cai, W. Bin; Zheng, G. Bio-Inspired Leaf-Mimicking Nanosheet/Nanotube Heterostructure as a Highly Efficient Oxygen Evolution Catalyst. *Adv. Sci.* **2015**, *2* (4), 1–8. https://doi.org/10.1002/advs.201500003.

(75) Wu, L.; Yu, L.; McElhenny, B.; Xing, X.; Luo, D.; Zhang, F.; Bao, J.; Chen, S.; Ren, Z. Rational Design of Core-Shell-Structured CoPx@FeOOH for Efficient Seawater Electrolysis. *Appl. Catal. B Environ.* **2021**, *294* (February), 120256. https://doi.org/10.1016/j.apcatb.2021.120256.

(76) Zhuang, L.; Ge, L.; Liu, H.; Jiang, Z.; Jia, Y.; Li, Z.; Yang, D.; Hocking, R. K.; Li, M.; Zhang, L.; Wang, X.; Yao, X.; Zhu, Z. A Surfactant-Free and Scalable General Strategy for Synthesizing Ultrathin Two-Dimensional Metal–Organic Framework Nanosheets for the Oxygen Evolution Reaction. *Angew. Chemie* **2019**, *131* (38), 13699–13706. https://doi.org/10.1002/ange.201907600.

(77) Li, X.; Zheng, K.; Zhang, J.; Li, G.; Xu, C. Engineering Sulfur Vacancies in Spinel-Phase Co3S4for Effective Electrocatalysis of the Oxygen Evolution Reaction. *ACS Omega* **2022**, *7* (14), 12430–12441. https://doi.org/10.1021/acsomega.2c01423.

(78) Manjunatha, C.; Lakshmikant, S.; Shreenivasa, L.; Srinivasa, N.; Ashoka, S.; Shivraj, B. W.; Selvaraj, M.; Meda, U. S.; Babu, G. S.; Pollet, B. G. Development of Non-Stoichiometric Hybrid Co3S4/Co0.85Se Nanocomposites for an Evaluation of Synergistic Effect on the OER Performance. *Surfaces and Interfaces* **2021**, *25* (January). https://doi.org/10.1016/j.surfin.2021.101161.

(79) Cui, M.; Yang, C.; Li, B.; Dong, Q.; Wu, M.; Hwang, S.; Xie, H.; Wang, X.; Wang, G.; Hu, L. High-Entropy Metal Sulfide Nanoparticles Promise High-Performance Oxygen Evolution Reaction. *Adv. Energy Mater.* **2021**, *11* (3), 1–8. https://doi.org/10.1002/aenm.202002887.

(80) Du, F.; Ling, X.; Wang, Z.; Guo, S.; Zhang, Y.; He, H.; Li, G.; Jiang, C.; Zhou, Y.; Zou, Z. Strained Heterointerfaces in Sandwich–like NiFe Layered Double Hydroxides/Co1-XS for Highly Efficient and Superior Long–Term Durable Oxygen Evolution Reaction. *J. Catal.* **2020**, *389*, 132–139. https://doi.org/10.1016/j.jcat.2020.05.026.

(81) Zhou, J.; Dou, Y.; He, T.; Zhou, A.; Kong, X. J.; Wu, X. Q.; Liu, T.; Li, J. R. Revealing the Effect of Anion-Tuning in Bimetallic Chalcogenides on Electrocatalytic Overall Water Splitting. *Nano Res.* **2021**, *12* (1). https://doi.org/10.1007/s12274-021-3370-7.

(82) Naya, S. I.; Kume, T.; Akashi, R.; Fujishima, M.; Tada, H. Red-Light-Driven Water Splitting by Au(Core)-CdS(Shell) Half-Cut Nanoegg with Heteroepitaxial Junction. *J. Am. Chem. Soc.* **2018**, *140* (4), 1251–1254. https://doi.org/10.1021/jacs.7b12972.

(83) Li, Z. J.; Wang, J. J.; Li, X. B.; Fan, X. B.; Meng, Q. Y.; Feng, K.; Chen, B.; Tung, C. H.; Wu, L. Z. An Exceptional Artificial Photocatalyst, Nih-CdSe/CdS Core/Shell Hybrid, Made in Situ from CdSe Quantum Dots and Nickel Salts for Efficient Hydrogen Evolution. *Adv. Mater.* **2013**, *25* (45), 6613–6618. https://doi.org/10.1002/adma.201302908.

(84) Su, D. W.; Ran, J.; Zhuang, Z. W.; Chen, C.; Qiao, S. Z.; Li, Y. D.; Wang, G. X.

Atomically Dispersed Ni in Cadmium-Zinc Sulfide Quantum Dots for High-Performance Visible-Light Photocatalytic Hydrogen Production. *Sci. Adv.* **2020**, *6* (33), 1–17. https://doi.org/10.1126/sciadv.aaz8447.

(85) Shao, Z.; Zeng, T.; He, Y.; Zhang, D.; Pu, X. A Novel Magnetically Separable CoFe2O4/Cd0.9Zn0.1S Photocatalyst with Remarkably Enhanced H2 Evolution Activity under Visible Light Irradiation. *Chem. Eng. J.* **2019**, *359* (September 2018), 485–495. https://doi.org/10.1016/j.cej.2018.11.163.

(86) Wang, J.; Wang, P.; Wang, C.; Ao, Y. In-Situ Synthesis of Well Dispersed CoP Nanoparticles Modified CdS Nanorods Composite with Boosted Performance for Photocatalytic Hydrogen Evolution. *Int. J. Hydrogen Energy* **2018**, *43* (32), 14934–14943. https://doi.org/10.1016/j.ijhydene.2018.06.101.

(87) Fang, B.; Xing, Z.; Du, F.; Kong, W.; Li, Z.; Zhou, W. CdS Nanocages@defective-CoNi-LDH with Bilayer Porous Hollow Frameworks toward Optimized Sono-Photocatalytic Performance. *J. Mater. Chem. A* **2022**, *10* (31), 16439–16447. https://doi.org/10.1039/d2ta03783a.

(88) Li, S.; Wang, L.; Li, Y. D.; Zhang, L.; Wang, A.; Xiao, N.; Gao, Y.; Li, N.; Song, W.; Ge, L.; Liu, J. Novel Photocatalyst Incorporating Ni-Co Layered Double Hydroxides with P-Doped CdS for Enhancing Photocatalytic Activity towards Hydrogen Evolution. *Appl. Catal. B Environ.* **2019**, *254* (April), 145–155. https://doi.org/10.1016/j.apcatb.2019.05.001.

(89) Zhang, T.; Meng, F.; Cheng, Y.; Dewangan, N.; Ho, G. W.; Kawi, S. Z-Scheme Transition Metal Bridge of Co9S8/Cd/CdS Tubular Heterostructure for Enhanced Photocatalytic Hydrogen Evolution. *Appl. Catal. B Environ.* **2021**, *286* (January). https://doi.org/10.1016/j.apcatb.2020.119853.

(90) Li, X.; Song, S.; Gao, Y.; Ge, L.; Song, W.; Ma, T.; Liu, J. Identification of the Charge Transfer Channel in Cobalt Encapsulated Hollow Nitrogen-Doped Carbon Matrix@CdS Heterostructure for Photocatalytic Hydrogen Evolution. *Small* **2021**, *17* (31), 1–10. https://doi.org/10.1002/smll.202101315.

(91) Liu, X.; Xu, S.; Chi, H.; Xu, T.; Guo, Y.; Yuan, Y.; Yang, B. Ultrafine 1D Graphene Interlayer in G-C3N4/Graphene/Recycled Carbon Fiber Heterostructure for Enhanced Photocatalytic Hydrogen Generation. *Chem. Eng. J.* **2019**, *359* (November 2018), 1352–1359. https://doi.org/10.1016/j.cej.2018.11.043.

(92) Kong, L.; Dong, Y.; Jiang, P.; Wang, G.; Zhang, H.; Zhao, N. Light-Assisted Rapid Preparation of a Ni/g-C3N4 Magnetic Composite for Robust Photocatalytic H2 Evolution from Water. *J. Mater. Chem. A* **2016**, *4* (25), 9998–10007. https://doi.org/10.1039/c6ta03178a.

(93) Zhang, Y.; Jin, Z.; Yan, X.; Wang, H.; Wang, G. Effect of Ni(OH) 2 on CdS@g-C 3 N 4 Composite for Efficient Photocatalytic Hydrogen Production. *Catal. Letters* **2019**, *149* (5), 1174–1185. https://doi.org/10.1007/s10562-019-02708-8.

(94) Vu, M. H.; Sakar, M.; Nguyen, C. C.; Do, T. O. Chemically Bonded Ni Cocatalyst onto the S Doped G-C3N4 Nanosheets and Their Synergistic Enhancement in H2 Production under Sunlight Irradiation. *ACS Sustain. Chem. Eng.* **2018**, *6* (3), 4194–4203. https://doi.org/10.1021/acssuschemeng.7b04598.

(95) Shen, J.; Luo, C.; Qiao, S.; Chen, Y.; Tang, Y.; Xu, J.; Fu, K.; Yuan, D.; Tang, H.; Zhang, H.; Liu, C. Single-Atom Cu Channel and N-Vacancy Engineering Enables Efficient Charge Separation and Transfer between C3N4 Interlayers for Boosting Photocatalytic Hydrogen Production. *ACS Catal.* **2023**, 6280–6288. https://doi.org/10.1021/acscatal.2c05789.

(96) Pan, Z.; Zheng, Y.; Guo, F.; Niu, P.; Wang, X. Decorating CoP and Pt

Nanoparticles on Graphitic Carbon Nitride Nanosheets to Promote Overall Water Splitting by Conjugated Polymers. *ChemSusChem* **2017**, *10* (1), 87–90. https://doi.org/10.1002/cssc.201600850.

(97) Zou, X.; Su, J.; Silva, R.; Goswami, A.; Sathe, B. R.; Asefa, T. Efficient Oxygen Evolution Reaction Catalyzed by Low-Density Ni-Doped Co3O4 Nanomaterials Derived from Metal-Embedded Graphitic C3N4. *Chem. Commun.* **2013**, *49* (68), 7522–7524. https://doi.org/10.1039/c3cc42891e.

(98) Zhu, Q.; Qiu, B.; Duan, H.; Gong, Y.; Qin, Z.; Shen, B.; Xing, M.; Zhang, J. Electron Directed Migration Cooperated with Thermodynamic Regulation over Bimetallic NiFeP/g-C3N4 for Enhanced Photocatalytic Hydrogen Evolution. *Appl. Catal. B Environ.* **2019**, *259* (July), 118078. https://doi.org/10.1016/j.apcatb.2019.118078.

(99) Qi, Y.; Xu, J.; Zhang, M.; Lin, H.; Wang, L. In Situ Metal–Organic Framework-Derived c-Doped Ni3S4/Ni2P Hybrid Co-Catalysts for Photocatalytic H2 Production over g-C3N4 via Dye Sensitization. *Int. J. Hydrogen Energy* **2019**, *44* (31), 16336–16347. https://doi.org/10.1016/j.ijhydene.2019.04.276.

(100) Nutting, D.; Felix, J. F.; Tillotson, E.; Shin, D.; Chang, H.; Cole, N.; Russo, S.; Woodgate, A.; Leontis, I.; Fernández, H. A.; Haigh, S.; Craciun, M. F.; Withers, F. Heterostructures Formed through Abraded van Der Waals Materials. *Nat. Commun.* **2020**, No. 2020, 1–37. https://doi.org/10.1038/s41467-020-16717-4.

(101) Matsukawa, R.; Miyamoto, A.; Yokota, T.; Someya, T. Skin Impedance Measurements with Nanomesh Electrodes for Monitoring Skin Hydration. *Adv. Healthc. Mater.* **2020**, *9* (22), 1–6. https://doi.org/10.1002/adhm.202001322.

(102) Gao, F.; Liu, C.; Zhang, L.; Liu, T.; Wang, Z.; Song, Z.; Cai, H.; Fang, Z.; Chen, J.; Wang, J.; Han, M.; Wang, J.; Lin, K.; Wang, R.; Li, M.; Mei, Q.; Ma, X.; Liang, S.; Gou, G.; Xue, N. Wearable and Flexible Electrochemical Sensors for Sweat Analysis: A Review. *Microsystems Nanoeng.* **2023**, *9* (1), 1–21. https://doi.org/10.1038/s41378-022-00443-6.

(103) Parrilla, M.; Cánovas, R.; Jeerapan, I.; Andrade, F. J.; Wang, J. A Textile-Based Stretchable Multi-Ion Potentiometric Sensor. *Adv. Healthc. Mater.* **2016**, *5* (9), 996–1001. https://doi.org/10.1002/adhm.201600092.

(104) Ma, X.; Wang, P.; Huang, L.; Ding, R.; Zhou, K.; Shi, Y.; Chen, F.; Zhuang, Q.; Huang, Q.; Lin, Y.; Zheng, Z. A Monolithically Integrated In-Textile Wristband for Wireless Epidermal Biosensing. **2023**, 1–11.

(105) Bollella, P.; Katz, E. Enzyme-Based Biosensors: Tackling Electron Transfer Issues. *Sensors (Switzerland)* **2020**, *20* (12), 1–32. https://doi.org/10.3390/s20123517.

(106) Zhang, Y.; Nandakumar, D. K.; Tan, S. C. Digestion of Ambient Humidity for Energy Generation. *Joule* **2020**, *4* (12), 2532–2536. https://doi.org/10.1016/j.joule.2020.10.003.

(107) Zhang, Y.; Guo, S.; Yu, Z. G.; Qu, H.; Sun, W.; Yang, J.; Suresh, L.; Zhang, X.; Koh, J. J.; Tan, S. C. An Asymmetric Hygroscopic Structure for Moisture-Driven Hygro-Ionic Electricity Generation and Storage. *Adv. Mater.* **2022**, *34* (21), 1–12. https://doi.org/10.1002/adma.202201228.

(108) Nandakumar, D. K.; Vaghasiya, J. V.; Yang, L.; Zhang, Y.; Tan, S. C. A Solar Cell That Breathes in Moisture for Energy Generation. *Nano Energy* **2020**, *68* (November 2019), 104263. https://doi.org/10.1016/j.nanoen.2019.104263.

(109) Kalkus, T. J.; Guha, A.; Scholten, P. B. V; Nagornii, D.; Coskun, A.; Ianiro, A.; Mayer, M. The Green Lean Amine Machine : Harvesting Electric Power While Capturing Carbon Dioxide from Breath. **2021**, *2100995*, 1–12.

https://doi.org/10.1002/advs.202100995.
(110) Lee, T. W.; Kim, H. J.; Park, J. S.; Baik, J. M. Electrocatalytically Driven Fast Removal of Moisture by Condensation of Vapor and Water Splitting. *Nano Energy* **2019**, *61* (February), 295–303. https://doi.org/10.1016/j.nanoen.2019.04.072.
(111) Liu, S.; Sun, C.; Xiao, J.; Luo, J. L. Unraveling Structure Sensitivity in CO2 Electroreduction to Near-Unity CO on Silver Nanocubes. *ACS Catal.* **2020**, *10* (5), 3158–3163. https://doi.org/10.1021/acscatal.9b03883.
(112) Jing, S.; Zhang, L.; Luo, L.; Lu, J.; Yin, S.; Kang, P. Applied Catalysis B : Environmental N-Doped Porous Molybdenum Carbide Nanobelts as E Ffi Cient Catalysts for Hydrogen Evolution Reaction. **2018**, *224* (October 2017), 533–540.
(113) Wang, X.; Li, F.; Li, W.; Gao, W.; Tang, Y.; Li, R. Hollow Bimetallic Cobalt-Based Selenide Polyhedrons Derived from Metal-Organic Framework: An Efficient Bifunctional Electrocatalyst for Overall Water Splitting. *J. Mater. Chem. A* **2017**, *5* (34), 17982–17989. https://doi.org/10.1039/c7ta03167j.
(114) Anjum, M. A. R.; Jeong, H. Y.; Lee, M. H.; Shin, H. S.; Lee, J. S. Efficient Hydrogen Evolution Reaction Catalysis in Alkaline Media by All-in-One MoS2 with Multifunctional Active Sites. *Adv. Mater.* **2018**, *30* (20), 1–9. https://doi.org/10.1002/adma.201707105.
(115) Ramalingam, V.; Varadhan, P.; Fu, H. C.; Kim, H.; Zhang, D.; Chen, S.; Song, L.; Ma, D.; Wang, Y.; Alshareef, H. N.; He, J. H. Heteroatom-Mediated Interactions between Ruthenium Single Atoms and an MXene Support for Efficient Hydrogen Evolution. *Adv. Mater.* **2019**, *1903841* (48), 1–10. https://doi.org/10.1002/adma.201903841.
(116) An, Y.; Long, X.; Ma, M.; Hu, J.; Lin, H.; Zhou, D.; Xing, Z.; Huang, B.; Yang, S. One-Step Controllable Synthesis of Catalytic Ni4Mo/MoOx/Cu Nanointerfaces for Highly Efficient Water Reduction. *Adv. Energy Mater.* **2019**, *9* (41), 1–10. https://doi.org/10.1002/aenm.201901454.
(117) Kim, J. K.; Bae, S.; Kim, W.; Jeong, M. J.; Lee, S. H.; Lee, C. L.; Choi, W. K.; Hwang, J. Y.; Park, J. H.; Son, D. I. Nano Carbon Conformal Coating Strategy for Enhanced Photoelectrochemical Responses and Long-Term Stability of ZnO Quantum Dots. *Nano Energy* **2015**, *13*, 258–266. https://doi.org/10.1016/j.nanoen.2015.02.013.
(118) Liu, S. Q.; Wen, H. R.; Ying-Guo; Zhu, Y. W.; Fu, X. Z.; Sun, R.; Wong, C. P. Amorphous Ni(OH) 2 Encounter with Crystalline CuS in Hollow Spheres: A Mesoporous Nano-Shelled Heterostructure for Hydrogen Evolution Electrocatalysis. *Nano Energy* **2018**, *44* (October 2017), 7–14. https://doi.org/10.1016/j.nanoen.2017.11.063.
(119) Najafi, L.; Bellani, S.; Oropesa-Nuñez, R.; Martín-García, B.; Prato, M.; Bonaccorso, F. Single-/Few-Layer Graphene as Long-Lasting Electrocatalyst for Hydrogen Evolution Reaction. *ACS Appl. Energy Mater.* **2019**, *2* (8), 5373–5379. https://doi.org/10.1021/acsaem.9b00949.
(120) Wang, G.; Chen, W.; Chen, G.; Huang, J.; Song, C.; Chen, D.; Du, Y.; Li, C.; Ostrikov, K. K. Trimetallic Mo–Ni–Co Selenides Nanorod Electrocatalysts for Highly-Efficient and Ultra-Stable Hydrogen Evolution. *Nano Energy* **2020**, *71* (October 2019), 104637. https://doi.org/10.1016/j.nanoen.2020.104637.
(121) Lei, Y.; Wei, L.; Zhai, S.; Wang, Y.; Karahan, H. E.; Chen, X.; Zhou, Z.; Wang, C.; Sui, X.; Chen, Y. Metal-Free Bifunctional Carbon Electrocatalysts Derived from Zeolitic Imidazolate Frameworks for Efficient Water Splitting. *Mater. Chem. Front.* **2018**, *2* (1), 102–111. https://doi.org/10.1039/C7QM00452D.

(122) Lin, Z.; Yang, Y.; Li, M.; Huang, H.; Hu, W.; Cheng, L.; Yan, W.; Yu, Z.; Mao, K.; Xia, G.; Lu, J.; Jiang, P.; Yang, K.; Zhang, R.; Xu, P.; Wang, C.; Hu, L.; Chen, Q. Dual Graphitic-N Doping in a Six-Membered C-Ring of Graphene-Analogous Particles Enables an Efficient Electrocatalyst for the Hydrogen Evolution Reaction. *Angew. Chemie - Int. Ed.* **2019**, *58* (47), 16973–16980. https://doi.org/10.1002/anie.201908210.

(123) Lu, X. F.; Yu, L.; Lou, X. W. Highly Crystalline Ni-Doped FeP/Carbon Hollow Nanorods as All-PH Efficient and Durable Hydrogen Evolving Electrocatalysts. *Sci. Adv.* **2019**, *5* (2), 1–10. https://doi.org/10.1126/sciadv.aav6009.

(124) Xu, W.; Zhao, R.; Li, Q.; Sun, B.; Wu, J.; Zhong, W.; Gao, Y.; Nan, X.; Huang, Q.; Yang, Y.; Li, X.; Yang, N.; Zhang, Q. Overall Water Splitting on The NiS/NiS2 Heterostructures Featuring Self-Equilibrium Orbital Occupancy. *Adv. Energy Mater.* **2023**, *2300978*, 1–12. https://doi.org/10.1002/aenm.202300978.

(125) Zhong, H.; Wang, X.; Sun, G.; Tang, Y.; Tan, S.; He, Q.; Zhang, J.; Xiong, T.; Diao, C.; Yu, Z.; Xi, S.; Lee, W. S. V.; Xue, J. Optimization of Oxygen Evolution Activity by Tuning Band Broadening in Nickel Oxyhydroxide. *Energy Environ. Sci.* **2023**, *16* (2), 641–652. https://doi.org/10.1039/d2ee03413a.

(126) Ma, D.; Shi, J. W.; Sun, L.; Sun, Y.; Mao, S.; Pu, Z.; He, C.; Zhang, Y.; He, D.; Wang, H.; Cheng, Y. Knack behind the High Performance CdS/ZnS-NiS Nanocomposites: Optimizing Synergistic Effect between Cocatalyst and Heterostructure for Boosting Hydrogen Evolution. *Chem. Eng. J.* **2022**, *431* (P4), 133446. https://doi.org/10.1016/j.cej.2021.133446.

(127) Zhang, L.; Fu, X.; Meng, S.; Jiang, X.; Wang, J.; Chen, S. Ultra-Low Content of Pt Modified CdS Nanorods: One-Pot Synthesis and High Photocatalytic Activity for H2 Production under Visible Light. *J. Mater. Chem. A* **2015**, *3* (47), 23732–23742. https://doi.org/10.1039/c5ta07459b.

(128) Wang, M.; Wang, J. Q.; Xi, C.; Cheng, C. Q.; Zou, C. Q.; Zhang, R.; Xie, Y. M.; Guo, Z. L.; Tang, C. C.; Dong, C. K.; Chen, Y. J.; Du, X. W. A Hydrogen-Deficient Nickel–Cobalt Double Hydroxide for Photocatalytic Overall Water Splitting. *Angew. Chemie - Int. Ed.* **2020**, *59* (28), 11510–11515. https://doi.org/10.1002/anie.202002650.

(129) Yan, Z.; Sun, Z.; Liu, X.; Jia, H.; Du, P. Cadmium Sulfide/Graphitic Carbon Nitride Heterostructure Nanowire Loading with a Nickel Hydroxide Cocatalyst for Highly Efficient Photocatalytic Hydrogen Production in Water under Visible Light. *Nanoscale* **2016**, *8* (8), 4748–4756. https://doi.org/10.1039/c6nr00160b.

(130) Zhao, F.; Law, Y. Lo; Zhang, N.; Wang, X.; Wu, W.; Luo, Z.; Wang, Y. Constructing Spatially Separated Cage-Like Z-scheme Heterojunction Photocatalyst for Enhancing Photocatalytic H 2 Evolution . *Small* **2023**, *2208266*, 2208266. https://doi.org/10.1002/smll.202208266.

(131) Lei, Y.; Ng, K. H.; Zhang, Y.; Li, Z.; Xu, S.; Huang, J.; Lai, Y. One-Pot Loading of Cadmium Sulfide onto Tungsten Carbide for Efficient Photocatalytic H2 Evolution under Visible Light Irradiation. *Chem. Eng. J.* **2022**, *434* (December 2021), 134689. https://doi.org/10.1016/j.cej.2022.134689.

(132) Zong, X.; Yan, H.; Wu, G.; Ma, G.; Wen, F.; Wang, L.; Li, C. Enhancement of Photocatalytic H2 Evolution on CdS by Loading MoS2 as Cocatalyst under Visible Light Irradiation. *J. Am. Chem. Soc.* **2008**, *130* (23), 7176–7177. https://doi.org/10.1021/ja8007825.

(133) Zhu, J.; Hu, L.; Zhao, P.; Lee, L. Y. S.; Wong, K. Y. Recent Advances in Electrocatalytic Hydrogen Evolution Using Nanoparticles. *Chem. Rev.* **2020**, *120* (2), 851–918. https://doi.org/10.1021/acs.chemrev.9b00248.

(134) Tong, R.; Ng, K. W.; Wang, X.; Wang, S.; Wang, X.; Pan, H. Two-Dimensional Materials as Novel Co-Catalysts for Efficient Solar-Driven Hydrogen Production. *J. Mater. Chem. A* **2020**, *8* (44), 23202–23230. https://doi.org/10.1039/d0ta08045d.

(135) Shen, Z.; Zhuang, Y.; Li, W.; Huang, X.; Oropeza, F. E.; Hensen, E. J. M.; Hofmann, J. P.; Cui, M.; Tadich, A.; Qi, D.; Cheng, J.; Li, J.; Zhang, K. H. L. Increased Activity in the Oxygen Evolution Reaction by Fe4+-Induced Hole States in Perovskite La1-: XSrxFeO3. *J. Mater. Chem. A* **2020**, *8* (8), 4407–4415. https://doi.org/10.1039/c9ta13313e.

(136) Yang, W.; Zhang, S.; Chen, Q.; Zhang, C.; Wei, Y.; Jiang, H.; Lin, Y.; Zhao, M.; He, Q.; Wang, X.; Du, Y.; Song, L.; Yang, S.; Nie, A.; Zou, X.; Gong, Y. Conversion of Intercalated MoO3 to Multi-Heteroatoms-Doped MoS2 with High Hydrogen Evolution Activity. *Adv. Mater.* **2020**, *32* (30), 1–9. https://doi.org/10.1002/adma.202001167.

(137) Chai, G. L.; Qiu, K.; Qiao, M.; Titirici, M. M.; Shang, C.; Guo, Z. Active Sites Engineering Leads to Exceptional ORR and OER Bifunctionality in P,N Co-Doped Graphene Frameworks. *Energy Environ. Sci.* **2017**, *10* (5), 1186–1195. https://doi.org/10.1039/c6ee03446b.

(138) Zhao, X.; Pachfule, P.; Li, S.; Ron, J.; Simke, J.; Schmidt, J.; Thomas, A. Water Splitting Hot Paper Bifunctional Electrocatalysts for Overall Water Splitting from an Iron / Nickel-Based Bimetallic Metal – Organic Framework / Dicyandiamide Composite Communications Angewandte. **2018**, 8921–8926. https://doi.org/10.1002/anie.201803136.

(139) Hu, H.; Wang, Z.; Cao, L.; Zeng, L.; Zhang, C.; Lin, W.; Wang, C. Metal–Organic Frameworks Embedded in a Liposome Facilitate Overall Photocatalytic Water Splitting. *Nat. Chem.* https://doi.org/10.1038/s41557-020-00635-5.

(140) Greeley, J.; Jaramillo, T. F.; Bonde, J.; Chorkendorff, I.; Nørskov, J. K. Computational High-Throughput Screening of Electrocatalytic Materials for Hydrogen Evolution. *Nat. Mater.* **2006**, *5* (11), 909–913. https://doi.org/10.1038/nmat1752.

(141) Wang, J.; Liao, T.; Wei, Z.; Sun, J.; Guo, J.; Sun, Z. Heteroatom-Doping of Non-Noble Metal-Based Catalysts for Electrocatalytic Hydrogen Evolution: An Electronic Structure Tuning Strategy. *Small Methods* **2021**, *2000988*, 1–27. https://doi.org/10.1002/smtd.202000988.

(142) Chen, Y.; Li, X.; Park, K.; Song, J.; Hong, J.; Zhou, L.; Mai, Y. W.; Huang, H.; Goodenough, J. B. Hollow Carbon-Nanotube/Carbon-Nanofiber Hybrid Anodes for Li-Ion Batteries. *J. Am. Chem. Soc.* **2013**, *135* (44), 16280–16283. https://doi.org/10.1021/ja408421n.

(143) Xue, H.; Meng, A.; Zhang, H.; Lin, Y.; Li, Z.; Wang, C. 3D Urchin like V-Doped CoP in Situ Grown on Nickel Foam as Bifunctional Electrocatalyst for Efficient Overall Water-Splitting. *Nano Res.* **2021**, *12* (1). https://doi.org/10.1007/s12274-021-3359-2.

(144) Pan, Y.; Heryadi, D.; Zhou, F.; Zhao, L.; Lestari, G.; Su, H.; Lai, Z. Tuning the Crystal Morphology and Size of Zeolitic Imidazolate Framework-8 in Aqueous Solution by Surfactants. *CrystEngComm* **2011**, *13* (23), 6937–6940. https://doi.org/10.1039/c1ce05780d.

(145) He, L.; Li, L.; Zhang, L.; Xing, S.; Wang, T.; Li, G.; Wu, X.; Su, Z.; Wang, C. ZIF-8 Templated Fabrication of Rhombic Dodecahedron-Shaped ZnO@SiO 2, ZIF-8@SiO2 Yolk-Shell and SiO2 Hollow Nanoparticles. *CrystEngComm* **2014**, *16* (29), 6534–6537. https://doi.org/10.1039/c4ce00755g.

(146) Zhao, J.; Quan, X.; Chen, S.; Liu, Y.; Yu, H. Cobalt Nanoparticles Encapsulated in Porous Carbons Derived from Core-Shell ZIF67@ZIF8 as Efficient Electrocatalysts for Oxygen Evolution Reaction. *ACS Appl. Mater. Interfaces* **2017**, *9* (34), 28685–28694. https://doi.org/10.1021/acsami.7b10138.
(147) Ji, L.; Wang, J.; Teng, X.; Meyer, T. J.; Chen, Z. CoP Nanoframes as Bifunctional Electrocatalysts for Efficient Overall Water Splitting. *ACS Catal.* **2020**, *10* (1), 412–419. https://doi.org/10.1021/acscatal.9b03623.
(148) Li, Y.; Lu, M.; Wu, Y.; Ji, Q.; Xu, H.; Gao, J.; Qian, G.; Zhang, Q. Morphology Regulation of Metal-Organic Framework-Derived Nanostructures for Efficient Oxygen Evolution Electrocatalysis. *J. Mater. Chem. A* **2020**, *8* (35), 18215–18219. https://doi.org/10.1039/d0ta05866a.
(149) Zhao, Z.; Zhou, X.; Kou, K.; Wu, H. PVP-Assisted Transformation of ZIF-67 into Cobalt Layered Double Hydroxide/Carbon Fiber as Electromagnetic Wave Absorber. *Carbon N. Y.* **2021**, *173*, 80–90. https://doi.org/10.1016/j.carbon.2020.11.009.
(150) Lai, Q.; Zhao, Y.; Liang, Y.; He, J.; Chen, J. In Situ Confinement Pyrolysis Transformation of ZIF-8 to Nitrogen-Enriched Meso-Microporous Carbon Frameworks for Oxygen Reduction. *Adv. Funct. Mater.* **2016**, *26* (45), 8334–8344. https://doi.org/10.1002/adfm.201603607.
(151) Lin, C.; Shinde, S. S.; Jiang, Z.; Song, X.; Sun, Y.; Guo, L.; Zhang, H.; Jung, J. Y.; Li, X.; Lee, J. H. In Situ Directional Formation of Co@CoOx-Embedded 1D Carbon Nanotubes as an Efficient Oxygen Electrocatalyst for Ultra-High Rate Zn-Air Batteries. *J. Mater. Chem. A* **2017**, *5* (27), 13994–14002. https://doi.org/10.1039/c7ta02215h.
(152) You, B.; Jiang, N.; Sheng, M.; Drisdell, W. S.; Yano, J.; Sun, Y. Bimetal-Organic Framework Self-Adjusted Synthesis of Support-Free Nonprecious Electrocatalysts for Efficient Oxygen Reduction. *ACS Catal.* **2015**, *5* (12), 7068–7076. https://doi.org/10.1021/acscatal.5b02325.
(153) Jin, H.; Wang, J.; Su, D.; Wei, Z.; Pang, Z.; Wang, Y. In Situ Cobalt-Cobalt Oxide/N-Doped Carbon Hybrids as Superior Bifunctional Electrocatalysts for Hydrogen and Oxygen Evolution. *J. Am. Chem. Soc.* **2015**, *137* (7), 2688–2694. https://doi.org/10.1021/ja5127165.
(154) Pan, Y.; Ren, H.; Chen, R.; Wu, Y.; Chu, D. Enhanced Electrocatalytic Oxygen Evolution by Manipulation of Electron Transfer through Cobalt-Phosphorous Bridging. *Chem. Eng. J.* **2020**, *398* (March), 125660. https://doi.org/10.1016/j.cej.2020.125660.
(155) Gorimbo, J.; Muvhiiwa, R.; Llane, E.; Hildebrandt, D. Cobalt Catalyst Reduction Thermodynamics in Fischer Tropsch: An Attainable Region Approach. *Reactions* **2020**, *1* (2), 115–129. https://doi.org/10.3390/reactions1020010.
(156) Bai, L.; Hsu, C. S.; Alexander, D. T. L.; Chen, H. M.; Hu, X. A Cobalt-Iron Double-Atom Catalyst for the Oxygen Evolution Reaction. *J. Am. Chem. Soc.* **2019**, *141* (36), 14190–14199. https://doi.org/10.1021/jacs.9b05268.
(157) Li, Y.; Li, S.; Wang, Y.; Wang, J.; Liu, H.; Liu, X.; Wang, L.; Liu, X.; Xue, W.; Ma, N. Electrochemical Synthesis of Phosphorus-Doped Graphene Quantum Dots for Free Radical Scavenging. *Phys. Chem. Chem. Phys.* **2017**, *19* (18), 11631–11638. https://doi.org/10.1039/c6cp06377b.
(158) Hao, J.; Yang, W.; Zhang, Z.; Tang, J. Metal-Organic Frameworks Derived CoxFe1-XP Nanocubes for Electrochemical Hydrogen Evolution. *Nanoscale* **2015**, *7* (25), 11055–11062. https://doi.org/10.1039/c5nr01955a.
(159) Chang, C. J.; Lin, S. C.; Chen, H. C.; Wang, J.; Zheng, K. J.; Zhu, Y.; Chen, H.

M. Dynamic Reoxidation/Reduction-Driven Atomic Interdiffusion for Highly Selective CO2 Reduction toward Methane. *J. Am. Chem. Soc.* **2020**. https://doi.org/10.1021/jacs.0c01859.

(160) Chen, L.; Zhang, Y.; Wang, H.; Wang, Y.; Li, D.; Duan, C. Cobalt Layered Double Hydroxides Derived CoP/Co2P Hybrids for Electrocatalytic Overall Water Splitting. *Nanoscale* **2018**, *10* (45), 21019–21024. https://doi.org/10.1039/c8nr07535b.

(161) Hu, X.; Luo, G.; Guo, X.; Zhao, Q.; Wang, R.; Huang, G.; Jiang, B.; Xu, C.; Pan, F. Origin of the Electrocatalytic Oxygen Evolution Activity of Nickel Phosphides: In-Situ Electrochemical Oxidation and Cr Doping to Achieve High Performance. *Sci. Bull.* **2021**, *66* (7), 708–719. https://doi.org/10.1016/j.scib.2020.11.009.

(162) Cao, X.; Tan, Y.; Zheng, H.; Hu, J.; Chen, X.; Chen, Z. Effect of Cobalt Phosphide (CoP) Vacancies on Its Hydrogen Evolution Activity via Water Splitting: A Theoretical Study. *Phys. Chem. Chem. Phys.* **2022**, *24* (7), 4644–4652. https://doi.org/10.1039/d1cp05739a.

(163) Liu, B.; Cao, B.; Cheng, Y.; Jing, P.; Zhao, J.; Gao, R.; O'Mullane, A.; Zhu, H.; Liu, K.; Sun, X.; Du, Y.; Zhang, J. Ultrafine CoP/Co2P Nanorods Encapsulated in Janus/Twins-Type Honeycomb 3D Nitrogen-Doped Carbon Nanosheets for Efficient Hydrogen Evolution. *iScience* **2020**, *23* (7), 101264. https://doi.org/10.1016/j.isci.2020.101264.

(164) Zhou, K.; Mousavi, B.; Luo, Z.; Phatanasri, S.; Chaemchuen, S.; Verpoort, F. Characterization and Properties of Zn/Co Zeolitic Imidazolate Frameworks vs. ZIF-8 and ZIF-67. *J. Mater. Chem. A* **2017**, *5* (3), 952–957. https://doi.org/10.1039/C6TA07860E.

(165) Shi, J.; Qiu, F.; Yuan, W.; Guo, M.; Lu, Z. H. Nitrogen-Doped Carbon-Decorated Yolk-Shell CoP@FeCoP Micro-Polyhedra Derived from MOF for Efficient Overall Water Splitting. *Chem. Eng. J.* **2021**, *403* (July 2020), 126312. https://doi.org/10.1016/j.cej.2020.126312.

(166) Song, L.; Chang, J.; Ma, Y.; Tan, X.; Xu, Y.; Guo, L.; Chen, Z.; Zhao, T.; Li, Y.; Liu, Y.; Zhang, Y.; Chu, W. Cobalt/Nitrogen Codoped Carbon Nanosheets Derived from Catkins as a High Performance Non-Noble Metal Electrocatalyst for Oxygen Reduction Reaction and Hydrogen Evolution Reaction. *RSC Adv.* **2020**, *10* (71), 43248–43255. https://doi.org/10.1039/d0ra08750e.

(167) Jin, Q.; Ren, B.; Cui, H.; Wang, C. Nitrogen and Cobalt Co-Doped Carbon Nanotube Films as Binder-Free Trifunctional Electrode for Flexible Zinc-Air Battery and Self-Powered Overall Water Splitting. *Appl. Catal. B Environ.* **2021**, *283* (June 2020), 119643. https://doi.org/10.1016/j.apcatb.2020.119643.

(168) Fei, H.; Dong, J.; Feng, Y.; Allen, C. S.; Wan, C.; Volosskiy, B.; Li, M.; Zhao, Z.; Wang, Y.; Sun, H.; An, P.; Chen, W.; Guo, Z.; Lee, C.; Chen, D.; Shakir, I.; Liu, M.; Hu, T.; Li, Y.; Kirkland, A. I.; Duan, X.; Huang, Y. General Synthesis and Definitive Structural Identification of MN4C4 Single-Atom Catalysts with Tunable Electrocatalytic Activities. *Nat. Catal.* **2018**, *1* (1), 63–72. https://doi.org/10.1038/s41929-017-0008-y.

(169) Xie, J.; Zhang, H.; Li, S.; Wang, R.; Sun, X.; Zhou, M.; Zhou, J.; Lou, X. W.; Xie, Y. Defect-Rich MoS2 Ultrathin Nanosheets with Additional Active Edge Sites for Enhanced Electrocatalytic Hydrogen Evolution. *Adv. Mater.* **2013**, *25* (40), 5807–5813. https://doi.org/10.1002/adma.201302685.

(170) Marceta Kaninski, M. P.; Nikolic, V. M.; Tasic, G. S.; Rakocevic, Z. L. Electrocatalytic Activation of Ni Electrode for Hydrogen Production by

Electrodeposition of Co and V Species. *Int. J. Hydrogen Energy* **2009**, *34* (2), 703–709. https://doi.org/10.1016/j.ijhydene.2008.09.024.

(171) Bajdich, M.; García-Mota, M.; Vojvodic, A.; Nørskov, J. K.; Bell, A. T. Theoretical Investigation of the Activity of Cobalt Oxides for the Electrochemical Oxidation of Water. *J. Am. Chem. Soc.* **2013**, *135* (36), 13521–13530. https://doi.org/10.1021/ja405997s.

(172) Papanikolaou, G.; Centi, G.; Perathoner, S.; Lanzafame, P. Catalysis for e - Chemistry: Need and Gaps for a Future De-Fossilized Chemical Production, with Focus on the Role of Complex (Direct) Syntheses by Electrocatalysis . *ACS Catal.* **2022**, 2861–2876. https://doi.org/10.1021/acscatal.2c00099.

(173) Wang, Y.; Zhang, M.; Shen, X.; Wang, H.; Wang, H.; Xia, K.; Yin, Z.; Zhang, Y. Biomass-Derived Carbon Materials: Controllable Preparation and Versatile Applications. *Small* **2021**, *17* (40), 1–32. https://doi.org/10.1002/smll.202008079.

(174) Wang, B.; Xu, L.; Liu, G.; Zhang, P.; Zhu, W.; Xia, J.; Li, H. Biomass Willow Catkin-Derived Co3O4/N-Doped Hollow Hierarchical Porous Carbon Microtubes as an Effective Tri-Functional Electrocatalyst. *J. Mater. Chem. A* **2017**, *5* (38), 20170–20179. https://doi.org/10.1039/c7ta05002j.

(175) Wang, C.; Chen, W.; Xia, K.; Xie, N.; Wang, H.; Zhang, Y. Silk-Derived 2D Porous Carbon Nanosheets with Atomically-Dispersed Fe-N x -C Sites for Highly Efficient Oxygen Reaction Catalysts. *Small* **2019**, *15* (7), 1–6. https://doi.org/10.1002/smll.201804966.

(176) Patil, A. B.; Meng, Z.; Wu, R.; Ma, L.; Xu, Z.; Shi, C.; Qiu, W.; Liu, Q.; Zhang, Y.; Lin, Y.; Lin, N.; Liu, X. Y. Tailoring the Meso-Structure of Gold Nanoparticles in Keratin-Based Activated Carbon Toward High-Performance Flexible Sensor. *Nano-Micro Lett.* **2020**, *12* (1), 1–13. https://doi.org/10.1007/s40820-020-00459-5.

(177) Sun, Q.; Yu, D.; Mo, F.; Wu, M.; Liu, Y.; Dong, X. Wool Textile-Derived Nitrogen-Doped Porous Carbon Cloth for a Binder-Free Electrode Material for High-Performance Flexible Solid-State Supercapacitors. *J. Mater. Sci.* **2021**, *56* (3), 2412–2424. https://doi.org/10.1007/s10853-020-05314-x.

(178) Yang, J.; Tian, Q.; Zhou, Y.; Wang, X. Y.; Zheng, X. C. Facile Synthesis and Superior Capacitive Behavior of Cattail Wool-Derived Hierarchical Porous Carbon. *J. Electroanal. Chem.* **2021**, *882*, 115025. https://doi.org/10.1016/j.jelechem.2021.115025.

(179) Cataldi, P.; Condurache, O.; Spirito, D.; Krahne, R.; Bayer, I. S.; Athanassiou, A.; Perotto, G. Keratin-Graphene Nanocomposite: Transformation of Waste Wool in Electronic Devices. *ACS Sustain. Chem. Eng.* **2019**, *7* (14), 12544–12551. https://doi.org/10.1021/acssuschemeng.9b02415.

(180) Bradbury, J. H.; Chapman, G. V. The Chemioal Oomposition of Wool. *Aust. J. Biol. Sci.* **1964**, *17*, 960–972.

(181) Grosvenor, A. J.; Deb-Choudhury, S.; Middlewood, P. G.; Thomas, A.; Lee, E.; Vernon, J. A.; Woods, J. L.; Taylor, C.; Bell, F. I.; Clerens, S. The Physical and Chemical Disruption of Human Hair after Bleaching – Studies by Transmission Electron Microscopy and Redox Proteomics. *Int. J. Cosmet. Sci.* **2018**, *40* (6), 536–548. https://doi.org/10.1111/ics.12495.

(182) Buchacher, M.; Bechtold, T.; Pham, T. Characterisation of Reduction State of Cystine Linkages on Wool Fibre Surface under Heterogeneous Reaction Conditions. *Polym. Test.* **2022**, *106* (November 2021), 107438. https://doi.org/10.1016/j.polymertesting.2021.107438.

(183) Patil, A. B.; Meng, Z.; Wu, R.; Ma, L.; Xu, Z.; Shi, C.; Qiu, W.; Liu, Q.; Zhang, Y.; Lin, Y.; Lin, N.; Liu, X. Y. Tailoring the Meso-Structure of Gold Nanoparticles in Keratin-Based Activated Carbon Toward High-Performance Flexible Sensor. *Nano-Micro Lett.* **2020**, *12* (1), 1–11. https://doi.org/10.1007/s40820-020-00459-5.

(184) Zhang, X.; Guo, Y.; Li, W.; Zhang, J.; Wu, H.; Mao, N.; Zhang, H. Magnetically Recyclable Wool Keratin Modified Magnetite Powders for Efficient Removal of Cu2+ Ions from Aqueous Solutions. *Nanomaterials* **2021**, *11* (5). https://doi.org/10.3390/nano11051068.

(185) Fronzi, M.; Assadi, M. H. N.; Ford, M. J. Ab Initio Investigation of Water Adsorption and Hydrogen Evolution on Co9S8 and Co3S4 Low-Index Surfaces. *ACS Omega* **2018**, *3* (9), 12215–12228. https://doi.org/10.1021/acsomega.8b00989.

(186) Wang, V.; Xu, N.; Liu, J. C.; Tang, G.; Geng, W. T. VASPKIT: A User-Friendly Interface Facilitating High-Throughput Computing and Analysis Using VASP Code. *Comput. Phys. Commun.* **2021**, *267*, 108033. https://doi.org/10.1016/j.cpc.2021.108033.

(187) Wojciechowska, E.; Włochowicz, A.; Wesełucha-Birczyńska, A. Application of Fourier-Transform Infrared and Raman Spectroscopy to Study Degradation of the Wool Fiber Keratin. *J. Mol. Struct.* **1999**, *511–512*, 307–318. https://doi.org/10.1016/S0022-2860(99)00173-8.

(188) Shao, Y.; Zhao, J.; Hu, W.; Xia, Z.; Luo, J.; Zhou, Y.; Zhang, L.; Yang, X.; Ma, N.; Yang, D.; Shi, Q.; Sun, J.; Zhang, L.; Hui, J.; Shao, Y. Regulating Interfacial Ion Migration via Wool Keratin Mediated Biogel Electrolyte toward Robust Flexible Zn-Ion Batteries. *Small* **2022**, *18* (10), 1–12. https://doi.org/10.1002/smll.202107163.

(189) Shavandi, A.; Silva, T. H.; Bekhit, A. A.; Bekhit, A. E. D. A. Keratin: Dissolution, Extraction and Biomedical Application. *Biomater. Sci.* **2017**, *5* (9), 1699–1735. https://doi.org/10.1039/c7bm00411g.

(190) Wang, K.; Li, R.; Ma, J. H.; Jian, Y. K.; Che, J. N. Extracting Keratin from Wool by Using L-Cysteine. *Green Chem.* **2016**, *18* (2), 476–481. https://doi.org/10.1039/c5gc01254f.

(191) Chen, N.; Liu, C. K.; Ashby, R. Modification of Wool Fibers via Base/Cationic Detergent Pretreatment and Transglutaminase-Mediated Reaction of Keratin. *J. Nat. Fibers* **2021**, *00* (00), 1–11. https://doi.org/10.1080/15440478.2021.2002780.

(192) Buchmann, W.; Spezia, R.; Tournois, G.; Cartailler, T.; Tortajada, J. Structures and Fragmentations of Cobalt(II)-Cysteine Complexes in the Gas Phase. *J. Mass Spectrom.* **2007**, *42* (4), 517–526. https://doi.org/10.1002/jms.1183.

(193) Zheng, W.; Liu, M.; Lee, L. Y. S. Electrochemical Instability of Metal-Organic Frameworks: In Situ Spectroelectrochemical Investigation of the Real Active Sites. *ACS Catal.* **2020**, *10* (1), 81–92. https://doi.org/10.1021/acscatal.9b03790.

(194) Barroso Bogeat, A. Understanding and Tuning the Electrical Conductivity of Activated Carbon: A State-of-the-Art Review. *Crit. Rev. Solid State Mater. Sci.* **2021**, *46* (1), 1–37. https://doi.org/10.1080/10408436.2019.1671800.

(195) Vivo-Vilches, J. F.; Bailón-García, E.; Pérez-Cadenas, A. F.; Carrasco-Marín, F.; Maldonado-Hódar, F. J. Tailoring the Surface Chemistry and Porosity of Activated Carbons: Evidence of Reorganization and Mobility of Oxygenated Surface Groups. *Carbon N. Y.* **2014**, *68*, 520–530. https://doi.org/10.1016/j.carbon.2013.11.030.

(196) Wu, Z.; Zhang, X.; Yang, P.; Yang, J.; Liu, Y.; Zhang, T.; Lu, M. Di-Oxidant Sandwich-Type Polymerization Strategy of Polypyrrole on CNTs@wool Felt for Supercapacitors. *Electrochim. Acta* **2021**, *392*, 139056. https://doi.org/10.1016/j.electacta.2021.139056.
(197) Dong, Z.; Jiang, C.; Cheng, H.; Zhao, Y.; Shi, G.; Jiang, L.; Qu, L. Facile Fabrication of Light, Flexible and Multifunctional Graphene Fibers. *Adv. Mater.* **2012**, *24* (14), 1856–1861. https://doi.org/10.1002/adma.201200170.
(198) Gan, W.; Wu, L.; Wang, Y.; Gao, H.; Gao, L.; Xiao, S.; Liu, J.; Xie, Y.; Li, T.; Li, J. Carbonized Wood Decorated with Cobalt-Nickel Binary Nanoparticles as a Low-Cost and Efficient Electrode for Water Splitting. *Adv. Funct. Mater.* **2021**, *2010951*, 1–10. https://doi.org/10.1002/adfm.202010951.
(199) Peng, S.; Li, N.; Han, X.; Sun, W.; Srinivasan, M.; Mhaisalkar, S. G.; Cheng, F.; Yan, Q.; Chen, J.; Ramakrishna, S. Cobalt Sulfide Nanosheet/Graphene/Carbon Nanotube Nanocomposites as Flexible Electrodes for Hydrogen Evolution. *Angew. Chemie - Int. Ed.* **2014**, *53* (46), 12594–12599. https://doi.org/10.1002/anie.201408876.
(200) Tian, Y.; Xu, L.; Li, M.; Yuan, D.; Liu, X.; Qian, J.; Dou, Y.; Qiu, J.; Zhang, S. Interface Engineering of CoS/CoO@N-Doped Graphene Nanocomposite for High-Performance Rechargeable Zn–Air Batteries. *Nano-Micro Lett.* **2021**, *13* (1). https://doi.org/10.1007/s40820-020-00526-x.
(201) Wang, J.; Zhong, H. X.; Wang, Z. L.; Meng, F. L.; Zhang, X. B. Integrated Three-Dimensional Carbon Paper/Carbon Tubes/Cobalt-Sulfide Sheets as an Efficient Electrode for Overall Water Splitting. *ACS Nano* **2016**, *10* (2), 2342–2348. https://doi.org/10.1021/acsnano.5b07126.
(202) Yao, N.; Wang, G.; Jia, H.; Yin, J.; Cong, H.; Chen, S.; Luo, W. Intermolecular Energy Gap-Induced Formation of High-Valent Cobalt Species in CoOOH Surface Layer on Cobalt Sulfides for Efficient Water Oxidation. *Angew. Chemie Int. Ed.* **2022**, *202117178*, 1–8. https://doi.org/10.1002/anie.202117178.
(203) Bai, N.; Li, Q.; Mao, D.; Li, D.; Dong, H. One-Step Electrodeposition of Co/CoP Film on Ni Foam for Efficient Hydrogen Evolution in Alkaline Solution. *ACS Appl. Mater. Interfaces* **2016**, *8* (43), 29400–29407. https://doi.org/10.1021/acsami.6b07785.
(204) Zhang, J.; Sun, R.; Zhang, X.; Wu, J.; Dou, Y.; Zhu, X.; Yu, L.; Guo, L.; Liu, M.; Guo, L.; Cao, L.; He, C.; Chen, X. Biodiversity Benefits for Size Modulation of Metal Nanoparticles to Achieve In Situ Semi-Oxidation toward Optimized Electrocatalytic Oxygen Evolution. **2022**, *2202119*, 1–10. https://doi.org/10.1002/adfm.202202119.
(205) Qian, Y.; Jiang, S.; Li, Y.; Yi, Z.; Zhou, J.; Li, T.; Han, Y.; Wang, Y.; Tian, J.; Lin, N.; Qian, Y. In Situ Revealing the Electroactivity of P O and P C Bonds in Hard Carbon for High-Capacity and Long-Life Li/K-Ion Batteries. *Adv. Energy Mater.* **2019**, *9* (34), 1–10. https://doi.org/10.1002/aenm.201901676.
(206) Chen, W.; Liu, X.; He, R. L.; Lin, T.; Zeng, Q. F.; Wang, X. G. Activated Carbon Powders from Wool Fibers. *Powder Technol.* **2013**, *234*, 76–83. https://doi.org/10.1016/j.powtec.2012.09.026.
(207) Han, Y.; Shen, N.; Zhang, S.; Li, D.; Li, X. Fish Gill-Derived Activated Carbon for Supercapacitor Application. *J. Alloys Compd.* **2017**, *694*, 636–642. https://doi.org/10.1016/j.jallcom.2016.10.013.
(208) Tang, W.; Fu, C.; Lyu, P.; Xu, W.; Chen, W. Influence of Cuticle Layers, Temperatures and Activators on the Properties of Size-Controllable Tubular Activated Carbon Powder from Wool Waste under Air Flow. *Powder Technol.*

2021, *392*, 38–46. https://doi.org/10.1016/j.powtec.2021.06.045.
(209) Wu, Z. Y.; Xu, S. L.; Yan, Q. Q.; Chen, Z. Q.; Ding, Y. W.; Li, C.; Liang, H. W.; Yu, S. H. Transition Metal–Assisted Carbonization of Small Organic Molecules toward Functional Carbon Materials. *Sci. Adv.* **2018**, *4* (7), 1–12. https://doi.org/10.1126/sciadv.aat0788.
(210) Zhang, P.; Zhang, J.; Dai, S. Mesoporous Carbon Materials with Functional Compositions. *Chem. - A Eur. J.* **2017**, *23* (9), 1986–1998. https://doi.org/10.1002/chem.201602199.
(211) Andreiadis, E. S.; Jacques, P. A.; Tran, P. D.; Leyris, A.; Chavarot-Kerlidou, M.; Jousselme, B.; Matheron, M.; Pécaut, J.; Palacin, S.; Fontecave, M.; Artero, V. Molecular Engineering of a Cobalt-Based Electrocatalytic Nanomaterial for H 2 Evolution under Fully Aqueous Conditions. *Nat. Chem.* **2013**, *5* (1), 48–53. https://doi.org/10.1038/nchem.1481.
(212) Dai, J. Y.; Balamurugan, J.; Kim, N. H.; Lee, J. H. Hierarchical CoS@MoS2 Core-Shell Nanowire Arrays as Free-Standing Electrodes for High-Performance Asymmetric Supercapacitors. *J. Alloys Compd.* **2020**, *825*, 154085. https://doi.org/10.1016/j.jallcom.2020.154085.
(213) Zhang, H.; Zhang, J.; Li, Y.; Jiang, H.; Jiang, H.; Li, C. Continuous Oxygen Vacancy Engineering of the Co3O4 Layer for an Enhanced Alkaline Electrocatalytic Hydrogen Evolution Reaction. *J. Mater. Chem. A* **2019**, *7* (22), 13506–13510. https://doi.org/10.1039/c9ta03652k.
(214) Wang, M.; Wan, Z.; Meng, X.; Li, Z.; Ding, X.; Li, P.; Li, C.; Wang, J. G.; Li, Z. Heterostructured Co/Mo-Sulfide Catalyst Enables Unbiased Solar Water Splitting by Integration with Perovskite Solar Cells. *Appl. Catal. B Environ.* **2022**, *309* (February), 121272. https://doi.org/10.1016/j.apcatb.2022.121272.
(215) Chen, Z.; Song, Y.; Cai, J.; Zheng, X.; Han, D.; Wu, Y.; Zang, Y.; Niu, S.; Liu, Y.; Zhu, J.; Liu, X.; Wang, G. Tailoring the D-Band Centers Enables Co4N Nanosheets To Be Highly Active for Hydrogen Evolution Catalysis. *Angew. Chemie - Int. Ed.* **2018**, *57* (18), 5076–5080. https://doi.org/10.1002/anie.201801834.
(216) Fabian, D. M.; Hu, S.; Singh, N.; Houle, F. A.; Hisatomi, T.; Domen, K.; Osterloh, F. E.; Ardo, S. Particle Suspension Reactors and Materials for Solar-Driven Water Splitting. *Energy Environ. Sci.* **2015**, *8* (10), 2825–2850. https://doi.org/10.1039/c5ee01434d.
(217) Liu, J.; Liu, Y.; Liu, N.; Han, Y.; Zhang, X.; Huang, H.; Lifshitz, Y.; Lee, S. T.; Zhong, J.; Kang, Z. Metal-Free Efficient Photocatalyst for Stable Visible Water Splitting via a Two-Electron Pathway. *Science (80-.).* **2015**, *347* (6225), 970–974. https://doi.org/10.1126/science.aaa3145.
(218) Xu, Q.; Zhang, L.; Cheng, B.; Fan, J.; Yu, J. S-Scheme Heterojunction Photocatalyst. *Chem* **2020**, *6* (7), 1543–1559. https://doi.org/10.1016/j.chempr.2020.06.010.
(219) Zheng, X.; Song, Y.; Liu, Y.; Li, J.; Yang, Y.; Wu, D.; Liu, W.; Shen, Y.; Tian, X. Synthesis of Phase Junction Cadmium Sulfide Photocatalyst under Sulfur-Rich Solution System for Efficient Photocatalytic Hydrogen Evolution. *Small* **2023**. https://doi.org/10.1002/smll.202207623.
(220) Cheng, C.; Zhang, J.; Zhu, B.; Liang, G.; Zhang, L.; Yu, J. Verifying the Charge-Transfer Mechanism in S-Scheme Heterojunctions Using Femtosecond Transient Absorption Spectroscopy. *Angew. Chemie - Int. Ed.* **2022**, *202218688*. https://doi.org/10.1002/anie.202218688.
(221) Chen, Y.; Zhao, S.; Wang, X.; Peng, Q.; Lin, R.; Wang, Y.; Shen, R.; Cao, X.;

Zhang, L.; Zhou, G.; Li, J.; Xia, A.; Li, Y. Synergetic Integration of Cu1.94S-ZnxCd1-XS Heteronanorods for Enhanced Visible-Light-Driven Photocatalytic Hydrogen Production. *J. Am. Chem. Soc.* **2016**, *138* (13), 4286–4289. https://doi.org/10.1021/jacs.5b12666.

(222) Li, K.; Pan, H.; Wang, F.; Zhang, Z.; Min, S. In-Situ Exsolved NiS Nanoparticle-Socketed CdS with Strongly Coupled Interfaces as a Superior Visible-Light-Driven Photocatalyst for Hydrogen Evolution. *Appl. Catal. B Environ.* **2023**, *321* (September 2022), 122028. https://doi.org/10.1016/j.apcatb.2022.122028.

(223) Yin, X. L.; Li, L. L.; Jiang, W. J.; Zhang, Y.; Zhang, X.; Wan, L. J.; Hu, J. S. MoS2/CdS Nanosheets-on-Nanorod Heterostructure for Highly Efficient Photocatalytic H2 Generation under Visible Light Irradiation. *ACS Appl. Mater. Interfaces* **2016**, *8* (24), 15258–15266. https://doi.org/10.1021/acsami.6b02687.

(224) Jian, W.; Cheng, X.; Huang, Y.; You, Y.; Zhou, R.; Sun, T.; Xu, J. Arrays of ZnO/MoS2 Nanocables and MoS2 Nanotubes with Phase Engineering for Bifunctional Photoelectrochemical and Electrochemical Water Splitting. *Chem. Eng. J.* **2017**, *328*, 474–483. https://doi.org/10.1016/j.cej.2017.07.056.

(225) Wang, Y.; Liu, Y. H.; Zhang, Y.; Wang, F.; Kowalski, P. J.; Rohrs, H. W.; Loomis, R. A.; Gross, M. L.; Buhro, W. E. Isolation of the Magic-Size CdSe Nanoclusters [(CdSe) 13(n- Octylamine) 13] and [(CdSe) 13(Oleylamine) 13]. *Angew. Chemie - Int. Ed.* **2012**, *51* (25), 6154–6157. https://doi.org/10.1002/anie.201202380.

(226) Nevers, D. R.; Williamson, C. B.; Hanrath, T.; Robinson, R. D. Surface Chemistry of Cadmium Sulfide Magic-Sized Clusters: A Window into Ligand-Nanoparticle Interactions. *Chem. Commun.* **2017**, *53* (19), 2866–2869. https://doi.org/10.1039/c6cc09549f.

(227) Smith, R. D. L.; Prévot, M. S.; Fagan, R. D.; Zhang, Z.; Sedach, P. A.; Siu, M. K. J.; Trudel, S.; Berlinguette, C. P. Photochemical Route for Accessing Amorphous Metal Oxide Materials for Water Oxidation Catalysis. *Science (80-.).* **2013**, *340* (6128), 60–63. https://doi.org/10.1126/science.1233638.

(228) Zhang, P.; Guan, B. Y.; Yu, L.; Lou, X. W. (David). Facile Synthesis of Multi-Shelled ZnS-CdS Cages with Enhanced Photoelectrochemical Performance for Solar Energy Conversion. *Chem* **2018**, *4* (1), 162–173. https://doi.org/10.1016/j.chempr.2017.10.018.

(229) Huang, D.; Wen, M.; Zhou, C.; Li, Z.; Cheng, M.; Chen, S.; Xue, W.; Lei, L.; Yang, Y.; Xiong, W.; Wang, W. ZnxCd1-XS Based Materials for Photocatalytic Hydrogen Evolution, Pollutants Degradation and Carbon Dioxide Reduction. *Appl. Catal. B Environ.* **2020**, *267* (September 2019), 118651. https://doi.org/10.1016/j.apcatb.2020.118651.

(230) Han, X.; Li, J.; Lu, J.; Luo, S.; Wan, J.; Li, B.; Hu, C.; Cheng, X. High Mass-Loading NiCo-LDH Nanosheet Arrays Grown on Carbon Cloth by Electrodeposition for Excellent Electrochemical Energy Storage. *Nano Energy* **2021**, *86* (March), 106079. https://doi.org/10.1016/j.nanoen.2021.106079.

(231) He, C.; Yang, L.; Peng, X.; Liu, S.; Wang, J.; Dong, C.; Du, D. Alkylamine-Confined Thickness-Tunable Synthesis of Co (OH) 2 - CoO Nanosheets toward Oxygen Evolution Catalysis. **2023**. https://doi.org/10.1021/acsnano.2c12735.

(232) Zeiri, L.; Patla, I.; Acharya, S.; Golan, Y.; Efrima, S. Raman Spectroscopy of Ultranarrow CdS Nanostructures. *J. Phys. Chem. C* **2007**, *111* (32), 11843–11848. https://doi.org/10.1021/jp072015q.

(233) Bai, X.; Ren, Z.; Du, S.; Meng, H.; Wu, J.; Xue, Y.; Zhao, X.; Fu, H. In-Situ Structure Reconstitution of NiCo2Px for Enhanced Electrochemical Water

Oxidation. *Sci. Bull.* **2017**, *62* (22), 1510–1518. https://doi.org/10.1016/j.scib.2017.10.019.
(234) Luo, M.; Liu, Y.; Hu, J.; Liu, H.; Li, J. One-Pot Synthesis of CdS and Ni-Doped CdS Hollow Spheres with Enhanced Photocatalytic Activity and Durability. *ACS Appl. Mater. Interfaces* **2012**, *4* (3), 1813–1821. https://doi.org/10.1021/am3000903.
(235) Song, F.; Hu, X. Exfoliation of Layered Double Hydroxides for Enhanced Oxygen Evolution Catalysis. *Nat. Commun.* **2014**, *5*. https://doi.org/10.1038/ncomms5477.
(236) Li, Z.; Zhou, Y.; Xie, M.; Cheng, H.; Wang, T.; Chen, J.; Lu, Y.; Tian, Z.; Lai, Y.; Yu, G. High-Density Cationic Defects Coupling with Local Alkaline-Enriched Environment for Efficient and Stable Water Oxidation. *Angew. Chemie - Int. Ed.* **2023**, *78712*. https://doi.org/10.1002/anie.202217815.
(237) Xiao, B.; Lv, T.; Zhao, J.; Rong, Q.; Zhang, H.; Wei, H.; He, J.; Zhang, J.; Zhang, Y.; Peng, Y.; Liu, Q. Synergistic Effect of the Surface Vacancy Defects for Promoting Photocatalytic Stability and Activity of ZnS Nanoparticles. *ACS Catal.* **2021**, *11* (21), 13255–13265. https://doi.org/10.1021/acscatal.1c03476.
(238) Liu, S.; Qi, W.; Liu, J.; Meng, X.; Adimi, S.; Attfield, J. P.; Yang, M. Modulating Electronic Structure to Improve the Solar to Hydrogen Efficiency of Cobalt Nitride with Lattice Doping. *ACS Catal.* **2023**, 2214–2222. https://doi.org/10.1021/acscatal.2c05075.
(239) Huang, M.; Liu, C.; Cui, P.; Wu, T.; Feng, X.; Huang, H.; Zhou, J.; Wang, Y. Facet-Dependent Photoinduced Transformation of Cadmium Sulfide (CdS) Nanoparticles. *Environ. Sci. Technol.* **2021**, *55* (19), 13132–13141. https://doi.org/10.1021/acs.est.1c04026.
(240) Hsieh, Y. H.; Huang, C. P. Photooxidative Dissolution of CdS(s) Part I. Important Factors and Mechanistic Aspects. *Colloids and Surfaces* **1991**, *53* (2), 275–295. https://doi.org/10.1016/0166-6622(91)80142-B.
(241) Tang, H.; Xu, G.; Weng, L.; Pan, L.; Wang, L. Luminescence and Photophysical Properties of Colloidal ZnS Nanoparticles. *Acta Mater.* **2004**, *52* (6), 1489–1494. https://doi.org/10.1016/j.actamat.2003.11.030.
(242) Lin, Y.; Zhang, Q.; Li, Y.; Liu, Y.; Xu, K.; Huang, J.; Zhou, X.; Peng, F. The Evolution from a Typical Type-I CdS/ZnS to Type-II and Z-Scheme Hybrid Structure for Efficient and Stable Hydrogen Production under Visible Light. *ACS Sustain. Chem. Eng.* **2020**, *8* (11), 4537–4546. https://doi.org/10.1021/acssuschemeng.0c00101.